Experimental and theoretical investigations of magnetic, electronic structure, and hyperfine interaction properties of new Fe-based superconductors and EuFeAs$_2$

Mohammed Albedah

Thesis submitted to the University of Ottawa

Department of Physics
University of Ottawa

© Mohammed Albedah, Ottawa, Canada, 2021

uOttawa

L'Université canadienne
Canada's university

Table of Contents

List of figures

Abstract

This thesis presents the experimental studies of the magnetic and hyperfine interaction properties of four novel Fe-based superconductors (ThFeAsN, $CsEuFe_4As_4$, $Rb_{1-\delta}EuFe_4As_4$, and $EuFe_{0.97}Ni_{0.03}As_2$) and one new non-superconducting compound ($EuFeAs_2$). It is supplemented by *ab-initio* calculations of the electronic structure and magnetism of the three superconductors. The experimental studies are based on the results of x-ray diffraction, magnetic susceptibility, magnetization, and ^{57}Fe and ^{151}Eu Mössbauer spectroscopy measurements.

The superconductor ThFeAsN crystallizes in the tetragonal space group $P4/nmm$ with the lattice parameters a = 4.0356(1) Å and c = 8.5286(1) Å. It is shown that there is no magnetic order of the Fe magnetic moments down to 2.0 K. We suggest that nonappearance of Fe magnetism in ThFeAsN may be because of an internal uniaxial chemical pressure whose presence is manifested by the unusually small c/a ratio. We provide theoretical evidence for a mixture of ionic and covalent chemical bonding and metallic characteristics. We present a detailed analysis of the calculated energy band structure of ThFeAsN. A quadrupole doublet well describes the shape of the Mössbauer spectra with a small quadrupole splitting that increases with lowering temperature. Good agreement is found between the calculated and extrapolated 0 K quadrupole splitting values. A fair agreement is noted between the experimental Debye temperature 332(2) K and 370 K of the calculated one.

We show that the superconductor $CsEuFe_4As_4$ crystallizes in the tetragonal space group $P4/mmm$ with the lattice parameters a = 3.8956(1) Å and c = 13.6628(5) Å. We show that the Fe atoms carry no magnetic moment down to 2.1 K and that the ferromagnetic order is related to the Eu magnetic moments. We establish that the Curie temperature T_C = 15.97(8) K found from the temperature dependence of the hyperfine magnetic field at ^{151}Eu nuclei is well-matched with the temperature dependence of the transferred hyperfine magnetic field at ^{57}Fe nuclei that is produced by the ferromagnetically ordered Eu sublattice. The magnetic moments of the Eu atoms are shown to be perpendicular to the crystallographic c-axis. The $T^{3/2}$ power-law perfectly describes the temperature dependence of the principal component of the electric field gradient tensor, both at Fe and Eu sites. The calculated and the measured parameters of the hyperfine-interaction are in excellent agreement with each other. We determine that the Debye temperature of $CsEuFe_4As_4$ is 295(3) K.

Ab-initio calculations suggest a mixture of ionic, covalent, and metallic bonding between the constituent atoms in the $CsEuFe_4As_4$ superconductor. We confirm that the strongly localized Eu f states are the origin of the magnetic moment of $CsEuFe_4As_4$, in agreement with the experimental results. We show that an almost zero magnetic moment carried by the Fe atoms is caused by the spin-up and spin-down states' apparent symmetry. We show that the Fermi surfaces have hole-like and electron-like pockets located at the center and corners of the Brillouin zone, respectively.

The superconductor $Rb_{1-\delta}EuFe_4As_4$ crystallizes in the tetragonal space group *P*4*/mmm* with the lattice parameters *a* = 3.8849(1) Å and *c* = 13.3370(3) Å. We show that the Fe atoms carry no magnetic moment down to 2.1 K and that the ferromagnetic order is associated solely with the Eu magnetic moments. The Curie temperature T_{C} = 16.54(8) K is found from the temperature dependence of both the hyperfine magnetic field at ^{151}Eu nuclei and the transferred hyperfine magnetic field at ^{57}Fe nuclei induced by the ferromagnetically ordered Eu sublattice. We find that the Eu magnetic moments lie in the *ab* plane. It is observed that the temperature dependence of the principal component of the electric field gradient tensor, at both Fe and Eu sites, is well described by a $T^{3/2}$ power-law relation. There is good agreement between the calculated and measured parameters of the hyperfine-interaction. We determine that the Debye temperature of $Rb_{1-\delta}EuFe_4As_4$ is 391(8) K.

Ab-initio calculations indicate the presence of a mixture of ionic, covalent, and metallic bonding between the constituent atoms in the $RbEuFe_4As_4$ superconductor. We show that the magnetic moment of $RbEuFe_4As_4$ is mainly a result of the strongly localized Eu *f* states. It is shown that an almost zero magnetic moment carried by the Fe atoms originates from an apparent symmetry of the spin-up and spin-down states. We show that the electrical and chemical properties of $RbEuFe_4As_4$ are closely associated with the presence of the Fe *3d* states in the Fermi energy region. The Fermi surfaces display hole-like and electron-like pockets, respectively, at the center and corners of the Brillouin zone.

We find that in both the $EuFeAs_2$ compound and 14 K superconductor $EuFe_{0.97}Ni_{0.03}As_2$ the antiferromagnetic ordering of the Fe sublattice is of a spin-density-wave type with the Néel temperatures and Fe saturation magnetic moments of 106.2(1.9) K, 0.78(1) μ_B and 56.6(2.2) K, 0.47(1) μ_B, respectively. We show that the Néel temperatures and the saturation hyperfine magnetic fields in the two compounds with the antiferromagnetically ordered Eu sublattice are 44.4(5) K, 294.2(7) kOe and 43.5(1) K, 290.5(1) kOe respectively. The 3% substitution of Fe by Ni in $EuFeAs_2$, aside from producing superconductivity in $EuFe_{0.97}Ni_{0.03}As_2$, radically reduces the strength of magnetism of the Fe sublattice and has nearly no impact on the magnetism of the Eu sublattice. The appearance of antiferromagnetically ordered Fe and Eu sublattices in $EuFe_{0.97}Ni_{0.03}As_2$ verifies that superconductivity and magnetism coexist in this compond. The growth of the magnitude of the main component of the electric field gradient tensor, at both Fe and Eu sites, with reducing temperature, is well described by a $T^{3/2}$ power-law relation. We determine the Debye temperatures of $EuFeAs_2$, $EuFe_{0.97}Ni_{0.03}As_2$, and the $FeAs_2$ impurity phase to be 355(18), 428(14), and 594(25) K, respectively.

In summary, for all of the studied compounds, there is no magnetic ordering associated with iron sub-lattices in the ThFeAsN, $CsEuFe_4As_4$, and $Rb_{1-\delta}EuFe_4As_4$ compounds. The iron sublattice is magnetically ordered in the $EuFeAs_2$ and the $EuFe_{0.97}Ni_{0.03}As_2$ superconductor. There is a coexistence of magnetism and superconductivity associated with europium in the $CsEuFe_4As_4$, $Rb_{1-\delta}EuFe_4As_4$, $EuFe_{0.97}Ni_{0.03}As_2$ compounds. There is a good agreement between the calculated and the measured hyperfine and magnetic parameters for most studied compounds.

Statement of originality and contributions of co-authors

To the best of his knowledge, the author declares that the studies of five novel compounds (ThFeAsN, $CsEuFe_4As_4$, $RbEuFe_4As_4$, $EuFeAs_2$, and $EuFe_{0.97}Ni_{0.03}As_2$) reported in this Ph.D. thesis constitute original research in the field of condensed-matter physics. In the following paragraphs, I provide detailed information on the contributions of each participant to these studies.

In regards to the ThFeAsN superconductor, I conducted all x-ray diffraction (XRD) and ^{57}Fe Mössbauer experiments, fitted all the XRD, Mössbauer, and magnetic data to appropriate models, and wrote the first draft of the paper. F. Nejadsattari carried out *ab-initio* calculations. Z.M. Stadnik suggested the project and wrote the final draft of the paper. Z.-C. Wang, C. Wang, and G.-H. Cao provided the specimen.

For the $CsEuFe_4As_4$ superconductor, I conducted all XRD and ^{57}Fe and ^{151}Eu Mössbauer experiments, evaluated XRD, Mössbauer, and magnetic data, and wrote the first draft of the paper. F. Nejadsattari carried out a*b-initio* calculations. Z.M. Stadnik designed the project and wrote the final version of the paper. Y. Liu and G.-H. Cao provided the sample.

In respect of the $Rb_{1-\delta}EuFe_4As_4$ superconductor, I conducted all XRD and ^{57}Fe and ^{151}Eu Mössbauer experiments, evaluated XRD, Mössbauer, and magnetic data, and wrote the first draft of the manuscript. F. Nejadsattari did a*b-initio* calculations. Z.M. Stadnik suggested the project and wrote the final version of the manuscript. Y. Liu and G.-H. Cao provided the sample.

Regarding the two compounds, $EuFeAs_2$, and $EuFe_{0.97}Ni_{0.03}As_2$, I conducted all ^{57}Fe, ^{151}Eu Mössbauer experiments, evaluated Mössbauer, and magnetic data, and wrote the first draft of the paper. O. Fedoryk participated in some of the ^{57}Fe Mössbauer experiments. Z.M. Stadnik designed the project and wrote the final version of the article. Y.-B. Liu and G.-H. Cao provided the specimens.

Acknowledgements

I want to express my sincere appreciation and deep regards to Prof. Zbigniew M. Stadnik for his excellent support, guidance, monitoring, and constant encouragement throughout the work on this thesis. The help and advice he has given will influence my future work and benefit me throughout my career.

I would also like to offer my sincere thanks and appreciation to Majmaah University for supporting me financially and academically in completing my degree.

Thanks may not suffice for my friend and research colleague, Dr. Farshad Nejadsattari, for his valuable help and advice.

Also, I would like to offer a heartfelt thanks and appreciation to my family. I thank my mother, who has helped me a lot during my studies. Dear mom: your blessings and prayers have been a tremendous help for me in enduring and completing my degree. Many thanks to my father for his support. My parents' support, patience, and guidance have played a major role in completing my degree.

Finally, there is a woman behind every important accomplishment. This woman is my wife. My wife has stood by me on this academic journey. Despite her health issue, she has given me a lot of encouragement and support. Dear Alaa: I owe you sincere thanks for your patience and understanding.

Chapter 1: Introduction

1.1 Motivation

The study of condensed matter physics is one of the most interesting research topics introduced in the scientific field. Numerous compounds have been discovered and studied over time. Driven by fast development in technology, the ability to make new compounds improved drastically. Amongst these compounds, superconductors are of primary interest in this research. The physical properties of superconductors are unique. This study's main objective is to look for the possible coexistence of magnetism and superconductivity in these new compounds.

In this thesis, the results of an experimental study of the magnetic and hyperfine-interaction properties of five novel compounds are presented. Those compounds have been chosen because of their novelty and some remarkable features that require further research. This experimental study is supplemented by *ab-initio* calculations of the magnetic and electronic structure properties of four studied superconductors.

The newly synthesized ThFeAsN compound is unusual because it is superconducting, with the critical temperature T_c = 30 K, without any doping or applying pressure. Our study's main objective is to provide evidence for the possible presence or absence of the magnetic moment carried by the Fe atoms. We use the local probe, ^{57}Fe Mössbauer spectroscopy, to report the possible magnetic order in ThFeAsN.

The $CsEuFe_4As_4$ compound is one of the new 35 K superconductors. It was discovered in 2016, and it is one of the new iron-based class of superconductors. The relation between superconductivity and possible long-range magnetic order is of current interest. The primary objective of our research is to examine whether the magnetic moment in $CsEuFe_4As_4$ is correlated only with atoms of Eu or Fe or with atoms of Eu and Fe, and what is their orientation relative to the crystallographic axes. To accomplish this target, ^{57}Fe and ^{151}Eu Mössbauer spectroscopy, which are confirmed to be an excellent method for investigating the local magnetism of Fe-based superconductors, supplemented by first principles calculations, are used.

$RbEuFe_4As_4$ is a newly synthesized superconductor. Similarly to the study of $CsEuFe_4As_4$, the main objective of this study is to figure out whether the magnetic moment in the superconductor is associated with either Eu or Fe atoms individually or with both Eu and Fe atoms. The study also focuses on determining the orientation of the magnetic moment relative to the crystallographic axes. The study is conducted using ^{57}Fe and ^{151}Eu Mössbauer spectroscopy and is supported by first-principles calculations.

$EuFeAs_2$ and $EuFe_{0.97}Ni_{0.03}As_2$ are recently discovered Eu-containing iron-pnictide compounds. A tiny substitution of Fe by Ni in $EuFeAs_2$ has been shown to produce superconductivity. What makes us curious about this new $EuFe_{0.97}Ni_{0.03}As_2$ superconductor is whether magnetism and superconductivity can coexist in such a compound. We use ^{57}Fe and ^{151}Eu Mössbauer spectroscopy to figure out the nature of the Fe and Eu magnetic ordering in the non-superconducting $EuFeAs_2$ and the superconducting $EuFe_{0.97}Ni_{0.03}As_2$ compounds.

1.2 Thesis outline

The remainder of this thesis includes nine chapters. Before describing the results and conclusions, the theoretical background relevant to the physical problems addressed in this thesis is described in Chapter two. At the end of Chapter 2 the experimental procedures is presented. Chapter three contains general discussion and conclusions, integrating the material presented in Chapters four, five, six, seven, eight, and nine. Chapter four is an article on ThFeAsN that was published in J. Alloys Comp. **695**, 1128 (2017). Chapter five is an article on $CsEuFe_4As_4$ that published in J. Phys.: Condens. Matter **30**, 155803 (2018). Chapter six is an article on $Rb_{1-\delta}EuFe_4As_4$ published in Phys. Rev. B **97**, 144426 (2018). Chapter seven is an article on $EuFeAs_2$ and $EuFe_{0.97}Ni_{0.03}As_2$ that was published in J. Magn. Magn. Mater. **503**, 166603 (2020). Chapter eight is an article on *ab-initio* calculations of the electronic structure and magnetism of $CsEuFe_4As_4$ published in J. Phys. Chem. Solids. **136**,109137 (2020). And chapter nine is an article on *ab-initio* study $RbEuFe_4As_4$ that was published in Philos. Mag. **100**, 894 (2020).

Chapter 2: Theoretical background

2.1 Magnetic properties of solids

The theoretical background that explains the magnetic effects of substances will be introduced in this chapter. In this research, the samples that were studied have different magnetic phases and are studied under multiple temperature regimes. The current theories of magnetism allow the understanding of the experimental magnetic properties of the studied compounds.

2.1.1 Introduction

The magnetic dipole moment $\boldsymbol{\mu}$ is the essential component of all magnetic materials, as well as of the emerging properties linked with magnetic phenomena. The combined behavior of these magnetic moments yields the magnetic features of materials. According to quantum mechanical theories [1], the magnetic dipole moments detected in substances arise from two major origins. Within the atom, the orbital angular momentum and the spin angular momentum of electrons are the main contributors to the magnetic moments. The electrons' orbital motion about the nucleus can create a very small current loop that produces a magnetic dipole moment. Furthermore, the degree of freedom of the spin angular momentum directly corresponds to the magnetic dipole moment making electrons ideal magnetic dipoles.

The diamagnetism phenomenon occurs when the magnetic field B interacts with the electrons of an atom causing an induced magnetic dipole moment. Evidently, diamagnetism is expected in most material since they are all composed of atoms having electrons in orbit.

Permanent magnetic moments might be allowed to exist in substances because of the atoms' electronic structure. Excluding diamagnetism, the magnetic properties are a result of the presence of permanent dipole moments. The permeant moments of atoms interact with each other. Materials can be categorized in regards to their magnetic properties determined by the intensity of the couplings of the magnetic moments. The substance is deemed paramagnetic when the coupling is weak or zero. With regards to paramagnetic materials, they exhibit the magnetic properties just at the time they are exposed to external magnetic fields. Once the external magnetic field is removed, the overall magnetic moment disappears. The phenomena of ferromagnetism and antiferromagnetism arise in the materials when there is a strong coupling between the dipole moments. The substance is known as ferromagnetic if the magnetic moments are aligned in a parallel fashion, and produces an intense net magnetic moment. Nonetheless, when the pairs of dipole moments line up in an antiparallel way, the overall magnetic moment will fade away due to the cancellations of the neighboring dipoles. In this situation, the material is said to be antiferromagnetic.

The magnetization of a substance is known as the magnetic moment per unit volume. For materials having a net magnetic moment, the magnetization $\mathbf{M}$ can be described as [1]

$$\mathbf{M} = \frac{d\boldsymbol{\mu}}{d^3x}, \qquad 1\text{–}1$$

where d^3x is a small volume element, and $d\boldsymbol{\mu}$ is the magnetic moment inside the volume dimension. The magnetization directly correlates to the applied magnetic field $\mathbf{H}$, and the constant of variation between the magnetization and magnetic field is called the magnetic susceptibility χ [1]

$$\mathbf{M} = \chi\mathbf{H}. \qquad 1\text{–}2$$

2.1.2 Diamagnetism and the susceptibility of diamagnetic materials

All materials display diamagnetism, and this phenomenon is due to Faraday's law. In essence, the variation in the magnetic flux in a current loop produces a current in a way that resist the external magnetic field. Since electrons around the nucleus move in an orbital motion, they produce small currents. Thus whenever the substance is exposed to an exterior magnetic field, a magnetic moment is produced in a way to lower the field. The induced diamagnetic moment persists only if the material is exposed to the external field. The induced magnetic dipole moment is given by [2]

$$\boldsymbol{\mu} = -\frac{e^2}{6mc^2}\langle x^2\rangle\mathbf{H}. \qquad 1\text{–}3$$

Here, e is the electron charge, m as the electron's mass, c as the speed of light, and $\langle x^2\rangle$ as the average square distance of the electron from the nucleus. Langevin, in addition to a modification completed by Wolfgang Pauli, proposed the diamagnetic susceptibility taking into account Z electrons in an atom and a number density of n atoms per unit volume of the material [2]

$$\chi_{\text{diamagnetic}} = -n\frac{e^2}{6mc^2}\sum_{\mathrm{i}=1}^{\mathrm{Z}}\langle \boldsymbol{x}_{\mathrm{i}}{}^2\rangle. \qquad 1\text{–}4$$

Some important details about the diamagnetic susceptibility follow from Equation 1–4: diamagnetism is negative, it is temperature-independent, and it is field-independent [3]. The magnetic susceptibility of diamagnetic materials is in order of 10^{-6}.

2.1.3 Paramagnetism

The paramagnetic occurrence is correlated to the presence of permanent magnetic moments in a substance in which those dipole moments have a tendency to line up themselves with the same orientation of an external applied magnetic field.

2.1.3.1 Curie's paramagnetic susceptibility law

The phenomenon of paramagnetism is observed in substances that have permanent magnetic dipole moments due to their physical and chemical structures. According to Curie and Weiss's earlier experiments, paramagnetic materials can be categorized into two major types. First of all, Curie's law describes the susceptibility of normal paramagnets materials to obey a certain dependence with altering temperature. The dependence occurs in a controlled pattern forcing the product of the susceptibility and the temperature to stay constant. This relation also applies to ferromagnetic and antiferromagneic materials above their ordering temperatures [4]

$$\chi_{\text{paramagnetic}} = \frac{C}{T}\,. \qquad 1\text{–}5$$

The other kind of paramagnetic materials follow susceptibilities that diverge from Curie's law. In this deviation, at the time that the temperature of the material reaches near absolute zero, the susceptibility reaches a finite value associated to what is identified as the paramagnetic Curie point, θ. The modified Curie law, which is recognized as the Curie-Weiss law, is expressed by the equation below [4]

$$\chi_{\text{paramagnetic}} = \frac{C}{T-\theta}\,, \qquad 1\text{–}6$$

where $T > \theta$. When employing the molecular field theory, the Curie-Weiss law will take into account the effects of neighboring atoms. As a result, a magnetic field of magnitude $N_{\text{W}}M$ will be added up to the external field. Thus, the entire field is deemed to be $H + N_{\text{W}}M$. The total result for the magnetization is given by [4, 5]

$$M = \chi(H + N_{\text{W}}M) \overset{\chi=\frac{C}{T}}{\Longrightarrow} M = \frac{CH}{T-CN_{\text{W}}} = \frac{CH}{T-\theta} \overset{\chi=\frac{M}{H}}{\Longrightarrow} \chi = \frac{C}{T-\theta}\,. \qquad 1\text{–}7$$

The atoms and the ions of transition group elements, which have unfilled inner shells, have permanent moments. In addition, odd-electron molecules experience permanent moments. Generally, metals do not obey Curie's law even though they are paramagnetic [4].

The classical kinetic theory of gases accounts for the particles' average energy at an absolute temperature T to be of the order of $k_{\text{B}}T$, where k_{B} is Boltzmann's constant. The particle's energy eigenstates in the system are degenerate based on the quantum mechanical total angular (for H = 0) momentum, J. Once an external magnetic field is applied, the degeneracy is broken and energy multiplets are revealed. A state with a total angular momentum quantum number J forms $2J + 1$ multiplets. According to the classical probability distribution, each state in a certain multiplet might be occupied. Furthermore, three regimes are investigated in regard to the spacing of the multiplets in energy in comparison to $k_{\text{B}}T$.

i) Wide multiplets compared to $k_{\mathrm{B}}T$

The excited states are unoccupied compared to the ground state in the regime $E_{\mathrm{e}} - E_{\mathrm{g}} \gg k_{\mathrm{B}}T$, where the energy levels are broadly separated. The ground state degeneracy, which is described by the angular momentum quantum number J, is eliminated by enforcing an external static magnetic field. The applied magnetic field produces magnetic moments with components $m_J g \mu_B$ along the field direction. The parameter m_{J} can take integer values between $+J$ and $-J$. The parameter g is the identified as gyromagnetic ratio, and μ_{B} is Bohr's magneton. Therefore, the energy of the dipoles is $-m_{\mathrm{J}} g \mu_{\mathrm{B}} H$, where H is the applied field. The average magnetization according to Boltzmann statistics is [4]

$$M = n\,\frac{\sum_{-\mathrm{J}}^{\mathrm{J}} m_{\mathrm{J}} g \mu_{\mathrm{B}}\, e^{\frac{m_{\mathrm{J}} g \mu_{\mathrm{B}} H}{k_{\mathrm{B}}T}}}{\sum_{-\mathrm{J}}^{\mathrm{J}} e^{\frac{m_{\mathrm{J}} g \mu_{\mathrm{B}} H}{k_{\mathrm{B}}T}}}\,. \qquad 1\text{–}8$$

For low values energy separations compared to $k_{\mathrm{B}}T$, the exponents can be expanded keeping just the first two leading terms [4,5]

$$e^x = \sum_{\mathrm{n}=0}^{\infty} \frac{x^n}{n!} = 1 + x + \frac{x^2}{2!} + \cdots \overset{x \ll 1}{\Longrightarrow} e^x \approx 1 + x. \qquad 1\text{–}9$$

Here $x \equiv \frac{m_{\mathrm{J}} g \mu_{\mathrm{B}} H}{k_{\mathrm{B}}T}$. The magnetization thus reads [4,5]

$$M = n\frac{\sum_{-\mathrm{J}}^{\mathrm{J}} m_{\mathrm{J}} g \mu_{\mathrm{B}} e^{\frac{m_{\mathrm{J}} g \mu_{\mathrm{B}} H}{k_{\mathrm{B}}T}}}{\sum_{-\mathrm{J}}^{\mathrm{J}} e^{\frac{m_{\mathrm{J}} g \mu_{\mathrm{B}} H}{k_{\mathrm{B}}T}}} = n\frac{\sum_{-\mathrm{J}}^{\mathrm{J}} m_{\mathrm{J}} g \mu_{\mathrm{B}} (1 + \frac{m_{\mathrm{J}} g \mu_{\mathrm{B}} H}{k_{\mathrm{B}}T})}{\sum_{-\mathrm{J}}^{\mathrm{J}} (1 + \frac{m_{\mathrm{J}} g \mu_{\mathrm{B}} H}{k_{\mathrm{B}}T})} = n\frac{g \mu_{\mathrm{B}} \sum_{-\mathrm{J}}^{\mathrm{J}} m_{\mathrm{J}} + \frac{g^2 \mu_{\mathrm{B}}^2 H}{k_{\mathrm{B}}T} \sum_{-\mathrm{J}}^{\mathrm{J}} m_{\mathrm{J}}^2}{\sum_{-\mathrm{J}}^{\mathrm{J}} 1 + \frac{g \mu_{\mathrm{B}} H}{k_{\mathrm{B}}T} \sum_{-\mathrm{J}}^{\mathrm{J}} m_{\mathrm{J}}}. \qquad 1\text{–}10$$

The summations can be carried out accordingly [4,5]

$$\sum_{-\mathrm{J}}^{\mathrm{J}} m_{\mathrm{J}} = -J + (-J) + 1 + (-J) + 2 + \cdots + J - 2 + J - 1 + J = 0,$$

$$\sum_{-\mathrm{J}}^{\mathrm{J}} 1 = 2J + 1,$$

$$\sum_{-\mathrm{J}}^{\mathrm{J}} m_{\mathrm{J}}^2 = 2[J^2 + (J-1)^2 + (J-2)^2 + \cdots] = \frac{J(J+1)(2J+1)}{3}.$$

An expression for the magnetization can be found by substituting these results into Equation 1–10, and the paramagnetic susceptibility confirming Curie's law [4,5]

$$M = \frac{n g^2 J(J+1) \mu_{\mathrm{B}}^2 H}{3 k_{\mathrm{B}}T} \xRightarrow{M = \chi H} \chi_{\mathrm{paramagnetic}} = \frac{n g^2 J(J+1) \mu_{\mathrm{B}}^2}{3 k_{\mathrm{B}}T}\,. \qquad 1\text{–}11$$

A complete expression for the susceptibility is derived from a quantum mechanical approach [6]

$$\chi_{\text{paramagnetic}} = \frac{ng^2J(J+1)\mu_{\text{B}}^2}{3k_{\text{B}}T} + \frac{n\mu_{\text{B}}^2}{6(2J+1)}\left[\frac{F(J+1)}{E_{\text{J}+1}-E_{\text{J}}} - \frac{F(J)}{E_{\text{J}}-E_{\text{J}-1}}\right], \qquad 1\text{–}12$$

where $F(J) = \frac{[(S+L+1)^2-J^2]\,[J^2-(S-L)^2]}{J}$, and S is the total spin quantum number, and L is the total orbital angular momentum quantum number. The second term of Equation 1–12, is a temperature-independent term that add to the paramagnetic susceptibility, and it can be put as $n\alpha(J)$, where $\alpha(J) = \frac{\mu_{\text{B}}^2}{6(2J+1)}\left[\frac{F(J+1)}{E_{\text{J}+1}-E_{\text{J}}} - \frac{F(J)}{E_{\text{J}}-E_{\text{J}-1}}\right]$.

ii) Multiplet widths comparable to $k_{\text{B}}T$

The excited, as well as the ground states, are filled with a probability distribution in multiplets with energies comparable to $k_{\text{B}}T$. Therefore, the overall magnetization will be composed of contributions coming from the total of all atoms in various states. The paramagnetic susceptibility can be assessed using a similar procedure as for the wide multiplets since the number of atoms with a given angular momentum quantum number J will be related to the Boltzmann factor $e^{\frac{-m_{\text{J}}g\mu_{\text{B}}H}{k_{\text{B}}T}}$ and the degree of degeneracy is $2J+1$. The result is [4]

$$\chi_{\text{paramagnetic}} = n\,\frac{\sum_{\text{J}=|\text{L}-\text{S}|}^{\text{L}+\text{S}}\left\{\left[\frac{g_{\text{J}}^2\mu_{\text{B}}^2J(J+1)}{3k_{\text{B}}T}\right] + \alpha(J)\right\}(2J+1)\,e^{-E(J)/k_{\text{B}}T}}{\sum(2J+1)e^{-E(J)/k_{\text{B}}T}}\,. \qquad 1\text{–}13$$

iii) Narrow multiplets compared to $k_{\text{B}}T$

If the multiplets are separated into energies far smaller than $k_{\text{B}}T$, the orbital angular momenta and spin angular momenta can be considered to be decoupled such that each term individually gives rise to the susceptibility. The magnetization in an exterior applied field H and the outcome paramagnetic susceptibility are [4,5]

$$M = n\left(\frac{\sum_{-\text{L}}^{\text{L}} M_{\text{L}}g_{\text{L}}\mu_{\text{B}}\,e^{\frac{M_{\text{L}}g_{\text{L}}\mu_{\text{B}}H}{k_{\text{B}}T}}}{\sum e^{\frac{M_{\text{L}}g_{\text{L}}\mu_{\text{B}}H}{k_{\text{B}}T}}} + \frac{\sum_{-S}^{S} M_{\text{S}}g_{\text{S}}\mu_{\text{B}}\,e^{\frac{M_{\text{S}}g_{\text{S}}\mu_{\text{B}}H}{k_{\text{B}}T}}}{\sum e^{\frac{M_{\text{S}}g_{\text{S}}\mu_{\text{B}}H}{k_{\text{B}}T}}}\right)$$

$$\xRightarrow{M=\chi H} \chi_{\text{paramagnetic}} = \frac{N\mu_{\text{B}}^2}{3k_{\text{B}}T}\left[L(L+1) + 4S(S+1)\right]. \qquad 1\text{–}14$$

The summations giving the above result are similar to the ones having the result of equation 1–11. Because of the relativistic effects, the gyromagnetic ratios related to the orbital angular momentum, g_{L} , and spin angular momentum, g_{S} , are taken as 1 and 2, respectively.

2.1.3.2 Saturation in paramagnetic substances

This last section on paramagnetism examines saturation in paramagnetic substances. Curie's law is invalid in conditions of low temperatures and high magnetic fields. In this region, the magnetization of a paramagnetic material can be described by [4]

$$M = ng\mu_\mathrm{B}JB_\mathrm{J}(x), \tag{1–15}$$

where $x = \frac{Jg\mu_\mathrm{B}H}{k_\mathrm{B}T}$ and $B_\mathrm{J}(x)$ is the Brillouin function given as [7]

$$B_\mathrm{J}(x) = \left[\frac{2J+1}{2J}\coth\left(\frac{2J+1}{2J}\right)x - \frac{1}{2J}\coth\frac{x}{2J}\right]. \tag{1–16}$$

The Brillouin function becomes the classical Langevin function in the classical limit of $J \to \infty$, which corresponds to magnetic dipoles oriented in all directions [4].

$$\lim_{\mathrm{J}\to\infty} B_\mathrm{J}(x) = \coth x - \frac{1}{x} = L(x). \tag{1–17}$$

The Brillouin and Langevin functions reach unity in the limit of large applied magnetic fields. The magnetic dipole moments become parallel to the applied field in these extreme conditions, and the magnetization saturates. The material reaches a saturation in terms of its magnetic value. Figure 2.1.1 illustrates the theoretical and experimental values of magnetization versus the applied magnetic field.

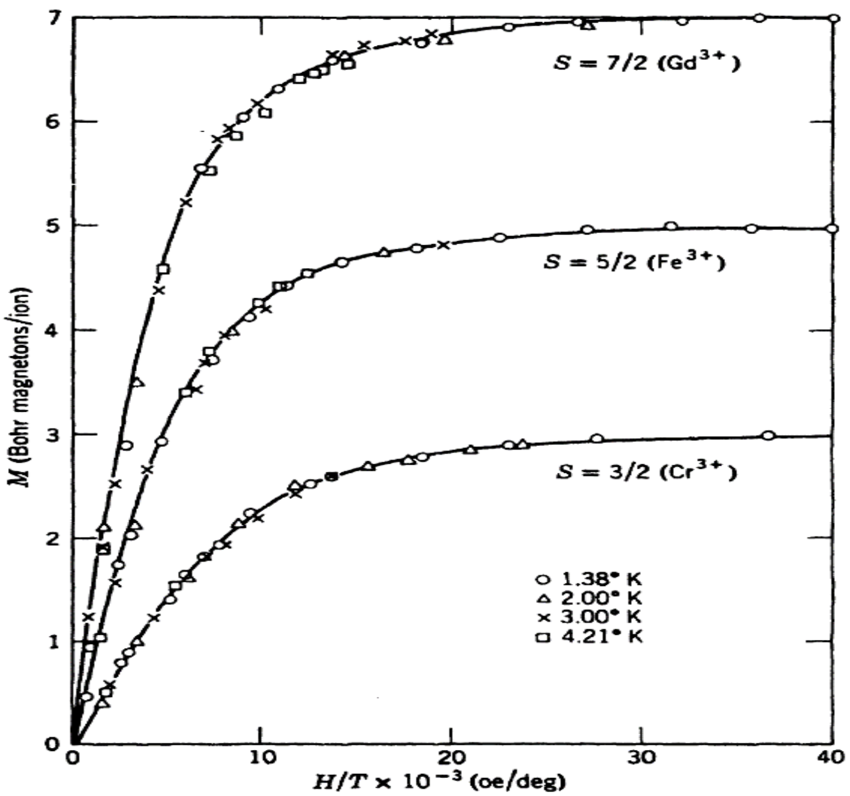

Figure 2.1.1 The effect of saturation in high fields and at low temperatures for various paramagnetic ions compared to the theoretical Brillouin functions [4].

2.1.4 Ferromagnetism

Since ferromagnetism in a material arises when the pairing of the magnetic moments of different atoms are in favor of parallel alignment, a non-zero magnetization exists even though external applied magnetic field is not present. This spontaneous magnetization is seen under specific temperature, specifically the ferromagnetic Curie temperature, T_f, which depends on the substance. At temperatures above T_f the dipole moments couplings breakdown, and the material becomes paramagnetic.

The most recognized ferromagnetic elements are iron, nickel, cobalt, and gadolinium. They are the only elements that display ferromagnetism. In contrast, most ferromagnetic substances are metals or alloys. In the absence of an applied field, many substances that fail to yield a net magnetization in the bulk form are considered to be ferromagnetic. Nevertheless, intense magnetic couplings between the magnetic dipole moments occur in an external magnetic field, even if it is weak. The existence of magnetic domains explains this phenomenon. The individual magnetic moments line up in a parallel fashion causing a net magnetization vector in every magnetic domain. The magnetization vectors are arbitrarily aligned in neighboring domains, and this leads to no net magnetization. The magnetic domains alter their volume when an external field is applied. Those that possess magnetization vectors in the same direction of the external field increase their volume, while the ones with magnetization vectors contrasting the magnetic field get smaller. Thus, the field which depends on magnetization will get larger upon an increase in an external field, and the magnetization will reach a saturation value. In many occurrences, the field-induced magnetization remains alive in spite of the external field having been turned off.

2.1.4.1 The classical molecular field theory

The molecular field, $\mathbf{H}_\mathrm{m}$, is the origin of powerful phenomena that leads to the tendency to line up the magnetic dipole moments in a ferromagnetic material, and is characterized by an interior magnetic field. The strength of the molecular field is proportional to the spontaneous magnetization of the ferromagnetic substance [4]

$$\mathbf{H}_\mathrm{m} = N_\mathrm{W}\mathbf{M}. \tag{1–18}$$

N_W in Equation 1–18 is the molecular field constant known as the Weiss constant. In the appearance of an external magnetic field, the overall field is [4]

$$\mathbf{H} = \mathbf{H}_\mathrm{ext} + \mathbf{H}_\mathrm{m} = \mathbf{H}_\mathrm{ext} + N_\mathrm{W}\mathbf{M}. \tag{1–19}$$

The magnetization, $\mathbf{M}$ of a ferromagnetic specimen is now given by [4]

$$\mathbf{M} = ng\mu_\mathrm{B}JB_\mathrm{J}(x), \tag{1–20}$$

where n is the number density of atoms, g is the gyromagnetic ratio, μ_B is the Bohr magneton, J is the total angular momentum of the atoms in the solid, $B_\mathrm{J}(x)$ is the classical Brillouin function (given as $B_\mathrm{J} = \frac{2J+1}{2J}\coth\frac{2J+1}{2J}x - \frac{1}{2J}\coth\frac{x}{2J}$), and x is a parameter defined below [4]

$$x = \frac{Jg\mu_\mathrm{B}H}{k_\mathrm{B}T}. \tag{1–21}$$

In Equation 1–21, H is given by Equation 1–19 for a ferromagnetic material, and therefore [4]

$$x = \frac{Jg\mu_\mathrm{B}}{k_\mathrm{B}T}(H_\mathrm{ext} + N_\mathrm{W}M). \tag{1–22}$$

2.1.4.1.1 The spontaneous magnetization region

Because the spontaneous magnetization of a sample comes from making H_ext equivalent to zero in Equation 1– 22, and taking into account the properties of the Brillouin function at extremely low temperatures, one finds [4]

$$\frac{M(T)}{M(0)} = \frac{k_\mathrm{B}T}{nN_\mathrm{W}g^2\mu_\mathrm{B}^2J^2}x, \quad \frac{M(T)}{M(0)} = B_\mathrm{J}(x) \tag{1–23}$$

where $M(0) = ng\mu_\mathrm{B}J$. The Equations in 1–23 can be simultaneously solved via a graphical method. The graphical method to determine spontaneous magnetization as a function of temperature is presented in Figure 2.1.2. T_f is the critical temperature of a case where the straight line is tangent to the Brillouin function at its origin. The curve and the straight line cross at two positions below this temperature: one at a non-zero value of $\frac{M(T)}{M(0)}$, and the other point at a zero value. Therefore, spontaneous magnetization is realized at temperatures under the critical temperature, T_f. The spontaneous magnetization vanishes beyond the critical temperature.

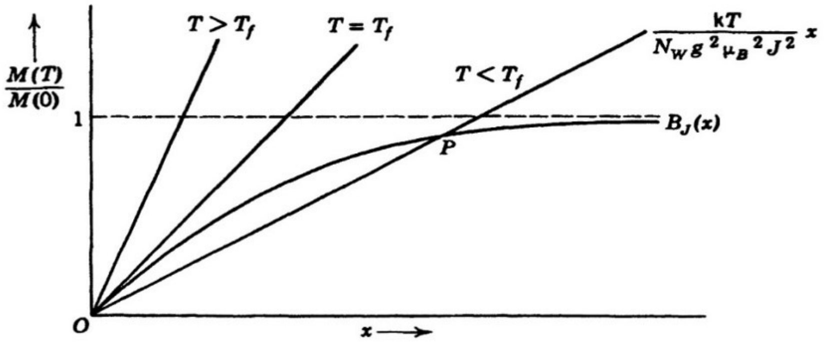

Figure 2.1.2 Illustration of a graphical process for the finding of the spontaneous magnetization at a temperature T, $M(T)$ [4].

The classical Brillouin function for small values of x can be estimated by [4]

$$B_\mathrm{J}(x) \approx \frac{J+1}{3J}x - \frac{J+1}{3J}\frac{2J^2+2J+1}{30J^2}x^3. \tag{1–24}$$

In Equation 1–24, as x reaches zero, the slope of the tangent line reaches $\frac{J+1}{3J}$. In contrast, the slope of the straight line is $\frac{k_\mathrm{B}T}{nN_\mathrm{W}g^2\mu_\mathrm{B}^2J^2}$. Thus, at the critical temperature, $T = T_\mathrm{f}$, the conclusion is [4]

$$T_\mathrm{f} = \frac{ng^2\mu_\mathrm{B}^2J(J+1)}{3k_\mathrm{B}}N_\mathrm{W}. \tag{1–25}$$

Based on Equations 1–23 and 1–25, the spontaneous magnetization at temperature T can be given as

$$\frac{M(T)}{M(0)} = \frac{J+1}{3J}\left(\frac{T}{T_\mathrm{f}}\right)x. \tag{1–26}$$

The curve $\frac{M(T)}{M(0)}$ as a function of $\left(\frac{T}{T_\mathrm{f}}\right)$ for a given J gives a universal curve [4]. Figure 2.1.3 illustrates such curves for $J = \frac{1}{2}$, $J = 1$, and $J = \infty$.

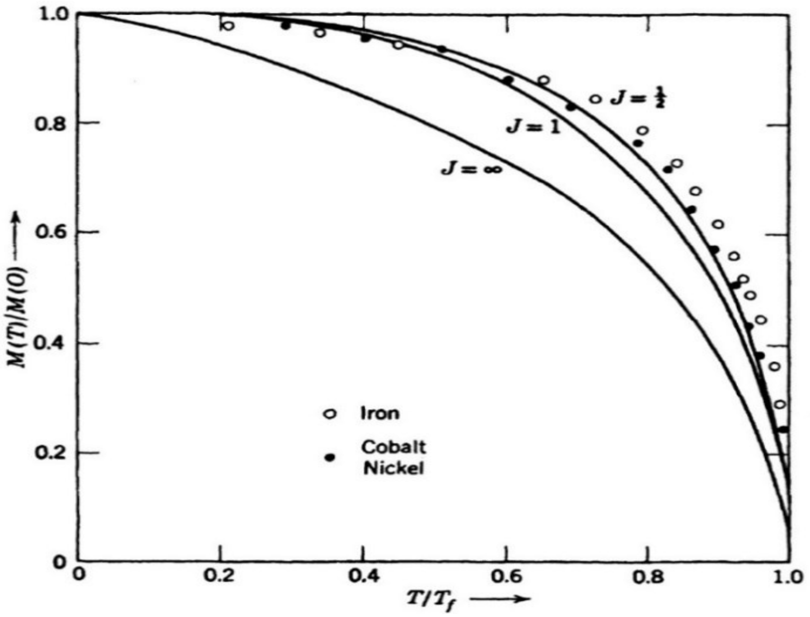

Figure 2.1.3 The spontaneous magnetization as a function of temperature. In the graph, the solid lines is found from theory, and the points stands for experimental results [4].

2.1.4.1.2 The paramagnetic region

The spontaneous magnetization disappears for temperatures beyond the ferromagnetic ordering temperature T_{f}, but magnetization is created if an external magnetic field is applied. The magnetization is expressed by the following equation, based on the assumption that the external magnetic field is not sufficient to cause the effects of saturation [4]

$$M = \frac{ng\mu_{\mathrm{B}}(J+1)}{3}x, \tag{1–27}$$

where $x = \frac{Jg\mu_{\mathrm{B}}}{k_{\mathrm{B}}T}(H_{\mathrm{ext}} + N_{\mathrm{W}}M)$. An expression for the magnetic susceptibility is found once substituting x into Equation 1–27

$$\chi = \frac{M}{H_{\mathrm{ext}}} = \frac{C}{T-\theta}, \tag{1–28}$$

where the constant $C = \frac{ng^2\mu_{\mathrm{B}}^2 J(J+1)}{3k_{\mathrm{B}}}$ and $\theta = N_{\mathrm{W}}\frac{Ng^2\mu_{\mathrm{B}}^2 J(J+1)}{3k_{\mathrm{B}}} = N_{\mathrm{W}}C$. In Figure 2.1.4, the reciprocal of ferromagnetic susceptibility is plotted versus temperature beyond the ordering temperature.

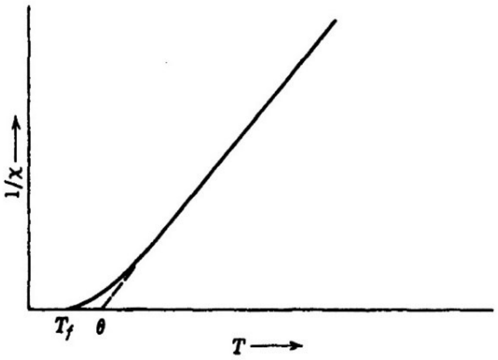

Figure 2.1.4 The susceptibility of a ferromagnetic metal beyond the Curie point. T_f is the ferromagnetic Curie point; θ is the paramagnetic Curie point. For temperatures slightly above the ordering temperature, the Curie-Weiss law of paramagnetism is realized [4].

2.1.5 Antiferromagnetism

When the coupling of the individual constituents' magnetic moments, atoms or molecules, prefers the anti-parallel orientation, antiferromagnetism in a substance happens. Néel suggested that an antiferromagnetic solid can be imagined to be of two sub-lattices, one of whose spins favor to line up anti-parallel the other's [4,8]. Consequently, the overall magnetic moment of the antiferromagnetic substance is zero. Néel's hypothesis can be experimentally studied, through neutron diffraction techniques, to reveal the magnetic dipole moments' arrangements in a material. It appears the diversity of different anti-ferromagnetic orderings is more abundant than Néel's straightforward model proposes. In the next section, an introduction to a number of theories of antiferromagnetism is presented.

2.1.5.1 The molecular field theory of antiferromagnetism

In this paragraph, an example of a simple antiferromagnetic ordering is explained by using the molecular field theory. A body-centered cubic structure can be visualized to consist of two interpenetrating cubic cells alongside the diagonal orientation in a way which one cell's corners are at the cores of the other cell. The two cubic sub-lattices called A and B in this picture have their dipole moments line up anti-parallel to each other [9]. To further clarify, an A site atom is in a non-parallel spin formation with its six nearest neighbors that are atoms on B sites and the other way around.

In this model (molecular field theory) one considers the interaction between a dipole moment and that of its nearest and next nearest neighbors. The molecular fields on the atomic sites of A and B can thus be expressed by [4]

$$H_{\mathrm{mA}} = -N_{\mathrm{AA}}M_{\mathrm{A}} - N_{\mathrm{AB}}M_{\mathrm{B}} \qquad , \qquad H_{\mathrm{mB}} = -N_{\mathrm{BA}}M_{\mathrm{A}} - N_{\mathrm{BB}}M_{\mathrm{B}}. \qquad 1\text{–}29$$

In Equation 1–29, if $i \neq j$, then N_{ij} is the molecular field constant for nearest-neighbour interactions and for the next nearest-neighbour interactions if $i = j$. The parameters M_{A} and M_{B} are the magnetizations of the sub-lattices A and B, respectively. If the lattice basis in monatomic is assumed, then the same type of atoms take place at the A and B sites. Therefore, $N_{\mathrm{AA}} = N_{\mathrm{BB}} = N_{\mathrm{ii}}$, and $N_{\mathrm{AB}} = N_{\mathrm{BA}}$. If an external magnetic field, H_{ext} is exposed on to the system of sub-lattices, the fields at sites A and B can be given by [4]

$$H_{\mathrm{A}} = H_{\mathrm{ext}} - N_{\mathrm{ii}}M_{\mathrm{A}} - N_{\mathrm{AB}}M_{\mathrm{B}} \quad , \quad H_{\mathrm{B}} = H_{\mathrm{ext}} - N_{\mathrm{AB}}M_{\mathrm{A}} - N_{\mathrm{ii}}M_{\mathrm{B}}. \tag{1–30}$$

The magnetizations and Brillouin functions for the sublattices A and B, are given by [4]

$$M_{\mathrm{A}} = \frac{1}{2}ng\mu_{\mathrm{B}}SB_{\mathrm{S}}(x_{\mathrm{A}}) \quad , \quad M_{\mathrm{B}} = \frac{1}{2}ng\mu_{\mathrm{B}}SB_{\mathrm{S}}(x_{\mathrm{B}}), \tag{1–31}$$

where $x_{\mathrm{A}} = \frac{Sg\mu_{\mathrm{B}}}{k_{\mathrm{B}}T}H_{\mathrm{A}}$, $x_{\mathrm{B}} = \frac{Sg\mu_{\mathrm{B}}}{k_{\mathrm{B}}T}H_{\mathrm{B}}$, $B_{\mathrm{S}}(x_{\mathrm{A}}) = \frac{2S+1}{2S}\coth\frac{2S+1}{2S}x_{\mathrm{A}} - \frac{1}{2S}\coth\frac{x_{\mathrm{A}}}{2S}$, and $B_{\mathrm{S}}(x_{\mathrm{B}}) = \frac{2S+1}{2S}\coth\frac{2S+1}{2S}x_{\mathrm{B}} - \frac{1}{2S}\coth\frac{x_{\mathrm{B}}}{2S}$.

In antiferromagnetic materials, the temperature at which the ordered anti-parallel arrangement of the dipoles diminishes is called the Néel temperature (T_{N}). In the following section, the molecular field theory of antiferromagnetism is discussed for temperatures above and below the Néel temperature. The next section also provides a short summary on the shift between the paramagnetism and antiferromagnetism regime when the external field is present.

2.1.5.1.1 The paramagnetic region above Néel temperature

In temperatures higher than the Néel temperature, magnetic ordering does not exist in an antiferromagnetic material. Because of thermal excitements, the dipole moments position themselves in arbitrary directions, from a classical perspective, resulting in a net-zero magnetization. However, a small magnetization is induced because of an external magnetic field. The Brillouin function can be replaced by $B_{\mathrm{S}}(x) \approx \frac{S+1}{3S}x$ if the applied field is not capable to cause saturation effects. In that case, the magnetization of the sub-lattices A and B turn out to be [4]

$$M_{\mathrm{A}} = \frac{ng^2\mu_{\mathrm{B}}^2S(S+1)}{6k_{\mathrm{B}}T}H_{\mathrm{A}} \quad , \quad M_{\mathrm{B}} = \frac{ng^2\mu_{\mathrm{B}}^2S(S+1)}{6k_{\mathrm{B}}T}H_{\mathrm{B}}. \tag{1–32}$$

Replacing the magnitude of the fields in equations 1–31 with their corresponding equations in equations 1–32, and as regards total magnetization $M = M_{\mathrm{A}} + M_{\mathrm{B}}$; therefore

$$M = \frac{ng^2\mu_{\mathrm{B}}^2S(S+1)}{6k_{\mathrm{B}}T}[2H_{\mathrm{ext}} - (N_{\mathrm{ii}} + N_{\mathrm{AB}})M]. \tag{1–33}$$

After the antiferromagnetic susceptibility after rearrangement of the terms to be solved for M, $\chi_{\mathrm{afm}} = \frac{M}{H}$, would be

$$\chi_{\mathrm{afm}} = \frac{C}{T+\theta} \ , \tag{1–34}$$

where $C = \frac{ng^2\mu_{\mathrm{B}}^2S(S+1)}{6k_{\mathrm{B}}T}$, and $\theta = \frac{1}{2}C(N_{\mathrm{ii}} + N_{\mathrm{AB}})$. Generally, θ is positive because the molecular field constant for nearest neighbour interactions is greater than the ones of next nearest neighbor interactions. In Figure 2.1.5, for three cases, the reciprocal magnetic susceptibility is plotted versus temperature: the Curie law of Equation 1–6, the Curie-Weiss law of Equation 1–7, and Equation 1–34).

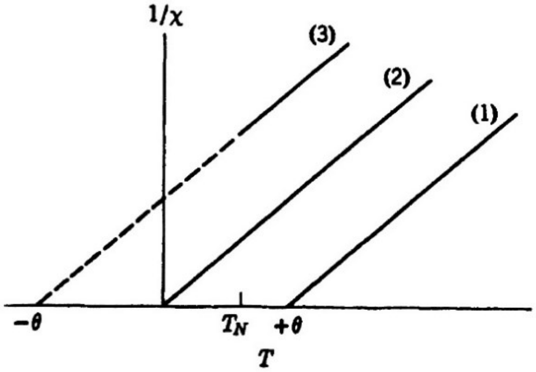

Figure 2.1.5 the graph illustrate the value of $1/\chi$ vs. temperature *T*. For Curve 1 the susceptibility, $\chi = C/(T - \theta)$ (representing the Curie -Weiss law); curve 2, $\chi = C/T$ (representing Curie's law), and curve 3, $\chi = C/(T + \theta)$ [4].

2.1.5.1.2 At the Néel temperature

The Equations of 1–32 along with 1–30, and in the lack of an external applied field yield [4]

$$M_{\mathrm{A}} = \frac{C}{2T}(-N_{\mathrm{ii}}M_{\mathrm{A}} - N_{\mathrm{AB}}M_{\mathrm{B}}) \quad , \quad M_{\mathrm{B}} = \frac{C}{2T}(-N_{\mathrm{AB}}M_{\mathrm{A}} - N_{\mathrm{ii}}M_{\mathrm{B}}). \tag{1–35}$$

An expression for the Néel temperature is found upon solving the pair of equations in Equation 1–35 for nonzero magnetizations [4]

$$T_{\mathrm{N}} = \frac{1}{2}C(N_{\mathrm{AB}} - N_{\mathrm{ii}}). \tag{1–36}$$

The ratio of the paramagnetic temperature, θ, is provided by substituting C from Equation 1–34 to the Néel temperature, T_{N} [4]

$$\frac{\theta}{T_{\mathrm{N}}} = \frac{N_{\mathrm{AB}}+N_{\mathrm{ii}}}{N_{\mathrm{AB}}-N_{\mathrm{ii}}}. \tag{1–37}$$

2.1.5.1.3 Susceptibility below the Néel temperature

The susceptibility of an antiferromagnetic material is expressed with respect to temperature in Figure 2.1.6. The figure shows that the susceptibility of the material less than the ordering temperature for a given spin separates into two divisions: the perpendicular susceptibility to the applied external field which is a constant function $\chi_{\perp}$; the susceptibility in the order that is parallel to the applied field which is $\chi_{\parallel}$. The functional formula of the susceptibilities at temperatures lower than the Néel temperature are stated below [4].

$$\chi_{\parallel} = \frac{n\mu_{\mathrm{B}}^2 g^2 S^2 \left(\frac{\partial B_{\mathrm{S}}}{\partial x}\right)_{x_0}}{k_{\mathrm{B}}T + \frac{1}{2}(N_{\mathrm{ii}} + N_{\mathrm{AB}})\mu_{\mathrm{B}}^2 g^2 S^2 N \left(\frac{\partial B_{\mathrm{S}}}{\partial x}\right)_{x_0}} \quad , \quad \chi_{\perp} = \frac{1}{N_{\mathrm{AB}}} , \tag{1–38}$$

$x_0 = \frac{g\mu_{\mathrm{B}}S}{k_{\mathrm{B}}T}[(N_{\mathrm{AB}} - N_{\mathrm{ii}})M_0]$ in the above equation, where M_0 is the magnetization of sub-lattice A when the external magnetic field is absent.

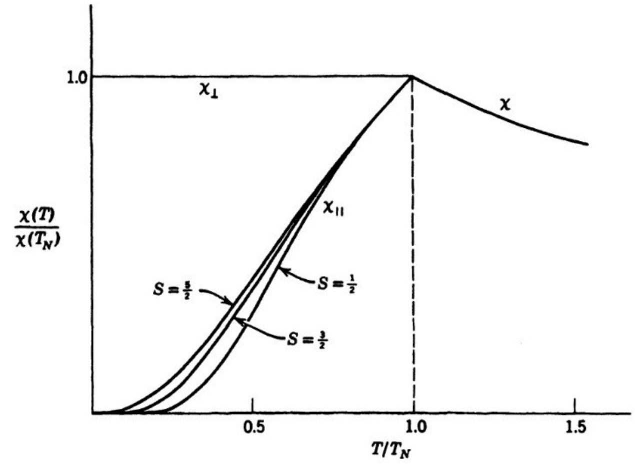

Figure 2.1.6 The susceptibility versus temperature for antiferromagnetic substance [4].

Suppose the applied magnetic field makes an angle, α, with the uniaxial crystal 's easy direction. In this case, the susceptibility of the antiferromagnetic substance is given by [4]

$$\chi_{\mathrm{afm-sc}} = x_{\parallel} cos^2\alpha + x_{\perp} sin^2\alpha. \tag{1–39}$$

Taking the average of Equation 1–39 over the unit sphere for a powdered or polycrystalline material to obtain

$$\chi_{\mathrm{afm-pc}} = x_{\parallel}\langle cos^2\alpha\rangle + x_{\perp}\langle sin^2\alpha\rangle = \frac{1}{3}x_{\parallel} + \frac{2}{3}x_{\perp}. \tag{1–40}$$

References

[1] K. H. J. Buschow and F. R. de Boer, *Physics of Magnetism and Magnetic Materials* (Kluwer Academic Publishers, New York, 2004).

[2] W. Pauli, Z. Physik. **2**, 201 (1920).

[3] P. Curie, Ann. Chim. Phys. **5,** 289 (1895).

[4] A. H. Morrish, *The Physical Principles of Magnetism* (John Wiley & Sons, New York, 1965).

[5] F. Nejadsattari, Theoretical and experimental studies of electronic structure, magnetic, and hyperfine interaction properties of novel compounds, Ph.D. Thesis (Ottawa, 2016).

[6] H. V. Vleck, *Theory of Electric and Magnetic Susceptibilities* (Oxford University Press, Oxford, 1932).
[7] L. Brillouin, J. Phys. Radium. **8**, 74 (1927).

[8] L. Néel, Ann. Phys. **17**, 64 (1932).

[9] L. Néel, Ann. Phys. **18**, 5 (1932); F. Bitter, Phys. Rev. **54**, 79 (1938); J. H. Van Vleck, J. Chem. Phys. **9***,* 85 (1941).

2.2 Superconductivity

In this section, a review of superconductors is briefly discussed. This overview is mostly focused on the magnetic properties of superconductors.

2.2.1 Introduction

The story of superconductivity started in 1911 when H. Kammerlingh Onnes found that mercury has no measurable electrical resistance value when it is cooled below 4.2 K. This phenomenon was also found in many other materials when they were cooled below a certain temperature which is called the critical temperature T_c. There are more than 20 metallic elements that could turn into superconductors. [1].

In metals, the resistivity relation can be given as [1]

$$\rho(T) = \rho_0 + BT^5 , \qquad 2\text{-}1$$

where $\rho(T)$ is the resistivity at a given temperature, ρ_0 is the resistivity at a temperature equal to zero, and B is constant. Below T_c the electric resistivity for superconductors drops to zero, as is shown in the graph below.

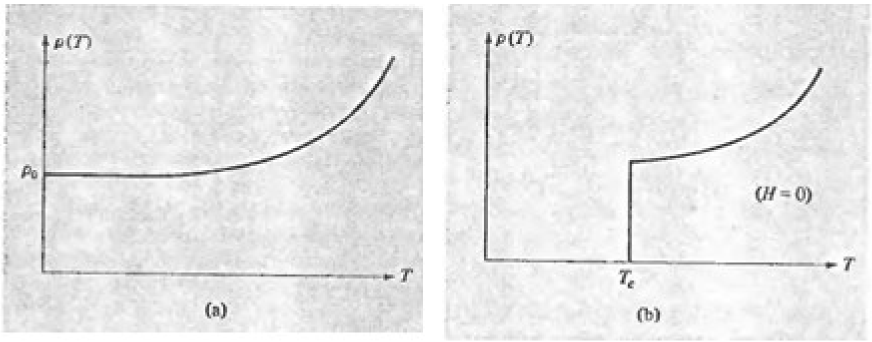

Figure 2.2.1 (a) Low–temperature resistivity of normal metal-containing nonmagnetic impurities; (b) Low-temperature resistivity of a superconductor (in a zero magnetic field) containing nonmagnetic impurities. At T_C, ρ drops abruptly to zero [1].

Some of the features of superconductors are [1]:

1- Although superconductors have no DC electrical resistivity in the absence of driving electrical field, electrical currents persevere without any obvious deterioration.
2- Superconductors can behave as a perfect diamagnet. They produce a magnetic field that opposes any external field within the superconductor.

2.2.1.1 Microscopic Theory

The isotope effect provided a valuable contribution to the microscopic explanation of superconductors. In 1950, both Maxwell (using ^{198}Hg) and Reynold et al. (using samples with average A=199.7, 202.0, and 203.4) discovered that there are variant T_c in different mercury isotopes [2]. Maxwell noticed a 0.021 K increase, while Reynold et al. observed shifts in T_c between +0.011 K (A=199.7) and -0.024 K (A=203.4) [2]. Consequently, the phonon mediation is the tool behind coupling electrons. The isotope effect states $T_c M^{\alpha} = const.$, where M is the isotope mass. The BCS theory assumes constant-phonon interaction and a spherical Fermi surface, which makes the math simpler.

Frohlich, in 1952 [2], showed that the electrons interact indirectly with each other in a crystal by releasing and absorbing phonons. Electron e_1 with wave vector $\vec{k}_1$ releases a phonon and moves to $\vec{k}'_1$. Electron e_2 with wave vector $\vec{k}_2$ gets this phonon and moves to $\vec{k}'_2$. This interaction indicates that electrons are attracted to one another within $\hbar\omega_D$ of the Fermi surface, where ω_D is the Debye frequency. Cooper in 1956 [2] concluded that the binding energy is negative between two electrons regardless of how minor the attraction is.

BCS theory joins the two concepts together, by supposing the attractive potential is mediated by the scattering of phonons. Bardeen, Cooper, and Schrieffer noticed that electron pairs within $\hbar\omega_D$ of the Fermi surface are dispersed from inside Fermi sphere to the outside of it. This increases the kinetic energy and decreases the potential energy [4]. If the potential energy is reduced in excess of the kinetic energy, the ground state becomes one in which some states beyond Fermi energy E_F are occupied, and some below E_F are empty.

Within the weak coupling BCS theory, T_c is expressed as [4]

$$T_c = \frac{1.13\hbar\omega_D}{k_B} e^{\frac{-1}{N(E_F)V_{eff}}}, \qquad 2\text{-}2$$

where k_B, $N(E_F)$, V_{eff} are Boltzman's constant, the density of states at the Fermi energy, and the potential of the effective interaction between electrons, respectively. According to the BCS theory, if two electrons interact with an attractive force from the lattice vibration above the Fermi sphere, the two electrons form a bond state. This bond state is called a Cooper pair.

To maximize the number of these pairs, all the electrons in every pair should have a momentum of equal amount but conflicting orientation, as well as inverse-parallel spins. If the spins make a singlet state ($S = 0$), then the spatial wave function should hold even parity values ($L = 0, 2, 4, \ldots$). If the spins make a triplet state ($S = 1$), the spatial wave function should hold an odd parity value ($L = 1, 3, 5, \ldots$). In order to simplify calculations, BCS theory assumes the Fermi surface to be spherical, the pair to have L = 0 and S = 0, and electron-phonon interaction $V_{kk'}$ is supposed to be constant [2]

$$V_{kk'} = \begin{cases} -V & |\epsilon_k| \le \hbar\omega_D \; \& \; |\epsilon_{k'}| \le \hbar\omega_D \\ 0 & |\epsilon_k| > \hbar\omega_D \; \& \; |\epsilon_{k'}| > \hbar\omega_D \, , \end{cases} \qquad \text{2-3}$$

with

$$\epsilon_k = \frac{\hbar^2 k^2}{2m} - \frac{\hbar^2 k_f^2}{2m} \, . \qquad \text{2-4}$$

One may write the excitation energy as [2]

$$E_k = \sqrt{\epsilon_k^2 + \Delta^2}, \qquad \text{2-5}$$

where Δ is the energy gap. In order to destroy one Cooper pair, an energy of at least 2Δ is required, where Δ is the superconductivity energy gap. This gap depends on temperature, and it goes to zero as $T \rightarrow T_c$. In addition, there are two temperature-dependent length scales associated with superconductivity: The first one is the London penetration depth, λ. The penetrated depth is related to the extent in which the magnetic field penetrates indie the material which falls off exponentially with depth [3]. λ gives the distance at which the magnetic field inside the superconductor falls to 1/e of the applied field. The second is the coherence length ξ. ξ in the BCS theory is the effective size of the Cooper pair [5]

2.2.1.2 Families of superconductors

The vast majority of superconducting non-transition elements show suppression of T_c with pressure, while transition metals and their alloys T_c increases with pressure [6].

The study for high temperature superconductors (HTS) resulted in the finding of superconductivity with $T_c \sim$ 35 K in the La-Ba-Cu-O compounds [6]. It prompted searching for HTS materials with T_c above the liquid nitrogen temperature. Researchers replaced La with Y, an isoelectronic element with a smaller size, to find superconductivity in Y-Ba-Cu-O with T_c= 93 K. This is the first superconductor with T_c above the liquid nitrogen temperature [7]. Currently, $HgBa_2Ca_2Cu_3O_{8+\delta}$ is the copper oxide superconductor with the highest T_c, 164 K at 31 GPa [8].

In 2008, the discovery of the superconductivity in iron-based materials triggered a great interest in condensed matter community [9]. $LaFeAsO_{1\_x}F_x$ shows the superconductivity at $T_c \sim$ 26 K [9], and it was the first compound in which significant amount of Fe does not suppress superconductivity.

Magnetism usually limits superconductivity [9]. Therefore, the finding of superconductivity in compounds with moment bearing Fe was fascinating. Because of this, other structure classes of Fe-based superconducting compounds were discovered. They include: RFeAsO "111", $A_1Fe_2As_2$ "122", A_2FeAs "111", FeSe "11", $CaA_3Fe_4As_4$ "1144" [3,9,10,11,12]. Here R is rare-earth metal, A_1=Na,K,Rb,Cs,Ca,Sr,Ba,Eu; A_2=Li,Na; A_3=K,Rb,Cs, respectively. The AFe_2As_2 compound generated interest since it can be grown in large single crystal form, and it has a simple structure. In the $BaFe_2As_2$ compound, the undoped parent compound goes through coupled magnetic and structural transitions near 140 K [13]. Superconductivity was found in the doped 122 materials, as well as under pressure [14].

2.2.2 The transition temperature (the critical temperature)

The critical temperature at which the material is turned into a superconductor depends on the type of material, and this temperature varies when an external magnetic field is applied. The material will be superconducting as long as it is below T_c.

The chemical purity of the sample and its crystalline perfection are also responsible in impacting the critical temperature. The strain and inhomogeneity in the purity of the sample plays an important role on broadening the temperature fluctuation at which the transition to the superconducting state occurs. The transition temperature scale may reach to a low temperature of 1 mK for a pure sample [15].

2.2.3 Magnetic properties of superconductor materials

Perfect diamagnetism and the critical magnetic field in superconductor materials are reviewed in this section

2.2.3.1 Perfect diamagnetism in superconductor materials

In metals in a normal state, the external magnetic field can go through the materials. However, in superconductors, the external magnetic field cannot penetrate the interior of the materials. This phenomenon is explained by the Meissner-Ochsenfeld effect [16]. It states that if a normal metal is cooled under its superconducting transition temperature in a magnetic field, the magnetic flux is instantly ejected from it. Hence, surface currents occur in a way that their magnetic fields eliminate those of the interior.

2.2.3.2 Critical field for superconductors

Consider a superconductor at temperature T below the critical temperature T_c. When the magnetic field, H, is turned on, a surface current is created. This surface current will produce a magnetic field which opposes the external magnetic field and leads to zero interior magnetic field. If the external field exceeds a critical value then it will penetrate through the superconductor. Two different kinds of reactions are then noticed. They lead to type I and type II superconductors.

Type I superconductors

The phase boundary diagram in type I superconductors is shown in Figure 2.2.2 (a), where both the normal state and the superconducting state can be observed. The temperature dependence of the critical field H_{c} is [16]

$$H_c(T) = H_c(0)\left[1-\left(\frac{T}{T_c}\right)^2\right], \tag{2-6}$$

where $H_{\mathrm{c}}(T)$ is the critical field at temperature T and $H_{\mathrm{c}}(0)$ is the critical field at absolute zero. Below T_{c} there will be no penetration of the field. When the applied field is higher than the critical field $H_{\mathrm{c}}(T)$, the whole specimen will go to its normal state, and the field penetrates the interior. As a result of this penetration, the superconductivity will diminish.

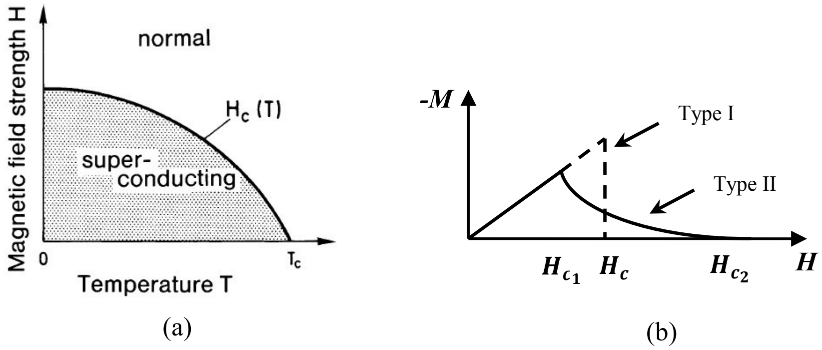

(a) (b)

Figure 2.2.2 (a) The magnetic field strength H versus temperature T in type I superconductors [16]; (b) Magnetization versus the magnetic field for the two types of superconductors type I and type II [15].

Type II superconductors

In the case of type II superconductors, there are two critical fields, $H_{\mathrm{c}_1}(T)$ and $H_{\mathrm{c}_2}(T)$. The applied magnetic field $H_{\mathrm{c}_2}(T)$ is higher than $H_{\mathrm{c}_1}(T)$, and for external fields under $H_{\mathrm{c}_1}(T)$ the flux does not penetrate the specimen. When the external field is higher than $H_{\mathrm{c}_2}(T)$, the specimen will revert to its normal state, and consequently, the magnetic flux will penetrate the specimen. For the situation when the external field is between $H_{\mathrm{c}_1}(T)$ and $H_{\mathrm{c}_2}(T)$, the flux partially penetrates the superconductor. This particular mechanism of both normal and superconducting states is called as a mixed state. Figure 2.2.2 (b), shows the magnetization versus applied field for the type II superconductor.

Usually, critical fields in type I superconductors are around 10^2 Gs well below the transition temperature. On the other hand, the critical field of type II superconductors can be as much as 10^5 Gs thus creating a significant market for type II superconductors in designing high-field magnets. [16].

2.2.4 Coexistence of superconductivity and magnetism

Superconductivity and magnetic ordering are two very unlike yet collective phenomena. The question of how superconductivity and magnetism coexist is paramount, given their antagonistic character. The Russian theorist Vitaly Ginzburg first posed this question in 1957, but early experiments in 1959 by Bernd Matthias, revealed that when ferromagnetic ordering exists, superconductivity vanishes [17]. The cause of this ruinous characteristic is a quantum mechanical interaction between electron spin and the atomic magnetic moment. Below the superconducting transition temperature, the interaction between the electron spin magnetic moments tend to align them, thus destroying the Cooper pairs, within which spins are antiparallel. Therefore, exchange interactions put restrictions on the presence of superconductivity. In antiferromagnetic materials, superconductivity and antiferromagnetism can exist at the same time because, on average, the Cooper pairs will not be influenced by the magnetic moments in these compounds [17].

In superconductors with ferromagnetic order, the superconductivity is destroyed at the ferromagnetic phase transition [17]. In the ferromagnetic phase, the magnetic moments will be aligned in the same direction with each other. When the aligned atomic magnetic moments interact with the electron spins, the Cooper pairs energy of the electrons will be affected. Consequently, the superconductivity cannot stop the magnetic transition.

In anisotropic ferromagnetic superconductors with regular lattices of magnetic ions, the coexistence phase with a domain-like transverse magnetic structure would be recognized under T_f ($\ll T_c$) [17]. Superconductivity has a gapless character in the coexistence phase in clean compounds. It is possible to realize the coexistence phase with the magnetic domain structure, the spontaneous vortex phase, and the Meissner ferromagnetic phase in superconductors with weak ferromagnetism.

Most of the magnetic superconductors are considered as type II superconductors. However, at temperatures slightly beyond T_f in a ferromagnet, or around T_N in an antiferromagnet, they become type I superconductors [17]. This behaviour relies on demagnetization factors, and on the relation between the parameters of both the electromagnetic and exchange interactions between electrons and localized moments [17].

In regular superconductors, the phase with a non-uniform superconducting order parameter as well as the Larkin-Ovchinikov-Fuld-Ferrel state (LOFF state), cannot be achieved [17]. Thus, magnetic superconductors present an exceptional opportunity for its experimental study, especially for the LOFF state, which can be observed in samples that were made in the shape of plates and put in a field which is in a perpendicular direction to the plate.

In order to partially or completely destroy superconductivity without diminishing the magnetic ordering, laser irradiation can be deployed [17]. The process of destroying the superconductivity offers the possibility to examine the magnetic structure without the presence of superconductivity, and in the temperature interval where the coexistence phase is realized. These experiments allow us to examine the impact of superconductivity on magnetic ordering

It has been shown that superconductivity and magnetism can coexist in some materials. Thus, magnetic superconductors present an exceptional opportunity for its experimental study, because they should allow us to examine the impact of superconductivity on magnetic ordering and, generally, to better understand the phenomenon of superconductivity, especially the intervening interactions. Therefore the reported recently Fe-based compounds that exhibit superconductivity, is of utmost importance. One of the iron-based materials is $EuAFe_4As_4$ (A = Rb, Cs). It exhibits a high T_c [18]. These high-T_c superconducting materials also have a magnetic transition at about 15 K. To show the coexistence of superconductivity and magnetic state, two samples $EuRbFe_4As_4$, and $EuCsFe_4As_4$ will be taken as an example [18].

The temperature dependence of electrical resistivity of these two compounds is shown in Figure 2.2.3.

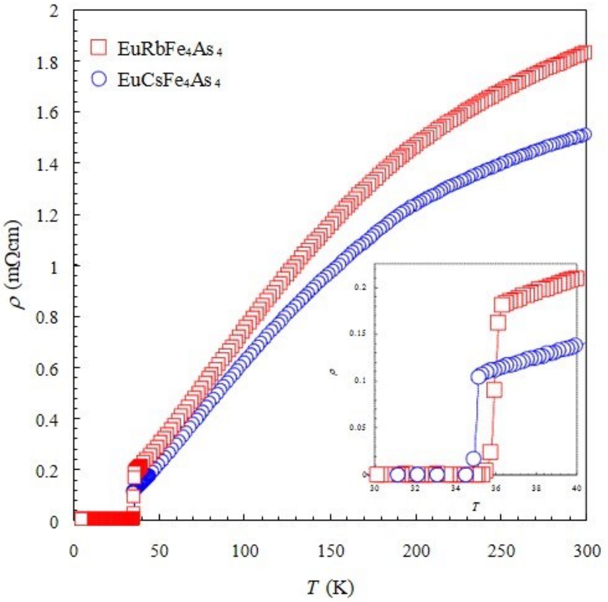

Figure 2.2.3 Temperature T dependence of $EuRbFe_4As_4$ and $EuCsFe_4As_4$ electrical resistivity ρ. Inset ρ near superconducting transition temperature T_c [18].

The results of the electrical resistivity measurements showed that the electrical resistivity reduced dramatically at around 36.2 and 35.1 K for $EuRbFe_4As_4$ and $EuCsFe_4As_4$, respectively. The resistivity reached zero at 35.8 and 34.9 K for those materials. This result confirmed the existence of superconductivity in those materials. In terms of the magnetic measurements, magnetic susceptibility measurements were conducted for both samples. Figure 2.2.4 shows the magnetic susceptibility as a function of temperature. Here, the magnetic susceptibility shows a clear

Meissner diamagnetic signal at roughly 35 K, which agrees well with the T_c confirmed from the electrical resistivity data (Figure 2.2.3). The measured T_c values are 36 and 35 K for EuRbFe$_4$As$_4$ and EuCsFe$_4$As$_4$, respectively. From the magnetic susceptibility data, we can see an anomalous magnetic transition at near 15 K. In EuAFe$_4$As$_4$, the anomalous behavior near 15 K is clear in the magnetic susceptibility data only (Figure 2.2.4), meanwhile the electrical resistivity is zero until to 5 K (Figure 2.2.3). There is a probability that the anomalous magnetic transition shown by EuAFe$_4$As$_4$ at near 15 K, that is under T_c, is a result of the existence of an Eu^{2+} ion-induced magnetic ordered state.

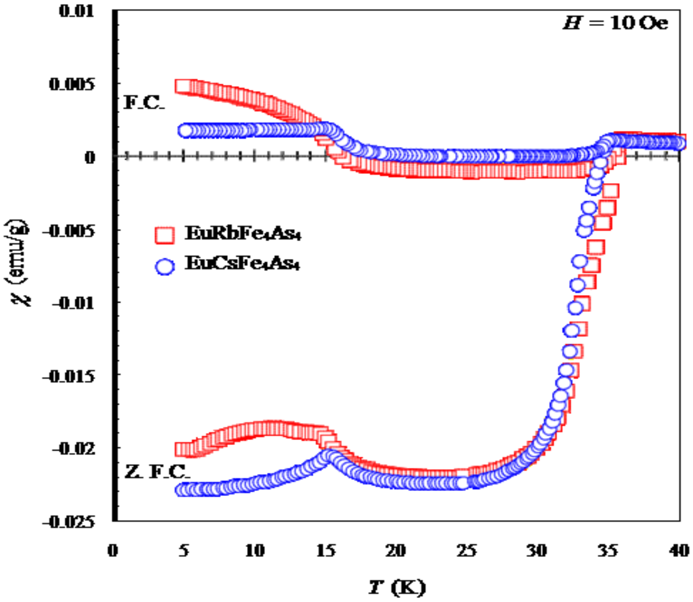

Figure 2.2.4. Temperature T dependence of EuAFe$_4$As$_4$ (A = Rb, Cs) magnetic susceptibility χ [18].

References

[1] N. W. Ashcroft and N. D. Mermin, *Solid State Physics*, (Harcourt, Orlando, 2011).

[2] A. N. Thaler, Structural and magnetic properties and superconductivity in Ba(Fe$_{1-x}$TM$_x$)$_2$As$_2$(TM=Ru, Mn, Cr/Co, Mn/Co) single crystals, Ph.D. Thesis (Iowa, 2012).

[3] W. R. Meier, T. Kong, U. S. Kaluarachchi, V. Taufour, N. H. Jo, G. Drachuck, A. E. Böhmer, S. M. Saunders, A. Sapkota, A. Kreyssig, M. A. Tanatar, R. Prozorov, A. I. Goldman, Fedor F. Balakirev, Alex Gurevich, S. L. Bud'ko, and P. C. Canfield, Phys. Rev. B **94**, 064501 (2016).

[4] J. Bardeen, L. N. Cooper, and J. R. Schrieffer, Phys. Rev. **108**, 1175 (1957).

[5] V. L. Ginzburg, and L. D. Landau, Zh. Eksp. Teor. Fiz. **20**, 1064 (1950).

[6] J. G. Bednorz, and K. A. Müller, Z. Phys. B. **64**, 189(1986).

[7] M. K. Wu, J. R. Ashburn, C. J. Torng, P. H. Hor, R. L. Meng, L. Gao, Z. J. Huang, Y. Q. Wang, and C. W. Chu, Phys. Rev. Lett. **58**, 908 (1987).

[8] L. Gao, Y. Y. Xue, F. Chen, Q. Xiong, R. L. Meng, D. Ramirez, C. W. Chu, J. H. Eggert, and H. K. Mao, Phys. Rev. B **50**, 4260 (1994).

[9] Y. Kamihara, T. Watanabe, M. Hirano, and H. Hosono, J. Am. Chem. Soc. **130**, 3296 (2008).

[10] M. Rotter, M. Tegel, and D. Johrendt, Phys. Rev. Lett. **101**, 107006 (2008).

[11] J. H. Tapp, Z. Tang, B. Lv, K. Sasmal, B. Lorenz, P. C. W. Chu, and A. M. Guloy, Phys. Rev. B **78**, 060505 (2008).

[12] F.Hsu, J. Luo, K. Yeh, T. Chen, T. Huang, P. M. Wu, Y. Lee, Y. Huang, Y. Chu, D. Yan, and M. P. Natl. Acad. Sci. USA. **105**, 14262 (2008).

[13] N. Ni, S. L. Bud'ko, A. Kreyssig, S. Nandi, G. E. Rustan, A. I. Goldman, S. Gupta, J. D. Corbett, A. Kracher, and P. C, Canfield. Phys. Rev. B **78**, 014507 (2008).

[14] P. L. Alireza, Y. T. C. Ko, J. Gillett, C. M. Petrone, J. M. Cole, G. G. Lonzarich, and S. E. Sebastian, J. Phys.: Condens. Matter **21**, 012208 (2009).

[15] J. R. Reitz, F. J. Milford, and R. W. Christy, *Foundations of Electromagnetic Theory*, (Pearson, San Francisco, 2009).

[16] H. Ibach and H. Lüth, Solid-State Physics, *An Introduction to Principles of Materials Science*, (Springer, Berlin, 2009).

[17] L. N. Bulaevskii, A. I. Buzdin, M. L. Kulić, S.V. Panjukov, Adv. Phys. **34**, 175 (1985).

[18] K. Kawashima, T. Kinjo, T. Nishio, S. Ishida, H. Fujihisa, Y. Gotoh, K. Kihou, H. Eisaki, Y. Yoshida, and A. Iyo, J. Phys.Soc. Jpn. **85**, 064710 (2016).

2.3 Mössbauer spectroscopy

2.3.1 Introduction

The Mössbauer effect was discovered by Rudolf Mössbauer in 1958. This phenomenon occurs when a nucleus emits recoil-free emissions and absorbs gamma rays.

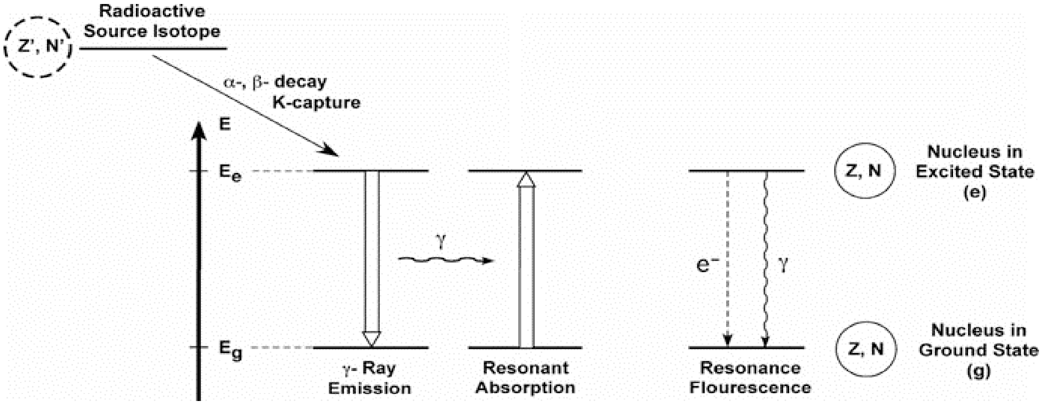

Figure 2.3.1 The nuclear resonance absorption of gamma-rays (Mössbauer effect) for nuclei with *Z* protons and *N* neutrons [1].

Figure 2.3.1 illustrates a radioactive isotope nucleus with atomic number Z' and neutron number N'. The nucleus undergoes atomic reaction, and loses its excitation through either α decay, or β decay or electron capture. The remaining nucleus, labeled as Z and N, is produced in the excited state, E_e, and afterward decays to its ground state, E_g, which yields in the process a gamma photon. Essentially, the produced gamma photon is captured by a nucleus in the ground state, and this nucleus will be send to the excited state (this process is called resonant absorption). Afterwards, the nucleus in its excited state will then re-release its energy in the form of a gamma ray and move back to the ground state (this operation is called resonant fluorescence). This is the primary process behind the Mössbauer effect. The natural linewidth of the transition energy is illustrated in Figure 2.3.2.

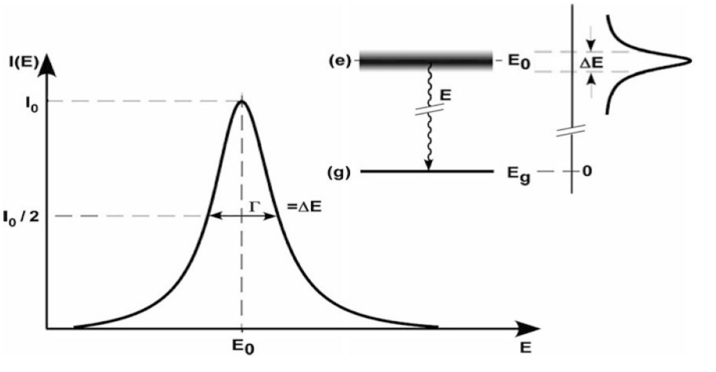

Figure 2.3.2 Illustration of the intensity distribution *I(E)* for the emission of gamma rays with the mean transition energy E_0 ,where the gamma transition energy between the excited state and ground state natural line width is shown [1].

The excited nuclear state's average lifetime is usually between 10^{-11} s and 10^{-6} s (the lifetime of the first excited state of ^{57}Fe is 1.43×10^{-7}s) [1]. The γ ray's transition energy appropriate for Mössbauer spectroscopy may vary between 10 to 100 keV. The transition energy is 14.4 keV for ^{57}Fe Mössbauer spectroscopy. The Lorentzian profile, which characterized by (Γ) where Γ is the full width at half maximum of the natural linewidth, is the uncertainty measure in the energy of the excited nuclear state (for ^{57}Fe, $\Gamma = 4.55 \times 10^{-9}$ eV).

Scientists did not think it would be possible to get the process of gamma radiation resonant emission and absorption before Mössbauer's finding. Scientists' belief was inspired by the energy and linear momentum transported to, or delivered by in the absorption event, the nucleus by gamma radiation. The centers of the emission and absorption lines move in separate directions due to the conservation of momentum and its recoil energy. Consequently, the emission and absorption lines would not converge, and thus the nuclear resonance will not occur. Some efforts were made using what is known as the relativistic Doppler effect thus widening and shifting the emission lines to promote a higher degree of overlap. Such efforts were accomplished using transducers to put the source and/or absorber of the emission lines in constant relative motion.

Based on Maxwell-Boltzmann's statistics, especially in gaseous systems, the velocity of the particles comprising the system appears to have a temperature-dependent distribution. Different particles in the system have broad variations (normal distribution) of speeds. Thus, the γ ray energy emitted resulting from nuclear state transitions go through Doppler shifts. These shifts caused by the recoiling of nuclei and rapid kinetic motion result in emission and absorption lines with a Gaussian profile shape, which as opposed to the natural linewidth that has a Lorentzian profile.

The Doppler broadening in energy related to gas particles at a temperature T is given by [1]

$$\Gamma_{\mathrm{D}} = 2\sqrt{E_{\mathrm{R}} k_{\mathrm{B}} T}, \qquad 3\text{–}1$$

where E_{R} is the nucleus' recoil energy shifting between the ground and the excited states, and k_{B} is the Boltzmann constant. According to Equation 3–1, the Doppler broadening and the recoil energy have the same order. For the 14.4 keV transition energy of ^{57}Fe and the recoil energy of 1.95×10^{-3}eV at room temperature Γ_{D} is about 10^{-2}eV [1]. Thus, the Doppler shifts' drop in recoil energy could be compensated for by the nuclei in gases and liquids. Nonetheless, the overlap of the emission and absorption lines is negligible, such that experimentally detecting the resonant result for gasses and liquid will become impractical.

Equation 3-1 shows that the Doppler broadening is directly proportional to the square root of the temperature and the resonant energy. The Mössbauer effect is easier to observe at lower temperatures, i.e., the nuclear resonant effect is more efficient at lower temperatures in solids. Only the quantum theory of solids can explain this phenomenon [2], and a brief explanation will be given below.

The nuclei within the solid are physically bound on lattice points and vibrate about equilibrium. The temperature plays a role in identifying the intensity of the vibration and their amplitude. The value of the vibrational frequencies can be in order of $\sim 10^{13}$ Hz [3]. Conversely, the vibration periods is less than the half-life time of the excited state nuclei by six orders of magnitude. Therefore, during the transition times, an average of zero displacement of the nuclei will not cause any Doppler shift in the emission profile. In addition, the entire crystal will absorb all the recoil momentum caused by the nuclear transition. This is due to the crystal's large mass, and the velocity on the emitting nuclei are insignificant which leads to a vanishing of the recoil energy [1]

$$P = M_{\text{crystal}} v, \ll 1 \Longrightarrow\ E_{\text{R}} = \frac{1}{2} M_{\text{crystal}} v^2 \approx 0, \tag{3–2}$$

where M_{crystal} is the mass of the crystal, v is the induced velocity of the emitter.

Phonons which are a form of lattice vibration excitations, absorb some part of the transition energy during the nuclear transition that takes place in solid state. In the creation process of these phonons, the energy transfer is significantly larger than the nuclear levels' natural linewidth, which does not make the resonant effects possible [1]. But in a solid without phonon creation or absorption, there is a limited probability of nuclear transitions named as zero-phonon processes. This non-zero possibility is directly related to a portion of nuclei which go through non-recoil emission and absorption of γ rays, resulting in resonant effects. The fraction that goes through non-recoil process is identified as the Mössbauer-Lamb factor, f, and it is equivalent to the Debye-Waller factor in X-ray diffraction from solids. At room temperature, a standard value of f for ^{57}Fe Mössbauer spectroscopy is 0.91 [1]. It is considered that the recoil-free factor, f, is associated with the local shift of the nucleus from its equilibrium position x by way of the equation below [1]

$$f = e^{-\frac{\langle x^2 \rangle E_\gamma}{(\hbar c)^2}}, \tag{3–3}$$

where $\langle x^2 \rangle$ is the average squared of displacement or the vibrational amplitude squared of the nucleus, c is the speed of light, $\hbar = h/2\pi$, where h is Planck's constant, and E_γ is the emitted (absorbed) photon energy. The Debye model overall describes the vibrations of the nuclei. In the Debye model there is a distribution of the frequencies from 0 to the Debye frequency ν_{D} and the density of states is proportional to ν^2 [4]. A given material within the Debye model is characterized by a Debye temperature which is related to the highest phonon energy $h\nu_{\text{D}}$. The Debye temperature is given by [4]

$$T_{\text{D}} = \frac{h\nu_{\text{D}}}{k_{\text{B}}}, \tag{3–4}$$

The recoil-free factor's temperature dependence is given by [1,2]

$$f(T) = e^{\left\{-\frac{3E_\lambda^2}{k_{\text{B}} T_{\text{D}} M c^2}\left[\frac{1}{4}+\left(\frac{T}{T_{\text{D}}}\right)^2 \int_0^{\frac{T_{\text{D}}}{T}} \frac{x}{e^x - 1} dx\right]\right\}}. \tag{3–5}$$

This equation may be analyzed in both high and low-temperature regions. The upper limit of the integral in the exponent approaches infinity at very low temperatures ($T \ll T_{\mathrm{D}}$) [1,2]

$$\int_0^{\infty} \frac{x}{e^x-1} dx = \frac{\pi^2}{6} \Rightarrow f(T) \approx e^{\left\{-\frac{3{E_\lambda}^2}{k_{\mathrm{B}} T_{\mathrm{D}} M c^2}\left[\frac{1}{4}+\left(\frac{T}{T_{\mathrm{D}}}\right)^2 \frac{\pi^2}{6}\right]\right\}} = e^{-\frac{{E_\lambda}^2}{2 k_{\mathrm{B}} T_{\mathrm{D}} M c^2}\left(\frac{3}{2}+\frac{\pi^2 T^2}{{T_{\mathrm{D}}}^2}\right)}. \qquad 3\text{–}6$$

The exponent is proportional with temperature in a quadratic ratio, but in high-temperature region ($T \gtrsim T_{\mathrm{D}}$), it is a linear behaviour for the exponent. In the integral e^x can be estimated by $1 + x$ (since x is of the order of $\frac{T}{T_{\mathrm{D}}}$) [1,2]

$$\int_0^{\frac{T_{\mathrm{D}}}{T}} \frac{x}{e^x-1} dx \approx \int_0^{\frac{T}{T_{\mathrm{D}}}} dx = \frac{T}{T_{\mathrm{D}}} \Rightarrow f(T) \approx e^{-\frac{3{E_\lambda}^2 T}{k_{\mathrm{B}} T_{\mathrm{D}}^2 M c^2}}. \qquad 3\text{–}7$$

Mössbauer spectrum's intensity depends on the recoil-free factor. Because the required time to acquire a sufficient signal to noise ratio is relative to the intensity square [1], the Mössbauer spectra can be significantly improved by lowering the temperature of the samples to temperatures equivalent to liquid nitrogen and liquid helium.

The Mössbauer effect, as stated earlier, is known as the recoilless emission and absorption of γ rays by nuclei in the solid state caused by the zero-phonon processes. To observe the Mössbauer effect one must have high enough value of the recoil-free factor *f*.

Overall, the increase in the recoil-free factor depends on three important parameters: decreasing the temperature of the system, decreasing the energy transitions, and by increasing the Debye temperature.

2.3.2 Hyperfine interactions

In Mössbauer atoms, an electromagnetic field is created because of the Mössbauer atoms' electrons. The electromagnetic field interacts with the Mössbauer nucleus causing what is called the hyperfine interaction. The hyperfine interaction results in either an alteration in the nuclear energy levels or a splitting in the nuclear energy states. Hyperfine interactions occur in three major forms. The first one is the electric monopole interaction, which is responsible for the isomer shift. The second interaction is between magnetic field and dipole moments. This process causes a split in the energy levels, and it is called the Zeeman effect. The third type is the electric quadrupole dipole interaction caused by the exchange of the component of electric fields and the charge distribution of the Mössbauer nucleus. The electric quadrupole interaction causes a degeneracy removal in the resonance transition lines between the ground state and excited state.

2.3.2.1 The isomer shift

The electric monopole interaction is associated with the total charge of the Mössbauer nucleus. The electric monopole interaction causes a shift in energy, and the shift in energy is given by [1]

$$E_{\text{I.S.}} = \delta E_{\text{el}} = -\frac{2\pi}{5} Ze^2R^2|\psi(0)|^2, \tag{3–8}$$

where Z is the atomic number, e is the electron charge, and R is the nuclear radius. From equation 3-8 it is clear that the electric monopole interaction is proportional to the square of the nucleus' average radius. Whereas similar nuclei have dissimilar radii ($R_{\text{g}} \neq R_{\text{e}}$), where R_{g} is the radius for the ground state and R_{e} is the radius for the excited state, the monopole interaction is not going be the same for the nuclei in their ground states as opposed to the ones in the excited states. In consequence, the shift in the nuclear energy level is not going to be same for the ground state $(\delta E)_{\text{g}}$ compared to the one for the excited state $(\delta E)_{\text{e}}$. This change causes the Mössbauer isomer shift (IS). A schematic of isomer shift and the derived shift in the Mössbauer spectrum is demonstrated below.

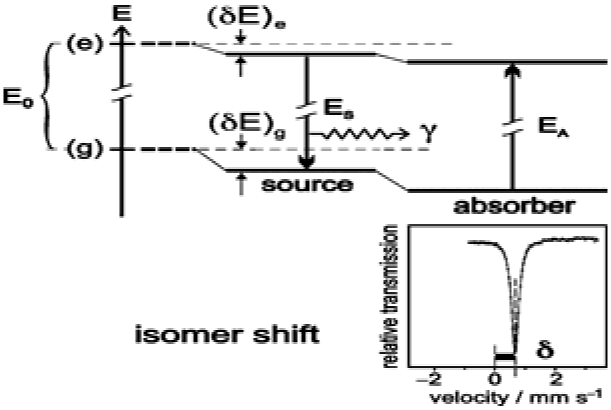

Figure 2.3.3 The interaction of the electric monopole between the nuclear charge and the electron density at the nucleus. The results of this interaction is the shift of the nuclear state, and it gives the isomer shift [1].

The isomer shift in the Mössbauer spectrum will be δ [1]

$$\delta = E_{\text{A}} - E_{\text{S}} = \frac{2\pi}{5} Ze^2\left[|\psi(0)|_{\text{A}}{}^2 - |\psi(0)|_{\text{S}}{}^2\right]\left(R_{\text{e}}{}^2 - R_{\text{g}}{}^2\right). \tag{3–9}$$

In the center shift, one should account for the second-order Doppler shift (SOD). Because of the thermal motion of the emitting and absorbing nuclei, there will be a relativistic shift in the energy of the γ phonons. This shift is represented by second-order Doppler shift which is given by the equation

$$\delta_{\text{SOD}} = -E_{\gamma}\frac{\langle v^2 \rangle}{2c^2}, \; \delta_{\text{exp}} = \delta + \delta_{\text{SOD}}, \tag{3–10}$$

where E_{γ} is the photon energy, and $\langle v^2 \rangle$ is the mean square velocity of the Mössbauer nuclei.

2.3.2.2 Electric quadrupole splitting

The electric quadruple interaction is caused by the interaction of the electric field and the charge distribution of the nucleus. When the system has a nuclear spin quantum number of more than $^1/_2$, the nucleus will have a nuclear quadrupole moment. As a result, splitting in the nuclear energy will occur, and the equation of the quadruple interaction energy eigenvalues can be given as [1]

$$E_Q = \frac{eQV_{zz}}{4I(2I-1)}[3m_I{}^2 - I(I+1)]\left(1+\frac{\eta^2}{3}\right)^{1/2}, \qquad 3\text{–}11$$

where η the asymmetry parameter of the electric field gradient (EFG) tensor $\eta = \frac{V_{xx}-V_{yy}}{V_{zz}}$, Q is the quadrupole moment of the nucleus, and V_{zz} is the main component of the electric field gradient. For the ^{57}Fe Mössbauer nuclei, the first nuclear excited state will split into a doublet as is shown in the figure below.

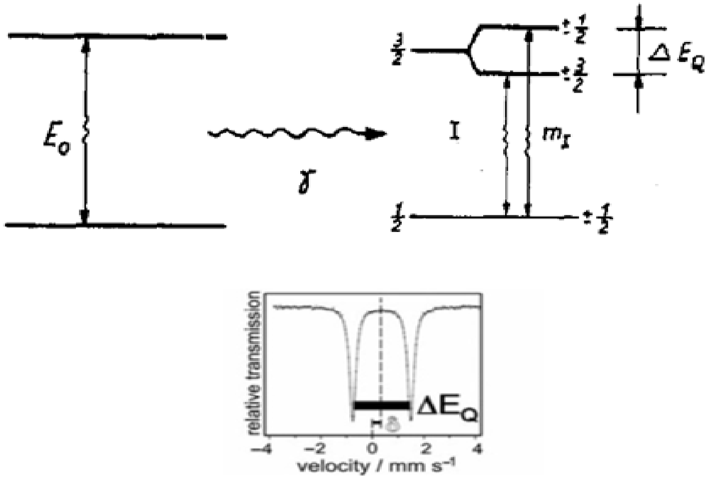

Figure 2.3.4 Quadruple interaction of the ^{57}Fe $|I = 3/2, m_{3/2}\rangle$ state and the resulted Mössbauer spectrum [1].

Similarly, for the ^{151}Eu Mössbauer isotopes, there will be splitting into three sublevels in the ground state, and into four sublevels in the excited state, as is shown in Figure 2.3.5. There will be eight allowed transitions.

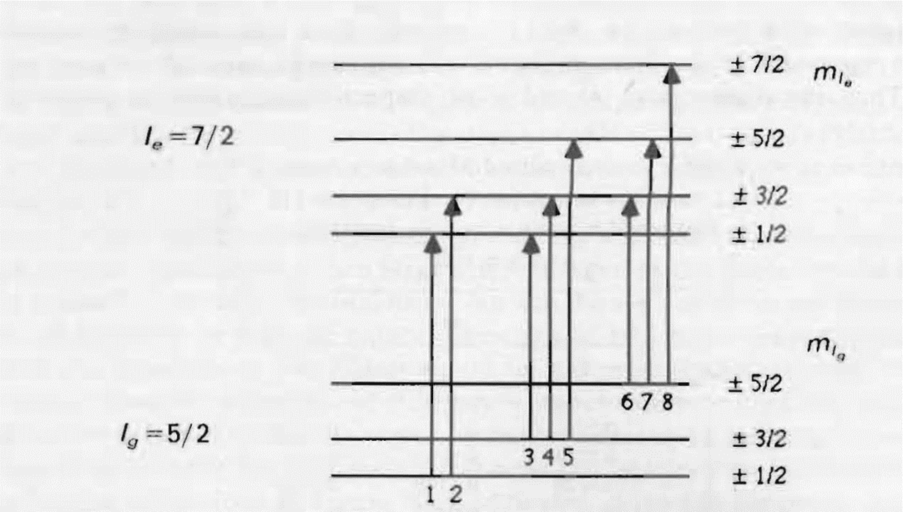

Figure 2.3.5 The allowed transitions between the nuclear energy levels of ^{151}Eu due to quadrupole interaction [5].

2.3.2.3 Magnetic dipole interaction and magnetic splitting

The Mössbauer nucleus possess a magnetic dipole moment μ, and this magnetic moment is a result of the nuclear spin angular momentum. The value of μ is giving by [6]

$$\mu = g_n \mu_{Bn} I, \qquad 3\text{–}12$$

where g_n is the nuclear Landé splitting factor, and μ_{Bn} is the nuclear Bohr magneton. If there is a magnetic field at the site of the nucleus, the magnetic dipole moment will split into $(2I + 1)$ sublevels with the eigenvalues [6]

$$E_m = -\frac{\mu H m_I}{I} = -g_n \mu_{Bn} H m_I\,, \qquad 3\text{–}13$$

where m_I is the nuclear magnetic quantum number with the values $m_I = I, I - 1, \dots. -I$, and H is the magnetic field.

From Equation 3–13 for ^{57}Fe nuclear states, the $I = 3/2$ state divides into four subsets, and the $I = 1/2$ state divides into two subsets. The transitions are selected by the selection rules of $\Delta m = 0\,, \pm 1$. There will be six allowed transitions, which are shown in the figure below.

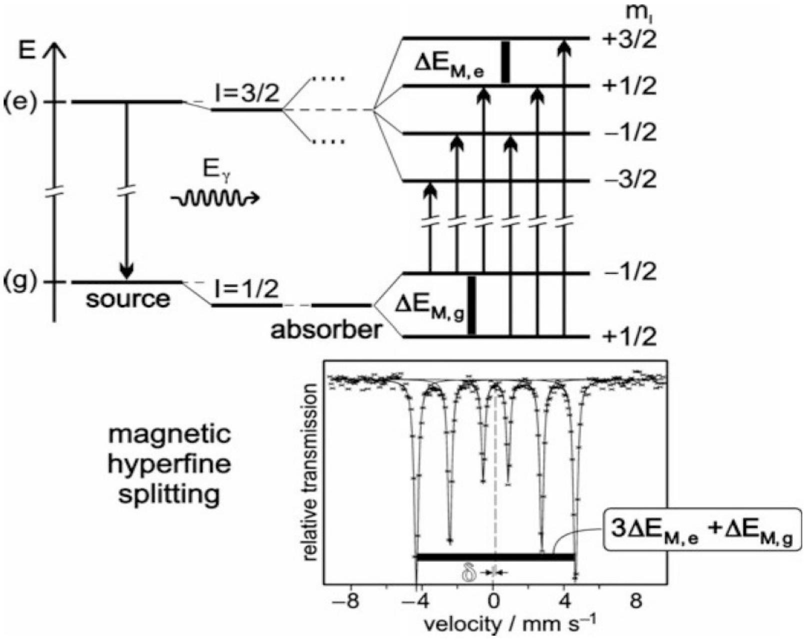

Figure 2.3.6 Magnetic dipole interaction splitting in ^{57}Fe and the resultant spectrum [1].

On the other hand, for the ^{151}Eu Mössbauer isotopes, it is clear from Figure 2.3.7 that there will be eighteen allowed transitions, and the spectra for a variety of linewidths are shown in Figure 2.3.8.

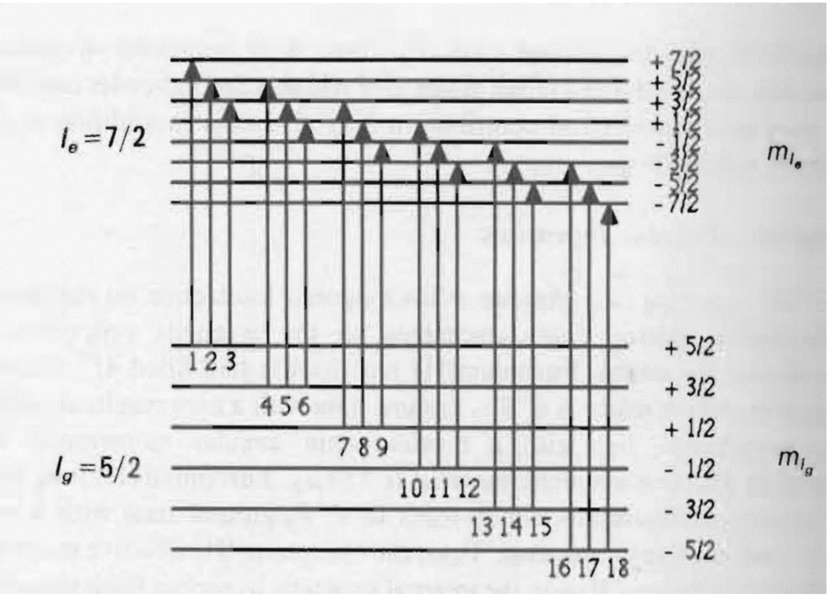

Figure 2.3.7 Nuclear energy levels for ^{151}Eu in the presence of a magnetic hyperfine interaction [5].

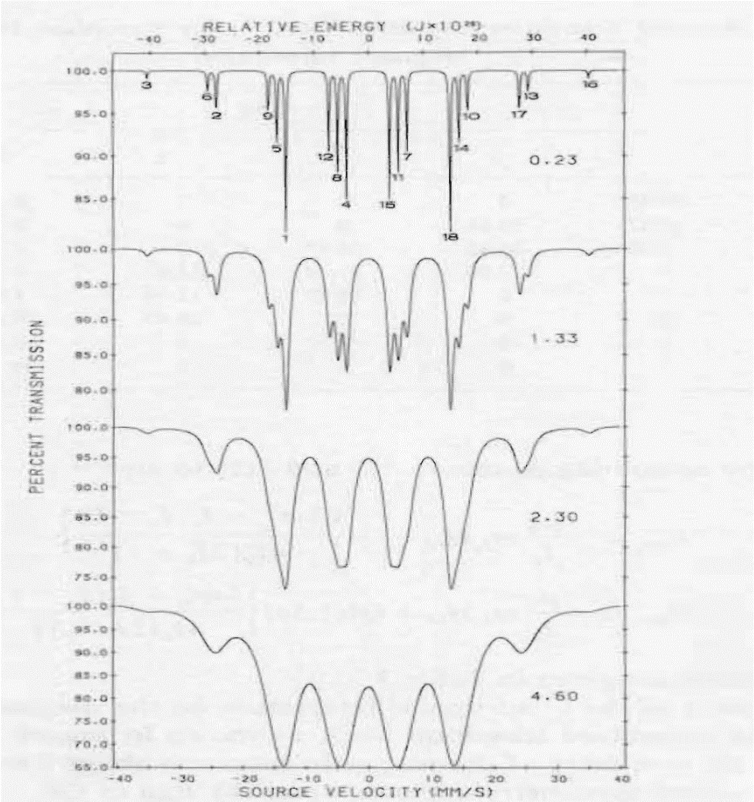

Figure 2.3.8 Theoretical ^{151}Eu Mössbauer spectra in the presence of a magnetic hyperfine field of -340 kOe, with isomer shift of 0.0 mm/s and four different linewidths given in mm/s [5].

2.3.2.4 The combined electric and magnetic interaction

Quadruple splitting, isomer shift, and magnetic dipole interaction could simultaneously occur in a typical Mössbauer spectrum. Figure 2.3.9 shows a ^{57}Fe Mössbauer spectrum.

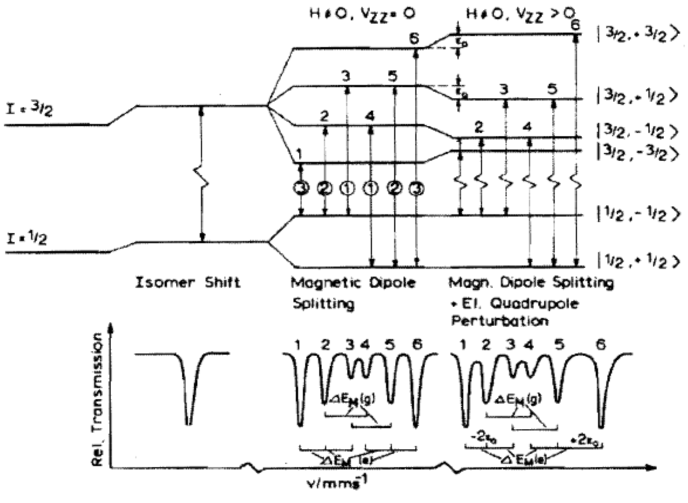

Figure 2.3.9 Quadruple splitting, magnetic dipole interaction splitting, and isomer shift in ^{57}Fe and the resultant Mössbauer spectrum [3].

2.3.3: Experimental procedure

This section outlines the procedures undertaken regarding sample and instrument setup while discussing the measuring technique used during the experiment.

2.3.3.1: Sample preparation

All of the samples studied in this thesis follow a certain sample preparation. The following paragraph summarizes the procedures used for weighing and preparing the samples.

2.3.3.1.1: Sample weighing

It is critical for this experiment to determine the weight of the sample accurately. Such accuracy is achieved through various measures of precautions including but not limited to clean environment, choosing appropriate sample portions and using higher precisions weighing machine. In this experiment, it is desirable to utilize larger lumps of the sample throughout the experiment to minimize risk of sample loss. The scale used to measure the sample is showing in Figure 2.3.10.

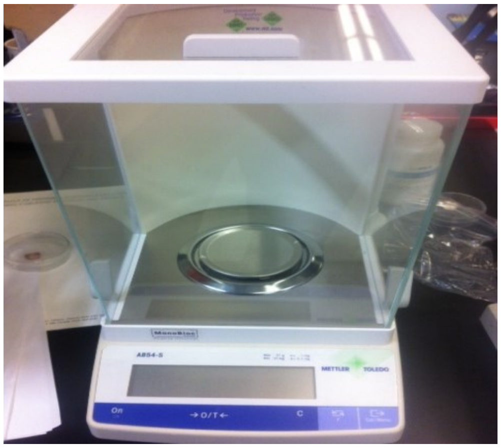

Figure 2.3.10 The scale used to weigh the sample during the experiment.

2.3.3.2: Mössbauer set-up

The complete set-up of the Mössbauer spectrometer consists of radioactive source, transducer, absorber, and detector.

A suitable radioactive source is required to provide resonant gamma radiation. Thus, a transducer is used to generate a mechanical movement for the source. An electronic signal generator drives the transducer to swing back and forth (side to side). The electrical waveforms from the generator could be modified to refine the movement of the transducer. The Mössbauer absorbers consist of a mixture of powder of the studied compound and boron nitride, which is pressed into a pellet that was put into an 8-μm-thick Al disk container to ensure a uniform temperature over the whole absorber. The detector is a proportional counter filled with Kr gas with some methane, and is directly connected to a pre-amplifier. The preamplifier is then connected to an amplifier as shown in Figure 2.3.11. The amplified signal then goes through a series of channel analyzers. A single channel analyzer (SCA) receives the signal and sends it to a multi-channel analyzer (MCA). The electronic signal generator controls the start-delay signals to the MCA and the voltage signals to the transducer creating a sync between the MCA and transducer.

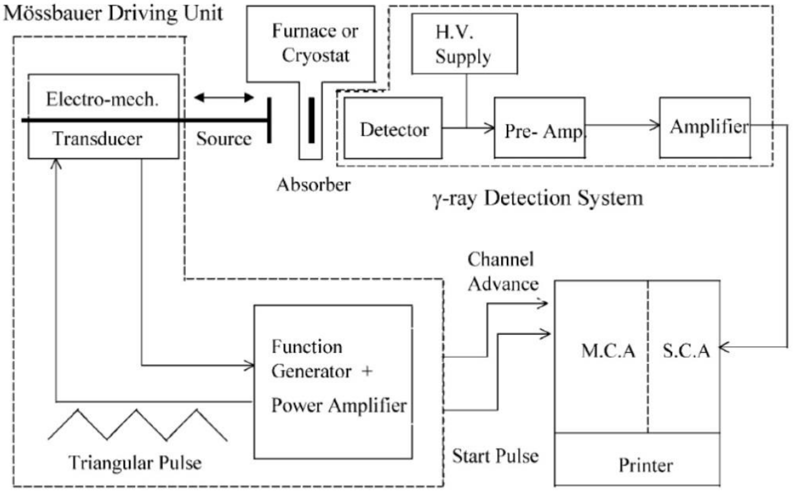

Figure 2.3.11 The schematic set up for the Mossbauer spectroscopy [7].

The radioactive source is installed on the transducer allowing it to ripple at a specific velocity profile v with respect to the fixed absorber. Accordingly, a Doppler effect is created resulting in the modulation of γ-ray energies upon arrival to the absorber. The γ photons and the transmission intensity are recorded using an attached detector. These results are later plotted as functions of the Doppler velocity v.

The ^{57}Fe and ^{151}Eu Mössbauer measurements were conducted using standard Mössbauer spectrometers operating in the sine mode, with sources ^{57}Co(Rh) and ^{151}Sm(SmF$_3$) at room temperature, respectively. The spectrometers were calibrated with a 6.35-μm-thick α-Fe foil. The absorber is put in a cryostat which is kept in a static exchange gas atmosphere at a pressure of 6×10^{-3}mbar. The low-temperature Mössbauer spectrometer used in this research is shown in the Figure below.

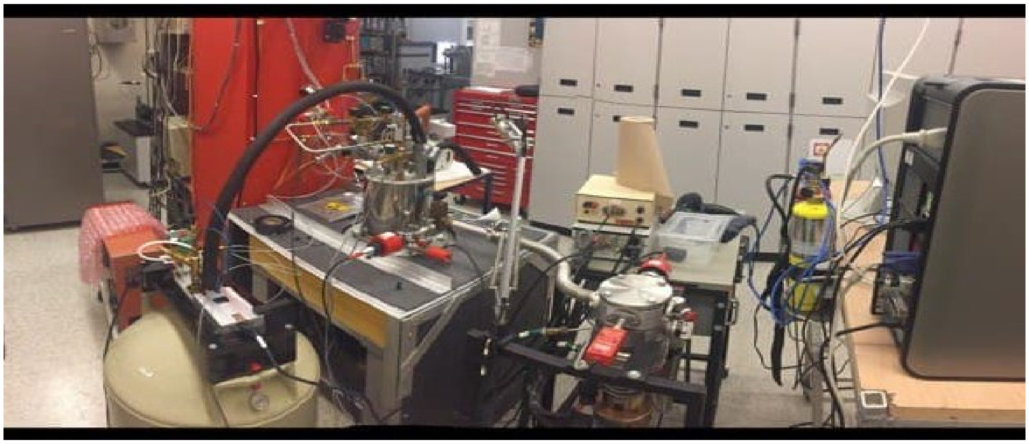

Figure 2.3.12 The low-temperature Mössbauer spectrometer.

Figure 2.3.13 shows the transducer and the detector which are used in the low-temperature Mössbauer spectrometer.

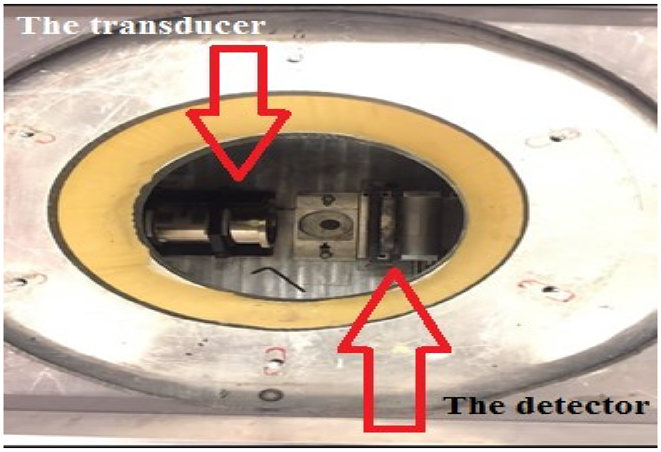

Figure 2.3.13 The transducer and the absorber of the low-temperature Mössbauer spectrometer.

References

[1] P. Gütlich, E. Bill, and A. Trautwein, *Mössbauer Spectroscopy and Transition Metal Chemistry* (Springer, Berlin, 2011).

[2] F. Nejadsattari, Theoretical and experimental studies of electronic structure, magnetic, and hyperfine interaction properties of novel compounds, Ph.D. Thesis (Ottawa, 2016).

[3] V. I. Goldanskii, R. Herber, *Chemical Applications of Mössbauer Spectroscopy* (Academic New York, 1968).

[4] N. W. Ashcroft and N. D. Mermin, *Solid State Physics*, (Harcourt, Orlando, 2011).

[5] F. Grandjean, and G. J. Long, *Mössbauer Spectroscopy Applied to Inorganic Chemistry*, Vol. 3 (Plenum, New York, 1989).

[6] U. Gonser, *Mössbauer Spectroscopy* (Springer, New York, 1975).

[7] D. Bandyopadhyay, Int. Mater. Rev. **51,** 174 (2006).

Chapter 3: Discussion and conclusions

In the following pages, I will discuss the results presented in chapters four through nine and draw conclusions.

The Rietveld analysis of the X-ray XRD spectrum of ThFeAsN showed that the studied material crystallizes in the tetragonal space group *P4/nmm*. The unit cell parameters determined from this analysis yielded the lattice parameters a = 4.0356(1) Å and c = 8.5286(1) Å. It was proved, based on the ^{57}Fe Mössbauer spectroscopy, that there is an absence of magnetic order of the Fe magnetic moments down to 2.0 K. The nonappearance of Fe magnetism was suggested to be as a result of an internal uniaxial chemical pressure whose presence is reflected in the unusually small c/a ratio. The Mössbauer spectra were all in the shape of a quadrupole doublet with a small quadrupole splitting that rise with lowering the temperature. The experimental extrapolated 0 K quadrupole splitting is in an excellent agreement with the calculated one. The calculated value of $Vzz = -3.908 \times 10^{20}$ V/m^2 corresponds to $\Delta = 0.0610$ mm/s. The fit of the $\Delta(T)$ data gives $\Delta(0)$ = 0.0664(8) mm/s. The value of $\Delta(0)$ is in a very good agreement with the calculated value of 0.0610 mm/s. The Debye temperature of ThFeAsN was found to be 332(2) K, and it agrees with the calculated value of 370 K. Theoretical discussion is offered for the presence of ionic and covalent chemical bonding and metallic characteristics. The energy band structure of ThFeAsN is analyzed in detail.

The room-temperature powder XRD pattern of $CsEuFe_4As_4$ reveals that the compound studied crystallizes in a tetragonal space group *P4/mmm*, as revealed by a Rietveld refinement analysis, with the lattice parameters of a = 3.8956(1) Å and c = 13.6628(5) Å. The detailed analysis of ^{57}Fe and ^{151}Eu Mössbauer spectra at different temperatures proved that the Fe atoms have no magnetic moment down to 2.1 K and that the ferromagnetic order is associated exclusively with the Eu magnetic moments. The Mössbauer spectrum of $CsEuFe_4As_4$ at 11.2 K is slightly broader than the 17.2 K spectrum (Fig. 7 in Chapter 5). This subtle effect of 0.010 mm s^{-1} broadening is the result of the appearance at 11.2 K of a very small H_{hf} that is transferred to the ^{57}Fe nuclei from the ferromagnetically ordered Eu sublattice. Its presence constitutes a clear proof for the ordering of the Eu sublattice. The calculated values of $Vzz = 7.142 \times 10^{20}$ V/m^2 at the Fe site corresponds to $\Delta = 0.1222$ mm/s^{-1}. The fit of the $\Delta(T)$ data gives $\Delta(0) = 0.1182(4)$ mm/s^{-1}.

The ^{151}Eu Mössbauer spectra of $CsEuFe_4As_4$ from room temperature down to 17.1 K were fitted with a large-spectral-area quadrupole pattern due to $CsEuFe_4As_4$ and a small-spectral-area singlet originating from an impurity phase. For the temperatures between 15.7 K and 4.8 K, the spectra were fitted with a large-spectral-area Zeeman pattern due to $CsEuFe_4As_4$ and a small-spectral-area singlet originating from an impurity phase. The temperature dependence of H_{hf} yielded the Curie temperature of the Eu sublattice T_C = 15.97(8) K. The detailed analysis of the low-temperature ^{151}Eu Mössbauer proved that the Eu magnetic moments lie in the *ab* plane. The temperature dependence of the main component of the electric field gradient tensor at both Fe and Eu sites is well described by a $T^{3/2}$ power-law relation. The calculated values of Vzz at the Eu site is -58.017×10^{20} V/m^2, and the fitted value of $Vzz(0)$ is $-0.516(5) \times 10^{22}$ V/m^2. There is a good agreement between the calculated and measured parameters of the hyperfine-interactions. The Debye temperature of $CsEuFe_4As_4$ was found to be 295(3) K.

Our *ab-initio* calculations provide evidence for a mixture of ionic, covalent, and metallic bonding in the $CsEuFe_4As_4$ superconductor. They show that, in agreement with the experiment, the magnetic moment of $CsEuFe_4As_4$ results from the strongly localized Eu *f* states. They also show that an almost zero magnetic moment of the Fe atoms results from an apparent symmetry of the spin-up and spin-down Fe *d* states. The Fermi surfaces are found to have the hole-like and electron-like pockets located at the center and corners of the Brillouin zone, respectively.

The Rietveld analysis of the room-temperature powder XRD spectrum of $Rb_{1-\delta}EuFe_4As_4$ showed that the compound studied crystallizes in the tetragonal space group *P*4*/mmm* and its lattice parameters are a = 3.8849(1) Å and c = 13.3370(3) Å. A careful analysis of the ^{57}Fe and ^{151}Eu Mössbauer spectra at various temperatures demonstrates that the Fe atoms have no magnetic moment down to 2.1 K and that the ferromagnetic order is associated entirely with the Eu magnetic moments. We show that the Eu magnetic moment induces the transferred hyperfine magnetic field H_{hf} at the ^{57}Fe nuclei and that the Curie temperature determined from the temperature dependence of the latter is consistent with that obtained from the temperature dependence of H_{hf} at the ^{151}Eu nuclei. The analysis of low-temperature ^{151}Eu Mössbauer proves that the Eu magnetic moments are perpendicular to the crystallographic *c* axis. At both the Fe and Eu sites, the temperature dependence of the main component of the electric-field-gradient tensor is well represented by a $T^{3/2}$ power-law relation. The calculated value of $Vzz = 5.270 \times 10^{20}$ V/m^2 at the Fe site corresponds to $\Delta = 0.0921$ mm/s^{-1}. The fit of the Δ(T) data gives $\Delta(0) = 0.1188(2)$ mm/s^{-1}. The calculated value of Vzz at the Eu site is -49.659×10^{20} V/m^2, and the fitted value of $Vzz(0)$ is $-0.470(6) \times 10^{22}$ V/m^2. The calculated and measured hyperfine-interaction parameters showed a good agreement. The Debye temperature of $Rb_{1-\delta}EuFe_4As_4$ was found to be 391(8) K.

Similarly to the *ab-initio* study of $CsEuFe_4As_4$, we find evidence for the presence of a mixture of ionic, covalent, and metallic bonding in the $RbEuFe_4As_4$ superconductor. The magnetic moment of $RbEuFe_4As_4$ is shown to be a result of the strongly localized Eu *f* states. We also find that an almost zero magnetic moment associated with the Fe atoms is the consequence of symmetry of the spin-up and spin-down Fe *d* states. The chemical and electrical properties are shown to be strongly linked with the Fe 3*d* states in the Fermi energy region. The hole-like and electron-like pockets that are located, respectively, at the center and corners of the Brillouin zone, are found in the Fermi surfaces of $RbEuFe_4As_4$.

Based on the analysis of the ^{57}Fe Mössbauer spectra of both the new $EuFeAs_2$ compound and the 14 K superconductor $EuFe_{0.97}Ni_{0.03}As_2$, it is concluded that in both systems the Fe sublattice orders in the antiferromagnetic spin-density-wave fashion. The Néel temperatures of the Fe sublattice and the Fe saturation magnetic moments are found to be 106.2(1.9) K, $0.78(1)\mu_B$ and 56.6(2.2) K, $0.47(1)\mu_B$, respectively. In addition, the fits of the ^{151}Eu Mössbauer spectra of $EuFeAs_2$ and $EuFe_{0.97}Ni_{0.03}As_2$ allow us to find out that the Néel temperatures and the saturation hyperfine magnetic fields of the antiferromagnetically ordered Eu sublattice in both compounds are, respectively, 44.4(5) K, 294.2(7) kOe, and 43.5(1) K, 290.5(1) kOe. These results show that a tiny substitution of Fe by Ni in $EuFeAs_2$, apart from inducing superconductivity in $EuFe_{0.97}Ni_{0.03}As_2$, significantly reduces the magnetism's strength of the Fe sublattice and has practically no influence on the magnetism of the Eu sublattice. The presence of antiferromagnetically ordered Fe and Eu sublattices in $EuFe_{0.97}Ni_{0.03}As_2$ constitutes evidence that superconductivity and magnetism do coexist in the $EuFe_{0.97}Ni_{0.03}As_2$ superconductor. We show that a $T^{3/2}$ power-law relation can explain the magnitude increase of the main component of the electric field gradient tensor at both Fe and Eu sites with lowering temperature. For $EuFeAs_2$ compound the fitted value of $Vzz(0)$ at the Eu site is $-0.498(5) \times 10^{22}$ V/m^2. For $EuFe_{0.97}Ni_{0.03}As_2$ the fitted value at the Fe site of the $\Delta(T)$ data gives $\Delta(0) = 0.1590(17)$ mm/s^{-1}, and at the Eu site, the fitted value of $Vzz(0)$ is $-0.448(5) \times 10^{22}$ V/m^2. The Debye temperatures of $EuFeAs_2$, $EuFe_{0.97}Ni_{0.03}As_2$, and the $FeAs_2$ impurity phase were determined to be 355(18), 428(14), and 594(25) K, respectively.

Chapter 4: Absence of the stripe antiferromagnetic order on ThFeAsN

Journal of Alloys and Compounds 695 (2017) 1128–1136

Contents lists available at ScienceDirect

Journal of Alloys and Compounds

journal homepage: http://www.elsevier.com/locate/jalcom

Absence of the stripe antiferromagnetic order in the new 30 K superconductor ThFeAsN

Mohammed A. Albedah [a, b], Farshad Nejadsattari [a], Zbigniew M. Stadnik [a, *],
Zhi-Cheng Wang [c], Cao Wang [d], Guang-Han Cao [c]

[a] Department of Physics, University of Ottawa, Ottawa, Ontario K1N 6N5, Canada
[b] Department of Physics, Majmaah University, P.O. Box 1712, Zulfi, Saudi Arabia
[c] Department of Physics and State Key Lab of Silicon Materials, Zhejiang University, Hangzhou 310027, China
[d] Department of Physics, Shandong University of Technology, Zibo 255049, China

ARTICLE INFO

Article history:
Received 26 August 2016
Received in revised form
22 October 2016
Accepted 25 October 2016
Available online 27 October 2016

Keywords:
^{57}Fe Mössbauer spectroscopy
Electric quadrupole splitting
Density of states
Energy band structure
Debye temperature

ABSTRACT

We report the results of X-ray diffraction and ^{57}Fe Mössbauer spectroscopy study, complemented by *ab-initio* calculations of the electronic structure, hyperfine-interaction parameters, and elastic properties of the new 30 K superconductor ThFeAsN. The superconductor crystallizes in the tetragonal space group *P4/nmm* with the lattice parameters a = 4.0356(1) Å and c = 8.5286(1) Å. Contrary to the claims in the literature, we demonstrate unequivocally that there is no magnetic order of the Fe magnetic moments down to 2.0 K. It is suggested that the absence of Fe magnetism may be due to an internal uniaxial chemical pressure whose presence is manifested by the unusually small c/a ratio. Evidence is provided for the presence of a mixture of ionic and covalent chemical bonding and of metallic characteristics. A detailed analysis of the energy band structure of ThFeAsN is presented. The shape of the Mössbauer spectra is accounted for by a quadrupole doublet with a small quadrupole splitting that increases with decreasing temperature. Excellent agreement between the calculated and measured 0 K quadrupole splittings is observed. Fair agreement between the experimental Debye temperature of 332(2) K and the calculated one of 370 K is observed.

© 2016 Elsevier B.V. All rights reserved.

1. Introduction

It has been well established [1] that high-critical temperature superconductivity in the iron pnictides and chalcogenides emerges from the suppression of the spin-density-wave antiferromagnetic order in their parent compounds either through carrier doping or by applying pressure. This results in phase diagrams similar to those in the copper-oxide-based superconductors [2].

Recently, a new parent-like compound, ThFeAsN, has been discovered [3]. What is unusual about this compound is that it is superconducting, with the critical temperature $T_c = 30$ K, without any doping or applying pressure [3]. The first-principles calculations [4,5] unambiguously predict the stripe antiferromagnetic order in this compound. However, no anomaly expected for such an order is observed in the electrical resistivity and magnetic susceptibility data [3]. Here we use the local probe, ^{57}Fe Mössbauer spectroscopy, to address the issue of the possible magnetic order in ThFeAsN.

2. Experimental and theoretical methods

The polycrystalline sample of composition ThFeAsN was prepared by solid-state reactions at high temperatures, as described earlier [3].

An X-ray diffraction measurement was carried out at 298 K in Bragg-Brentano geometry on a PANalytical X'Pert scanning diffractometer using Cu $K\alpha$ radiation in the 2θ range 8–120° in steps of 0.02°. The $K\beta$ line was eliminated by using a Kevex PSi2 Peltier-cooled solid-state Si detector.

The ^{57}Fe Mössbauer measurements [6] were conducted using a standard Mössbauer spectrometer operating in the sine mode and a ^{57}Co(Rh) source at room temperature. The spectrometer was calibrated with a 6.35-μm-thick α-Fe foil [7] and the spectra were folded. The Mössbauer absorber consisted of a mixture of powdered ThFeAsN, and powdered boron nitride, which was

---

* Corresponding author.
E-mail address: stadnik@uottawa.ca (Z.M. Stadnik).

http://dx.doi.org/10.1016/j.jallcom.2016.10.239
0925-8388/© 2016 Elsevier B.V. All rights reserved.

pressed into a pellet and put into a high-purity, 8-μm-thick Al disk container to ensure a uniform temperature over the whole absorber. The Mössbauer absorber was put into a Mössbauer cryostat in which it was kept in a static exchange gas atmosphere at a pressure of ~ 6×10^{-3} mbar. The surface density of the Mössbauer absorber was 23.8 mg/cm^2. This corresponds to an effective thickness parameter [6] $t_a = 2.1 f_a$, where f_a is the Debye-Waller factor of the absorber. Since $t_a > 1$, the resonance line shape of the Mössbauer spectra was described using a transmission integral formula [8].

Ab-initio electronic structure and Mössbauer hyperfine-interaction parameter calculations have been performed within the framework of density functional theory using the full-potential linearized augmented-plane-wave plus local orbitals (FP-LAPW+lo) method as implemented in the WIEN2k package [9]. In this method, one partitions the unit cell into two regions: a region of non-overlapping muffin-tin (MT) spheres centered at the atomic sites and an interstitial region. The wave functions in the MT regions are a linear combination of atomic radial functions times spherical harmonics, whereas in the interstitial regions they are expanded in plane waves. The basis set inside each MT sphere is split into a core and a valence subset. The core states are treated within the spherical part of the potential only and are assumed to have a spherically symmetric charge density in the MT spheres. The valence wave functions in the interstitial region were expanded in spherical harmonics up to $l = 4$, whereas in the MT region they were expanded to a maximum of $l = 12$ harmonics. For the exchange-correlation potential, the generalized gradient approximation (GGA) scheme of Perdew, Burke, and Ernzerhof [10] was used. A separation energy of -6.0 Ry between the valence and core states of individual atoms in the unit cell was chosen. The values of 2.47, 2.32, 2.20, and 1.92 a.u. were used as the MT radii for Th, Fe, As, and N, respectively. The plane-wave cut-off parameter was set to $R_{MT} \times K_{MAX} = 6.0$, where R_{MT} is the smallest MT radius in the unit cell and K_{MAX} is the maximum K vector used in the plane-wave expansion in the interstitial region. A total number of 735 inequivalent k-points was used within a shifted $27 \times 27 \times 13$ k-mesh in the irreducible wedge of the first Brillouin zone. A convergence criterion for self-consistent field calculations was chosen in such a way that the difference in energy between two successive iterations did not exceed 10^{-5} Ry. The experimental lattice parameters (a and c) and the atomic position parameters in the space group $P4/nmm$ (*vide infra*) were used in the calculations.

3. Results and discussion

3.1. Structural characterization

The room-temperature powder X-ray diffraction pattern of ThFeAsN is shown in Fig. 1. The compound studied, analogously to the antiferromagnetically ordered parent compound GdFeAsO [11], crystallizes in the tetragonal space group $P4/nmm$ [3]. A Rietveld refinement [12] of the X-ray powder diffraction data was carried out, yielding the lattice parameters $a = 4.0356(1)$ Å and $c = 8.5286(1)$ Å, and the atomic positional parameters that are listed in Table 1. The occupancy of Th deviates slightly from 1.0 (Table 1), yielding a formula $Th_{0.99}FeAsN$ for the compound of the nominal composition ThFeAsN. No second phase/phases could be detected in the X-ray diffraction pattern of ThFeAsN (Fig. 1).

Fig. 2 shows the crystal structure of ThFeAsN. The central region of the unit cell [Fig. 2 (a)] is occupied by Fe and As atoms which interact with each other via metallic bonds (*vide infra*). These bonds are shown schematically in Fig. 2(a) by rods connecting these atoms. The Fe and As atoms are surrounded by layers of Th and N atoms that are located at equal distances above and below the Fe and As atoms along the c-direction. The elongation of the unit cell along the c-direction significantly reduces the Coulomb interaction between neighboring Fe/As sheets. In fact, the Th/N layers above and below the Fe/As conducting sheets serve as insulating layers that are separated from the neighboring Fe/As conducting layers along the c-direction. The nature of these bonds is discussed below based on the density of states (DOS) calculations.

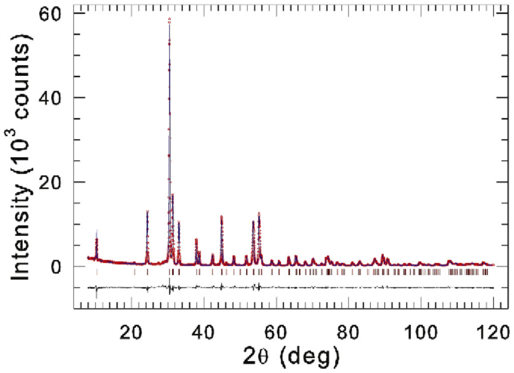

Fig. 1. Powder X-ray diffraction pattern of ThFeAsN at 298 K. The experimental data are denoted by open circles, while the line through the circles represents the results of the Rietveld refinement. The row of vertical bars shows the Bragg peak positions for the $P4/nmm$ space group. The lower solid line represents the difference curve between experimental and calculated patterns.

The alternating layered structure of ThFeAsN along the c-axis can be clearly seen in Fig. 2(b). The connecting rods indicate the possibility of charge transfer (electrical conduction) along the $z = 0.5$ planes, whereas the absence of such connections along the c-axis indicates ionic bonding which suppresses electrical conduction along the c-direction. These properties are justified based on the calculated electronic charge density distributions (*vide infra*).

3.2. Ab-initio calculations

3.2.1. Charge density distributions

Fig. 3 displays the calculated valence charge density distributions along three different planes. The mid-plane of the unit cell of ThFeAsN is occupied by Fe atoms (Fig. 2) that weakly interact. This results in a non-negligible electron charge density that uniformly fills the space between neighboring Fe atoms [yellow regions in Fig. 3(a)].

The layered structure of the ThFeAsN superconductor is clearly evidenced in the electron charge density distribution along the $z = 0.25$ plane [Fig. 3(b)]. The virtual absence of the charge density between the Th/N and Fe/As layers [yellow regions in Fig. 3(b)] indicate the ionic nature of the chemical bonding between these

Table 1
Atomic positions for the tetragonal ThFeAsN (space group $P4/nmm$, origin choice 2) obtained through Rietveld analysis.

Atom	Site	Point symmetry	Occupancy	x	y	z
Th	$2c$	$4mm$	0.991	$\frac{1}{4}$	$\frac{1}{4}$	0.1377
Fe	$2b$	$\bar{4}m2$	1.000	$\frac{3}{4}$	$\frac{1}{4}$	$\frac{1}{2}$
As	$2c$	$4mm$	1.000	$\frac{1}{4}$	$\frac{1}{4}$	0.6534
N	$2a$	$\bar{4}m2$	1.000	$\frac{3}{4}$	$\frac{1}{4}$	0

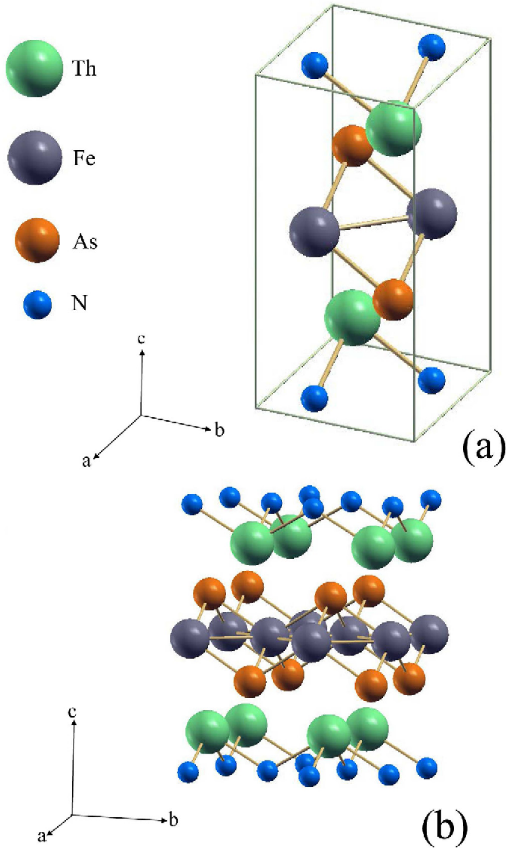

Fig. 2. The unit cell (a) and the layered crystal structure (b) of ThFeAsN.

layers, resulting in alternating insulating sheets along the *c*-direction. This supports an earlier argument based on the physical separation of the constituent atoms in the unit cell of ThFeAsN. The presence of large charge density between Fe and As atoms [blue/green regions in Fig. 3(b)] indicates the strong covalent and also metallic bonds between these atoms. One can observe that the charge density distribution is widely spread out from the As atoms (blue regions) to form bonds with the neighboring Fe atoms. This can be explained by the semi-metallic nature of As that is widely used as an *n*-type dopant in a semiconductor industry.

Due to a relatively small separation between the Fe atoms in the (110) plane, there is a persistent charge density along the line connecting these atoms [yellow-green regions in Fig. 3(c)]. This is not the case for the N atoms where the charges are bound to them. One can also observe [Fig. 3(c)] that there is essentially no charge density between the Fe/N regions. This can be explained by a relatively large separation between the Fe and N atoms in the unit cell of ThFeAsN (Fig. 2). As a result, the Coulomb interaction between these atoms will be not large enough to distort their electron configurations.

The valence charge density distributions discussed above are not unique to the ThFeAsN superconductor but seem to be characteristic for Fe-based superconductors generally. For example, the valence charge density distributions of the recently discovered 40 K superconductor (Li$_{0.8}$Fe$_{0.2}$)OHFeSe with no long-range magnetic order, that also crystallizes in the tetragonal space group $P4/nmm$, are very similar [13] to those of ThFeAsN.

3.2.2. Density of states

The calculated total and atom-resolved DOS of ThFeAsN is shown in Fig. 4. One notices that the Fermi energy (E_F) region is dominated by the Fe *d* states. A minimum in the DOS, centered at ~0.30 eV above E_F and with a width of ~1.0 eV, is observed. The Fe *d* states mainly occupy the energy region between about $-5 - 2$ eV. A highly peaked DOS structure, that is almost entirely due to Th atoms, occurs in the energy region between 2.5 to about 5.0 eV. The states in this region essentially do not overlap with the Fe *d* states. One thus can conclude that a strong ionic bond exists between the Th and Fe atoms, which supports the earlier conclusion that was based on the electron charge density distributions. On the contrary, the As and Th states overlap considerably, especially in the energy region between -5 and 0 eV. A relatively intense peak in the DOS, located at 3.0 eV below E_F, is observed (Fig. 4). It is due to Fe—As *p*-*d* hybridization. The strong overlap between the As and Th states constitutes evidence for the covalent nature of the chemical bonding between the Fe and As atoms.

One observes a wide gap in the DOS in the energy region between -10 and -5 eV (Fig. 4). Below this region is the realm of semi-core and core states that have sharp DOS, resembling atomic-like states. In particular, a sharp peak located at 10.6 eV below E_F, that is mainly due to the As core states, is observed. These states do not participate in chemical bonding.

Fig. 5 shows the Fe total and orbital-resolved DOS. The peak in the Fe DOS located in the energy region between 0.8 and 1.0 eV arises from the Fe $d_{x^2-y^2}$ orbitals, which generally have higher energies than the other Fe *d* orbitals. There are two major peaks in the Fe DOS located below E_F. The first one at -0.23 eV is due to the Fe d_{xz+yz} orbitals. The contribution to the second peak at -0.44 eV is mainly from the Fe d_{xy} orbitals. The presence of a shallow dip in the Fe DOS between 0.2 and 0.6 eV may account for a relatively large electrical resistivity of ThFeAsN [3] as compared to that of typical metals.

3.2.3. Energy band structure

The calculated electronic band structure of non-magnetic ThFeAsN for the energy range between -15 and 10 eV is shown in Fig. 6(a). There are three energy regions in which the band structure is dense, i.e., there is a large number of accessible states. By inspecting a specific symmetry point in the Brillouin zone, one can study these states. Due to the very high symmetry of the Γ point, many electronic states are degenerate. The first dense region in the band structure appears around 3 eV below E_F. The energy bands in this region are mainly due to the As and N states of *p*-like character. As one moves away from Γ in any direction (for example, from Γ to R or from Γ to M), the symmetry of the *k*-space reduces and, as a result, the energy bands start to split and spread in energy. Energy bands of *s*- and *p*-like character spread widely in energy.

The second energy region of interest is in the vicinity of E_F. This region contains energy bands of *d* character arising from the Fe states. Compared to the bands in the first region, these energy bands are localized in energy, which indicates their *d*-like origin. A closer look at these energy bands [Fig. 6(b)] shows that three valence bands and two conduction bands cross the Fermi level. At the symmetry point Γ, the three valence bands have their maximum energy. Of these three, two are degenerate and are located 0.1 eV above E_F. These bands are indicated by light brown and black colors and refer to heavy-hole and light-hole bands,

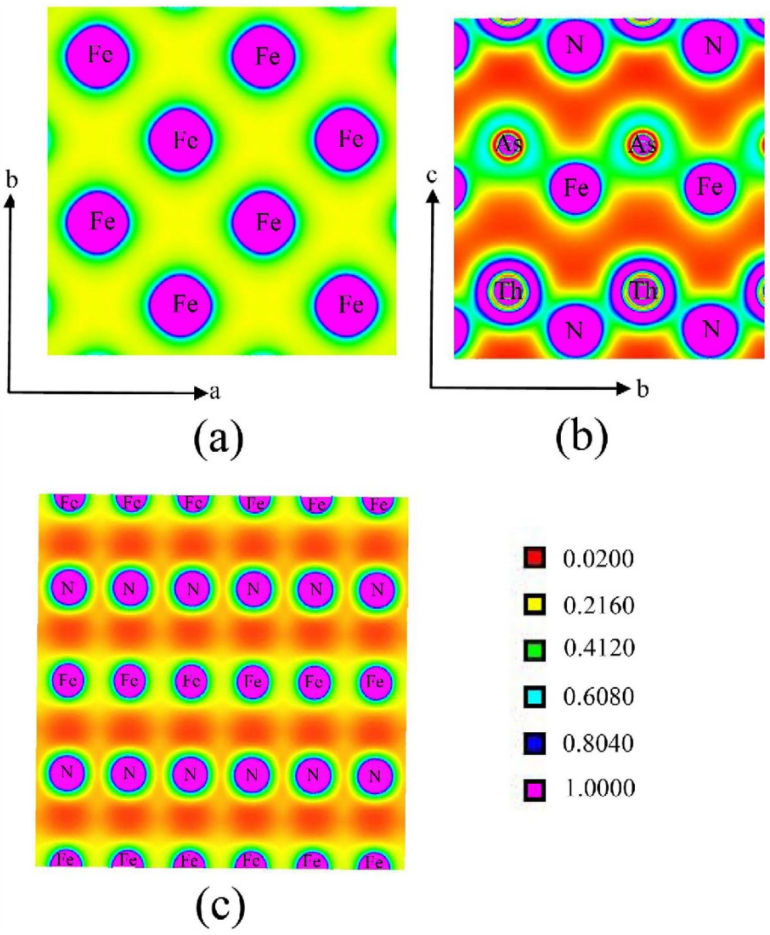

Fig. 3. Electron charge density distribution (in units of e/Å^3) along the z=0.5 (a), z=0.25 (b), and (110) (c) planes.

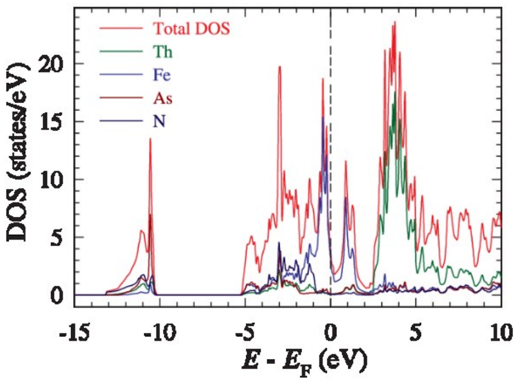

Fig. 4. Total and atom-resolved density of states of ThFeAsN.

respectively. The spin-split off band (indicated by cyan color) is located at a slightly lower energy in the vicinity of E_F. The heavy-hole bands originate from the $\mathrm{Fe}\left|\frac{3}{2}, \pm\frac{1}{2}\right>$ states and have a larger effective mass with respect to the light-hole bands which originate from the $\mathrm{Fe}\left|\frac{3}{2}, \pm\frac{3}{2}\right>$ states. The spin-split off band is related to the $\mathrm{Fe}\left|\frac{1}{2}, \pm\frac{1}{2}\right>$ states. The minimum of the two conduction bands is located at the M point in the Brillouin zone, about 0.1 eV below E_F and is two-fold degenerate. These electron-like bands are shown in black and green colors [Fig. 6(b)]. The fact that the maximum of the valence band and the minimum of the conduction band cross the Fermi level can explain the non-zero electrical conductivity of ThFeAsN.

The third energy region, which contains a large number of bands, is located between about 3 and 5 eV above E_F [Fig. 6(a)]. The numerous bands in this region are due to the Th conduction states. One observes that these energy bands do not cross with the Fe

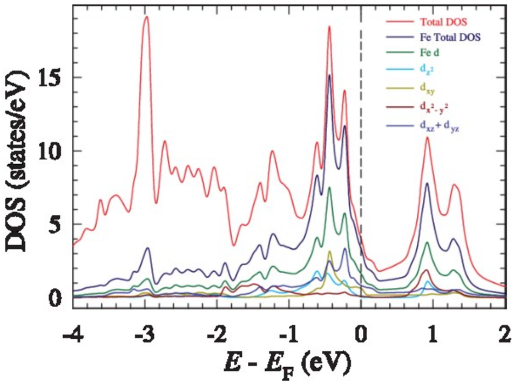

Fig. 5. Total and orbital-resolved Fe density of states in ThFeAsN.

energy bands, as expected from the ionic nature of the bonding between these atoms.

In the energy region between −10 and −5 eV [Fig. 6(a)], a wide gap separating the low-lying core and semi-core states from the higher valence states exists.

It is perhaps useful to notice that the conclusions derived from our electron charge density distribution, DOS, and energy band structure calculations are consistent with each other.

3.2.4. *Elastic parameters*

The elastic parameters discussed here were calculated for the optimized lattice parameters derived from the minimization of the total energy (Fig. 7). The energy minimum of −120501.423 Ry occurs for the optimized volume of the tetragonal unit cell of 919.550 (a.u.)^3. The value of the optimized volume is close to the value of 937.335 (a.u.)^3 obtained from the Rietveld refinement. The calculated equilibrium bulk modulus, B_0, of ThFeAsN is 153.55 GPa. Its pressure derivative, B'_0, is 4.553. Although no experimental value of B_0 is known for ThFeAsN, the calculated B_0 compares reasonably well with the experimental value of 102(2) GPa for the NdFeAsO$_{0.88}$F$_{0.12}$ superconductor of the same crystal structure as that of ThFeAsN [14].

The calculated density ρ of ThFeAsN is 9.0097 g/cm^3. For the tetragonal structure of ThFeAsN, the calculated second-order elastic constants C_{11}, C_{12}, C_{13}, C_{33}, C_{44}, and C_{66} are 489.76, 115.35, 283.51, 102.49, 374.72, and 63.16 GPa, respectively. By averaging the elastic moduli representing the basic transversal acoustic modes, the relevant modulus for the tetragonal structure is $G_t = [C_{44}C_{66}(C_{11} - C_{12})/2]^{1/3}$ [15]. Using the calculated elastic constants, one finds $G_t = 164.24$ GPa. This allows one to calculate the Debye temperature from the relation $\Theta_D = \Theta_{D,ref} + \frac{1}{2.03}\left[\frac{G_t}{Ms^{1/2}} - \left(\frac{G_t}{Ms^{1/2}}\right)_{ref}\right]$ that is obtained from the fit of the Θ_D data for different compounds with tetragonal structure [15]. In this relation, a is the lattice parameter, M is the arithmetic average of the atomic weight of the elements of a compound, s is the number of atoms in a unit cell, and $\Theta_{D,ref}$, $\left(\frac{G_t}{Ms^{1/2}}\right)_{ref}$ are the quantities corresponding to a given reference compound (Table III in Ref. [15]). Using the Rietveld refinement value of $a = 4.0356$ Å and the value of $M = 94.204 \times 10^{-3}$ kg obtained from the *ab-initio* calculations, one finds that $\Theta_D = 370$ K.

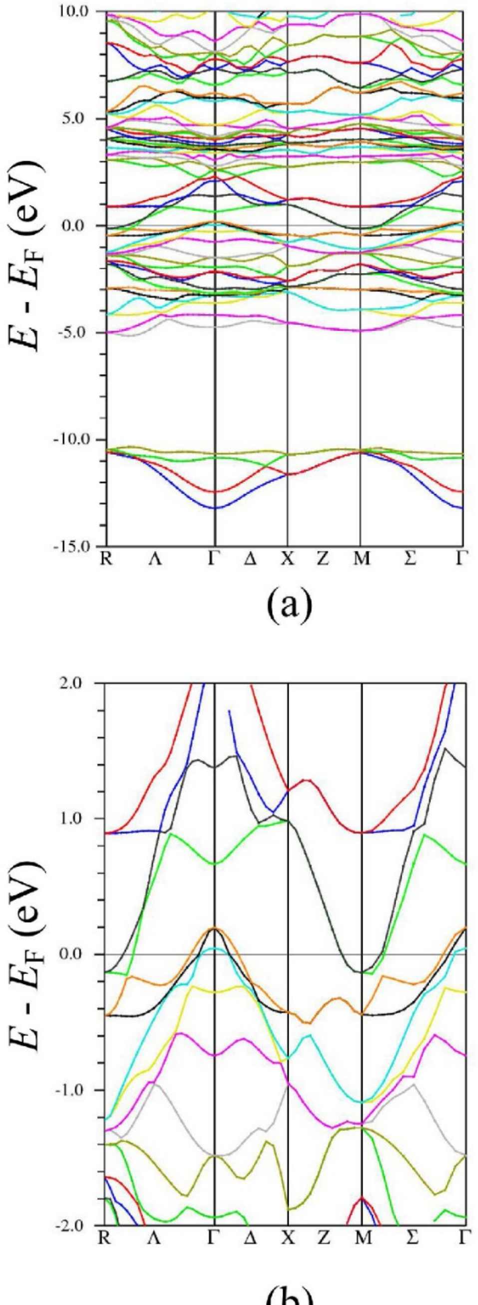

(a)

(b)

Fig. 6. Energy band structure of ThFeAsN for the energy range between −15 and 10 eV (a) and between −2 and 2 eV (b).

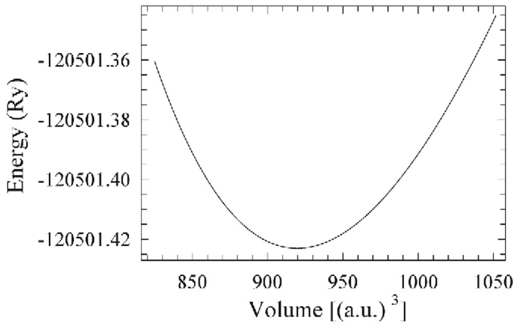

Fig. 7. Total energy as a function of volume of the tetragonal unit cell of ThFeAsN.

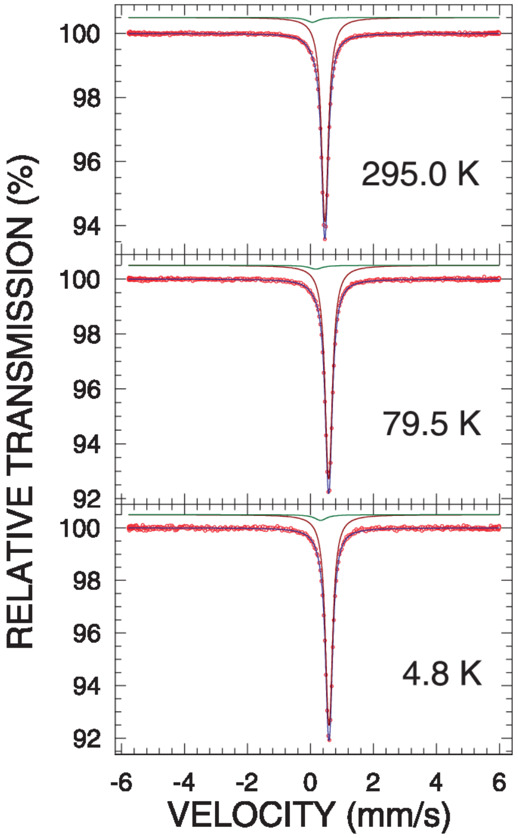

Fig. 8. Room-, liquid-nitrogen, and liquid-helium temperature ^{57}Fe Mössbauer spectra of ThFeAsN measured in a large velocity range fitted (blue solid line) with a quadrupole doublet (dark red solid line) and a broad singlet (dark green line), as described in the text. The zero-velocity origin is relative to α-Fe at room temperature. (For interpretation of the references to colour in this figure legend, the reader is referred to the web version of this article.)

3.2.5. *Hyperfine interaction parameters*

Mössbauer spectra of a compound with no magnetic order yield two important hyperfine-interaction parameters: the quadrupole splitting (the separation between two resonance lines in a ^{57}Fe Mössbauer quadrupole doublet) $\Delta = \frac{1}{2}eQ\left|V_{zz}\right|\sqrt{1+\eta^2/3}$, where e is the proton charge, Q is the electric quadrupole moment of the ^{57}Fe nucleus (0.15 b) [16], V_{zz} is the principal component of the electric field gradient (EFG) tensor, and η is the asymmetry parameter, and the isomer shift, δ_0 [6]. For a crystalline compound of known crystal structure, V_{zz}, η, and δ_0 can be also obtained from *ab-initio* calculations [17].

For the compound studied here, the Fe atoms are located at the 2*b* sites with the point symmetry $\bar{4}$m2 (Table 1), which ensures that $\eta = 0$. The calculated value of $V_{zz} = -3.908 \times 10^{20}$ V/m^2 corresponds to $\Delta = 0.0610$ mm/s. This calculated value of Δ will be compared below with that determined experimentally.

The isomer shift $\delta_0 = \alpha[\rho(0) - \rho_{ref}(0)]$ results from the difference in the total electron density at the Mössbauer nucleus in the compound studied, $\rho(0)$, and in the reference compound, $\rho_{ref}(0)$; α is a calibration constant. In calculating $\rho(0)$, relativistic spin-orbit effects were invoked in order to account for the possibility of the penetration of the $p_{1/2}$ electrons into the ^{57}Fe nuclei. An α-Fe (with the *bcc* structure and the lattice constant of 2.8665 Å) was chosen as a reference compound. The calculated value of $\rho_{ref}(0)$ and $\rho(0)$ are 15309.905 and 15308.321 (a.u.)$^{-3}$, respectively. Using the calibration constant $\alpha = -0.291$ (a.u.)^3 (mm/s) [18], the calculated values of $\rho(0)$ and $\rho_{ref}(0)$ lead to $\delta_0 = 0.461$ mm/s. The calculated δ_0 value

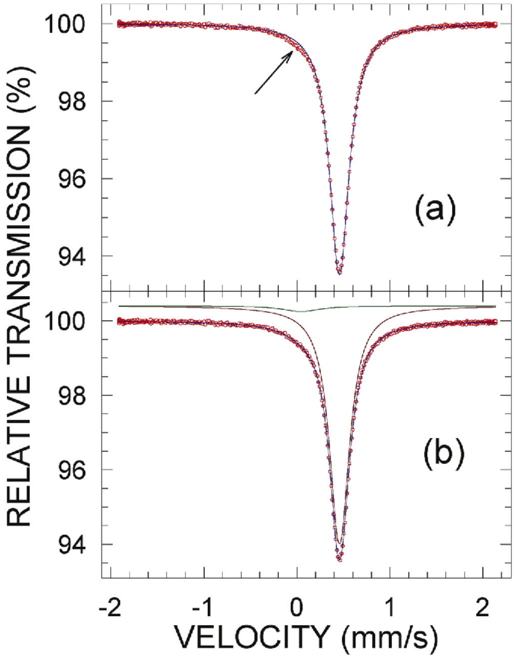

Fig. 9. ^{57}Fe Mössbauer spectrum of ThFeAsN at 297.0 K fitted (blue solid line) with (a) a quadrupole doublet (dark red solid line) and (b) a quadrupole doublet (dark red solid line) and a broad singlet (dark green line), as described in the text. The zero-velocity origin is relative to α-Fe at room temperature. (For interpretation of the references to colour in this figure legend, the reader is referred to the web version of this article.)

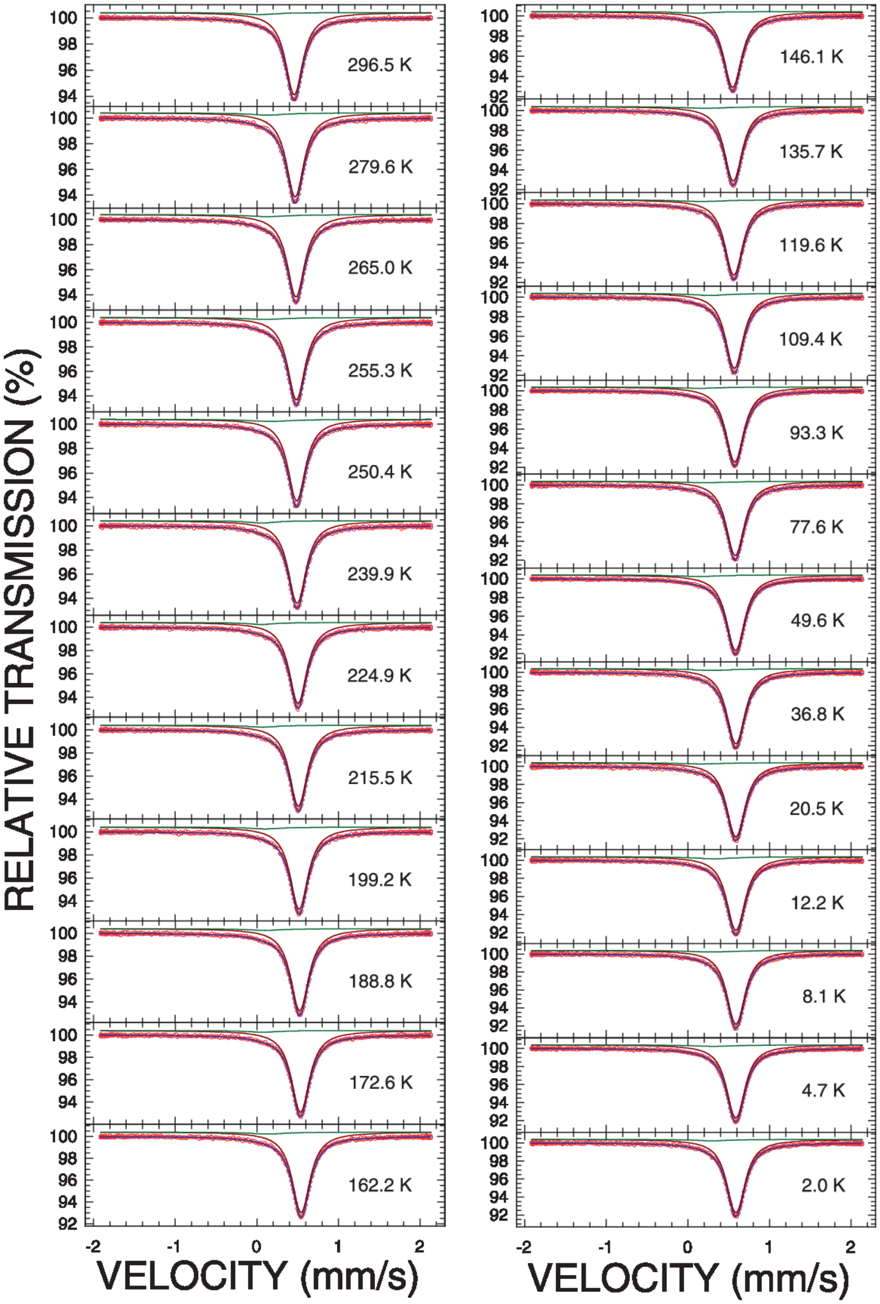

Fig. 10. ^{57}Fe Mössbauer spectra of ThFeAsN at the indicated temperatures fitted (blue solid lines) with a quadrupole doublet (dark red solid lines) and a broad singlet (dark green lines), as described in the text. The zero-velocity origin is relative to α-Fe at room temperature. (For interpretation of the references to colour in this figure legend, the reader is referred to the web version of this article.)

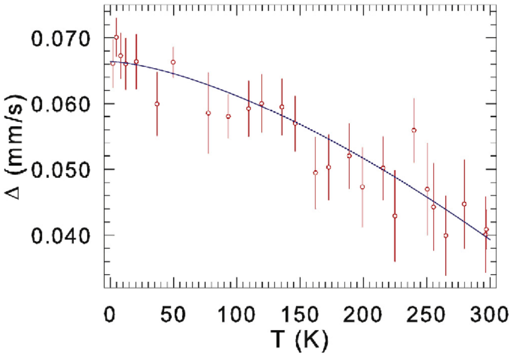

Fig. 11. Temperature dependence of the quadrupole splitting of ThFeAsN. The solid line is the fit to Eq. (1), as explained in the text.

will be compared below with the experimental one.

3.3. Mössbauer spectroscopy

In order to access the possibility of the presence of Fe-containing, magnetically-ordered impurity phase in the studied sample, the room-, liquid-nitrogen, and liquid-helium temperature ^{57}Fe Mössbauer spectra of ThFeAsN were measured over a large velocity range (Fig. 8). Apart from a quadrupole doublet (with very small Δ) originating from the main phase and a broad singlet originating from a paramagnetic impurity phase (*vide infra*), no Zeeman pattern due to a possible magnetic impurity phase present in the studied specimen can be discerned in the spectra (Fig. 8). If the compound studied does contain Fe-based magnetic impurity phase, its amount must be below the ^{57}Fe Mössbauer spectroscopy detection limit.

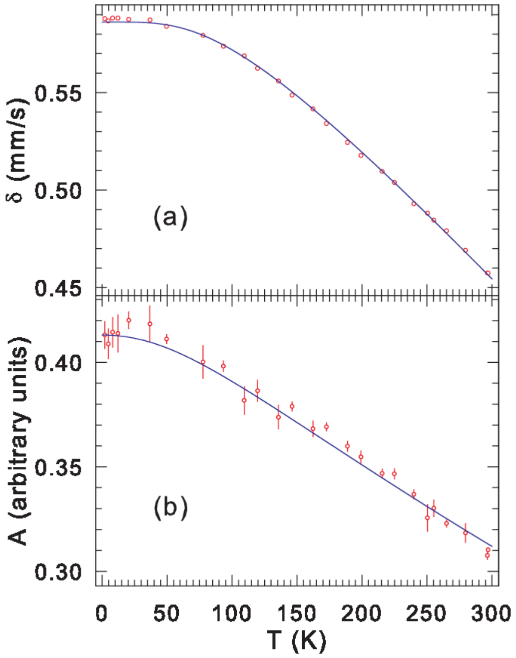

Fig. 12. Temperature dependence of (a) the centre shift δ and (b) the absorption spectral area *A*. The solid lines are the fits to Eq. (2) in (a) and to Eq. (4) in (b), as explained in the text.

Fig. 9 shows the room-temperature Mössbauer spectrum of ThFeAsN measured over a small velocity range. The fit of this spectrum with a quadrupole doublet with very small Δ, which has an appearance of a singlet, is clearly unsatisfactory [an arrow in Fig. 9(a) indicates the velocity range over which the spectrum is not fitted well]. A satisfactory fit can be obtained only by including an additional broad singlet [Fig. 9(b)] that must originate from a tiny amount of a paramagnetic impurity phase of unknown composition.

The Mössbauer spectra of ThFeAsN at various temperatures down to 2.0 K are shown in Fig. 10. Their shape is exactly the same as that of the spectrum in Fig. 9, i.e., excellent fits of these spectra can be obtained with a quadrupole doublet originating from the main phase and a broad singlet due to a paramagnetic impurity phase. The persistence of a quadrupole doublet component down to 2.0 K, i.e., the absence of any sign of a Zeeman pattern originating from the main phase, proves that the superconductor studied does not order magnetically down to 2.0 K. Thus, contrary to the theoretical predictions [4,5], no stripe antiferromagnetic order exists in the ThFeAsN superconductor.

A question naturally arises: why magnetic order does not exist in ThFeAsN while it persists in most parent compounds of Fe-based superconductors [1,2,11]? It is speculated here that the absence of Fe magnetism in ThFeAsN might be caused by an internal uniaxial chemical pressure since the *c*/*a* value for ThFeAsN is particularly small [3].

Fig. 11 shows the temperature dependence of Δ obtained from the fits of the spectra in Figs. 9(b) and 10. A clear increase of Δ with decreasing temperature is observed. Such a temperature dependence of Δ has been observed in many metallic systems [19,20]. It is well described by the empirical equation

$$\Delta(T) = \Delta(0)\left(1 - BT^{3/2}\right), \tag{1}$$

where Δ(0) is the value of Δ at 0 K and *B* is a constant. The fit of the Δ(*T*) data (Fig. 11) to Eq. (1) gives $\Delta(0) = 0.0664(8)$ mm/s and $B = 7.85(46) \times 10^{-5}$ K$^{-3/2}$. The value of *B* is similar to that found for other compounds [19,20]. The value of Δ(0) is in a very good agreement with the calculated value of 0.0610 mm/s.

The temperature dependence of the centre shift, δ, that was determined from the fits of the spectra in Figs. 9(b) and 10, is shown in Fig. 12(a). The centre shift at temperature *T*, δ(*T*), consists of two contributions

$$\delta(T) = \delta_0 + \delta_{SOD}(T), \tag{2}$$

where δ_0 is the intrinsic, temperature-independent isomer shift and $\delta_{SOD}(T)$ is the second-order Doppler (SOD) shift which depends on the lattice vibrations of the Fe atoms [6]. The latter contribution can be expressed in terms of the Debye approximation of the lattice vibrations as

$$\delta_{SOD}(T) = -\frac{9}{2}\frac{k_B T}{Mc}\left(\frac{T}{\Theta_D}\right)^3 \int_0^{\Theta_D/T} \frac{x^3 dx}{e^x - 1}, \tag{3}$$

where k_B is the Boltzmann constant, *M* is the mass of the Mössbauer nucleus, c is the speed of light, and Θ_D is the Debye temperature. The fits of the experimental data $\delta(T)$ [Fig. 12(a)] to Eq. (2) yields $\delta_0 = 0.586(1)$ mm/s and $\Theta_D = 383(3)$ K. We note that the experimental value of δ_0 found here is by 27% larger than the calculated δ_0.

There is another method of determining the Debye temperature from Mössbauer spectra. Fig. 12(b) shows the temperature dependence of the absorption spectral area A derived from the fits of the Mössbauer spectra in Figs. 9(b) and 10. This area is proportional to f_a, which is given in the Debye theory by Ref. [6].

$$f_a(T) = \exp\left\{ -\frac{3}{4}\frac{E_\gamma^2}{Mc^2 k_B \Theta_D}\left[1 + 4\left(\frac{T}{\Theta_D}\right)^2 \int_0^{\Theta_D/T} \frac{x dx}{e^x - 1}\right]\right\}, \tag{4}$$

where E_γ is the energy of the Mössbauer transition. The fit of the experimental dependence $A(T)$ [Fig. 12(b)] to Eq. (4) gives $\Theta_D = 332(2)$ K. The weighted average of the above two Θ_D values determined from the temperature dependence of two different Mössbaue parameters is 347(2) K. It is noted here that this experimental value of Θ_D is in fair agreement with the calculated value of 370 K.

One observes that the value of Θ_D determined from the $A(T)$ data is clearly smaller than the one derived from the $\delta(T)$ data. In fact, the Θ_D values determined from the $A(T)$ data are always smaller than the ones obtained from the $\delta(T)$ data. This results from the way in which Θ_D is calculated. One recalls that f_a and δ_{SOD} are related to the mean-square vibrational displacement $\langle x^2 \rangle$ and the mean-square velocity $\langle v^2 \rangle$ of the Mössbauer nucleus, respectively [6]. Since $\langle x^2 \rangle$ weights the phonon frequency distribution by ω^{-1} whilst $\langle v^2 \rangle$ weights it by ω^{+1} [21], the Θ_D values derived from the $A(T)$ data are necessarily lower than those determined from the $\delta(T)$ data.

4. Summary

The results of X-ray diffraction and ^{57}Fe Mössbauer spectroscopy study, complemented by *ab-initio* calculations of the electronic structure, hyperfine-interaction parameters, and elastic properties of the new 30 K superconductor ThFeAsN are presented. It is confirmed that the superconductor crystallizes in the tetragonal space group $P4/nmm$ with the lattice constants $a = 4.0356(1)$ Å and $c = 8.5286(1)$ Å. It is demonstrated that, despite recent claims to the contrary, there in no magnetic order of the Fe magnetic moments down to 2.0 K. The absence of Fe magnetism is proposed to be due to an internal uniaxial chemical pressure whose presence is reflected in the unusually small c/a ratio. Theoretical arguments are presented for the presence of a mixture of ionic and covalent chemical bonding and of metallic characteristics. The energy band structure of ThFeAsN is analyzed in detail. The Mössbauer spectra are all in the form of a quadrupole doublet with a small quadrupole splitting that increases with decreasing temperature. The experimental 0 K quadrupole splitting is in a very good agreement with the calculated one. The Debye temperature of ThFeAsN is found to be 332(2) K; it is in fair agreement with the calculated value of 370 K.

Acknowledgements

This work was supported by the Natural Sciences and Engineering Research Council of Canada.

References

[1] P. Dai, Rev. Mod. Phys. 87 (2015) 855.
[2] D.C. Johnston, Adv. Phys. 59 (2010) 803.
[3] C. Wang, Z.-C. Wang, Y.-X. Mei, Y.-K. Li, L. Li, Z.-T. Tang, Y. Liu, P. Zhang, H.-F. Zhai, Z.-A. Xu, G.-H. Cao, J. Am. Chem. Soc. 138 (2016) 2170.
[4] G. Wang, X. Shi, Europhys. Lett. 113 (2016) 67006.
[5] D.J. Singh, J. Alloys Compd. 687 (2016) 786.
[6] N.N. Greenwood, T.C. Gibb, Mössbauer Spectroscopy, Chapman and Hall, London, 1971. P. Gütlich, E. Bill, and A. Trautwein, Mössbauer Spectroscopy and Transition Metal Chemistry (Springer, Berlin, 2011).
[7] Certificate of Calibration, Iron Foil Mössbauer Standard, Natl. Bur. Stand. (U.S.) Circ. No. 1541, edited by J. P. Cali (U.S. GPO, Washington, D.C., 1971).
[8] S. Margulies, J.R. Ehrman, Nucl. Instrum. Methods 12 (1961) 131; G. K. Shenoy, J. M. Friedt, H. Maletta, and S. L. Ruby, in Mössbauer Effect Methodology, edited by I. J. Gruverman, C. W. Seidel, and D. K. Dieterly (Plenum, New York, 1974), Vol. 10, p. 277.
[9] P. Blaha, K. Schwartz, G. Madsen, D. Kvasnicka, J. Luitz, WIEN2k, an Augmented Plane Wave Plus Local Orbitals Program for Calculating Crystal Properties, Karlheinz Schwarz, Technical Universität Wien, Austria, 1999.
[10] J.P. Perdew, S. Burke, M. Ernzerhof, Phys. Rev. Lett. 77 (1996) 3865.
[11] P. Wang, Z.M. Stadnik, C. Wang, G.-H. Cao, J. Phys. Condens. Matter 22 (2010) 145701.
[12] R.A. Young, The Rietveld Method, Oxford University Press, Oxford, 1993.
[13] F. Nejadsattari, Z.M. Stadnik, J. Alloys Compd. 652 (2015) 470.
[14] J. Zhao, L. Wang, D. Dong, Z. Liu, H. Liu, G. Chen, D. Wu, J. Luo, N. Wang, Y. Yu, C. Jin, Q. Guo, J. Am. Chem. Soc. 130 (2008) 13828.
[15] H. Siethoff, K. Ahlborn, J. Appl. Phys. 79 (1996) 2968.
[16] G. Martínez-Pinedo, P. Schwerdtfeger, E. Caurier, K. Langanke, W. Nazarewich, T. Söhnel, Phys. Rev. Lett. 87 (2001) 062701.
[17] P. Blaha, J. Phys. Conf. Ser. 217 (2010) 012009.
[18] U.D. Wdowik, K. Ruebenbauer, Phys. Rev. B 76 (2007) 155118.
[19] M.A. Albedah, F. Nejadsattari, Z.M. Stadnik, J. Przewoźnik, J. Alloys Compd. 619 (2015) 839 (and references therein).
[20] Z.M. Stadnik, P. Wang, H.-D. Wang, C.-H. Dong, M.-H. Fang, J. Alloys Compd. 561 (2013) 82 (and references therein).
[21] R.M. Housley, F. Hess, Phys. Rev. 146 (1966) 517.

Chapter 5: Ferromagnetic order in $CsEuFe_4As_4$

IOP Publishing
Journal of Physics: Condensed Matter
J. Phys.: Condens. Matter **30** (2018) 155803 (11pp)
https://doi.org/10.1088/1361-648X/aab4af

Magnetism of the 35 K superconductor $CsEuFe_4As_4$

Mohammed A Albedah[1,2], **Farshad Nejadsattari**[1], **Zbigniew M Stadnik**[1], **Yi Liu**[3] **and Guang-Han Cao**[3]

[1] Department of Physics, University of Ottawa, Ottawa, Ontario, K1N 6N5, Canada
[2] Department of Physics, Majmaah University, PO Box 1712, Zulfi, Saudi Arabia
[3] Department of Physics, Zhejiang University, Hangzhou 310027, People's Republic of China

E-mail: stadnik@uottawa.ca

Received 16 January 2018, revised 2 March 2018
Accepted for publication 7 March 2018
Published 21 March 2018

Abstract

The results of *ab initio* hyperfine-interaction parameters calculations, and of x-ray diffraction and ^{57}Fe and ^{151}Eu Mössbauer spectroscopy study of the new 35 K superconductor $CsEuFe_4As_4$ are reported. The superconductor crystallizes in the tetragonal space group $P4/mmm$ with the lattice parameters $a = 3.8956(1)$ Å and $c = 13.6628(5)$ Å. It is demonstrated unequivocally that there is no magnetic order of the Fe magnetic moments down to 2.1 K and that the ferromagnetic order is associated with the Eu magnetic moments. The Curie temperature $T_C = 15.97(8)$ K determined from the temperature dependence of the hyperfine magnetic field at ^{151}Eu nuclei is shown to be compatible with the temperature dependence of the transferred hyperfine magnetic field at ^{57}Fe nuclei that is induced by the ferromagnetically ordered Eu sublattice. The Eu magnetic moments are shown to be perpendicular to the crystallographic c-axis. The temperature dependence of the principal component of the electric field gradient tensor, both at Fe and Eu sites, is well described by a $T^{3/2}$ power-law relation. Good agreement between the calculated and measured hyperfine-interaction parameters is observed. The Debye temperature of $CsEuFe_4As_4$ is found to be 295(3) K.

Keywords: ^{57}Fe and ^{151}Eu Mössbauer sepctroscopy, ferromagnet, electric quadrupole splitting, Debye temperature

(Some figures may appear in colour only in the online journal)

1. Introduction

$AeAFe_4As_4$ (Ae = Ca, Sr, Eu and A = K, Rb, Cs) compounds, discovered in 2016, are a new iron-based class of superconductors with the critical temperature T_c in the range 31.6–36.8 K [1–4]. Unlike in solid solutions, such as intensively studied $(Ba_{1-x}K_x)Fe_2As_2$ or $(Sr_{1-x}Na_x)Fe_2As_2$, the Ae and A atoms in $AeAFe_4As_4$ occupy the crystallographically inequivalent positions, which changes the space group from $I4/mmm$ to $P4/mmm$. The crystal structure of these new superconductors consists of the Ae and A layers alternately stacked along the crystallographic c axis between the Fe_2As_2 slabs. Thus, these fully ordered, stoichiometric iron-based superconductors offer a unique opportunity to study, among other things, the relation between superconductivity and possible long-range magnetic order.

The new superconductor $CsEuFe_4As_4$ with $T_c = 35.1$–35.2 K shows a magnetic transition at ~15.0–15.5 K in the magnetic susceptibility data [2, 4]. The magnetic transition at 15.2 K has also been observed in the heat capacity data [4]. The isothermal magnetization measurements allowed it to identify this transition as being ferromagnetic [4]. It has been suggested [4] that ferromagnetism in the $CsEuFe_4As_4$ superconductor results from the ordering of the Eu magnetic moments, which is equivalent to assuming that the Fe atoms carry no magnetic moment. No orientation of the magnetic moment in $CsEuFe_4As_4$ with respect to the crystallographic axes has been established.

The primary goal of this study is to find out whether the magnetic moment in the $CsEuFe_4As_4$ superconductor is associated only with Eu or Fe atoms, or with Eu and Fe atoms, and what is its orientation relative to the crystallographic axes.

1361-648X/18/155803+11$33.00

© 2018 IOP Publishing Ltd Printed in the UK

To achieve this goal, ^{57}Fe and ^{151}Eu Mössbauer spectroscopy, which proved to be an excellent tool to investigate local magnetism of Fe-based superconductors [5], supplemented by the first-principles calculations, will be utilized.

2. Experimental and theoretical methods

The polycrystalline sample of composition $CsEuFe_4As_4$ was synthesized by a solid-state reaction method in a vacuum and at high temperatures, as described earlier [3, 4].

An x-ray diffraction measurement was carried out at 298 K in Bragg-Brentano geometry on a PANalytical X'Pert scanning diffractometer using Cu $K\alpha$ radiation in the 2θ range 10–120° in steps of 0.02°. The $K\beta$ line was eliminated by using a Kevex PSi2 Peltier-cooled solid-state Si detector.

The ^{57}Fe and ^{151}Eu Mössbauer measurements [6] were conducted using standard Mössbauer spectrometers operating in the sine mode, with sources ^{57}Co(Rh) and ^{151}Sm(SmF_3) at room temperature, respectively. The Mössbauer source ^{151}Sm(SmF_3) is not a monochromatic source as ^{151}Sm nuclei are located in the SmF_3 matrix at a site of noncubic symmetry. By measuring the ^{151}Eu Mössbauer spectra of a cubic EuSe compound, we determined that the electric quadrupole coupling constant [6] eQ_gV_{zz} (here e is the proton charge, $Q_g = 0.903$ b is the ground-state electric quadrupole moment of the ^{151}Eu nucleus [7], and V_{zz} is the principal component of the electric field gradient (EFG) tensor) in our source is $-3.69(13)$ mm s^{-1}, which is close to the value of -3.6 mm s^{-1} found in ([8]). The precise shape of the source emission line was taken into account in the fits of the ^{151}Eu Mössbauer spectra.

The 14.4 and 21.5 keV γ-rays were detected with a proportional counter. The spectrometers were calibrated with a 6.35-μm-thick α-Fe foil [9] and the spectra were folded. The Mössbauer absorbers consisted of a mixture of powder $CsEuFe_4As_4$ and boron nitride, which was pressed into a pellet that was put into a 8-μm-thick Al disk container to ensure a uniform temperature over the whole absorber. The Mössbauer absorbers were put into a Mössbauer cryostat in which they were kept in a static exchange gas atmosphere at a pressure of $\sim 6 \times 10^{-3}$ mbar. The surface densities of the ^{57}Fe and ^{151}Eu Mössbauer absorbers were 20.6 and 37.2 mg cm^{-2}, respectively. They correspond to the effective thickness parameter [6] t_a of $3.33 f_a$ and $3.15 f_a$, respectively (here f_a is the Debye–Waller factor of the absorber). Since $t_a > 1$, the resonance line shape of the Mössbauer spectra was described using a transmission integral formula [10]. The Mössbauer spectra at temperatures below the magnetic transition temperature were analyzed using a least-squares fitting procedure which entailed calculations of the positions and relative intensities of the absorption lines by numerical diagonalization of the full hyperfine interaction Hamiltonian.

Ab initio magnetic moment and Mössbauer hyperfine-interaction parameter calculations have been performed within the framework of density functional theory using the full-potential linearized augmented-plane-wave plus local orbitals (FP-LAPW + lo) method as implemented in the WIEN2k package [11]. The experimental lattice parameters (a and c) and the atomic position parameters in the space group $P4/mmm$ (*vide infra*) were used in the calculations.

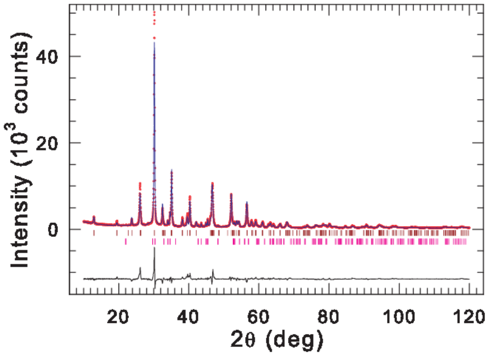

Figure 1. Powder x-ray diffraction pattern of $CsEuFe_4As_4$ at 298 K. The experimental data are denoted by open circles, while the line through the circles represents the results of the Rietveld refinement. The upper set of vertical dark red bars represents the Bragg peak positions corresponding to the $CsEuFe_4As_4$ phase, while the lower set refers to the positions of the impurity phase of FeAs (space group *Pnma*). The lower black solid line represents the difference curve between experimental and calculated patterns.

Table 1. The Rietveld refined atomic positions for the tetragonal $CsEuFe_4As_4$ (space group *P*4/*mmm*).

Atom	Site	Point symmetry	Occupancy	x	y	z
Cs	1*d*	4/*mmm*	1.0	$\frac{1}{2}$	$\frac{1}{2}$	$\frac{1}{2}$
Eu	1*a*	4/*mmm*	1.0	0	0	0
Fe	4*i*	2mm.	1.0	0	$\frac{1}{2}$	0.2262(2)
As1	2*g*	4 mm	1.0	0	0	0.3274(2)
As2	2*h*	4 mm	1.0	$\frac{1}{2}$	$\frac{1}{2}$	0.1238(3)

3. Results and discussion

3.1. Structural characterization

The room-temperature powder x-ray diffraction pattern of $CsEuFe_4As_4$ is shown in figure 1. The compound studied crystallizes in the tetragonal space group *P*4/*mmm* [4]. A Rietveld refinement [12] of the x-ray powder diffraction data was carried out, yielding the lattice parameters $a = 3.8956(1)$ Å and $c = 13.6628(5)$ Å, and the atomic positional parameters that are listed in table 1. We note (figure 1) that the $CsEuFe_4As_4$ specimen contains a second phase of FeAs [13] in the amount of 7.7(2) wt%.

The unit cell and the layered crystal structure of $CsEuFe_4As_4$ are shown in figure 2. The interactions between the Cs, Fe, and As atoms in the compound studied are depicted by various connecting rods. One observes that the layers of Eu atoms are completely isolated from the Fe_4As_4 blocks and that two neighboring Fe_4As_4 blocks are separated by sheets of Cs atoms along the c-direction.

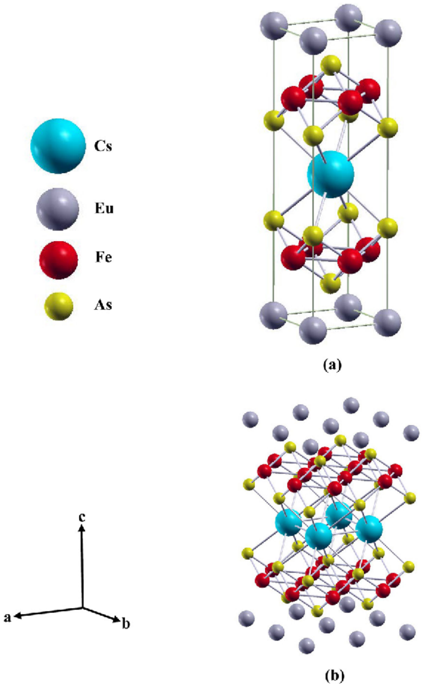

Figure 2. The unit cell (a) and the layered crystal structure (b) of $CsEuFe_4As_4$.

The interatomic distances between various atoms in the $CsEuFe_4As_4$ superconductor play an important role in determining the type of interactions between these atoms. As the dominant physical interaction between the atoms in a solid is electromagnetic in origin, one can conclude that the strength of the Coulomb interaction between the atoms can determine the type of chemical bonding between the constituent atoms of the compound studied. It is seen (figure 2(b)) that the density of atoms within the Fe_4As_4 blocks is greater than that of the Cs and Eu sheets. One thus expects stronger electric interactions to exist within these blocks than within the sheets. This is shown qualitatively in figure 2(b) by a dense network of connecting rods between the Fe and As atoms and the absence of such connecting rods between the Eu atoms.

The $CsFe_4As_4$ units are separated by sheets of Eu atoms (figure 2(b)). The absence of connecting rods between the Eu atoms and the $CsEuFe_4As_4$ units indicates that these units are chemically independent of each other. The Eu sheets act as insulating layers along the *c*-axis, which can be the result of ionic interactions between them and the blocks of Fe_4As_4. Furthermore, the elongated along the *c*-axis tetragonal unit cell rules out the possibility of any strong interaction between the Eu layers. In particular, no magnetic coupling is expected to exist between the Eu atoms along the *c*-direction. One may thus predict that the interatomic interactions between the Eu atoms must occur in the *ab* plane and that a 2D magnetic interaction mechanism, if any, between neighboring Eu atoms in each layer, should exist. Also, the Eu atoms in each layer

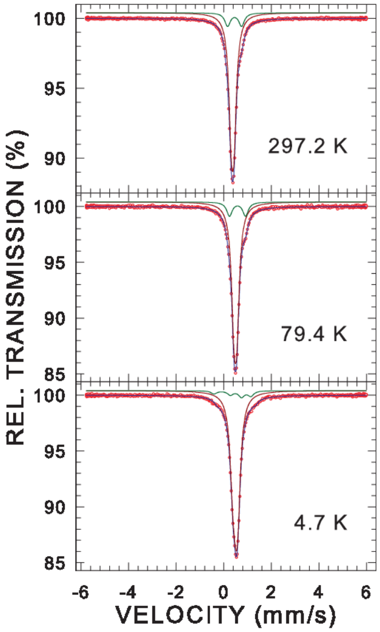

Figure 3. Room-, liquid-nitrogen, and liquid-helium temperature ^{57}Fe Mössbauer spectra of $CsEuFe_4As_4$ measured over a large velocity range and fitted (solid blue lines) with a large spectral area quadrupole doublet at 297.2 and 79.4 K and a Zeeman pattern at 4.7 K (solid dark red lines) due to $CsEuFe_4As_4$, and with a small spectral area doublet at 297.2 and 79.4 K and a Zeeman pattern at 4.7 K (solid dark green lines) due to the FeAs impurity phase, as described in the text. The zero-velocity origin is relative to α-Fe at room temperature.

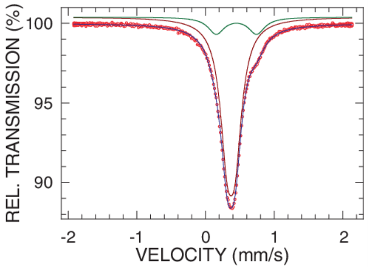

Figure 4. ^{57}Fe Mössbauer spectrum of $CsEuFe_4As_4$ at 297.0 K fitted (solid blue line) with a large spectral area quadrupole doublet due to $CsEuFe_4As_4$ (solid dark red lines) and a small spectral area quadrupole doublet originating from the FeAs impurity phase (solid dark green lines), as described in the text. The zero-velocity origin is relative to α-Fe at room temperature.

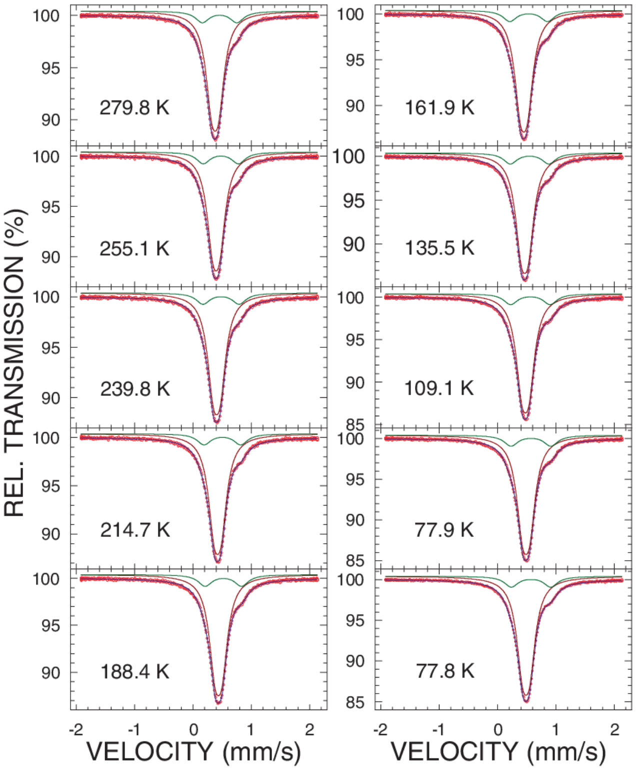

Figure 5. ^{57}Fe Mössbauer spectra of $CsEuFe_4As_4$ at the indicated temperatures fitted (solid blue lines) with a large spectral area quadrupole doublet due to $CsEuFe_4As_4$ (dark red solid lines) and a small spectral area quadrupole doublet originating from the FeAs impurity phase (solid dark green lines), as described in the text. The zero-velocity origin is relative to α-Fe at room temperature.

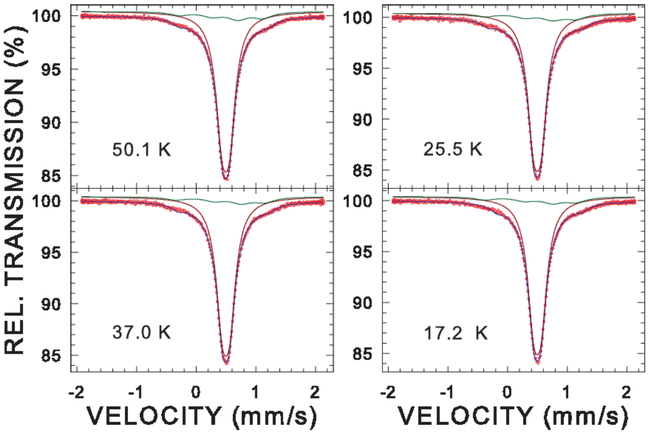

Figure 6. ^{57}Fe Mössbauer spectra of $CsEuFe_4As_4$ at the indicated temperatures fitted (solid blue lines) with a large spectral area quadrupole doublet due to $CsEuFe_4As_4$ (dark red solid lines) and a small spectral area Zeeman pattern originating from the FeAs impurity phase (solid dark green lines), as described in the text. The zero-velocity origin is relative to α-Fe at room temperature.

are themselves isolated from each other, as depicted by the absence of connecting rods between them.

3.2. Calculated magnetic moments and hyperfine interaction parameters

The calculated magnetic moments of the Cs, Eu, Fe, As1, and As2 atoms in the ferromagnetic $CsEuFe_4As_4$ are −0.0060, 6.7057, 1.1229, −0.0709, and −0.0854 μ_B, respectively. It is thus predicted that the magnetism of $CsEuFe_4As_4$ is associated predominantly with the Eu atoms, and to a lesser extent with the Fe atoms. A comparison between the calculated and experimental magnetic moments carried by the Eu and Fe atoms will be made below.

^{57}Fe Mössbauer spectra of a non-magnetic compound, or of a magnetically ordered compound at temperatures above its ordering temperature, yield two important hyperfine-interaction parameters: the quadrupole splitting (the separation between two resonance lines in a ^{57}Fe Mössbauer quadrupole doublet) $\Delta = \frac{1}{2} eQ|V_{zz}|\sqrt{1+\eta^2/3}$, where Q is the electric quadrupole moment of the ^{57}Fe nucleus (0.15 b) [14] and η is the asymmetry parameter, and the isomer shift, δ_0 [6]. For a crystalline compound of known crystal structure, V_{zz}, η, and δ_0 can also be obtained from *ab initio* calculations [15].

The calculated values of V_{zz} and η at the $4i$ site occupied by the Fe atoms (table 1) are 7.142×10^{20} V m^{-2} and 0.7795, respectively. These values correspond to the predicted $\Delta = 0.1222$ mm s^{-1}.

The isomer shift $\delta_0 = \alpha[\rho(0) - \rho_{\mathrm{ref}}(0)]$ results from the difference in the total electron density at the Mössbauer nucleus in the compound studied, $\rho(0)$, and in the reference compound, $\rho_{\mathrm{ref}}(0)$; α is a calibration constant. In calculating $\rho(0)$, relativistic spin-orbit effects were invoked to account for the possibility of the penetration of the $p_{1/2}$ electrons into the ^{57}Fe nuclei. An α-Fe (with the *bcc* structure and the lattice constant of 2.8665 Å) was chosen as a reference compound. The calculated values of $\rho_{\mathrm{ref}}(0)$ and $\rho(0)$ are 15309.905 and 15308.531 (a.u.)$^{-3}$, respectively. Using the calibration constant $\alpha = -0.291$(a.u.)^3(mm s^{-1}), [16] the calculated values of $\rho(0)$ and $\rho_{\mathrm{ref}}(0)$ lead to $\delta_0 = 0.400$ mm s^{-1}.

And finally, the calculated hyperfine magnetic field at 0 K (Fermi contact term) at ^{57}Fe nuclei, $H_{\mathrm{hf}}(0)$, is −57.7 kOe for the ferromagnetic $CsEuFe_4As_4$.

The analysis of the ^{151}Eu Mössbauer spectra at different temperatures yields similar hyperfine-interaction parameters. The calculated values of V_{zz} and η at the $1a$ site occupied by the Eu atoms (table 1) are -58.017×10^{20} V m^{-2} and 0.0, respectively. The $\eta = 0.0$ value is expected as the point symmetry 4/*mmm* of the $1a$ sites ensures the axially symmetric EFG tensor. The calculated $H_{\mathrm{hf}}(0)$ at ^{151}Eu nuclei is 467 kOe for the ferromagnetic $CsEuFe_4As_4$.

3.3. ^{57}Fe Mössbauer spectroscopy

To access the possibility of the presence of a Zeeman pattern resulting from a possible magnetic ordering of the Fe atoms in $CsEuFe_4As_4$, and of a Zeeman pattern due to a magnetically-ordered and Fe-containing impurity phase in the sample studied, the room, liquid-nitrogen, and liquid-helium temperature ^{57}Fe Mössbauer spectra were measured over a large velocity range (figure 3). A visual inspection of these spectra shows the absence of Zeeman patterns corresponding to the main and impurity phases with typical values of the hyperfine magnetic field, H_{hf}. As will be shown in detail below, the large spectral area component of these spectra (figure 3) is due to $CsEuFe_4As_4$ and is in the form of a quadrupole doublet with small Δ at 297.2 and 79.4 K and a Zeeman pattern with very small H_{hf} at 4.7 K. The small spectral area component of the spectra in figure 3 originates from the FeAs impurity phase and is in the form of a quadrupole doublet at 297.2 and 79.4 K and a Zeeman pattern at 4.7 K.

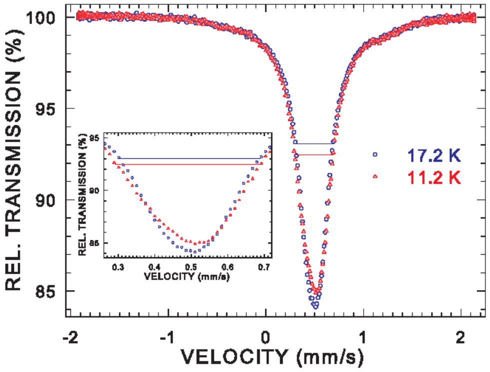

Figure 7. Comparison of the ^{57}Fe Mössbauer spectra of $CsEuFe_4As_4$ at 17.2 and 11.2 K. The inset shows the spectra with the enlarged horizontal and vertical scales. The horizontal bars indicate the full width at half maximum of the 17.2 K spectrum (0.386 mm s^{-1}) and the 11.2 K spectrum (0.396 mm s^{-1}). The zero-velocity origin is relative to α-Fe at room temperature.

The room-temperature Mössbauer spectrum of $CsEuFe_4As_4$ measured over a small velocity range is shown in figure 4. A feature on the right shoulder of the spectrum indicates the presence of an impurity phase in the compound studied. A satisfactory fit of the spectrum can be obtained with a large spectral area quadrupole doublet component with small Δ that originates from $CsEuFe_4As_4$ and with a small spectral area quadrupole doublet component due to the FeAs impurity phase [17–19].

The Mössbauer spectra of $CsEuFe_4As_4$ at various temperatures down to the liquid nitrogen temperature are shown in figure 5. Their shape is the same as that of the spectrum in figure 4, that is, excellent fits of these spectra could be obtained with two quadrupole doublet components originating from $CsEuFe_4As_4$ and the FeAs impurity phase.

The FeAs impurity component in the Mössbauer spectra of $CsEuFe_4As_4$ at temperatures below the liquid nitrogen temperature (figure 6) is in the form of a complex Zeeman pattern, which indicates that the magnetic ordering temperature of the impurity phase lies in the range 77.8–50.1 K (figures 5 and 6). This agrees with the reported Néel temperature of FeAs (77(1) K in [13] and 69.2(1) K in [19]).

The Mössbauer spectra of $CsEuFe_4As_4$ at 17.2 and 11.2 K are compared in figure 7. One observes that the 11.2 K

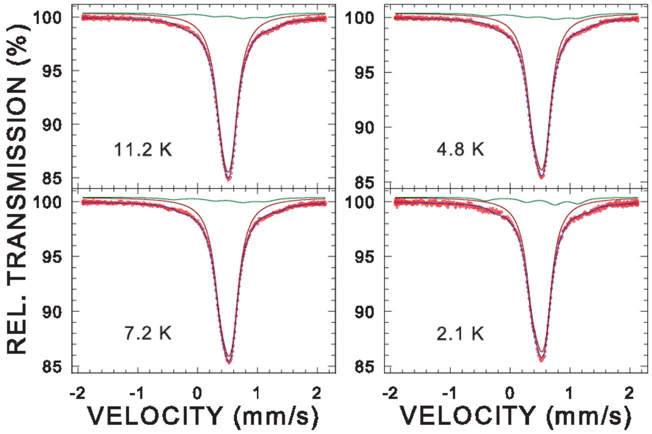

Figure 8. ^{57}Fe Mössbauer spectra of $CsEuFe_4As_4$ at the indicated temperatures fitted (solid blue lines) with a large spectral area Zeeman pattern due to $CsEuFe_4As_4$ (dark red solid lines) and a small spectral area Zeeman pattern originating from the FeAs impurity phase (solid dark green lines), as described in the text. The zero-velocity origin is relative to α-Fe at room temperature.

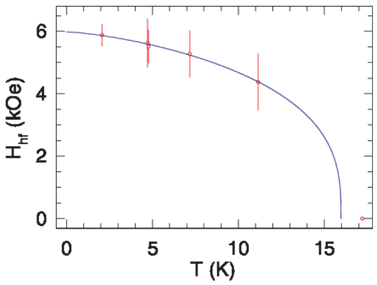

Figure 9. Temperature dependence of the transferred hyperfine magnetic field. The solid line is the fit to equation (1), as explained in the text.

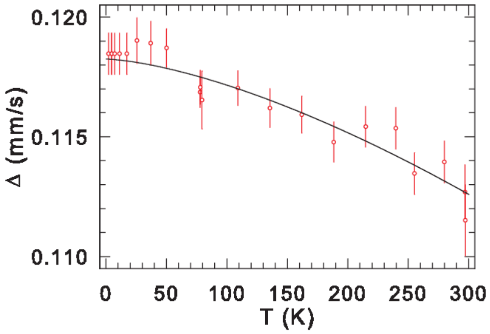

Figure 10. Temperature dependence of the quadrupole splitting. The solid line is the fit to equation (2), as explained in the text.

spectrum is slightly, but visibly broader than the 17.2 K spectrum. This 0.010 mm s^{-1} broadening (figure 7) is the consequence of the appearance at 11.2 K of a very small H_{hf} that is transferred to the ^{57}Fe nuclei from the ferromagnetically ordered Eu sublattice (*vide infra*). It should be stressed that this *transferred* hyperfine magnetic field does not result from the ordering of the Fe sublattice. Its presence constitutes a direct evidence for the ordering of the Eu sublattice. Such a transferred hyperfine magnetic field at a single temperature has been observed for the first time in the $EuFe_2(As_{1-x}P_x)_2$ superconductors [20]. Thus, the Mössbauer spectra at 11.2 K and lower temperatures were fitted (figure 8) with a large spectral area Zeeman pattern component (the value of Δ was fixed in the fit to that obtained from the fit of the 17.2 K spectrum) that originates from $CsEuFe_4As_4$ and with a small spectral area complex Zeeman pattern component that is due to the FeAs impurity phase.

The temperature dependence of the transferred H_{hf} (figure 9), observed here for the first time, was derived from the fits of the spectra in figures 3 and 8. As expected, H_{hf} increases with decreasing temperature. In principle, one could determine from this dependence the ferromagnetic ordering temperature of the Eu sublattice (the Curie temperature), T_C, as the temperature at which $H_{hf} = 0$. However, the paucity of H_{hf} data between 11.2 K and T_C makes it difficult to reliably determine the value of T_C. One can state with certainty (figure 9) that T_C lies between 11.2 and 17.2 K.

The value of T_C derived from the ^{151}Eu Mössbauer spectra is 15.97(8) K (*vide infra*). To show the compatibility of the $H_{hf}(T)$ data in figure 9 with that value of T_C, the $H_{hf}(T)$ dependence was fitted using the phenomenological form [21]

$$H_{hf}(T) = H_{hf}(0)\left[1 - \left(\frac{T}{T_C}\right)^{\alpha}\right]^{\beta}, \qquad (1)$$

where $T_C = 15.97$ K, $H_{hf}(0)$ is the value of H_{hf} at 0 K, and α and β are exponents describing the behavior of $H_{hf}(T)$ near 0 K and T_C, respectively. The fit yields $H_{hf}(0) = 5.98(13)$

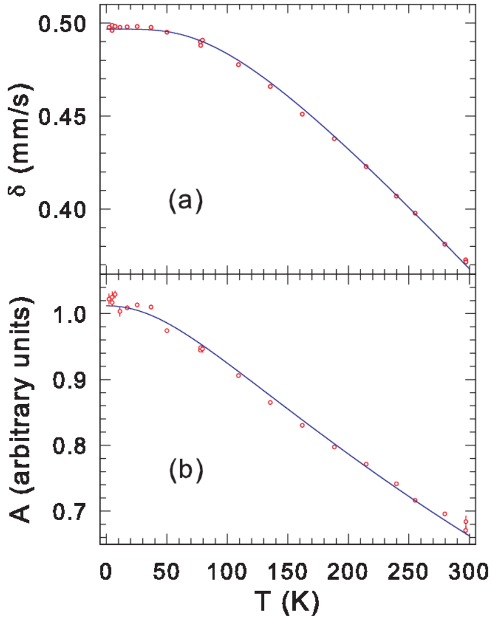

Figure 11. Temperature dependence of (a) the centre shift δ and (b) the absorption spectral area A. The solid lines are the fits to equation (3) in (a) and to equation (5) in (b), as explained in the text.

kOe, $\alpha = 1.39(38)$, and $\beta = 0.33(6)$. The values of α and β found here are comparable to those obtained for other compounds [22–24].

The calculations predict a non-zero, but the small value of $|H_{\mathrm{hf}}(0)|$ at the ^{57}Fe nuclei and of the magnetic moment carried by the Fe atoms (*vide supra*). This is at variance with the experimentally observed zero value of the intrinsic, i.e. not transferred, H_{hf} down to 2.1 K, and consequently zero-value of the ordered Fe magnetic moment.

Figure 10 shows the temperature dependence of Δ obtained from the fits of the spectra in figures 3–6 and 8. A small increase of Δ with decreasing temperature is observed. Such a temperature dependence of Δ has been observed in many metallic systems [25–27]. It is well described by the empirical equation

$$\Delta(T) = \Delta(0)\left(1 - BT^{3/2}\right), \tag{2}$$

where $\Delta(0)$ is the value of Δ at 0 K and B is a constant. The fit of the $\Delta(T)$ data (figure 10) to equation (2) gives $\Delta(0) = 0.1182(4)\,\mathrm{mm\,s^{-1}}$ and $B = 9.20(1.47) \times 10^{-6}\,\mathrm{K^{-3/2}}$. The value of B is similar to that found for other compounds [25–27]. The value of $\Delta(0)$ is very close to the calculated value of $0.1222\,\mathrm{mm\,s^{-1}}$.

The temperature dependence of the centre shift, δ, that was obtained from the fits of the spectra in figures 3–6 and 8, is shown in figure 11(a). The centre shift at temperature T, $\delta(T)$, consists of two terms

$$\delta(T) = \delta_0 + \delta_{\mathrm{SOD}}(T), \tag{3}$$

where δ_0 is the intrinsic, temperature-independent isomer shift and $\delta_{\mathrm{SOD}}(T)$ is the second-order Doppler (SOD) shift which depends on the lattice vibrations of the Fe atoms [6]. The latter contribution can be expressed in terms of the Debye approximation of the lattice vibrations as

$$\delta_{\mathrm{SOD}}(T) = -\frac{9}{2}\frac{k_{\mathrm{B}}T}{Mc}\left(\frac{T}{\Theta_{\mathrm{D}}}\right)^3 \int_0^{\Theta_{\mathrm{D}}/T} \frac{x^3\mathrm{d}x}{\mathrm{e}^x - 1}, \tag{4}$$

where k_{B} is the Boltzmann constant, M is the mass of the Mössbauer nucleus, c is the speed of light, and Θ_{D} is the Debye temperature. The fits of the experimental data $\delta(T)$ (figure 11(a)) to equation (3) gives $\delta_0 = 0.491(1)\,\mathrm{mm\,s^{-1}}$ and $\Theta_{\mathrm{D}} = 399(7)$ K. We note that the experimental value of δ_0 found here is 19% larger than the calculated δ_0.

Another method of finding the Debye temperature from Mössbauer spectra involves determining their spectral area at various temperatures. The temperature dependence of the spectral area A derived from the fits of the Mössbauer spectra in figures 3–6 and 8 is displayed in figure 11(b). The spectral area is proportional to f_{a}, which is given in the Debye theory by [6]

$$f_{\mathrm{a}}(T) = \exp\left\{-\frac{3}{4}\frac{E_\gamma^2}{Mc^2k_{\mathrm{B}}\Theta_{\mathrm{D}}}\left[1 + 4\left(\frac{T}{\Theta_{\mathrm{D}}}\right)^2 \int_0^{\Theta_{\mathrm{D}}/T} \frac{x\mathrm{d}x}{\mathrm{e}^x - 1}\right]\right\}, \tag{5}$$

where E_γ is the energy of the Mössbauer transition. The fit of the experimental dependence $A(T)$ (figure 11(b)) to equation (5) gives $\Theta_{\mathrm{D}} = 276(3)$ K. The weighted average of the above two Θ_{D} values determined from the temperature dependence of two different Mössbaue parameters is 295(3) K.

The value of Θ_{D} determined from the $A(T)$ data is significantly smaller than the one derived from the $\delta(T)$ data. In fact, the Θ_{D} values determined from the $A(T)$ data are always smaller than the ones obtained from the $\delta(T)$ data. This results from the way in which Θ_{D} is calculated. One recalls that f_{a} and δ_{SOD} are related to the mean-square vibrational displacement $\langle x^2 \rangle$ and the mean-square velocity $\langle v^2 \rangle$ of the Mössbauer nucleus, respectively [6]. Since $\langle x^2 \rangle$ weights the phonon frequency distribution by ω^{-1} while $\langle v^2 \rangle$ weights it by ω^{+1} [28], the Θ_D values derived from the $A(T)$ data are necessarily lower than those determined from the $\delta(T)$ data.

3.4. ^{151}Eu Mössbauer spectroscopy

The ^{151}Eu Mössbauer spectra of $\mathrm{CsEuFe_4As_4}$ measured over the velocity range $\mp 20\,\mathrm{mm\,s^{-1}}$ and at temperatures between room- and liquid-nitrogen temperatures are shown in figure 12. The large spectral area component originates from $\mathrm{Eu^{2+}}$ ions in $\mathrm{CsEuFe_4As_4}$ and is in the form of an unresolved quadrupole octet [6, 29]. The small spectral area component is due to $\mathrm{Eu^{3+}}$ ions in an unidentified foreign phase and is in the form of a single line. The Mössbauer spectra of $\mathrm{CsEuFe_4As_4}$ measured over the velocity range $\mp 50\,\mathrm{mm\,s^{-1}}$ and at temperatures

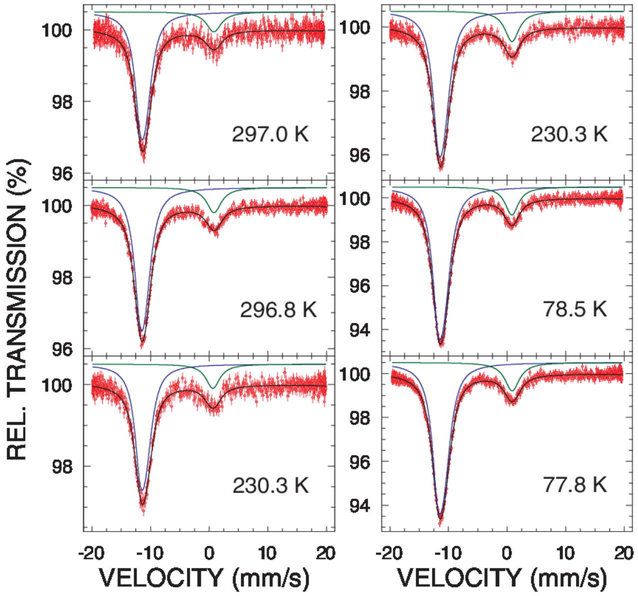

Figure 12. ^{151}Eu Mössbauer spectra of $CsEuFe_4As_4$ at the indicated temperatures fitted (solid black lines) with a large spectral area quadrupole pattern due to $CsEuFe_4As_4$ (blue solid lines) and a small spectral area singlet originating from an impurity phase (solid dark green lines), as described in the text. The zero-velocity origin is relative to the source.

between liquid-nitrogen temperatures and 17.1 K (figure 13) have the same structure as those in figure 12, that is, the studied compound is in the paramagnetic state down to 17.1 K.

The Mössbauer spectrum of $CsEuFe_4As_4$ measured at 8.8 K, that is, below T_C is shown in figure 14. It can be fitted with a large spectral area Zeeman pattern component that originates from $CsEuFe_4As_4$ and a small spectral area single line component due to an impurity phase. The quadrupole coupling constant eQ_gV_{zz} of the Zeeman component was fixed in the fit to the value of $-6.660\,\mathrm{mm\ s^{-1}}$ derived from the fit of the 17.1 K spectrum (*vide infra*). The Eu atoms in $CsEuFe_4As_4$ are located at the 1*a* site with the point symmetry 4/*mmm* (table 1), which ensures an axially symmetric (the asymmetry parameter $\eta = 0$) EFG tensor at this site. Also, V_{zz} is parallel to the *c*-axis. The values of the relevant fitted parameters of the Zeeman component are $\delta = -11.220(37)$ mm s^{-1}, $H_{hf} = 223.9(1.0)$ kOe, and the angle between V_{zz} and H_{hf}, $\beta = 87.7(8.1)°$. Since V_{zz} is parallel to the *c*-axis, the value of β shows that the Eu magnetic moment is perpendicular to the *c*-axis, that is, the Eu magnetic moment must lie in the *ab* plane.

As shown above, the determination of the angle β allows one to specify the direction of the Eu magnetic moment with respect to the crystallographic axes. To demonstrate the high reliability of such determination by this hyperfine interaction method, the ^{151}Eu Mössbauer spectra were generated (they include the single-line component contribution due to an impurity), using the hyperfine interaction parameters obtained from the fit of the spectrum in figure 14, for two β values of 0° and 90° that correspond, respectively, to the direction of the Eu magnetic moment being parallel and perpendicular to the *c*-axis (figure 15). One notices a dramatic change in the shape of the generated spectra (figure 15), that is, their strong dependence on the value of β.

Figure 16 shows the spectra at other temperatures below T_C. They were fitted in the same way as the spectrum in figure 14.

The temperature dependence of H_{hf} determined from the fits to the Mössbauer spectra in figures 14 and 16 is shown in figure 17(a). It is usually assumed that the temperature variation of H_{hf} in a magnetically ordered material can be reasonably explained in term of the molecular field model, assuming that H_{hf} is proportional to the sublattice magnetization. In terms of this model, $H_{hf}(T)$ can be expressed as

$$H_{hf}(T) = H_{hf}(0)B_J(x), \tag{6}$$

where $H_{hf}(0)$ is the saturation hyperfine magnetic field, $B_J(x)$ is the Brillouin function defined as

$$B_J(x) = \frac{2J+1}{2J}\coth\left(\frac{2J+1}{2J}x\right) - \frac{1}{2J}\coth\left(\frac{x}{2J}\right) \tag{7}$$

and

$$x = \frac{3J}{J+1}\frac{H_{hf}(T)}{H_{hf}(0)}\frac{T_C}{T}. \tag{8}$$

The fit of the $H_{hf}(T)$ data ((figure 17(a)) to equation (6) with $J = S = 7/2$ (corresponding to a free Eu^{2+} ion) yields $H_{hf}(0) = 272.9(2.8)$ kOe and $T_C = 15.97(8)$ K. The experimental value of $H_{hf}(0)$ is significantly smaller than the calculated Fermi contact value of 467 kOe. This discrepancy can

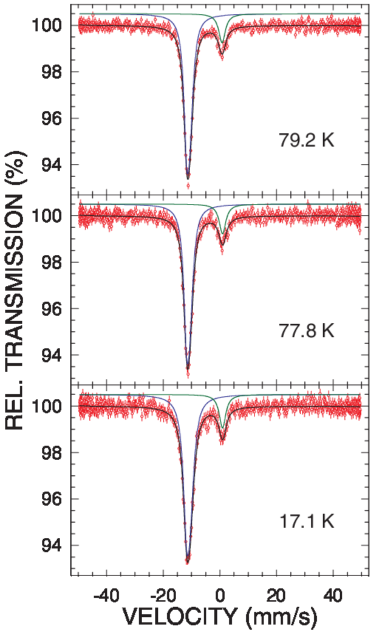

Figure 13. ^{151}Eu Mössbauer spectra of $CsEuFe_4As_4$ at the indicated temperatures fitted (solid black lines) with a large spectral area quadrupole pattern due to $CsEuFe_4As_4$ (blue solid lines) and a small spectral area singlet originating from an impurity phase (solid dark green lines), as described in the text. The zero-velocity origin is relative to the source.

be explained by the fact that the measured hyperfine magnetic field at the ^{151}Eu nuclei is the sum of the Fermi contact term, the contribution from the valence and conduction band electrons, and the contribution due to the neighboring magnetic moments [30]. Clearly, the latter two contributions when added to the Fermi contact term must account for the measured $H_{hf}(0)$.

For ^{151}Eu Mössbauer spectroscopy [29, 30], as opposed to ^{57}Fe Mössbauer spectroscopy [31], there is no simple relation between the measured $H_{hf}(0)$ and the magnetic moment carried by Eu atoms. We note here that the calculated Eu magnetic moment of 6.7057 μ_B is larger than the experimental moment of 5.9 μ_B at 2 K determined from the magnetization measurements [4].

The temperature dependence of the angle β determined from the fits of the spectra in figures 14 and 16 is shown in figure 17(b). One can observe that the β values are close to 90°. This constitutes an experimental proof that the Eu magnetic moments lie in the *ab* plane.

Figure 18(a) shows the temperature dependence of V_{zz} derived from the fits of the spectra in figures 12 and 13. Similarly to the $\Delta(T)$ dependence in figure 10, the magnitude of V_{zz} increases with decreasing temperature. The $V_{zz}(T)$ data can be fitted to an empirical $T^{3/2}$ power-law relation

$$V_{zz}(T) = V_{zz}(0)\left(1 - BT^{3/2}\right), \qquad (9)$$

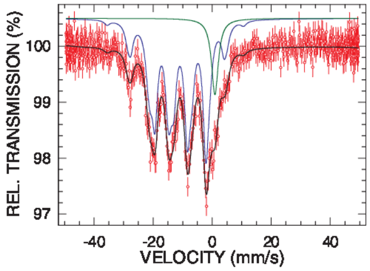

Figure 14. ^{151}Eu Mössbauer spectrum of $CsEuFe_4As_4$ at 8.8 K fitted (solid black line) with a large spectral area Zeeman pattern due to $CsEuFe_4As_4$ (blue solid line) and a small spectral area singlet originating from an impurity phase (solid dark green line), as described in the text. The zero-velocity origin is relative to the source.

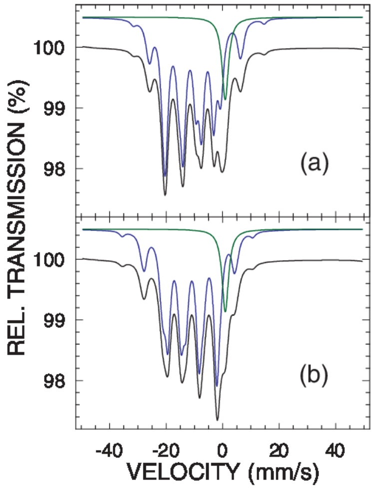

Figure 15. Simulated two-component ^{151}Eu Mössbauer spectra (solid black line). The hyperfine parameters of the single-line component (solid dark green line) and the Zeeman component (blue solid line) are the same as those obtained from the fit of the spectrum in figure 14 with $\beta = 0.0°$ (a) and $\beta = 90°$ (b). The zero-velocity origin is relative to the source.

where $V_{zz}(0)$ is the value of V_{zz} at 0 K and B is a constant. The fit of the $V_{zz}(T)$ data (figure 18(a)) to equation (9) yields $V_{zz}(0) = -0.516(5) \times 10^{22}$ V m^{-2} and $B = 5.28(55) \times 10^{-5} K^{-3/2}$. The experimental value of $V_{zz}(0)$ compares well with the calculated value of -0.580×10^{22} V m^{-2}.

The temperature dependence of δ, that was derived from the fits of the spectra in figures 12–14 and 16, is shown in figure 18(b). The values of $\delta(T)$ prove [29] that at all temperatures the Eu atoms are in the $^8S_{7/2}$ ground state, that is, are divalent. Because of a relatively large scatter and error of the experimental $\delta(T)$ points (figure 18(b)), and of the small rate of temperature change of δ_{SOD} at high temperatures (-2.76×10^{-4} mm (s · K)$^{-1}$ for ^{151}Eu versus -7.31×10^{-4} mm (s · K)$^{-1}$ for ^{57}Fe), it is not feasible to fit the $\delta(T)$ data to

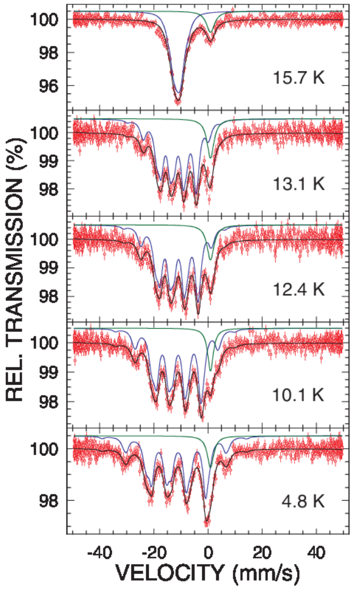

Figure 16. ^{151}Eu Mössbauer spectra of $CsEuFe_4As_4$ at the indicated temperatures fitted (solid black lines) with a large spectral area Zeeman pattern due due to $CsEuFe_4As_4$ (blue solid lines) and a small spectral area singlet originating from an impurity phase (solid dark green lines), as described in the text. The zero-velocity origin is relative to the source.

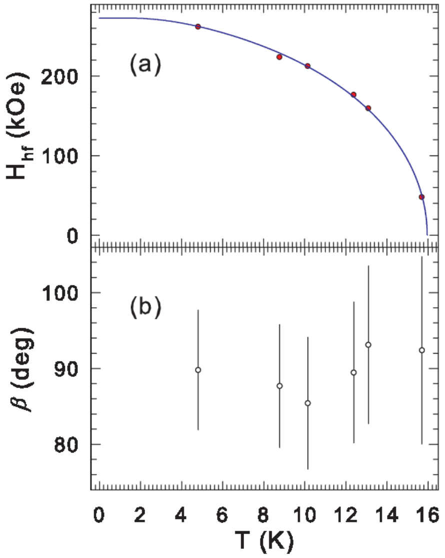

Figure 17. Temperature dependence of the hyperfine magnetic field H_{hf} (a) and the angle β (b) determined from the fits of the spectra in figures 14 and 16. The solid line in (a) is the fit to equation (6), as explained in the text.

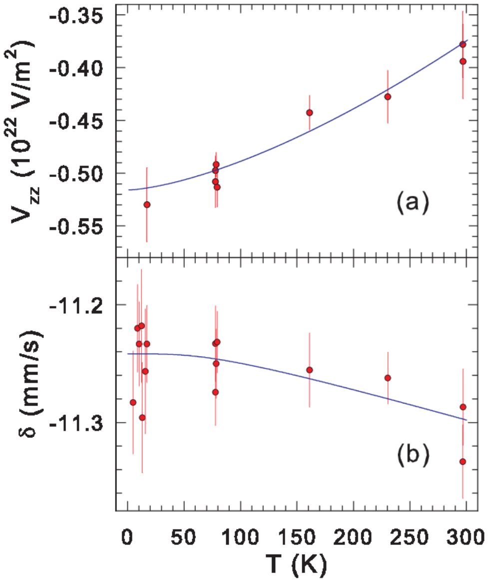

Figure 18. Temperature dependence of the principal component of the electric field gradient tensor V_{zz} derived from the fits of the spectra in figures 12 and 13(a) and of the centre shift δ derived from the fits of the spectra in figures 12–14 and 16. The solid line in (a) is the fit to equation (9), and the solid line in (b) is the variation of $\delta_{SOD}(T)$ calculated for $\Theta_D = 295$ K, as explained in the text.

equation (3) to derive the value of Θ_D. Instead, the temperature variation of δ_{SOD} was calculated for the value of $\Theta_D = 295$ K derived from the ^{57}Fe spectra (solid line in figure 18(b)). The calculated $\delta_{SOD}(T)$ variation approximately accounts for the increase of δ with decreasing temperature.

4. Conclusions

We present the results of *ab initio* hyperfine-interaction parameters calculations, and of x-ray diffraction and ^{57}Fe and ^{151}Eu Mössbauer spectroscopy study of the new 35 K superconductor $CsEuFe_4As_4$. We confirm that the superconductor crystallizes in the tetragonal space group *P*4/*mmm* with the lattice parameters $a = 3.8956(1)$ Å and $c = 13.6628(5)$ Å. We show that the Fe atoms carry no magnetic moment down to 2.1 K and that the ferromagnetic order is associated with the Eu magnetic moments. We establish that the Curie temperature $T_C = 15.97(8)$ K determined from the temperature dependence of the hyperfine magnetic field at ^{151}Eu nuclei is compatible with the temperature dependence of the transferred hyperfine magnetic field at ^{57}Fe nuclei that is induced by the ferromagnetically ordered Eu sublattice. We find that the Eu magnetic moments are lying in the *ab* plane. We observe that the temperature dependence of the principal component of the electric field gradient tensor is well described by a $T^{3/2}$ power-law relation at both the Fe and Eu sites. Good agreement is found between the calculated and measured hyperfine-interaction parameters. We determine that the Debye temperature of $CsEuFe_4As_4$ is 295(3) K.

Acknowledgments

This work was supported by the Natural Sciences and Engineering Research Council of Canada (NSERC).

ORCID iDs

Zbigniew M Stadnik https://orcid.org/0000-0002-2785-3930

References

[1] Iyo A, Kawashima K, Kinjo T, Nishio T, Ishida S, Fujihisa H, Gotoh Y, Kihou K, Eisaki H and Yoshida Y 2016 *J. Am. Chem. Soc.* **138** 3410

[2] Kawashima K, Kinjo T, Nishio T, Ishida S, Fujihisa H, Gotoh Y, Kihou K, Eisaki H, Yoshida Y and Iyo A 2016 *J. Phys. Soc. Japan* **85** 064710

[3] Liu Y, Liu Y-B, Jiang H, Wang Z-C, Ablimit A, Jiao W-H, Tao Q, Feng C-M, Xu Z-A and Cao G-H 2016 *Phys. Rev.* B **93** 214503

[4] Liu Y, Liu Y-B, Chen Q, Tang Z-T, Jiao W-H, Tao Q, Xu Z-A and Cao G-H 2016 *Sci. Bull.* **61** 1213

[5] Pissas M, Sanakis Y, Psycharis V, Simopoulos A, Devlin E, Ren Z-A, Shen X-L, Che G-C and Zhao Z-X 2008 *Supercond. Sci. Technol.* **21** 115015
Albedah M A, Nejadsattari F, Stadnik Z M, Wang Z-C, Wang C and Cao G-H 2017 *J. Alloys Compd.* **695** 1128

[6] Greenwood N N and Gibb T C 1971 *Mössbauer Spectroscopy* (London: Chapman and Hall)
Gütlich P, Bill E and Trautwein A 2011 *Mössbauer Spectroscopy and Transition Metal Chemistry* (Berlin: Springer)

[7] Tanaka Y, Steffen R M, Shera E B, Reuter W, Hoehn M V and Zumbro J D 1984 *Phys. Rev.* C **29** 1830

[8] Nowik I and Felner I 1986 *Hyperfine Interact.* **28** 959

[9] Cali J P (ed) 1971 *Certificate of Calibration, Iron Foil Mössbauer Standard* vol 1541 (Washington, DC: US GPO)

[10] Margulies S and Ehrman J R 1961 *Nucl. Instrum. Methods* **12** 131
Shenoy G K, Friedt J M, Maletta H and Ruby S L 1974 *Mössbauer Effect Methodology* vol 10, ed I J Gruverman *et al* (New York: Plenum) p 277

[11] Blaha P, Schwartz K, Madsen G, Kvasnicka D and Luitz J 1999 *WIEN2k, An Augmented Plane Wave Plus Local Orbitals Program for Calculating Crystal Properties* ed K Schwarz (Austria: Technical Universität Wien)
Nejadsattari F, Wang P, Stadnik Z M, Nagata Y and Ohnishi T 2017 *J. Alloys Compd.* **725** 1098

[12] Young R A 1993 *The Rietveld Method* (Oxford: Oxford University Press)

[13] Selte K, Kjekshus A and Andersen A F 1972 *Acta Chem. Scand.* **26** 3101

[14] Martínez-Pinedo G, Schwerdtfeger P, Caurier E, Langanke K, Nazarewich W and Söhnel T 2001 *Phys. Rev. Lett.* **87** 062701

[15] Blaha P 2010 *J. Phys.: Conf. Ser.* **217** 012009

[16] Wdowik U D and Reubenbauer K 2007 *Phys. Rev.* B **76** 155118

[17] Kulshreshtha S K and Raj P 1979 *J. Phys. F: Met. Phys.* **9** 2253

[18] Häggström L, Gustavsson-Seidel A and Fjellvåg H 1989 *Europhys. Lett.* **9** 87

[19] Błachowski A, Ruebenbauer K, Żukrowski J and Bukowski Z 2014 *J. Alloys. Compd.* **582** 167

[20] Nowik I, Felner I, Ren Z, Cao G H and Xu Z A 2011 *J. Phys.: Condens. Matter* **23** 065701

[21] Blundell S J, Steer C A, Pratt F L, Marshall I M, Hayes W and Ward R C C 2003 *Phys. Rev.* B **67** 224411

[22] Baker P J, Franke I, Lancaster T, Bundell S J, Kerslake L and Clarke S J 2009 *Phys. Rev.* B **79** 060402

[23] Baker P J, Lewtas H J, Bundell S J, Lancaster T, Franke I, Hayes W, Pratt F L, Bohatý L and Becker P 2010 *Phys. Rev.* B **81** 214403

[24] Li Z, Fang Y, Ma X, Pang H and Li F 2011 *Phys. Rev.* B **84** 134509

[25] Albedah M A, Nejadsattari F, Stadnik Z M and Przewoźnik J 2015 *J. Alloys Compd.* **619** 839

[26] Stadnik Z M, Wang P, Wang H-D, Dong C-H and Fang M-H 2013 *J. Alloys Compd.* **561** 82

[27] Stadnik Z M and Wang P 2006 *J. Phys.: Condens. Matter* **18** 8383

[28] Housley R M and Hess F 1966 *Phys. Rev.* **146** 517

[29] Grandjean F and Long G L 1989 *Mössbauer Spectroscopy Applied to Inorganic Chemistry* vol 3, ed G J Long and F Grandjean (New York: Plenum) p 513

[30] Albedah M A, Al-Qadi K, Stadnik Z M and Przewoźnik J 2014 *J. Alloys Compd.* **613** 344

[31] Nejadsattari F, Stadnik Z M, Przewoźnik J and Buschow K H J 2015 *Physica* B **477** 113

Chapter 6: Mössbauer spectroscopy and magnetic study of $RbEuFe_4As_4$

PHYSICAL REVIEW B **97**, 144426 (2018)

Mössbauer spectroscopy measurements on the 35.5 K superconductor $Rb_{1-\delta}EuFe_4As_4$

Mohammed A. Albedah,[1,2] Farshad Nejadsattari,[1] Zbigniew M. Stadnik,[1,*] Yi Liu,[3] and Guang-Han Cao[3]
[1] *Department of Physics, University of Ottawa, Ottawa, Ontario, Canada K1N 6N5*
[2] *Department of Physics, Majmaah University, P.O. Box 1712, Zulfi, Saudi Arabia*
[3] *Department of Physics, Zhejiang University, Hangzhou 310027, China*

(Received 23 February 2018; revised manuscript received 14 April 2018; published 30 April 2018)

The results of x-ray diffraction and ^{57}Fe and ^{151}Eu Mössbauer spectroscopy measurements, supplemented with *ab initio* hyperfine-interaction parameter calculations, on the new 35.5 K superconductor $Rb_{1-\delta}EuFe_4As_4$ are presented. The superconductor crystallizes in the tetragonal space group $P4/mmm$ with the lattice parameters $a = 3.8849(1)$ Å and $c = 13.3370(3)$ Å. It is shown that there is no magnetic order of the Fe magnetic moments down to 2.1 K and that the ferromagnetic order is associated solely with the Eu magnetic moments. The Curie temperature $T_C = 16.54(8)$ K is determined from the temperature dependence of both the hyperfine magnetic field at ^{151}Eu nuclei and the transferred hyperfine magnetic field at ^{57}Fe nuclei that is induced by the ferromagnetically ordered Eu sublattice. The Eu magnetic moments are demonstrated to be perpendicular to the crystallographic c axis. The temperature dependence of the principal component of the electric field gradient tensor, at both Fe and Eu sites, is well described by a $T^{3/2}$ power-law relation. Good agreement between the calculated and measured hyperfine-interaction parameters is observed. The Debye temperature of $Rb_{1-\delta}EuFe_4As_4$ is found to be 391(8) K.

DOI: 10.1103/PhysRevB.97.144426

I. INTRODUCTION

Discovered in 2016, $AeAFe_4As_4$ (Ae = Ca, Sr, Eu and A = K, Rb, Cs) compounds are a new Fe-based class of superconductors with the critical temperature T_c in the range 31.6–36.8 K [1–4]. Unlike in solid solutions, such as intensively studied $(Ba_{1-x}K_x)Fe_2As_2$ or $(Sr_{1-x}Na_x)Fe_2As_2$, the Ae and A atoms in $AeAFe_4As_4$ occupy crystallographically inequivalent positions, which changes the space group from $I4/mmm$ to $P4/mmm$. The crystal structure of these new superconductors consists of the Ae and A layers alternately stacked along the crystallographic c axis between the Fe_2As_2 slabs. Therefore, these fully ordered, stoichiometric Fe-based superconductors offer a unique opportunity to study, among other things, the relation between superconductivity and possible long-range magnetic order.

The superconductor $RbEuFe_4As_4$ with a critical superconducting temperature $T_c = 36.5$ K exhibits an anomaly at ∼15.0 K in the magnetic-susceptibility and specific-heat data [3]. The isothermal magnetization measurements allowed the identification of this anomaly as a ferromagnetic transition [3]. The ferromagnetism in the $RbEuFe_4As_4$ superconductor has been suggested [3] to result from the ordering of the Eu magnetic moments. This is equivalent to assuming that the Fe atoms in $RbEuFe_4As_4$ carry no magnetic moment. No orientation of the magnetic moment in $RbEuFe_4As_4$ with respect to the crystallographic axes has been established.

The main goal of this study is to determine whether the magnetic moment in the $RbEuFe_4As_4$ superconductor is associated with only Eu or Fe atoms or with Eu and Fe atoms and what its orientation is relative to the crystallographic axes. To achieve this goal, ^{57}Fe and ^{151}Eu Mössbauer spectroscopy, supplemented by the first-principles calculations, will be utilized.

II. EXPERIMENTAL AND THEORETICAL METHODS

The $Rb_{1-\delta}EuFe_4As_4$ polycrystalline sample was prepared with a solid-state reaction method in an Ar atmosphere and at high temperatures, as described elsewhere [3].

An x-ray diffraction pattern was measured at 298 K in Bragg-Brentano geometry on a PANalytical X'Pert scanning diffractometer using Cu $K\alpha$ radiation in the 2θ range of 10°–120° in steps of 0.02°. The $K\beta$ line was eliminated by using a Kevex PSi2 Peltier-cooled solid-state Si detector. The chemical composition of the crystallites of the sample was determined using an energy-dispersive x-ray spectrometer (Model Octane Plus) equipped with a field-emission scanning electron microscope (Hitachi S-4800). The dc magnetization measurements were carried out using a Quantum Design magnetic property measurement system (MPMS-5).

The ^{57}Fe and ^{151}Eu Mössbauer measurements [5] were conducted using standard Mössbauer spectrometers operating in the sine mode, with sources ^{57}Co(Rh) and ^{151}Sm(SmF$_3$) at room temperature, respectively. The Mössbauer source ^{151}Sm(SmF$_3$) is not a monochromatic source as ^{151}Sm nuclei are located in the SmF$_3$ matrix at a site of noncubic symmetry. By measuring the ^{151}Eu Mössbauer spectra of a cubic EuSe compound, we determined that the electric quadrupole coupling constant [5] eQ_gV_{zz} [here e is the proton charge, $Q_g = 0.903$ b is the ground-state electric quadrupole moment of the ^{151}Eu nucleus [6], and V_{zz} is the principal component of the electric-field-gradient (EFG) tensor] in our source is $-3.69(13)$ mm/s, which is close to the value of -3.6 mm/s

---

[*] stadnik@uottawa.ca

2469-9950/2018/97(14)/144426(9)

©2018 American Physical Society

found in Ref. [7]. The precise shape of the source emission line was taken into account in the fits of the ^{151}Eu Mössbauer spectra.

The 14.4 and 21.5 keV γ rays were detected with a proportional counter. The spectrometers were calibrated with a 6.35-μm-thick α-Fe foil [8], and the spectra were folded. The Mössbauer absorbers consisted of a mixture of powder $Rb_{1-\delta}EuFe_4As_4$ and boron nitride, which was pressed into a pellet that was put into an 8-μm-thick Al disk container to ensure a uniform temperature over the whole absorber. The Mössbauer absorbers were put into a Mössbauer cryostat in which they were kept in a static exchange gas atmosphere at a pressure of $\sim 6\times 10^{-3}$ mbar. The surface densities of the ^{57}Fe and ^{151}Eu Mössbauer absorbers were 17.23 and 29.1 mg/cm^2, respectively. They correspond to an effective thickness parameter t_a [5] of $2.96 f_\mathrm{a}$ and $2.62 f_\mathrm{a}$, respectively (here f_a is the Debye-Waller factor of the absorber). Since $t_a > 1$, the resonance line shape of the Mössbauer spectra was described using a transmission integral formula [9]. The Mössbauer spectra at temperatures below the magnetic transition temperature were analyzed using a least-squares fitting procedure which entailed calculations of the positions and relative intensities of the absorption lines by numerical diagonalization of the full hyperfine interaction Hamiltonian.

Ab initio magnetic moment and Mössbauer hyperfine-interaction parameter calculations were performed within the framework of density functional theory using the full-potential linearized augmented plane wave plus local orbitals method as implemented in the WIEN2K package [10,11]. The experimental lattice parameters (a and c) and the atomic position parameters in the space group $P4/mmm$ (see below) were used in the calculations.

III. RESULTS AND DISCUSSION

A. Structural characterization

Figure 1 displays the room-temperature powder x-ray diffraction pattern of $Rb_{1-\delta}EuFe_4As_4$. The compound studied was shown [3] to crystallize in the tetragonal space group $P4/mmm$. A Rietveld refinement [12] of the x-ray powder diffraction data was carried out, yielding the lattice parameters $a = 3.8849(1)$ Å and $c = 13.3370(3)$ Å and the atomic positional parameters that are listed in Table I. We note (Fig. 1) that the specimen studied contains the second phases of FeAs [13] in the amount of 3.1(4) wt% and of Eu_2O_3 in the amount of 0.7(2) wt%. The values of a and c found here are, respectively, shorter and longer than the corresponding values in Ref. [3].

We found with energy-dispersive x-ray spectroscopy that the chemical composition of the crystallites studied was $Rb_{0.67(5)}EuFe_{4.1(7)}As_{4.3(5)}$. This indicates the existence of a significant Rb deficiency in the specimen. This deficiency induces an additional hole doping, which naturally explains the changes in the lattice parameters. The extra hole doping places the sample in an overdoped regime, which leads to a slight decrease of the superconducting transition temperature (see below).

The unit cell and the layered crystal structure of $RbEuFe_4As_4$ are shown in Fig. 2. The interactions between the Rb, Fe, and As atoms in the compound studied are depicted by various connecting rods. One observes that the layers of Eu atoms are completely isolated from the Fe_4As_4 blocks and that two neighboring Fe_4As_4 blocks are separated by sheets of Rb atoms along the c direction.

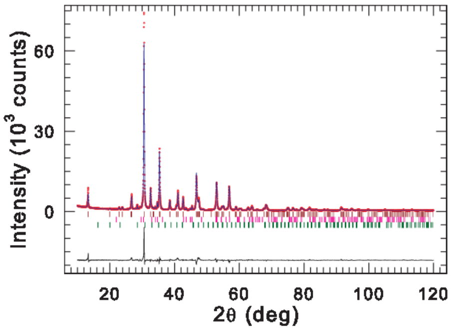

FIG. 1. Powder x-ray diffraction pattern of $Rb_{1-\delta}EuFe_4As_4$ at 298 K. The experimental data are denoted by open circles, while the line through the circles represents the results of the Rietveld refinement. The upper set of vertical dark red bars represents the Bragg peak positions corresponding to the $Rb_{1-\delta}EuFe_4As_4$ phase, the middle set of vertical pink bars corresponds to the positions of the impurity phase of FeAs (space group $Pnma$), and the lower set of vertical dark green bars refers to the positions of the impurity phase of Eu_2O_3 (space group $Ia\bar{3}$). The black solid line represents the difference curve between experimental and calculated patterns.

The physical dimensions of the unit cell play an important role in some of the electronic transfer properties of the compound studied. In particular, each unit cell of $RbEuFe_4As_4$ is separated along the c direction from its neighboring cells by two planes formed by the Eu atoms. As a direct result of the elongation of the unit cell in the c direction, the $RbFe_4As_4$ units are practically isolated from the neighboring cells. Consequently, no direct electronic charge transfer between the neighboring $RbFe_4As_4$ units along the c direction is expected. Hence, one can consider the Eu layers to form barriers for the conduction electrons, forbidding them from freely propagating along the c direction. The absence of connecting rods in Fig. 2(b) between these layers of the Eu atoms and the $RbFe_4As_4$ units indicates this point. Thus, the insulating behavior of the compound studied along the c axis results from strong ionic interactions between the Eu layers and the $RbFe_4As_4$ units, leading to the charge delocalization that exists only within the $RbFe_4As_4$ units. In other words, the valence electrons of the Eu atoms are completely transferred to the $RbFe_4As_4$ units to form the aforementioned ionic couplings.

TABLE I. The Rietveld refined atomic positions for the tetragonal $RbEuFe_4As_4$ (space group $P4/mmm$).

Atom	Site	Point symmetry	Occupancy	x	y	z
Rb	$1d$	$4/mmm$	1.0	$\frac{1}{2}$	$\frac{1}{2}$	$\frac{1}{2}$
Eu	$1a$	$4/mmm$	1.0	0	0	0
Fe	$4i$	$2mm.$	1.0	0	$\frac{1}{2}$	0.2316(2)
As1	$2g$	$4mm$	1.0	0	0	0.3362(2)
As2	$2h$	$4mm$	1.0	$\frac{1}{2}$	$\frac{1}{2}$	0.1273(3)

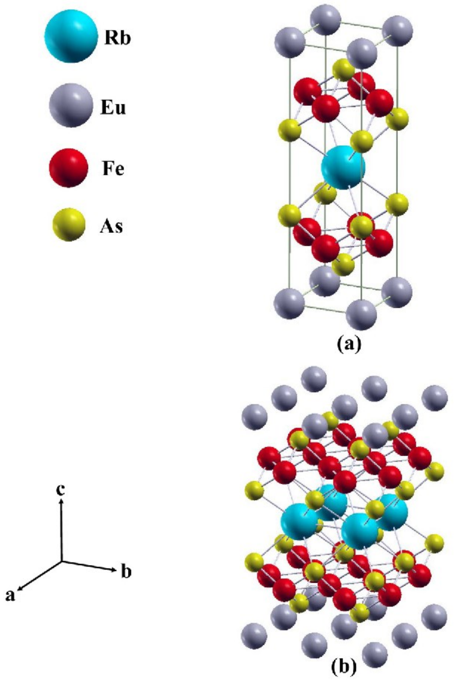

FIG. 2. (a) The unit cell and (b) the layered crystal structure of $RbEuFe_4As_4$.

The tetragonal unit cell elongated along the c axis rules out the possibility of any strong interaction between the Eu layers. Therefore, no magnetic coupling is expected to exist between the Eu atoms along the c direction. One may thus predict that the interatomic interactions between the Eu atoms must occur in the ab plane and that a two-dimensional magnetic interaction mechanism, if any, between neighboring Eu atoms in each layer should exist.

B. Magnetic characterization

Superconductivity and ferromagnetism of the polycrystalline sample of $Rb_{1-\delta}EuFe_4As_4$ were verified by magnetic measurements. As shown in Fig. 3(a), bulk superconductivity is seen from the large magnetic shielding fraction (the volume fraction exceeds 100% because of the demagnetization effect). The superconducting transition temperature T_c is 35.5 K, 1 K lower than reported previously [3]. The slight decrease in T_c is probably due to the existence of the Rb deficiency (see above) that induces an overdoping effect.

The field-cooled magnetic susceptibility [Fig. 3(a)] shows an upturn below 20 K and levels off at $T_C = 15.0$ K, which is defined as the Curie temperature [3]. The anomalous magnetic response reflects the Eu-spin ferromagnetism, which is manifested by the isothermal magnetization shown in Fig. 3(b). Below T_C, an S-shaped magnetic hysteresis loop, one of the hallmarks of ferromagnetism, appears. The saturation magnetization of 6.0 μ_B/f.u. is close to the value of 7.0 μ_B/f.u. expected for full Eu^{2+}-spin ferromagnetism (the deviation might be due to the existence of the FeAs and Eu_2O_3 impurities in the sample studied). In fact, the hysteresis loop at 2.0 K is superposed by superconducting signals, as seen from the bifurcation of the magnetization at high fields [Fig. 3(b)]. At 20 K, the $M(H)$ loop mainly originates from type-II superconductivity with flux pinning and Brillouin-function-type paramagnetism. No magnetic hysteresis is observed at 40 K, consistent with the loss of ferromagnetism and superconductivity at that temperature. Thus, the data presented in Fig. 3 unambiguously confirm the presence of superconductivity and ferromagnetism below their respective transition temperatures in the $Rb_{1-\delta}EuFe_4As_4$ specimen.

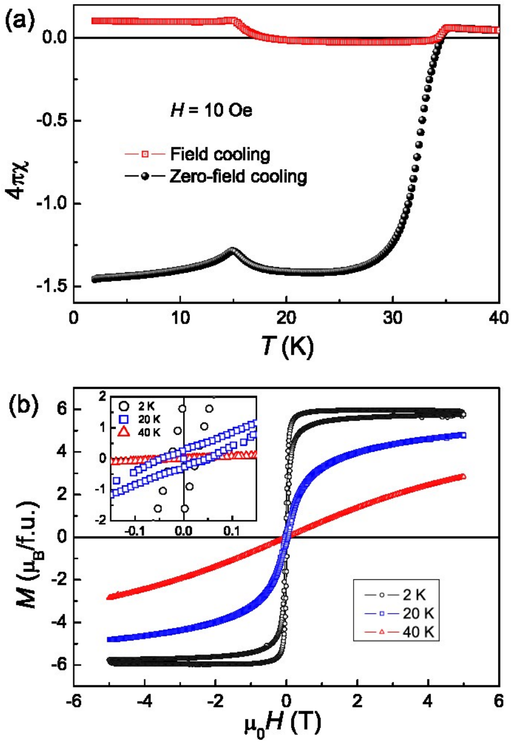

FIG. 3. (a) Temperature dependence of the field-cooled and zero-field-cooled dc magnetic susceptibility ($4\pi\chi$, in Gaussian units) of $Rb_{1-\delta}EuFe_4As_4$. (b) Field dependence of the magnetization of $Rb_{1-\delta}EuFe_4As_4$ at selected temperatures. The inset shows a close-up at low fields.

C. Calculated magnetic moments and hyperfine interaction parameters

The calculated magnetic moments of the Rb, Eu, Fe, As1, and As2 atoms in ferromagnetic $RbEuFe_4As_4$ are $-0.0038\mu_B$, $6.7095\mu_B$, $1.1037\mu_B$, $-0.0688\mu_B$, and $-0.0857\mu_B$, respectively. It is thus predicted that the magnetism of $RbEuFe_4As_4$

is associated predominantly with the Eu atoms and to a lesser extent with the Fe atoms. A comparison between the calculated and experimental magnetic moments carried by the Eu and Fe atoms will be made below.

^{57}Fe Mössbauer spectra of a nonmagnetic compound or of a magnetically ordered compound at temperatures above its ordering temperature yield two important hyperfine-interaction parameters: the quadrupole splitting (the separation between two resonance lines in an ^{57}Fe Mössbauer quadrupole doublet) $\Delta = \frac{1}{2}eQ|V_{zz}|\sqrt{1+\eta^2/3}$, where Q is the electric quadrupole moment of the ^{57}Fe nucleus (0.15 b) [14] and η is the asymmetry parameter, and the isomer shift δ_0 [5]. For a crystalline compound of known crystal structure, V_{zz}, η, and δ_0 can also be obtained from *ab initio* calculations [15].

The calculated values of V_{zz} and η at the $4i$ site occupied by the Fe atoms (Table I) are 5.270×10^{20} V/m^2 and 0.8734, respectively. These values correspond to the predicted $\Delta = 0.0921$ mm/s.

The isomer shift $\delta_0 = \alpha[\rho(0) - \rho_{\mathrm{ref}}(0)]$ results from the difference in the total electron density at the Mössbauer nucleus in the compound studied, $\rho(0)$, and in the reference compound, $\rho_{\mathrm{ref}}(0)$; α is a calibration constant. In calculating $\rho(0)$, relativistic spin-orbit effects were invoked to account for the possibility of the penetration of the $p_{1/2}$ electrons into the ^{57}Fe nuclei. An α-Fe metal (with a bcc structure and a lattice constant of 2.8665 Å) was chosen as a reference compound. The calculated values of $\rho_{\mathrm{ref}}(0)$ and $\rho(0)$ are 15309.905 and 15308.603 (a.u.)$^{-3}$, respectively. Using the calibration constant $\alpha = -0.291$ (a.u.)^3 (mm/s) [16], the calculated values of $\rho(0)$ and $\rho_{\mathrm{ref}}(0)$ lead to $\delta_0 = 0.379$ mm/s.

Finally, the calculated hyperfine magnetic field at 0 K (Fermi contact term) at ^{57}Fe nuclei, $H_{\mathrm{hf}}(0)$, is -56.2 kOe for ferromagnetic RbEuFe$_4$As$_4$. The Fermi contact term arises from a net spin-up and spin-down s-electron density at the nucleus as a result of spin polarization of inner filled s shells by spin-polarized partially filled outer shells [5,17].

The analysis of the ^{151}Eu Mössbauer spectra at different temperatures yields similar hyperfine-interaction parameters. The calculated values of V_{zz} and η at the $1a$ site occupied by the Eu atoms (Table I) are -49.659×10^{20} V/m^2 and 0.0, respectively. The $\eta = 0.0$ value is expected as the point symmetry $4/mmm$ of the $1a$ sites ensures an axially symmetric EFG tensor. The calculated $H_{\mathrm{hf}}(0)$ at ^{151}Eu nuclei is 483 kOe for ferromagnetic RbEuFe$_4$As$_4$.

D. ^{57}Fe Mössbauer spectroscopy

^{57}Fe Mössbauer spectra of Rb$_{1-\delta}$EuFe$_4$As$_4$ at selected temperatures between room and liquid-helium temperatures were measured over a large velocity range (Fig. 4) in order to access the possibility of the presence of a Zeeman pattern resulting from a possible magnetic ordering of the Fe atoms in Rb$_{1-\delta}$EuFe$_4$As$_4$ and of a Zeeman pattern due to a magnetically ordered and Fe-containing impurity phase in the sample studied. A visual inspection of these spectra shows the absence of Zeeman patterns corresponding to the main and impurity phases with typical values of the hyperfine magnetic field H_{hf}. As will be shown in detail below, the large-spectral-area component of these spectra (Fig. 4) is due to Rb$_{1-\delta}$EuFe$_4$As$_4$ and is in the form of a quadrupole doublet with small Δ at 295.3, 191.0, and 77.9 K and a Zeeman pattern with very small H_{hf} at 4.3 K. The small-spectral-area component of the spectra in Fig. 4 originates from the FeAs impurity phase and is in the form of a quadrupole doublet at 295.3, 191.0, and 77.9 K and a complex Zeeman pattern at 4.3 K.

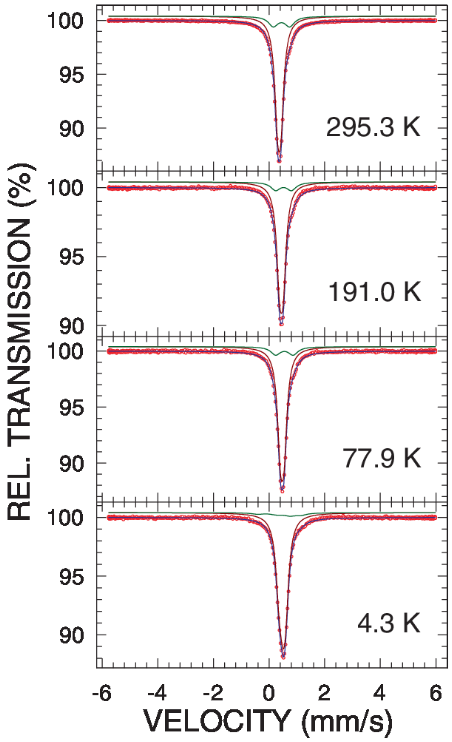

FIG. 4. ^{57}Fe Mössbauer spectra of Rb$_{1-\delta}$EuFe$_4$As$_4$ at selected temperatures measured over a large velocity range and fitted (solid blue lines) with a large-spectral-area quadrupole doublet at 295.3, 191.0, and 77.9 K and a Zeeman pattern at 4.3 K (solid dark red lines) due to Rb$_{1-\delta}$EuFe$_4$As$_4$ and with a small-spectral-area doublet at 295.3, 191.0, and 77.9 K and a Zeeman pattern at 4.3 K (solid dark green lines) due to the FeAs impurity phase, as described in the text. The zero-velocity origin is relative to α-Fe at room temperature.

Figure 5 shows the Mössbauer spectra of Rb$_{1-\delta}$EuFe$_4$As$_4$ at various temperatures down to the liquid-nitrogen temperature measured over a small velocity range. A feature on the right shoulder of the spectra indicates the presence of an impurity phase in the compound studied. Excellent fits of the spectra can be obtained with a large-spectral-area quadrupole doublet component with small Δ that originates from Rb$_{1-\delta}$EuFe$_4$As$_4$ and with a small-spectral-area quadrupole doublet component due to the FeAs impurity phase [18–20]. The spectral weight of the latter component, which is proportional to the product of the number of Fe atoms in the FeAs impurity and the Debye-Waller factor of the impurity, is 18(1)% and is larger than that expected from the amount of 3.1(4) wt% of the FeAs impurity derived from the x-ray diffraction spectrum.

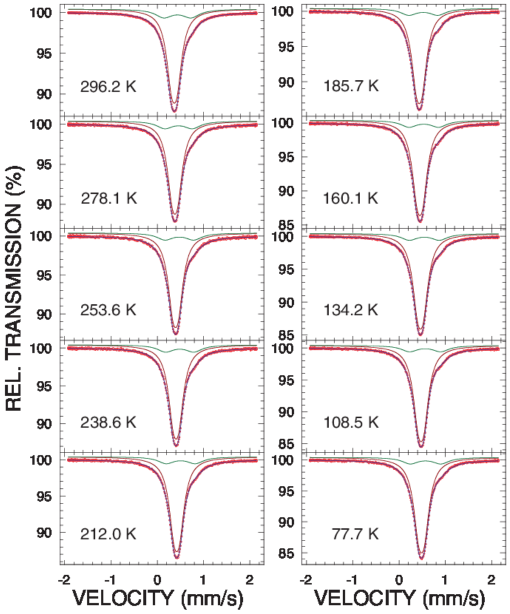

FIG. 5. ^{57}Fe Mössbauer spectra of $Rb_{1-\delta}EuFe_4As_4$ at the indicated temperatures fitted (solid blue lines) with a large-spectral-area quadrupole doublet due to $Rb_{1-\delta}EuFe_4As_4$ (dark red solid lines) and a small-spectral-area quadrupole doublet originating from the FeAs impurity phase (solid dark green lines), as described in the text. The zero-velocity origin is relative to α-Fe at room temperature.

A feature on the right shoulder of the spectra at temperatures below the liquid-nitrogen temperature (Fig. 6) disappears because the FeAs impurity component in these Mössbauer spectra is in the form of a complex Zeeman pattern. This indicates that the magnetic ordering temperature of the impurity phase lies in the range 77.7–50.9 K (Figs. 5 and 6). This agrees with the reported Néel temperature of FeAs (77(1) K in Ref. [13] and 69.2(1) K in Ref. [20]).

The temperature dependence of Δ obtained from the fits of the spectra in Figs. 5 and 6 is shown in Fig. 7(a). A small increase in Δ with decreasing temperature is observed. Such a temperature dependence of Δ has been observed in many metallic systems. It is well described by the empirical equation

$$\Delta(T) = \Delta(0)(1 - BT^{3/2}), \tag{1}$$

where $\Delta(0)$ is the value of Δ at 0 K and B is a constant. The fit of the $\Delta(T)$ data [Fig. 7(a)] to Eq. (1) gives $\Delta(0) = 0.1188(2)$ mm/s and $B = 10.1(8)\times10^{-6}$ K$^{-3/2}$. The value of B is similar to that found for a wide variety of other compounds, such as the ThFeAsN superconductor [21], crystalline approximants $Al_{76}Ni_9Fe_{15}$ [22] and $Al_{13}Fe_4$ [23] to quasicrystals, icosahedral $Al_{60}Cr_{19.9}Fe_{0.1}Ge_{20}$ [24] and decagonal $Al_{70}Co_{15}Ni_{14.9}Fe_{0.1}$ [25] quasicrystals, and amorphous $Zr_{65}Al_{7.5}Ni_{10}Cu_{7.3}Fe_{0.2}Ag_{10}$ [26]. The value of $\Delta(0)$ is close to the calculated value of 0.0921 mm/s.

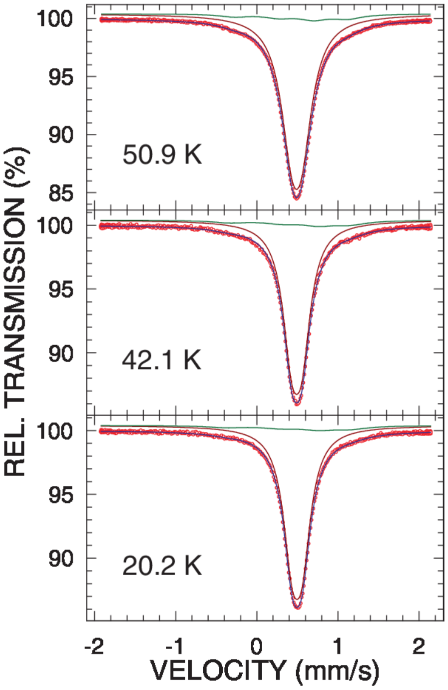

FIG. 6. ^{57}Fe Mössbauer spectra of $Rb_{1-\delta}EuFe_4As_4$ at the indicated temperatures fitted (solid blue lines) with a large-spectral-area quadrupole doublet due to $Rb_{1-\delta}EuFe_4As_4$ (dark red solid lines) and a small-spectral-area Zeeman pattern originating from the FeAs impurity phase (solid dark green lines), as described in the text. The zero-velocity origin is relative to α-Fe at room temperature.

The Mössbauer spectra of $Rb_{1-\delta}EuFe_4As_4$ at 20.2 and 16.4 K are compared in Fig. 7(b). One observes that the 16.4 K spectrum is slightly, but visibly, broader than the 20.2 K spectrum. This 0.014 mm/s broadening [Fig. 7(b)] over a very narrow temperature range of 3.8 K is the consequence of the appearance at 16.4 K of a very small H_{hf}. We surmise that this H_{hf} is transferred to the ^{57}Fe nuclei from the ferromagnetically ordered Eu sublattice (see below). A *transferred* hyperfine magnetic field at a given Mössbauer nucleus results from the neighboring magnetic moments [27]. It should be stressed that this transferred hyperfine magnetic field does not result from the ordering of the Fe sublattice. Its presence constitutes direct evidence of the ordering of the Eu sublattice. Such a transferred hyperfine magnetic field at a single temperature was observed first in the $EuFe_2(As_{1-x}P_x)_2$ superconductors [28]. Thus, the Mössbauer spectra at 16.4 K and lower temperatures were fitted (Fig. 8) with a large-spectral-area Zeeman pattern component [the value of Δ was fixed in the fit to that obtained from the fit of the $\Delta(T)$ dependence in Fig. 7(a)] that originates from $Rb_{1-\delta}EuFe_4As_4$ and with a small-spectral-area Zeeman pattern component that is due to the FeAs impurity phase.

Figure 9 displays the temperature dependence of the transferred H_{hf} that was derived from the fits of the spectra in Fig. 8.

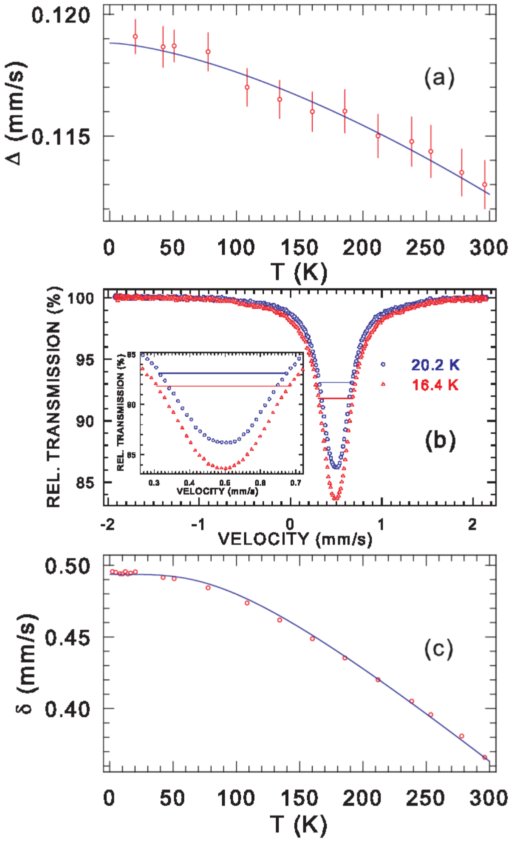

FIG. 7. (a) Temperature dependence of the quadrupole splitting. The solid line is the fit to Eq. (1), as explained in the text. (b) Comparison of the ^{57}Fe Mössbauer spectra of $Rb_{1-\delta}EuFe_4As_4$ at 20.2 and 16.4 K. The inset shows the spectra with enlarged horizontal and vertical scales. The horizontal bars indicate the full width at half maximum of the 20.2 K spectrum (0.359 mm/s) and the 16.4 K spectrum (0.373 mm/s). The zero-velocity origin is relative to α-Fe at room temperature. (c) Temperature dependence of the center shift δ. The solid line is the fit to the equation $\delta(T) = \delta_0 + \delta_{\rm SOD}(T)$, as explained in the text.

As expected, $H_{\rm hf}$ increases with decreasing temperature. The $H_{\rm hf}(T)$ dependence was fitted using the phenomenological form [29]

$$H_{\rm hf}(T) = H_{\rm hf}(0)\left[1 - \left(\frac{T}{T_C}\right)^{\alpha}\right]^{\beta}, \tag{2}$$

where $H_{\rm hf}(0)$ is the value of $H_{\rm hf}$ at 0 K and α and β are exponents describing the behavior of $H_{\rm hf}(T)$ near 0 K and T_C, respectively. The fit yields $H_{\rm hf}(0) = 6.17(2)$ kOe, $T_C = 16.63(16)$ K, $\alpha = 1.96(10)$, and $\beta = 0.21(2)$. The values of α and β found here are comparable to those obtained for other compounds [30–32].

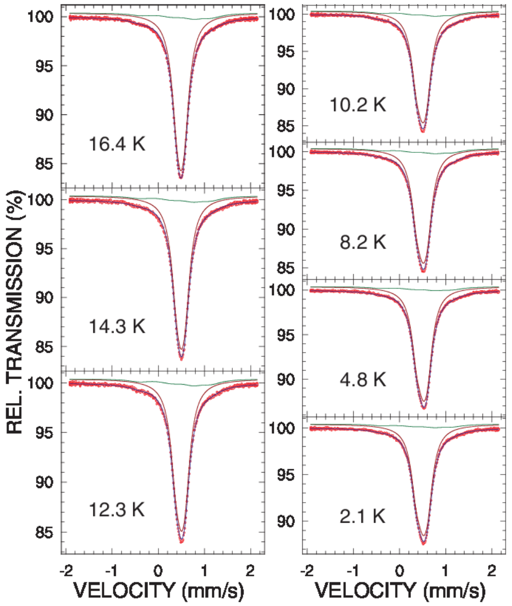

FIG. 8. ^{57}Fe Mössbauer spectra of $Rb_{1-\delta}EuFe_4As_4$ at the indicated temperatures fitted (solid blue lines) with a large-spectral-area Zeeman pattern due to $Rb_{1-\delta}EuFe_4As_4$ (dark red solid lines) and a small-spectral-area Zeeman pattern originating from the FeAs impurity phase (solid dark green lines), as described in the text. The zero-velocity origin is relative to α-Fe at room temperature.

The calculations predict a nonzero, but small, value of $|H_{\rm hf}(0)|$ at the ^{57}Fe nuclei and of the magnetic moment carried by the Fe atoms $\mu_{\rm Fe}$ (see above). This is at odds with the experimentally observed zero value of the intrinsic, i.e., not transferred, $H_{\rm hf}$ down to 2.1 K and, consequently, the zero value of $\mu_{\rm Fe}$. The failure of theory in predicting the zero values

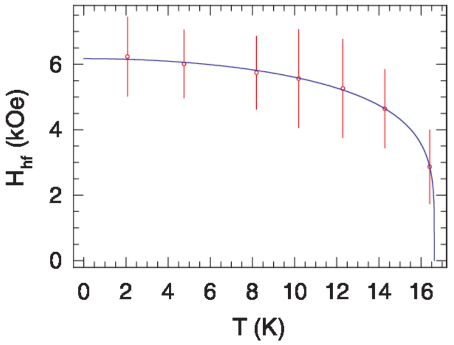

FIG. 9. Temperature dependence of the transferred hyperfine magnetic field. The solid line is the fit to Eq. (2), as explained in the text.

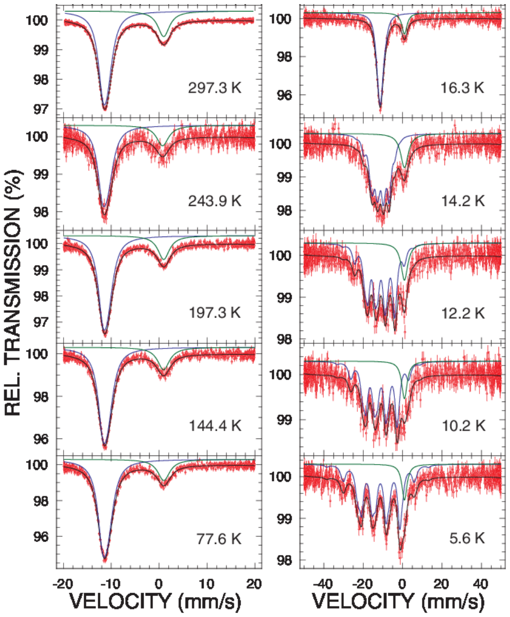

FIG. 10. ^{151}Eu Mössbauer spectra of $Rb_{1-\delta}EuFe_4As_4$ in the paramagnetic temperature region (left column) and the magnetic temperature region (right column). They are fitted (solid black lines) with a large-spectral-area quadrupole pattern (left column) and a large-spectral-area Zeeman pattern (right column) due to $Rb_{1-\delta}EuFe_4As_4$ (blue solid lines) and a small-spectral-area singlet originating from the Eu_2O_3 impurity phase (solid dark green lines), as described in the text. The zero-velocity origin is relative to the source.

of H_{hf} and μ_{Fe} may be related to the inherent limitations of standard density functional theory, especially as applied to the strongly correlated systems or the d- or f-electron compounds with localized electrons [33].

The temperature dependence of the center shift δ that was obtained from the fits of the spectra in Figs. 5, 6, and 8, is shown in Fig. 7(c). The center shift at temperature T, $\delta(T)$, consists of two terms, $\delta(T) = \delta_0 + \delta_{\mathrm{SOD}}(T)$, where δ_0 is the intrinsic, temperature-independent isomer shift and $\delta_{\mathrm{SOD}}(T)$ is the second-order Doppler (SOD) shift. The latter is the function of the Debye temperature Θ_{D} [5]. The fit of the experimental data $\delta(T)$ [Fig. 7(c)] gives $\delta_0 = 0.494(2)$ mm/s and $\Theta_{\mathrm{D}} = 391(8)$ K. We note that the experimental value of δ_0 found here is 30% larger than the calculated δ_0.

E. ^{151}Eu Mössbauer spectroscopy

The ^{151}Eu Mössbauer spectra of $Rb_{1-\delta}EuFe_4As_4$ at temperatures between room and liquid-helium temperatures are shown in Fig. 10. The spectra in the paramagnetic temperature region (left column in Fig. 10) consist of a large-spectral-area component in the form of an unresolved quadrupole octet [5,34] that originates from Eu^{2+} ions in $Rb_{1-\delta}EuFe_4As_4$ and a small-spectral-area component in the form of a single line due to Eu^{3+} ions in the Eu_2O_3 impurity phase. The spectral weight of the latter component is 22(1)% and is larger than that expected from the amount of 0.7(2) wt% of the Eu_2O_3 impurity derived from the Rietveld refinement of the x-ray diffraction spectrum. The Eu atoms in $Rb_{1-\delta}EuFe_4As_4$ are located at the $1a$ site with the point symmetry $4/mmm$ (Table I), which ensures an axially symmetric ($\eta = 0$) EFG tensor at this site. Also, V_{zz} is parallel to the c axis. The temperature dependence of V_{zz} derived from the fits of the spectra in the paramagnetic temperature region is shown in Fig. 11. Similar to the $\Delta(T)$ dependence in Fig. 7(a), the magnitude of V_{zz} increases with decreasing temperature. The $V_{zz}(T)$ data can be fitted to the same empirical $T^{3/2}$ power-law relation [Eq. (1)] in which $\Delta(T)$ and $\Delta(0)$ are replaced with $V_{zz}(T)$ and $V_{zz}(0)$, respectively. The fit of the $V_{zz}(T)$ data (Fig. 11) yields $V_{zz}(0) = -0.470(6)\times 10^{22}$ V/m^2 and $B = 2.66(42)\times 10^{-5}$ K$^{-3/2}$. The experimental value of $V_{zz}(0)$ compares very well with the calculated value of -0.497×10^{22} V/m^2.

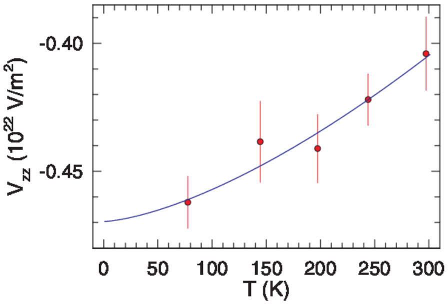

FIG. 11. Temperature dependence of the principal component of the electric-field-gradient tensor V_{zz} derived from the fits of the spectra in Fig. 10 (left column). The solid line is the fit to an empirical $T^{3/2}$ power-law relation, as explained in the text.

The spectra in the magnetic temperature region (right column in Fig. 10) were fitted with a large-spectral-area Zeeman pattern component that originates from $Rb_{1-\delta}EuFe_4As_4$ and a small-spectral-area single-line component due to an impurity phase. The value of V_{zz} was fixed in the fit to that obtained from the fit of the $V_{zz}(T)$ dependence in Fig. 10. The temperature dependence of H_{hf} determined from the fits of these Mössbauer spectra is shown in Fig. 12(a). It is usually assumed that the temperature variation of H_{hf} in a magnetically ordered material can be reasonably explained within the framework of the molecular field model, assuming that H_{hf} is proportional to the sublattice magnetization. In terms of this model, $H_{\mathrm{hf}}(T)$ can be expressed as

$$H_{\mathrm{hf}}(T) = H_{\mathrm{hf}}(0)B_J(x), \qquad (3)$$

where $H_{\mathrm{hf}}(0)$ is the saturation hyperfine magnetic field; $B_J(x)$ is the Brillouin function, defined as

$$B_J(x) = \frac{2J+1}{2J}\coth\left(\frac{2J+1}{2J}x\right) - \frac{1}{2J}\coth\left(\frac{x}{2J}\right); \qquad (4)$$

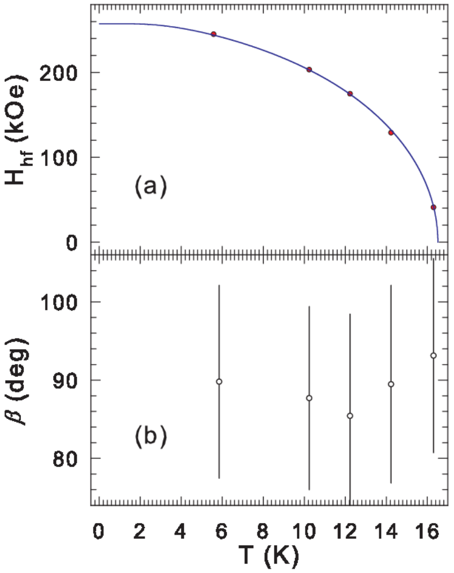

FIG. 12. Temperature dependence of (a) the hyperfine magnetic field H_{hf} and (b) the angle β determined from the fits of the spectra in Fig. 10 (right column). The solid line in (a) is the fit to Eq. (3), as explained in the text.

and

$$x = \frac{3J}{J+1}\frac{H_{hf}(T)}{H_{hf}(0)}\frac{T_C}{T}. \tag{5}$$

The fit of the $H_{hf}(T)$ data [Fig. 12(a)] to Eq. (3) with $J = S = 7/2$ (corresponding to a free Eu^{2+} ion) yields $H_{hf}(0) = 257.4(4.3)$ kOe and $T_C = 16.51(10)$ K. The T_C found here is very close to the value of 16.63(16) K derived from the temperature dependence of the transferred H_{hf} at ^{57}Fe nuclei. We take a weighted average of these two T_C values, 16.54(8) K, as the T_C of the studied superconductor. The experimental value of $H_{hf}(0)$ is significantly smaller than the calculated Fermi contact value of 483 kOe. This discrepancy can be explained by the fact that the measured hyperfine magnetic field at the ^{151}Eu nuclei is divided into three equally important contributions: $H_{hf} = H_c + H_{op} + H_n$. Here H_c is the core-polarization field (the Fermi contact term), H_{op} is due to conduction-electron polarization by the ion itself, and H_n includes all contributions from neighboring magnetic ions [35]. Clearly, the latter two contributions when added to the Fermi contact term must account for the measured $H_{hf}(0)$. Often, the H_{op} contribution has a sign opposite to that of the H_c contribution [34,35].

For ^{151}Eu Mössbauer spectroscopy [34,35], as opposed to ^{57}Fe Mössbauer spectroscopy [36], there is no simple relation between the measured $H_{hf}(0)$ and the magnetic moment carried by Eu atoms. We note here that the calculated Eu magnetic moment of $6.7095\mu_B$ is slightly larger than the experimental moment of $6.0\mu_B$ at 2 K [Fig. 3(b)].

The temperature dependence of the angle β (the angle between V_{zz} and H_{hf}) determined from the fits of the spectra in the magnetic temperature region (right column in Fig. 10) is shown in Fig. 12(b). One observes that the β values are close to 90°. This constitutes experimental proof that the Eu magnetic moments are perpendicular to the crystallographic *c* axis, that is, that they lie in the *ab* plane.

F. Discussion summary

A previous study concluded that $RbEuFe_4As_4$ bears both superconductivity and Eu-spin ferromagnetism but without any information about the Eu-spin direction [3]. Here, using the local-probe technique of Mössbauer spectroscopy, we have demonstrated that the Eu magnetic moments lie within the *ab* plane, akin to the case of nondoped $EuFe_2As_2$ in which an A-type antiferromagnetic (i.e., in-plane ferromagnetic but interplane antiferromagnetic) ordering occurs at 19 K [37–39]. Since $RbEuFe_4As_4$ can be viewed as a modified $EuFe_2As_2$ in which every other Eu layer is replaced by a Rb layer [Fig. 2(b)], one naturally expects that the Eu-layer spins in $RbEuFe_4As_4$ will become ferromagnetically ordered. Furthermore, the Eu spins are likely to be in the same direction as the Eu spins in $EuFe_2As_2$, i.e., along the crystallographic [110] direction [38,39]. We note that the Eu-spin direction in $RbEuFe_4As_4$ is in sharp contrast to the corresponding direction in doped $EuFe_2As_2$ systems where the Eu magnetic moments are basically along the *c* axis [28,40,41]. This phenomenon calls for a theoretical explanation.

The previous demonstration of the Eu-spin ferromagnetism is based mainly on the isothermal magnetization curves [3]. However, there could be a possibility that the observed ferromagnetism is field induced. In other words, the zero-field state may not necessarily be ferromagnetic. The present study rules out such a possibility because, at zero field, the ^{57}Fe nuclei feel the transferred hyperfine magnetic field $H_{hf}(0) = 6.17(2)$ kOe that results from the Eu-spin ferromagnetism. Indeed, the Eu-spin ferromagnetic polarization gives rise to an internal magnetic field of 4.5 kOe, which is close to the value of $H_{hf}(0)$.

IV. CONCLUSIONS

We presented the results of *ab initio* hyperfine-interaction parameters calculations and of x-ray diffraction and ^{57}Fe and ^{151}Eu Mössbauer spectroscopy study of the new 35.5 K superconductor $Rb_{1-\delta}EuFe_4As_4$. We confirmed that the superconductor crystallizes in the tetragonal space group $P4/mmm$ with the lattice parameters $a = 3.8847(1)$ Å and $c = 13.3370(3)$ Å. We showed that the Fe atoms carry no magnetic moment down to 2.1 K and that the ferromagnetic order is associated with the Eu magnetic moments. The Curie temperature $T_C = 16.54(8)$ K is determined from the temperature dependence of both the hyperfine magnetic field at ^{151}Eu nuclei and the transferred hyperfine magnetic field at ^{57}Fe nuclei that is induced by the ferromagnetically ordered Eu sublattice. We found that the Eu magnetic moments lie in the *ab* plane. We observed that the temperature dependence of the principal component of the electric-field-gradient tensor is well described by a $T^{3/2}$ power-law relation at both the Fe and Eu sites. Good agreement was found between the calculated and measured hyperfine-interaction parameters. We determined that the Debye temperature of $Rb_{1-\delta}EuFe_4As_4$ is 391(8) K.

ACKNOWLEDGMENT

This work was supported by the Natural Sciences and Engineering Research Council of Canada (NSERC) and the National Natural Science Foundation of China (Grant No. 11474252).

---

[1] A. Iyo, K. Kawashima, T. Kinjo, T. Nishio, S. Ishida, H. Fujihisa, Y. Gotoh, K. Kihou, H. Eisaki, and Y. Yoshida, J. Am. Chem. Soc. **138**, 3410 (2016).

[2] K. Kawashima, T. Kinjo, T. Nishio, S. Ishida, H. Fujihisa, Y. Gotoh, K. Kihou, H. Eisaki, Y. Yoshida, and A. Iyo, J. Phys. Soc. Jpn. **85**, 064710 (2016).

[3] Y. Liu, Y.B. Liu, Z.-T. Tang, H. Jiang, Z.-C. Wang, A. Ablimit, W.-H. Jiao, Q. Tao, C.-M. Feng, Z.-A. Xu, and G.-H. Cao, Phys. Rev. B **93**, 214503 (2016).

[4] Y. Liu, Y.-B. Liu, Q. Chen, Z.-T. Tang, W.-H. Jiao, Q. Tao, Z.-A. Xu, and G.-H. Cao, Sci. Bull. **61**, 1213 (2016).

[5] N. N. Greenwood and T. C. Gibb, *Mössbauer Spectroscopy* (Chapman and Hall, London, 1971); P. Gütlich, E. Bill, and A. Trautwein, *Mössbauer Spectroscopy and Transition Metal Chemistry* (Springer, Berlin, 2011).

[6] Y. Tanaka, R. M. Steffen, E. B. Shera, W. Reuter, M. V. Hoehn, and J. D. Zumbro, Phys. Rev. C **29**, 1830 (1984).

[7] I. Nowik and I. Felner, Hyperfine Interact. **28**, 959 (1986).

[8] *Certificate of Calibration, Iron Foil Mössbauer Standard*, edited by J. P. Cali, Natl. Bur. Stand. (US) Circ. 1541 (1971).

[9] S. Margulies and J. R. Ehrman, Nucl. Instrum. Methods **12**, 131 (1961); G. K. Shenoy, J. M. Friedt, H. Maletta, and S. L. Ruby, in *Mössbauer Effect Methodology*, edited by I. J. Gruverman, C. W. Seidel, and D. K. Dieterly (Plenum, New York, 1974), Vol. 10, p. 277.

[10] P. Blaha, K. Schwartz, G. Madsen, D. Kvasnicka, and J. Luitz, *WIEN2k: An Augmented Plane Wave Plus Local Orbitals Program for Calculating Crystal Properties* (Technische Universität Wien, Austria, 2001).

[11] F. Nejadsattari, P. Wang, Z. M. Stadnik, Y. Nagata, and T. Ohnishi, J. Alloys Compd. **725**, 1098 (2017).

[12] R. A. Young, *The Rietveld Method* (Oxford University Press, Oxford, 1993).

[13] K. Selte, A. Kjekshus, and A. F. Andersen, Acta Chem. Scand. **26**, 3101 (1972).

[14] G. Martínez-Pinedo, P. Schwerdtfeger, E. Caurier, K. Langanke, W. Nazarewicz, and T. Söhnel, Phys. Rev. Lett. **87**, 062701 (2001).

[15] P. Blaha, J. Phys.: Conf. Ser. **217**, 012009 (2010).

[16] U. D. Wdowik and K. Ruebenbauer, Phys. Rev. B **76**, 155118 (2007).

[17] A. J. Freeman and R. E. Watson, Phys. Rev. **131**, 2566 (1963).

[18] S. K. Kulshreshtha and P. Raj, J. Phys. F **9**, 2253 (1979).

[19] L. Häggström, A. Gustavsson-Seidel, and H. Fjellvåg, Europhys. Lett. **9**, 87 (1989).

[20] A. Błachowski, K. Ruebenbauer, J. Żukrowski, and Z. Bukowski, J. Alloys. Compd. **582**, 167 (2014).

[21] M. A. Albedah, F. Nejadsattari, Z. M. Stadnik, Z.-C. Wang, C. Wang, and G.-H. Cao, J. Alloys Compd. **695**, 1128 (2017)

[22] F. Nejadsattari, Z. M. Stadnik, J. Przewoźnik, and B. Grushko, J. Alloys Compd. **662**, 612 (2016).

[23] M. A. Albedah, F. Nejadsattari, Z. M. Stadnik, and J. Przewoźnik, J. Alloys Compd. **619**, 839 (2015).

[24] Z. M. Stadnik and P. Wang, J. Phys.: Condens. Matter **18**, 8383 (2006).

[25] Z. M. Stadnik and G. Zhang, J. Phys.: Condens. Matter **16**, 7303 (2004).

[26] Z. M. Stadnik, Ö. Rapp, V. Srinivas, J. Saida, and A. Inoue, J. Phys.: Condens. Matter **14**, 6883 (2002).

[27] W. Zinn, J. Phys. (Paris) Colloq. **32**, C1-724 (1971); Ch. Sauer, U. Köbler, W. Zinn, and G. M. Kalvius, *ibid.* **35**, C6-269 (1974); G. Czjzek, V. Oestreich, H. Schmidt, K. Łątka, and K. Tomala, J. Magn. Magn. Mater. **79**, 42 (1989); I. Nowik, Y. Levi, I. Felner, and E. R. Bauminger, *ibid.* **147**, 373 (1995).

[28] I. Nowik, I. Felner, Z. Ren, G. H. Cao, and Z. A. Xu, J. Phys.: Condens. Matter **23**, 065701 (2011).

[29] S. J. Blundell, C. A. Steer, F. L. Pratt, I. M. Marshall, W. Hayes, and R. C. C. Ward, Phys. Rev. B **67**, 224411 (2003).

[30] P. J. Baker, I. Franke, T. Lancaster, S. J. Blundell, L. Kerslake, and S. J. Clarke, Phys. Rev. B **79**, 060402(R) (2009).

[31] P. J. Baker, H. J. Lewtas, S. J. Blundell, T. Lancaster, I. Franke, W. Hayes, F. L. Pratt, L. Bohaty, and P. Becker, Phys. Rev. B **81**, 214403 (2010).

[32] Z. Li, Y. Fang, X. Ma, H. Pang, and F. Li, Phys. Rev. B **84**, 134509 (2011).

[33] W. Chibani, X. Ren, M. Scheffler, and P. Rinke, Phys. Rev. B **93**, 165106 (2016), and references therein; T. Schickling, J. Bünemann, F. Gebhard, and L. Boeri, *ibid.* **93**, 205151 (2016), and references therein; K. Cao, H. Lambert, P. G. Radaelli, and F. Giustino, *ibid.* **97**, 024420 (2018), and references therein.

[34] F. Grandjean and G. L. Long, in *Mössbauer Spectroscopy Applied to Inorganic Chemistry*, edited by G. J. Long and F. Grandjean (Plenum, New York, 1989), Vol. 3, p. 513, and references therein.

[35] I. Nowik, B. D. Dunlap, and J. H. Wernick, Phys. Rev. B **8**, 238 (1973).

[36] F. Nejadsattari, Z. M. Stadnik, J. Przewoźnik, and K. H. J. Buschow, Phys. B (Amsterdam, Neth.) **477**, 113 (2015), and references therein.

[37] S. Jiang, Y. Luo, Z. Ren, Z. Zhu, C. Wang, X. Xu, Q. Tao, G. Cao, and Z. Xu, New J. Phys. **11**, 025007 (2009).

[38] J. Herrero-Martín, V. Scagnoli, C. Mazzoli, Y. Su, R. Mittal, Y. Xiao, T. Brueckel, N. Kumar, S. K. Dhar, A. Thamizhavel, and L. Paolasini, Phys. Rev. B **80**, 134411 (2009).

[39] Y. Xiao, Y. Su, M. Meven, R. Mittal, C. M. N. Kumar, T. Chatterji, S. Price, J. Persson, N. Kumar, S. K. Dhar, A. Thamizhavel, and Th. Brueckel, Phys. Rev. B **80**, 174424 (2009).

[40] W. T. Jin, S. Nandi, Y. Xiao, Y. Su, O. Zaharko, Z. Guguchia, Z. Bukowski, S. Price, W. H. Jiao, G. H. Cao, and Th. Brückel, Phys. Rev. B **88**, 214516 (2013).

[41] S. Nandi, W. T. Jin, Y. Xiao, Y. Su, S. Price, D. K. Shukla, J. Strempfer, H. S. Jeevan, P. Gegenwart, and Th. Brückel, Phys. Rev. B **89**, 014512 (2014).

Chapter 7: Magnetic and Mössbauer spectroscopy study of $EuFeAs_2$ and $EuFe_{0.97}Ni_{0.03}As_2$

Journal of Magnetism and Magnetic Materials 503 (2020) 166603

Contents lists available at ScienceDirect

Journal of Magnetism and Magnetic Materials

journal homepage: www.elsevier.com/locate/jmmm

Research articles

Magnetic properties of $EuFeAs_2$ and the 14 K superconductor $EuFe_{0.97}Ni_{0.03}As_2$

Mohammed A. Albedah[a,b], Zbigniew M. Stadnik[a,*], Olha Fedoryk[a], Ya-Bin Liu[c], Guang-Han Cao[c]

[a] *Department of Physics, University of Ottawa, Ottawa, Ontario K1N 6N5, Canada*
[b] *Department of Physics, Majmaah University, P.O. Box 1712, Zulfi, Saudi Arabia*
[c] *Department of Physics, Zhejiang University, Hangzhou 310027, China*

A R T I C L E I N F O

Keywords:
Spin-density-wave antiferromagnetism
Superconductivity

A B S T R A C T

The findings of a ^{57}Fe and ^{151}Eu Mössbauer spectroscopy investigation between 1.8 and 299.5 K of $EuFeAs_2$ and the 14 K superconductor $EuFe_{0.97}Ni_{0.03}As_2$ are reported. In both compounds, the Fe sublattice orders in the antiferromagnetic spin-density-wave fashion with the Néel temperatures and Fe saturation magnetic moments of 106.2(1.9) K, 0.78(1)μ_B and 56.6(2.2) K, 0.47(1)μ_B, respectively. The Néel temperatures and the saturation hyperfine magnetic fields of the antiferromagnetically ordered Eu sublattice in both compounds are 44.4(5) K, 294.2(7) kOe and 43.5(1) K, 290.5(1) kOe, respectively. The 3% substitution of Fe by Ni in $EuFeAs_2$ has a dramatic effect on the magnetism of the Fe sublattice and virtually no effect on the magnetism of the Eu sublattice. The presence of Fe and Eu magnetic order in $EuFe_{0.97}Ni_{0.03}As_2$ is direct proof of the coexistence of superconductivity and magnetism. The increase of the magnitude of the main component of the electric field gradient tensor, at both Fe and Eu sites, with decreasing temperature is explained by a $T^{3/2}$ power-law relation. The Debye temperatures of $EuFeAs_2$, $EuFe_{0.97}Ni_{0.03}As_2$, and the $FeAs_2$ impurity phase are 355(18), 428(14), and 594(25) K, respectively.

1. Introduction

Recently, a new Eu-containing iron-pnictide compound $EuFeAs_2$ has been discovered [1]. The crystal structure of this compound is similar to that of the 112-type iron-pnictide $(Ca,R)FeAs_2$ (R = rare earth) superconductors. It consists of two Eu planes, Fe_2As_2 layers, and As_2-zigzag chain layers [2,3]. There is some discrepancy regarding the space group in which the $EuFeAs_2$ compound crystallizes. The monoclinic space group $P2_1/m$ was used in Refs. [1,4], and the orthorhombic space group $Imm2$ was employed in Ref. [3].

The two anomalies in the temperature dependence of the normalized resistivity of $EuFeAs_2$ at about 110 and 40 K were attributed to the probable antiferromagnetic spin-density-wave (SDW) transition of the Fe^{2+} ions, or the structural transition, and to the antiferromagnetic transition of the Eu^{2+} ions, respectively [1]. The antiferromagnetic transition at 41 K was also noticed in the temperature dependence of the magnetic susceptibility [1]. Similar anomalies (at about 100 and 40 K) were found in the resistivity data in Ref. [4]. However, a much more complex set of possible magnetic transitions was suggested based on the interpretation of the magnetic susceptibility and specific heat data [4].

It has been demonstrated recently that a small substitution of Fe by Ni in $EuFeAs_2$ induces superconductivity in $EuFe_{1-x}Ni_xAs_2$ with $x = 0.03$, 0.04, and 0.07 [4,5]. The critical temperature T_c for these three superconductors is 13.8, 17.5–18.2, and 13.7 K, respectively [4,5]. For the $x = 0.04$ superconductor, no antiferromagnetic SDW order of the Fe sublattice was observed, and the Eu sublattice was found to order antiferromagnetically below 38.5 K, followed by a putative spin-glass freezing at 15.5 K and a possible Eu-spin canting at 6.2 K [4]. What is remarkable about these new $EuFe_{1-x}Ni_xAs_2$ superconductors is the apparent coexistence of magnetism and superconductivity.

The Mössbauer spectroscopy technique proved to be a useful tool to study the possibility of incommensurate SDW order in a given compound. Its usefulness results from the fact that incommensurability leads to the complex shape of the Mössbauer spectra [6–9]. In this paper, we employ ^{57}Fe and ^{151}Eu Mössbauer spectroscopy to identify the nature of the Fe and Eu antiferromagnetic ordering in the non-superconducting $EuFeAs_2$ and the superconducting $EuFe_{0.97}Ni_{0.03}As_2$. We

---

[*] Corresponding author.
E-mail address: stadnik@uottawa.ca (Z.M. Stadnik).

https://doi.org/10.1016/j.jmmm.2020.166603
Received 2 January 2020; Received in revised form 8 February 2020; Accepted 9 February 2020
Available online 14 February 2020
0304-8853/ © 2020 Elsevier B.V. All rights reserved.

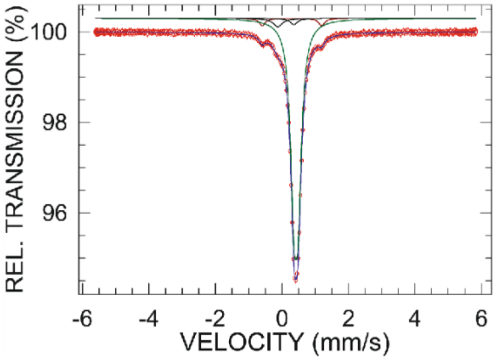

Fig. 1. High-statistics, ^{57}Fe Mössbauer spectrum of $EuFeAs_2$ at 299.8 K measured over a broad velocity range and fitted (solid blue line) with a large spectral area quadrupole doublet (solid dark green line) due to $EuFeAs_2$, a small spectral area quadrupole doublet (solid dark red line) originating from the $FeAs_2$ impurity phase, and two small spectral area single lines (solid black lines) which simulate the spectrum due to the presence of a tiny amount of Fe in the two Al foils of the absorber and in the two cryostat mylar windows, as described in the text. The zero-velocity origin is relative to α-Fe at room temperature.

show that both in $EuFeAs_2$ and $EuFe_{0.97}Ni_{0.03}As_2$, the Fe sublattice orders in the incommensurate SDW fashion, and with the magnetic parameters of the latter significantly smaller than those of the former. The Eu sublattice is shown to be also magnetically ordered in both compounds, but with the magnetic parameters that are practically the same.

2. Experimental methods

The polycrystalline samples of $EuFeAs_2$ and $EuFe_{0.97}Ni_{0.03}As_2$ used in this study were synthesized using a standard solid-state reaction method [4]. The powder X-ray diffraction spectra showed [4,5] that the $EuFeAs_2$ specimen contains a small amount of $FeAs_2$ impurity and the $EuFe_{0.97}Ni_{0.03}As_2$ specimen is impurity free.

The methodology of the ^{57}Fe and ^{151}Eu Mössbauer spectroscopy [10] measurements used here is the same as that described in Ref. [11]. The ^{57}Fe and ^{151}Eu Mössbauer spectra measured at temperatures below the Néel temperature T_N were analyzed using a first-order perturbation treatment [10] because the magnetic dipole interaction is much larger than the electric quadrupole interaction in the compounds studied.

The dc magnetic susceptibility was measured using a magnetic property measurement system (MPMS-5, Quantum Design). A standard four-electrode method was used to measure electrical resistivity.

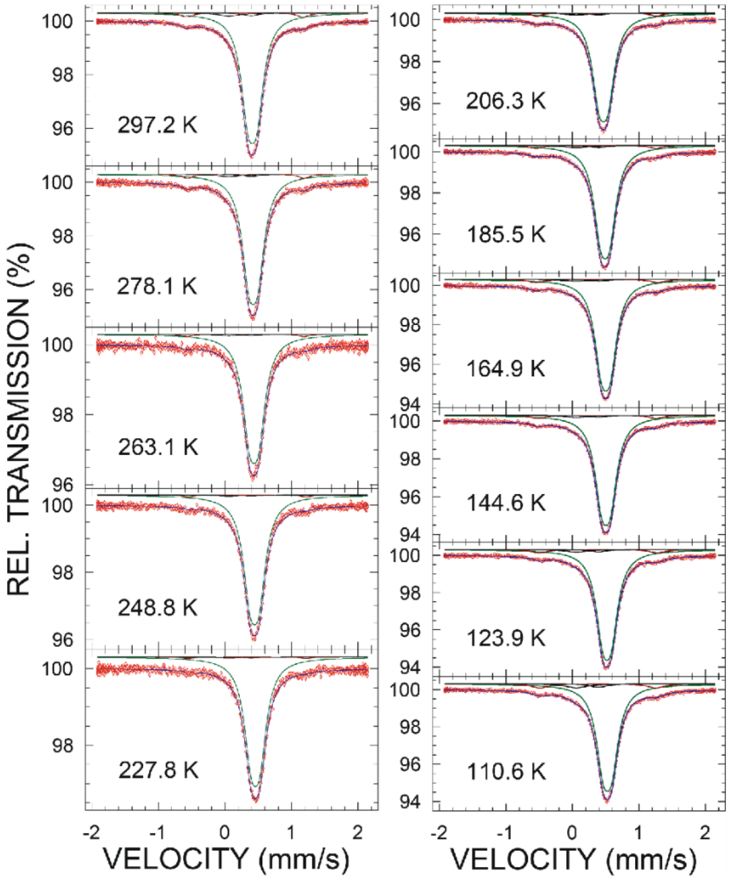

Fig. 2. ^{57}Fe Mössbauer spectra of $EuFeAs_2$ at temperatures above T_N of the Fe sublattice fitted in the same way as the spectrum in Fig. 1. The zero-velocity origin is relative to α-Fe at room temperature.

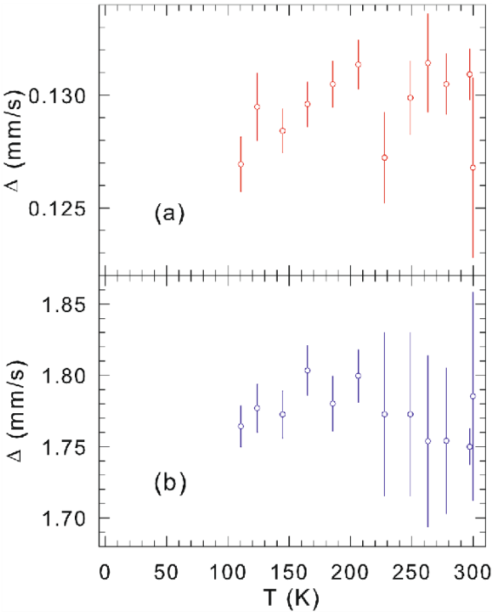

Fig. 3. Temperature dependence of the ^{57}Fe quadrupole splitting Δ of $EuFeAs_2$ (a) and $FeAs_2$ (b).

3. Experimental results and discussion

3.1. *$EuFeAs_2$ compound*

The high-statistics, room-temperature ^{57}Fe Mössbauer spectrum of $EuFeAs_2$ was measured over a broad velocity range (Fig. 1) to check whether the sample studied contains any magnetically-ordered, Fe-containing impurity phase. The absence of any Zeeman pattern in the spectrum proves that such impurity is not present in the sample. The spectrum is the superposition of a quadrupole doublet (with a very small quadrupole splitting $\Delta = \frac{1}{2}eQ|V_{zz}|\sqrt{1+\eta^2/3}$, where the symbols e, Q, V_{zz}, and η have their usual meaning [10,11]) originating from the main phase, a quadrupole doublet (with a very large Δ) due to the $FeAs_2$ impurity [12], and two single lines (at ~ − 0.24 and ~0.25 mm/s) which simulate the spectrum of a tiny amount of Fe present in the two Al foils of the absorber and the two cryostat mylar windows.

Fig. 2 displays the ^{57}Fe Mössbauer spectra of $EuFeAs_2$ measured in the paramagnetic temperature region, that is, above T_N of the Fe sublattice, and over a narrow velocity range. They can be fitted well with three components, similarly as the spectrum in Fig. 1.

The temperature dependence of Δ of $EuFeAs_2$ obtained from the fits of the spectra in Figs. 1,2 is shown in Fig. 3(a). Within the statistical error, it appears to be temperature independent. A similar conclusion is arrived at for the temperature dependence of Δ of the $FeAs_2$ impurity [Fig. 3(b)].

The ^{57}Fe Mössbauer spectrum of $EuFeAs_2$ at 47.7 K, that is, much below T_N of the Fe sublattice, is shown in Fig. 4(a). It is in the form of an immensely broadened, asymmetric, six-line Zeeman pattern that differs significantly from the spectrum expected for an antiferromagnet with Fe atoms occupying one crystallographic site (sharp, symmetric, six-line Zeeman pattern) [10]. The significant line broadening must arise from the presence of wide distribution, $P(H)$, of hyperfine magnetic fields H. There are two possible sources of such a wide distribution of H [9]. First, it can result from significant structural disorder present in $EuFeAs_2$. Second, it may also arise from the incommensurate modulation of the antiferromagnetic structure (the incommensurate SDW). As there is no dopant-induced (substituting Fe with another metal) structural disorder in $EuFeAs_2$, one can assert that the complex shape of the spectrum in Fig. 4(a) originates from the incommensurate antiferromagnetic SDW.

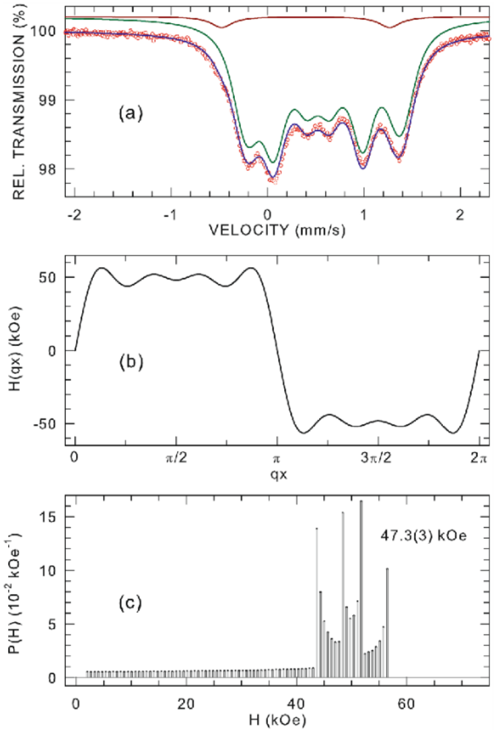

Fig. 4. (a) ^{57}Fe Mössbauer spectrum of $EuFeAs_2$ at 47.7 K fitted (solid blue line) with an incommensurate modulation of the hyperfine magnetic field pattern (solid dark green line) due to $EuFeAs_2$ and a quadrupole doublet (solid dark red line) originating from the $FeAs_2$ impurity phase, as described in the text. The zero-velocity origin is relative to α-Fe at room temperature. (b) Resulting shape of the SDW. (c) Resulting hyperfine magnetic field distribution labeled with the corresponding root-mean-square value of the hyperfine magnetic field. (For interpretation of the references to colour in this figure legend, the reader is referred to the web version of this article.)

To generate Mössbauer spectra caused by the incommensurate SDW, we follow the procedure described in detail in Ref. [7]. Briefly, the amplitude of the hyperfine magnetic field H due to the SDW along the x-direction that is parallel to the wave vector **q** is expressed as a series of odd harmonics [8]

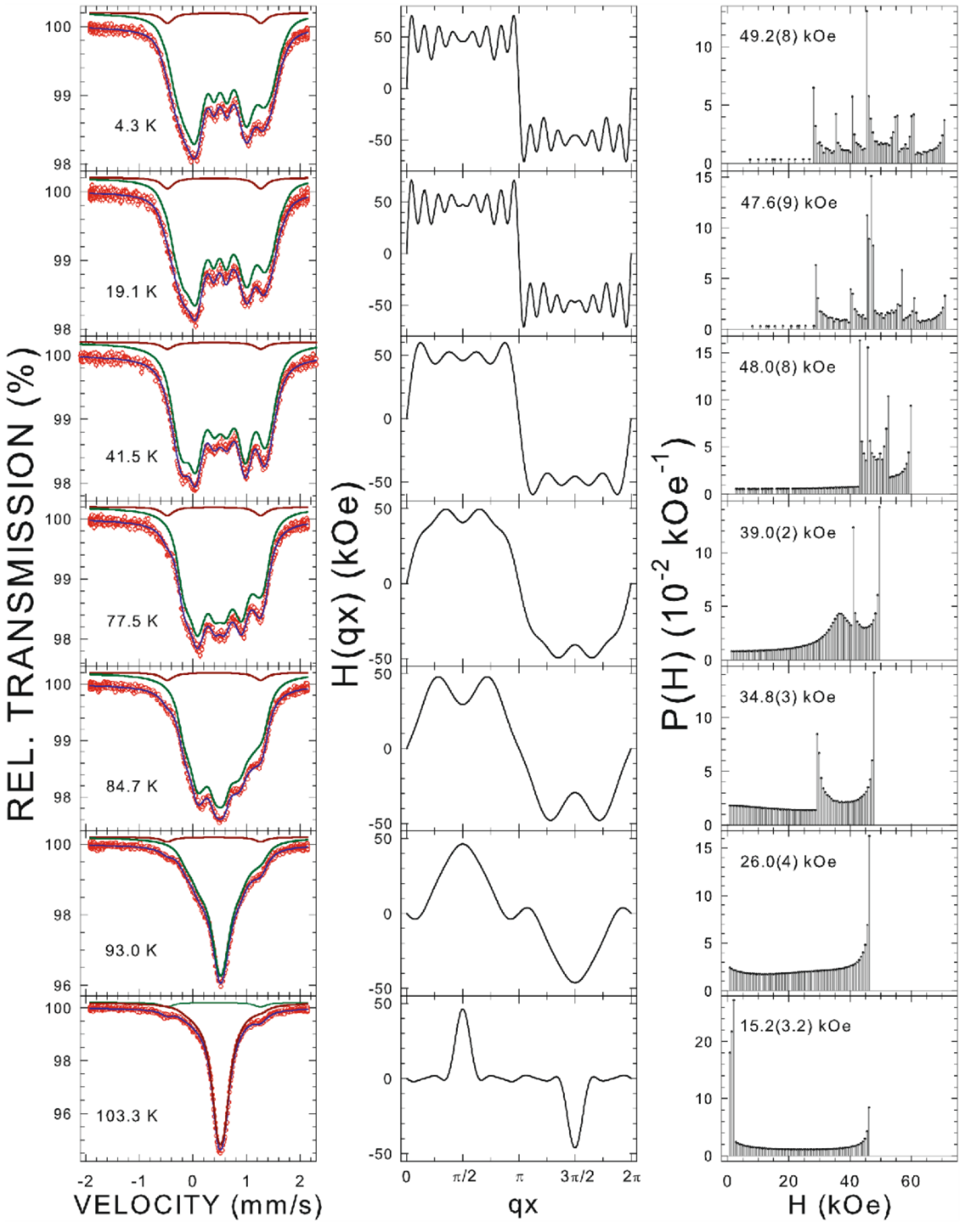

Fig. 5. ^{57}Fe Mössbauer spectra of EuFeAs$_2$ at the indicated temperatures fitted (solid blue line) with an incommensurate modulation of the hyperfine magnetic field pattern (solid dark green line) due to EuFeAs$_2$ and a quadrupole doublet (solid dark red line) arising from the FeAs$_2$ impurity phase (left panel), corresponding shapes of the SDW (middle panel), and resulting hyperfine magnetic field distributions labeled with the corresponding root-mean-square value of the hyperfine magnetic field (right panel). (For interpretation of the references to colour in this figure legend, the reader is referred to the web version of this article.)

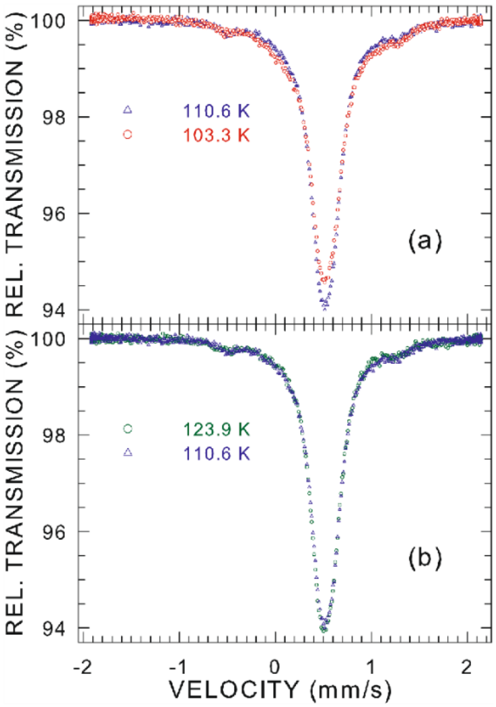

Fig. 6. Comparison of the ^{57}Fe Mössbauer spectra of EuFeAs$_2$ at 110.6 and 103.3 K (a) and at 123.9 and 110.6 K (b). The zero-velocity origin is relative to α-Fe at room temperature.

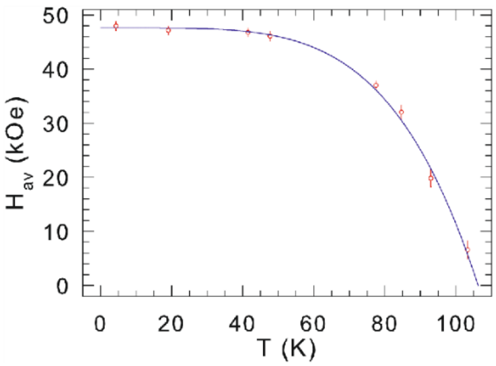

Fig. 7. Temperature dependence of H_{av} at ^{57}Fe nuclei derived from the distributions $P(H)$ in Figs. 4 and 5. The solid line is the power-law fit.

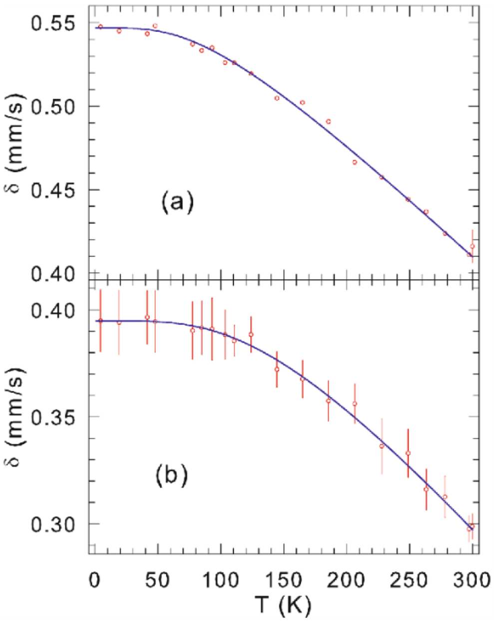

Fig. 8. Temperature dependence of the ^{57}Fe center shift δ of EuFeAs$_2$ (a) and FeAs$_2$ (b). The solid lines are the fits to Eq. (2), as explained in the text.

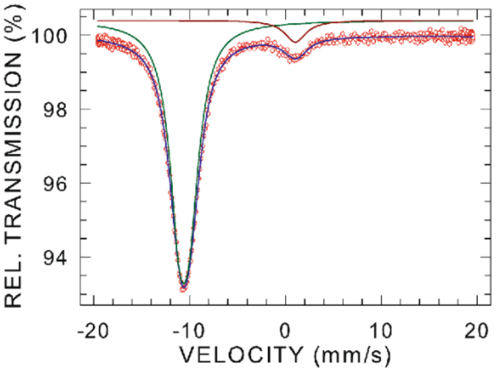

Fig. 9. ^{151}Eu Mössbauer spectrum of EuFeAs$_2$ at 298.2 K fitted (solid blue line) with a large spectral area quadrupole pattern due to EuFeAs$_2$ (solid dark green line) and a small spectral area singlet originating from an impurity phase (solid dark red line), as described in the text. The zero-velocity origin is relative to the source. (For interpretation of the references to colour in this figure legend, the reader is referred to the web version of this article.)

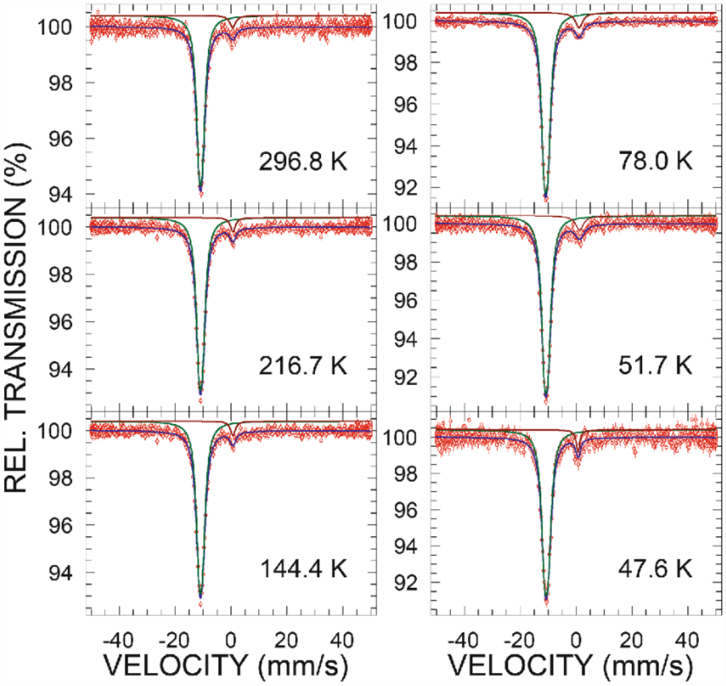

Fig. 10. ^{151}Eu Mössbauer spectra of $EuFeAs_2$ at the indicated temperature fitted in the same way as the spectrum in Fig. 9. The zero-velocity origin is relative to the source.

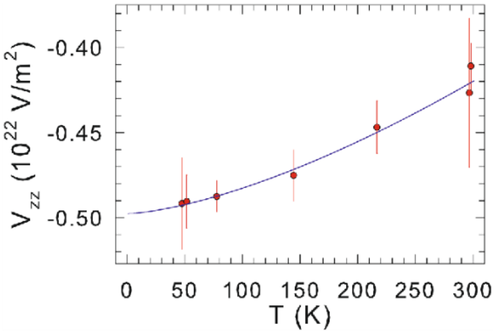

Fig. 11. Temperature dependence of the principal component of the electric field gradient tensor V_{zz} at ^{151}Eu nuclei derived from the fits of the spectra in Figs. 9 and 10. The solid line is the fit to Eq. (4), as explained in the text.

$$H(qx) = \sum_{i=1}^{n} h_{2i-1} \sin[(2i-1)qx], \tag{1}$$

where h_{2i-1} denotes the amplitude of the (2i-1) th harmonic and n is the maximum number of harmonics. One fits then an experimental Mössbauer spectrum with a finite number of six-line Zeeman patterns corresponding to H values that are calculated from Eq. (1) for individual qx values from the range $(0, 2\pi)$. The amplitudes h_{2i-1} obtained from the fit are used to calculate the resulting distribution $P(H)$. They can also be used to calculate the root-mean-square value of H, $H_{rms} = \sqrt{\frac{1}{2}\sum_{i=1}^{n} h_{2i-1}^2}$, which is proportional to the magnetic moment μ_{Fe} carried by the Fe atoms. The knowledge of the $P(H)$ distribution allows one to calculate the average hyperfine magnetic field $H_{av} \equiv <|H|>$.

The ^{57}Fe Mössbauer spectrum in Fig. 4(a) was fitted with two components. The first, large spectral area, SDW component originates from $EuFeAs_2$. The second, small spectral area, quadrupole doublet component arises from the $FeAs_2$ impurity. Because the spectrum of a tiny amount of Fe present in the two Al foils of the absorber and the two cryostat mylar windows in the form of two single lines (Figs. 1 and 2) completely overlaps with the central portion of the experimental spectrum in Fig. 4(a), it was not possible to include it in the fit. A good fit of the Mössbauer spectrum in Fig. 4(a) was obtained with $n = 4$ harmonics. The resulting shape of the SDW and corresponding distribution $P(H)$ are shown in Figs. 4(b) and 4(c), respectively. The parameters obtained from the fit are: the centre shift [10] $\delta = 0.552(1)$ mm/s, the quadrupole shift [10] $\varepsilon = 0.027(1)$ mm/s, $H_{max} = 56.5(1)$ kOe, $H_{av} = 46.1(1)$ kOe, and $H_{rms} = 47.3(3)$ kOe.

The ^{57}Fe Mössbauer spectra of $EuFeAs_2$ at other temperatures below T_N (Fig. 5) were fitted in like manner as the 47.7 K spectrum (Fig. 4).

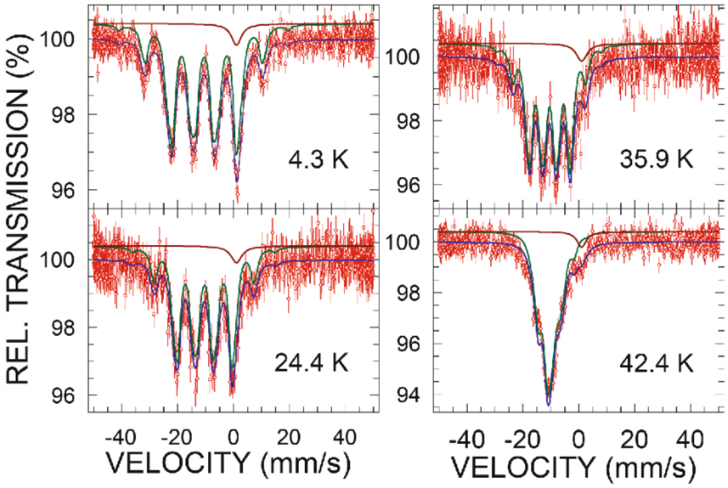

Fig. 12. ^{151}Eu Mössbauer spectrum of $EuFeAs_2$ at the indicated temperatures fitted (solid blue lines) with a large spectral area Zeeman pattern due to $EuFeAs_2$ (solid dark green lines) and a small spectral area single line originating from an impurity phase (solid dark red lines), as described in the text. The zero-velocity origin is relative to the source. (For interpretation of the references to colour in this figure legend, the reader is referred to the web version of this article.)

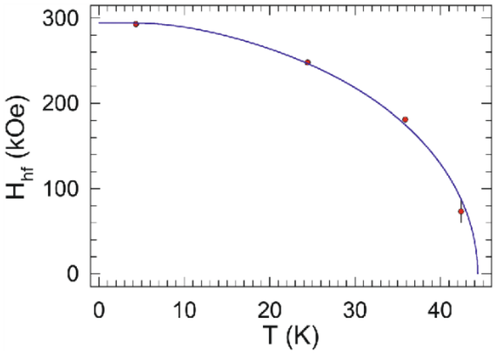

Fig. 13. Temperature dependence of the hyperfine magnetic field H_{hf} at ^{151}Eu nuclei obtained from the fits of the spectra in Fig. 12. The solid line is the fit to Eq. (5), as explained in the text.

One observes that the shape of the SDW (Figs. 4 and 5) changes from the nearly rectangular one at low temperatures to the nearly triangular one at high temperatures (close to T_N).

One could wonder why the spectrum at 103.6 K (Fig. 5), which visually looks the same as the paramagnetic spectrum at 110.6 K (Fig. 2), is fitted with a SDW component. A comparison of these two spectra [Fig. 6(a)] reveals two differences. The width and the relative transmission of the 103.3 K spectrum are larger than the corresponding width and the relative transmission of the 110.6 K spectrum. Such differences are not observed between the neighboring 123.9 and 110.6 K paramagnetic spectra [Fig. 6(b)]. This proves that the 103.3 K spectrum must be due to a magnetically ordered component. Fig. 6(a) also indicates that T_N of the Fe sublattice must be between 103.3 and

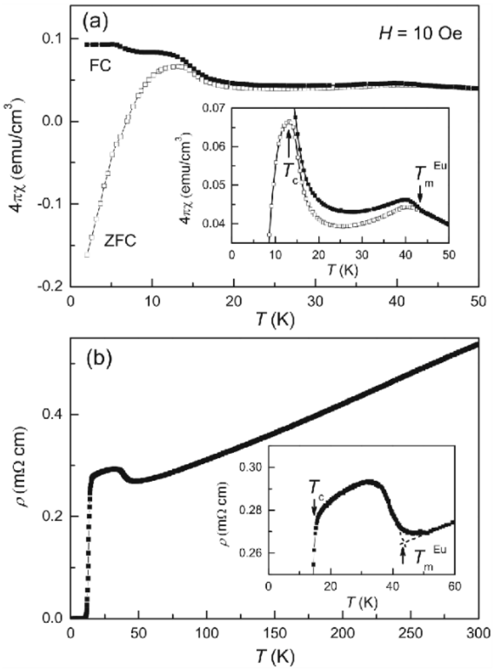

Fig. 14. Temperature dependence of the ZFC and FC magnetic susceptibility (a) and the electrical resistivity (b) of $EuFe_{0.97}Ni_{0.03}As_2$. The insets show the ordinate magnifications around the T_c and T_m^{Eu} temperatures.

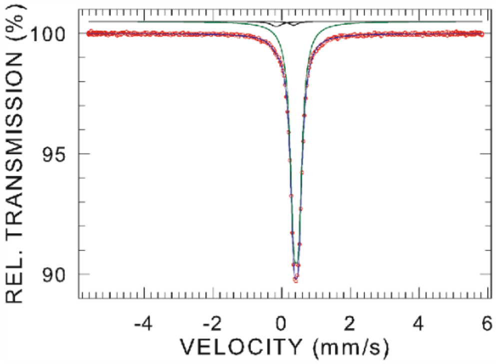

Fig. 15. High-statistics, ^{57}Fe Mössbauer spectrum of $EuFe_{0.97}Ni_{0.03}As_2$ at 298.9 K measured over a broad velocity range and fitted (solid blue line) with a large spectral area quadrupole doublet (solid dark green line) due to $EuFe_{0.97}Ni_{0.03}As_2$ and two small spectral area single lines (solid black lines) which simulate the spectrum due to the presence of a tiny amount of Fe in the two Al foils of the absorber and in the two cryostat mylar windows, as described in the text. The zero-velocity origin is relative to α-Fe at room temperature. (For interpretation of the references to colour in this figure legend, the reader is referred to the web version of this article.)

110.6 K.

The temperature dependence of the H_{av} values, that were calculated from the distributions $P(H)$ shown in Figs. 4 and 5, is displayed in Fig. 7. The expected increase of H_{av} with decreasing temperature is observed. Fitting the H_{av} data to the power law over the limited temperature range yields the value of H_{av} at 0 K, $H_{av}(0) = 47.6(9)$ kOe, and $T_N = 106.2(1.9)$ K. The value of T_N found here is comparable to the value of ~110 K estimated from the resistivity and magnetic susceptibility data [1,4].

By extrapolating the $H_{rms}(T)$ data (Fig. 5) to 0 K, the value of H_{rms} at 0 K, $H_{rms}(0)$, was found to be 49.4(4) kOe. The hyperfine magnetic field is approximately proportional to the Fe magnetic moment through the relation $H = a\mu_{Fe}$. The value of the proportionality constant a depends on a compound [10,13]. We used $a = 63$ kOe/μ_B (Ref. [9]) to convert $H_{rms}(0)$ to $\mu_{Fe}(0)$. Thus, $H_{rms}(0) = 49.4(4)$ kOe corresponds to $\mu_{Fe}(0) = 0.78(1)\mu_B$.

The temperature dependence of the centre shift [10] $\delta(T)$ of $EuFeAs_2$, obtained from the fits of the spectra in Figs. 1, 2, 4, and 5, is shown in Fig. 8(a). $\delta(T)$ is the sum of two physical quantities [10]

$$\delta(T) = \delta_0 + \delta_{SOD}(T). \tag{2}$$

The first quantity δ_0 is the intrinsic isomer shift. The second quantity $\delta_{SOD}(T)$ is the second-order Doppler (SOD) shift. The latter can be expressed in terms of the Debye temperature, Θ_D, as

$$\delta_{SOD}(T) = -\frac{9}{2}\frac{k_B T}{Mc}\left(\frac{T}{\Theta_D}\right)^3 \int_0^{\Theta_D/T} \frac{x^3 dx}{e^x - 1}. \tag{3}$$

Here the symbols k_B, M, and c have their usual meaning [10]. The fit of the experimental data in Fig. 8(a) to Eq. (2) yields $\delta_0 = 0.547(2)$ mm/s and $\Theta_D = 355(18)$ K.

A similar fit of the $\delta(T)$ data for the $FeAs_2$ impurity [Fig. 8(b)] gives $\delta_0 = 0.387(3)$ mm/s and $\Theta_D = 594(25)$ K.

The room-temperature ^{151}Eu Mössbauer spectrum of $EuFeAs_2$ measured over the velocity range ∓20 mm/s is shown in Fig. 9. The component with a large spectral area arises from Eu atoms in $EuFeAs_2$ and appears as an unresolved 12-line quadrupole pattern [10,14]. The component with a small spectral area derives from Eu^{3+} ions in an unknown foreign phase and comes out as a single line. The following parameters are obtained from the fit of the spectrum in Fig. 9: the isomer shift [relative to the $^{151}Sm(SmF_3)$ source] $\delta = -10.56(1)$ mm/s, $V_{zz} = -0.411(14) \times 10^{22}$ V/m^2, and $\eta = 0.74(9)$. The value of δ proves that Eu in $EuFeAs_2$ is in the divalent state [10,14].

The ^{151}Eu Mössbauer spectra of $EuFeAs_2$ measured over the velocity range ∓50 mm/s at other temperatures above T_N of the Eu sublattice are shown in Fig. 10. They are fitted analogously as the spectrum in Fig. 9.

Fig. 11 displays the temperature dependence of V_{zz} derived from the fits of the spectra in Figs. 9 and 10. One notices an increase of the magnitude of V_{zz} with decreasing temperature. The empirical $T^{3/2}$ power-law relation

$$V_{zz}(T) = V_{zz}(0)(1 - BT^{3/2}) \tag{4}$$

fits well the $V_{zz}(T)$ data. Here $V_{zz}(0)$ is the value of V_{zz} at 0 K and B is a constant. The fit of the $V_{zz}(T)$ data (Fig. 11) to Eq. (4) gives $V_{zz}(0) = -0.498(5) \times 10^{22}$ V/m^2 and $B = 3.01(18) \times 10^{-5}$ K$^{-3/2}$. It should be noted here that a similar $T^{3/2}$ dependence of $V_{zz}(T)$ has been observed in other Eu-containing compounds, such as $EuPdGe_3$ [15], $CsEuFe_4As_4$ [11], and $RbEuFe_4As_4$ [16]. Such a $T^{3/2}$ dependence of V_{zz} at ^{57}Fe nuclei has also been observed in hundreds of Fe-containing metallic compounds [16]. Its origin still remains elusive [17].

Fig. 12 displays the ^{151}Eu Mössbauer spectra of $EuFeAs_2$ measured at temperatures below T_N of the Eu sublattice. They are fitted with a Zeeman pattern component of a large spectral area which is due to $EuFeAs_2$, and a single line component of a small spectral area which arises from an unknown Eu^{3+}-containing impurity phase.

The temperature dependence of the hyperfine magnetic field H_{hf} obtained from the fits to the Mössbauer spectra in Fig. 12 is shown in Fig. 13. Within the molecular field model, it is assumed that H_{hf} in a magnetically ordered compound is proportional to the sublattice magnetization. Thus, the $H_{hf}(T)$ dependence can be written as

$$H_{hf}(T) = H_{hf}(0)B_J(x). \tag{5}$$

Here $H_{hf}(0)$ represents the saturation hyperfine magnetic field (the field at 0 K), $B_J(x)$ is the Brillouin function [18]

$$B_J(x) = \frac{2J+1}{2J}\coth\left(\frac{2J+1}{2J}x\right) - \frac{1}{2J}\coth\left(\frac{x}{2J}\right) \tag{6}$$

and

$$x = \frac{3J}{J+1}\frac{H_{hf}(T)}{H_{hf}(0)}\frac{T_N}{T}. \tag{7}$$

The fit of the $H_{hf}(T)$ data (Fig. 13) to Eq. (5) with $J = S = 7/2$ gives $H_{hf}(0) = 294.2(7)$ kOe and $T_N = 44.4(5)$ K. For ^{151}Eu Mössbauer spectroscopy [14,19], there is no simple relation between $H_{hf}(0)$ and the saturation magnetic moment of the Eu atoms, $\mu_{Eu}(0)$. Consequently, one thus cannot determine reliably $\mu_{Eu}(0)$ from $H_{hf}(0)$.

The ^{57}Fe and ^{151}Eu Mössbauer data presented above show that in $EuFeAs_2$, the Fe sublattice orders in the incommensurate SDW fashion with $T_N = 106.2(1.9)$ K and $\mu_{Fe}(0) = 0.78(1)\mu_B$, whereas the Eu sublattice is magnetically ordered below $T_N = 44.4(5)$ K and with $H_{hf}(0) = 294.2(7)$ kOe.

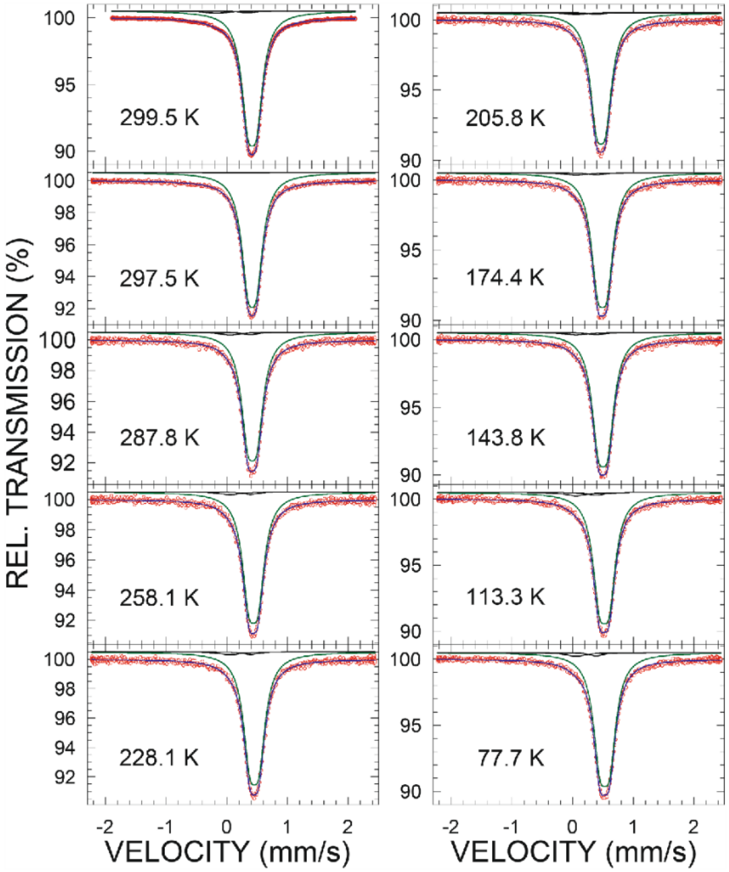

Fig. 16. ^{57}Fe Mössbauer spectra of $EuFe_{0.97}Ni_{0.03}As_2$ at temperatures above T_N of the Fe sublattice fitted in the same way as the spectrum in Fig. 15. The zero-velocity origin is relative to α-Fe at room temperature.

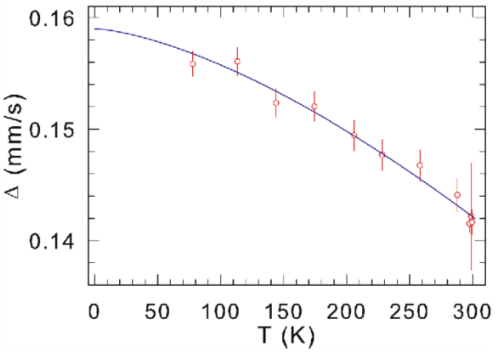

Fig. 17. Temperature dependence of the ^{57}Fe quadrupole splitting Δ of $EuFe_{0.97}Ni_{0.03}As_2$ obtained from the fits of the spectra in Figs. 15 and 16. The solid line is the fit to the $T^{3/2}$ power-law relation, as explained in the text.

3.2. *$EuFe_{0.97}Ni_{0.03}As_2$ superconductor*

The temperature dependence of the zero-field-cooled (ZFC) and field-cooled (FC) magnetic susceptibility χ of $EuFe_{0.97}Ni_{0.03}As_2$ measured in an applied field of 10 Oe is shown in Fig. 14(a). The bifurcation of the ZFC and FC χ data occurs at about 14 K. The diamagnetic ZFC χ decreases with decreasing temperature and this proves that the compound studied is a superconductor. The anomaly of the χ data at the temperature T_m^{Eu} of about 43 K may be possibly associated with the magnetic transition of the Eu sublattice. The temperature dependence of the resistivity ρ of $EuFe_{0.97}Ni_{0.03}As_2$ [Fig. 14(b)] indicates that $T_c = 13.8$ K. The anomaly at T_m^{Eu} probably results from the magnetic ordering of the Eu sublattice.

Fig. 15 shows the high-statistics, room-temperature ^{57}Fe Mössbauer spectrum of $EuFe_{0.97}Ni_{0.03}As_2$ measured over a large velocity range. The absence of any Zeeman pattern shows that the specimen studied is free of any Fe-containing magnetic impurity. In contrast to a similar spectrum of $EuFeAs_2$ (Fig. 1), no contribution originating from the

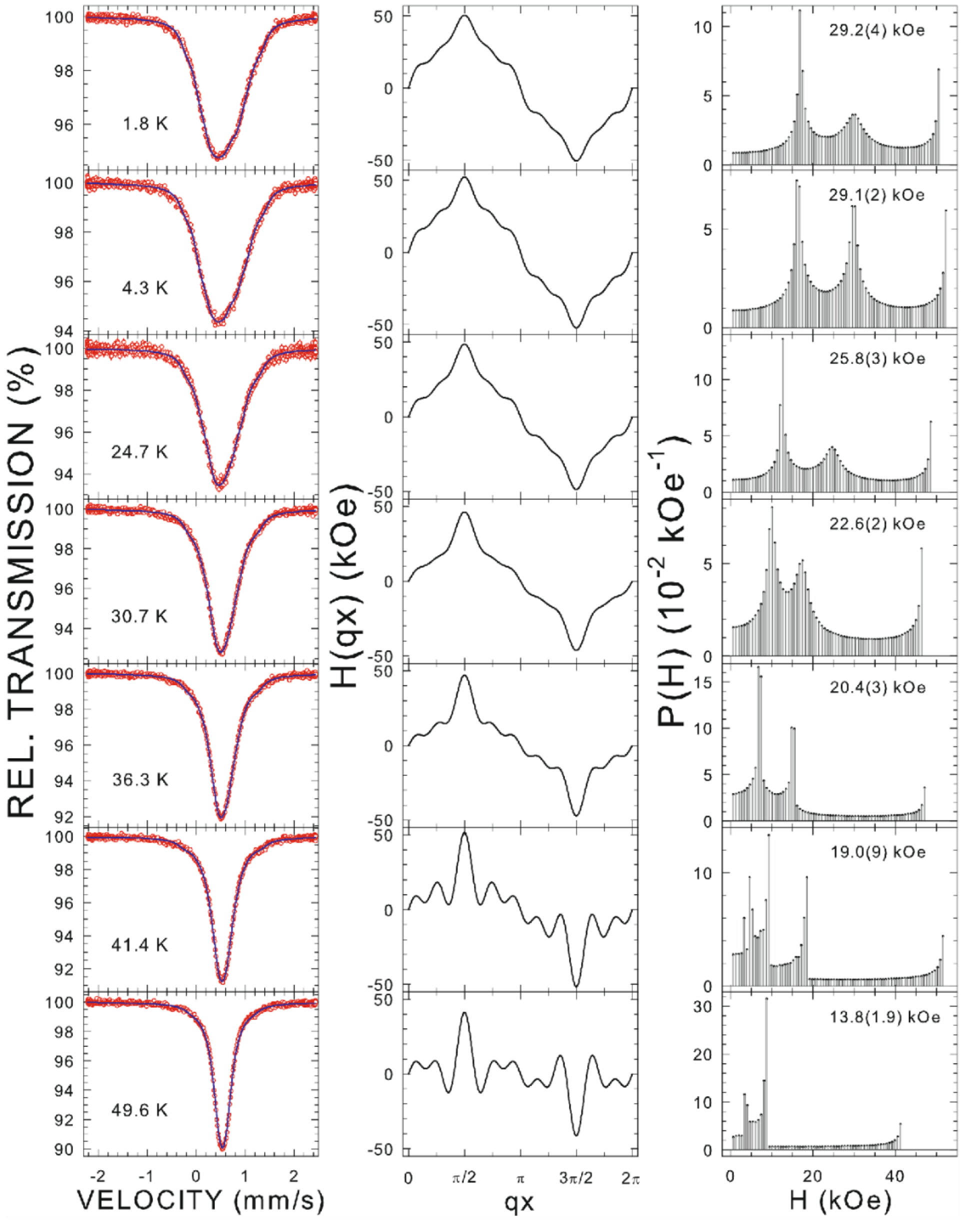

Fig. 18. ^{57}Fe Mössbauer spectra of $EuFe_{0.97}Ni_{0.03}As_2$ at the indicated temperatures fitted (solid blue line) with an incommensurate modulation of the hyperfine magnetic field pattern (left panel), corresponding shapes of the SDW (middle panel), and resulting hyperfine magnetic field distributions labeled with the corresponding root-mean-square value of the hyperfine magnetic field (right panel).

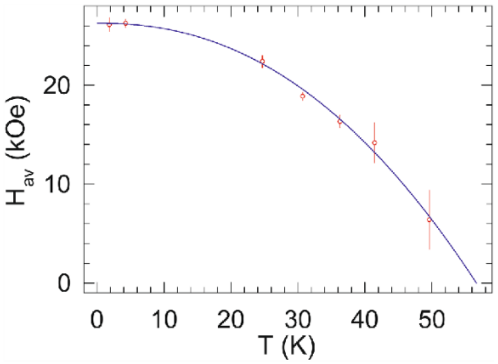

Fig. 19. Temperature dependence of H_{av} at ^{57}Fe nuclei obtained from the distributions $P(H)$ in Fig. 18. The solid line is the power-law fit.

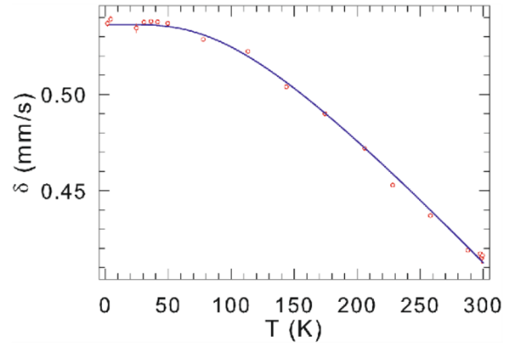

Fig. 20. Temperature dependence of the ^{57}Fe center shift δ of $EuFe_{0.97}Ni_{0.03}As_2$. The solid line is the fit to Eq. (2), as explained in the text.

$FeAs_2$ impurity can be detected (Fig. 15), in agreement with the X-ray diffraction results [4,5]. The only external contribution in the form of two single lines comes from a tiny amount of Fe present in the two Al foils of the absorber and the two cryostat mylar windows.

The ^{57}Fe Mössbauer spectra of $EuFe_{0.97}Ni_{0.03}As_2$ measured at temperatures above T_N of the Fe sublattice, and over a small velocity range, are shown in Fig. 16. They are fitted well with two components in the same way as the spectrum in Fig. 15.

Fig. 17 displays the temperature dependence of Δ of $EuFe_{0.97}Ni_{0.03}As_2$ derived from the fits of the spectra in Figs. 15,16. Analogously to the $V_{zz}(T)$ dependence in Fig. 11, one observes that Δ increases with decreasing temperature. The fit of the $\Delta(T)$ data to the same empirical $T^{3/2}$ power-law relation [(Eq. (4)], in which $V_{zz}(T)$ is substituted by $\Delta(T)$ and $V_{zz}(0)$ by $\Delta(0)$, yields $\Delta(0) = 0.1590(17)$ mm/s and $B = 20.4(2.6) \times 10^{-6}$ $K^{-3/2}$. The value of B determined here is close to that observed for other crystalline, quasicrystalline, and amorphous compounds [16].

The ^{57}Fe Mössbauer spectra of $EuFe_{0.97}Ni_{0.03}As_2$ at temperatures below T_N of the Fe sublattice are shown in Fig. 18. They were fitted with an incommensurate SDW pattern. No two-single line component, originating from a tiny amount of Fe present in the two Al foils of the absorber and the two cryostat mylar windows, could be included in the fit for the same reason as that given for the fits of the spectra in Figs. 4 and 5 (*vide supra*).

The values of H_{av} that were calculated from the distributions $P(H)$ in Fig. 18 are shown in Fig. 19. The fit of the H_{av} data to the power law (Fig. 19) gives $H_{av}(0) = 26.3(8)$ kOe and $T_N = 56.6(2.4)$ K. Extrapolating the $H_{rms}(T)$ data (Fig. 18) to 0 K gives $H_{rms}(0) = 29.5(4)$ kOe. This value of $H_{rms}(0)$ corresponds to $\mu_{Fe}(0) = 0.47(1)\mu_B$.

Implicit in the above analysis is the assumption that the hyperfine magnetic field at the ^{57}Fe nuclei in $EuFe_{0.97}Ni_{0.03}As_2$ is an intrinsic one, that is, it results from the non-zero magnetic moment carried by the Fe atoms. However, one should also consider the possibility that the Fe atoms carry no magnetic moment and that the observed hyperfine magnetic field is due only to the transferred hyperfine magnetic field, H_{tr} [20], from the magnetically ordered Eu sublattice (*vide infra*). Experimentally, the value of H_{tr} at 0 K in superconductors containing Fe and Eu atoms was found to be below 10 kOe [11,16,21]. The value of $H_{rms}(0)$ found here is significantly larger than 10 kOe. It, therefore, appears that the observed hyperfine magnetic field in $EuFe_{0.97}Ni_{0.03}As_2$ is due to the non-zero Fe magnetic moment rather than to the transferred hyperfine magnetic field.

Fig. 20 presents the temperature dependence of $\delta(T)$ derived from the fits of the spectra in Figs. 15,16,18. The fit of the $\delta(T)$ data to Eq. (2) yields $\delta_0 = 0.536(2)$ mm/s and $\Theta_D = 428(14)$ K.

The ^{151}Eu Mössbauer spectra of $EuFe_{0.97}Ni_{0.03}As_2$ measured at temperatures above T_N of the Eu sublattice are displayed in Fig. 21. They are fitted in like manner as the spectra in Fig. 10. The values of V_{zz} obtained from the fits of the spectra in Fig. 21 are plotted in Fig. 22. One observes that the magnitude of V_{zz} increases with decreasing temperature. The fit of the $V_{zz}(T)$ data (Fig. 22) to Eq. (4) yields $V_{zz}(0) = -0.448(5) \times 10^{22}$ V/m^2 and $B = 3.28(29) \times 10^{-5}$ $K^{-3/2}$.

Fig. 23 shows the ^{151}Eu Mössbauer spectra of $EuFe_{0.97}Ni_{0.03}As_2$ measured at temperatures below T_N of the Eu sublattice. They are fitted with a Zeeman pattern component of a large spectral area that derives from $EuFe_{0.97}Ni_{0.03}As_2$ and a single line component of a small spectral area that originates from a Eu^{3+}-containing an unknown impurity.

Fig. 24 displays the temperature dependence of H_{hf} determined from the fits to the Mössbauer spectra in Fig. 23. The fit of the $H_{hf}(T)$ dependence to Eq. (5) with $J = S = 7/2$ yields $H_{hf}(0) = 290.5(1)$ kOe and $T_N = 43.5(1)$ K.

The analysis of the ^{57}Fe and ^{151}Eu Mössbauer spectra of $EuFe_{0.97}Ni_{0.03}As_2$ presented above shows that, similarly as in $EuFeAs_2$, the Fe sublattice orders in the incommensurate SDW fashion, but with a significantly smaller values of $T_N = 56.6(2.4)$ K and of $\mu_{Fe}(0) = 0.47(1)\mu_B$. On the other hand, the Eu sublattice in $EuFe_{0.97}Ni_{0.03}As_2$ is magnetically ordered below marginally lower $T_N = 43.5(1)$ K and with slightly lower $H_{hf}(0) = 290.5(1)$ kOe as compared to the corresponding values for $EuFeAs_2$. One can thus conclude that a 3% substitution of Fe by Ni in $EuFeAs_2$ dramatically reduces the magnetism of the Fe sublattice, but has virtually no effect on the magnetism of the Eu sublattice. The presence of the Fe and Eu antiferromagnetic order in $EuFe_{0.97}Ni_{0.03}As_2$ proves that superconductivity and antiferromagnetism coexist in this compound.

4. Conclusions

We describe the results of ^{57}Fe and ^{151}Eu Mössbauer spectroscopy measurements in the temperature range 1.8–299.5 K of $EuFeAs_2$ and the 14 K the superconductor $EuFe_{0.97}Ni_{0.03}As_2$. We find that in both

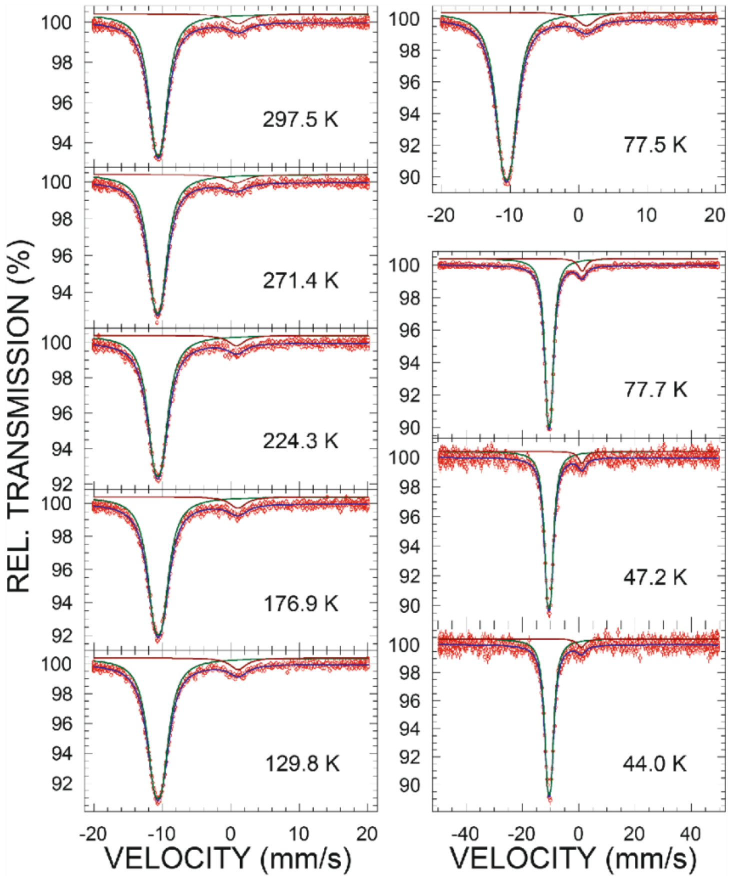

Fig. 21. ^{151}Eu Mössbauer spectra of $EuFe_{0.97}Ni_{0.03}As_2$ at the indicated temperature fitted in the same way as the spectra in Fig. 10. The zero-velocity origin is relative to the source.

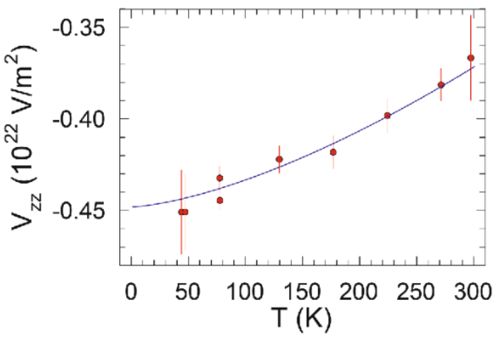

Fig. 22. Temperature dependence of the principal component of the electric field gradient tensor V_{zz} at ^{151}Eu nuclei determined from the fits of the spectra in Fig. 21. The solid line is the fit to Eq. (4), as explained in the text.

compounds the antiferromagnetic ordering of the Fe sublattice is of a spin-density-wave type with the Néel temperatures and Fe saturation magnetic moments of 106.2(1.9) K, 0.78(1)μ_B and 56.6(2.2) K, 0.47(1)μ_B, respectively. We demonstrate that the Néel temperatures and the saturation hyperfine magnetic fields of the antiferromagnetically ordered Eu sublattice in both compounds are, respectively, 44.4(5) K, 294.2(7) kOe, and 43.5(1) K, 290.5(1) kOe. These findings show that a minimal substitution of Fe by Ni in $EuFeAs_2$, apart from inducing superconductivity in $EuFe_{0.97}Ni_{0.03}As_2$, dramatically diminishes the strength of the magnetism of the Fe sublattice and has virtually no effect on the magnetism of the Eu sublattice. The presence of antiferromagnetically ordered Fe and Eu sublattices in $EuFe_{0.97}Ni_{0.03}As_2$ proves that superconductivity and magnetism coexist in this compound. We observe that the increase of the magnitude of the main component of the electric field gradient tensor, at both Fe and Eu sites, with decreasing temperature is explained by a $T^{3/2}$ power-law relation. We determine the Debye temperatures of $EuFeAs_2$, $EuFe_{0.97}Ni_{0.03}As_2$, and the $FeAs_2$ impurity phase to be 355(18), 428(14), and 594(25) K, respectively.

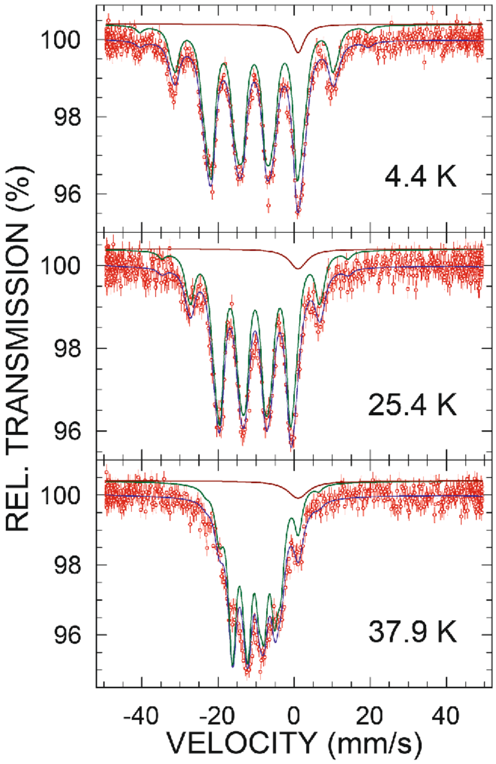

Fig. 23. ^{151}Eu Mössbauer spectra of $EuFe_{0.97}Ni_{0.03}As_2$ at the indicated temperatures fitted in the same way as the spectra in Fig. 12. The zero-velocity origin is relative to the source.

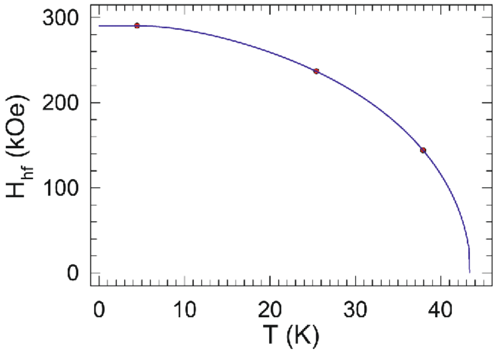

Fig. 24. Temperature dependence of the hyperfine magnetic field H_{hf} at ^{151}Eu nuclei determined from the fits of the spectra in Fig. 23. The solid line is the fit to Eq. (5), as explained in the text.

Author statement

Authors contributed equally to this work.

Declaration of Competing Interest

The authors declare that they have no known competing financial interests or personal relationships that could have appeared to influence the work reported in this paper.

Acknowledgments

This work was supported by the Natural Sciences and Engineering Research Council of Canada and the National Key Research and Development Program of China (Grant No. 2016YFA0300202).

References

[1] J. Yu, T. Liu, B.-J. Pan, B.-B. Ruan, X.-C. Wang, Q.-G. Mu, K. Zhao, G.-F. Chen, Z.-A. Ren, Sci. Bull. 62 (2017) 218.
[2] H. Yakita, H. Ogino, T. Okada, A. Yamamoto, K. Kishio, T. Tohei, Y. Ikuhara, Y. Gotoh, H. Fujihisa, K. Kataoka, H. Eisaki, J. Shimoyama, J. Am. Chem. Soc. 136 (2014) 846.
[3] J. Yu, T. Liu, K. Zhao, B.-J. Pan, Q.-G. Mu, B.-B. Ruan, Z.-A. Ren, Acta Phys. Sin. 67 (2018) 207403.
[4] Y.-B. Liu, Y. Liu, W.-H. Jiao, Z. Ren, G.-H. Cao, Sci. China-Phys. Mech. Astron. 61 (2018) 127405.
[5] G.-H. Cao (private communication).
[6] R. Street, B.C. Munday, B. Window, I.R. Williams, J. Appl. Phys. 39 (1968) 1050.
[7] J. Cieślak, S.M. Dubiel, Nucl. Instrum. Meth. Phys. Res. B 95 (1995) 131 and references therein.
[8] P. Bonville, F. Rullier-Albenque, D. Colson, A. Forget, EPL 89 (2010) 67008.
[9] P. Wang, Z.M. Stadnik, J. Żukrowski, A. Thaler, S.L. Bud'ko, P.C. Canfield, Phys. Rev. B 84 (2011) 024509.
[10] N.N. Greenwood, T.C. Gibb, Mössbauer Spectroscopy, Mössbauer Spectroscopy and Transition Metal Chemistry, Springer, Berlin, 2011.
[11] M.A. Albedah, F. Nejadsattari, Z.M. Stadnik, Y. Liu, G.-H. Cao, J. Phys.: Condens. Matter 30 (2018) 155803.
[12] P. Imbert, A. Gérard, and M. Wintenberger, CR Acad. Sci. (France) 256 (1963) 439; M. Yuzuri, R. Tahara, and Y. Nakamura, J. Phys. Soc. Jpn. 48 (1980) 1937.
[13] P. Panissod, J. Durand, J.I. Budnik, Nucl. Instrum. Meth. 199 (1982) 99; P. Panissod, Hyperfine Interact. 24-26 (1985) 607; O. Eriksson, A. Svane, J. Phys.: Condens. Matter 1 (1989) 1589; S.M. Dubiel, J. Alloys Compd. 488 (2009) 18.
[14] F. Grandjean, G.L. Long, in: G.J. Long, F. Grandjean (Eds.), Mössbauer Spectroscopy Applied to Inorganic Chemistry, Plenum, New York, 1989, vol. 3, p. 513.
[15] M.A. Albedah, K. Al-Qadi, Z.M. Stadnik, J. Przewoźnik, J. Alloys Compd. 613 (2014) 344.
[16] M.A. Albedah, F. Nejadsattari, Z.M. Stadnik, Y. Liu, G.-H. Cao, Phys. Rev. B 97 (2018) 144426 and references therein.
[17] D. Torumba, K. Parlinski, M. Rots, S. Cottenier, Phys. Rev. B 74 (2006) 144306.
[18] N.W. Ashcroft, N.D. Mermin, Solid State Physics, Saunders, Philadelphia, 1976.
[19] I. Nowik, B.D. Dunlap, J.H. Wernick, Phys. Rev. B 8 (1973) 238.
[20] W. Zinn, J. de Physique, Colloque, 32 (1971) C1-724; Ch. Sauer, U. Köbler, W. Zinn, G.M. Kalvius, J. de Physique, Colloque, 35 (1974) C6-269; G. Czjzek, V. Oestreich, H. Schmidt, K. Łątka, K. Tomala, J. Magn. Magn. Mater. 42 (1989) 79; I. Nowik, Y. Levi, I. Felner, E.R. Bauminger, J. Magn. Magn. Mater. 147 (1995) 373.
[21] I. Nowik, I. Felner, Z. Ren, G.H. Cao, Z.A. Xu, J. Phys.: Condens. Matter 23 (2011) 065701.

Chapter 8: Electronic structure and magnetism of CsEuFe4As4

Journal of Physics and Chemistry of Solids 136 (2020) 109137

Contents lists available at ScienceDirect

Journal of Physics and Chemistry of Solids

journal homepage: www.elsevier.com/locate/jpcs

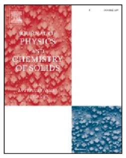

Electronic structure and magnetism of the 35 K superconductor $CsEuFe_4As_4$

Farshad Nejadsattari[a], Mohammed A. Albedah[a,b], Zbigniew M. Stadnik[a,*]

[a] *Department of Physics, University of Ottawa, Ottawa, Ontario, K1N 6N5, Canada*
[b] *Department of Physics, Majmaah University, P.O. Box 1712, Zulfi, Saudi Arabia*

A R T I C L E I N F O

Keywords:
Density of states
Energy band structure
Magnetic moment
Hyperfine interaction

A B S T R A C T

The results of *ab-initio* calculations of the electronic structure and magnetism of the new 35 K superconductor $CsEuFe_4As_4$ are reported. The electronic band structure and the density of states are presented and discussed in detail. The origin of the chemical bonding between the constituent atoms is discussed in detail. The evidence is provided for the existence of a mixture of ionic, covalent, and metallic bonding. It is demonstrated that the magnetic moment is mainly due to the strongly localized Eu *f* states. No spin polarization at the Fe sites is found. It is demonstrated that the electrical conductivity in $CsEuFe_4As_4$ originates from the Fe contribution to the density of states. The electrical and chemical properties of the studied compound are closely linked with the presence of the Fe *d* states in the Fermi energy region. The Fermi surfaces show the presence of the hole-like and electron-like pockets, respectively, at the center and corners of the Brillouin zone. The results of the calculations of the ^{57}Fe and ^{151}Eu hyperfine-interaction parameters are also presented.

1. Introduction

The discovery of a new Fe-based class of superconductors $AeAFe_4As_4$ (Ae= Ca, Sr, Eu and A= K, Rb, Cs) with the critical temperature T_c in the range 31.6–36.8 K [1–4] is significant for two reasons. First, in contrast to the intensively studied solid solutions of $(Ba_{1-x}K_x)Fe_2As_2$ or $(Sr_{1-x}Na_x)Fe_2As_2$, the *Ae* and *A* atoms in $AeAFe_4As_4$ are located at the crystallographically inequivalent positions, which causes the change of the space group from *I*4/*mmm* characteristic for solid-solution superconductors to *P*4/*mmm*. In these new superconductors, the *Ae* and *A* layers are alternately stacked along the crystallographic *c*-axis between the Fe_2As_2 slabs. Consequently, the absence of structural disorder in $AeAFe_4As_4$ allows for the investigations of their intrinsic physical properties that are not hindered by the structural disorder present in solid-solution superconductors. Second, the presence of the Eu and Fe atoms, which potentially can order magnetically, points toward the possibility of the coexistence of two, generally incompatible phenomena, magnetism and superconductivity [5].

The magnetic susceptibility measurements [2,4] indicate that the $CsEuFe_4As_4$ superconductor with T_c= 35.1–35.2 K has a magnetic transition at ~15.0–15.5 K. Such a magnetic transition has also been found in the heat capacity data at 15.2 K [4] and at 15.97 (8) K in the ^{151}Eu Mössbauer data [6]. The isothermal magnetization data made it possible to identify this transition as being ferromagnetic [4]. Ferromagnetism in $CsEuFe_4As_4$ has been hypothesized [4] to be associated only with the Eu magnetic moments, that is, it has been assumed that the Fe atoms have no magnetic moment. These suggestions have been confirmed experimentally in the ^{151}Eu and ^{57}Fe Mössbauer study of $CsEuFe_4As_4$ [6].

The main goal of this work is to elucidate the origin of some of the physical properties of $CsEuFe_4As_4$ via detailed electronic structure calculations. In particular, the formation and type of chemical bonds in this compound and the charge transport properties are studied. The type of chemical interactions between various atoms in $CsEuFe_4As_4$ are similar to those observed in other compounds of the same crystallographic structure [7]. A thorough discussion of the Fermi surface topology allows for the understanding of the electronic characteristics of $CsEuFe_4As_4$. Furthermore, a framework to test and, to some extent, predict the properties of this compound is provided. A comparison is made between the calculated physical quantities and those obtained from the magnetic and Mössbauer spectroscopy measurements.

2. Theoretical method

We performed *ab initio* calculations of the electronic structure and Mössbauer hyperfine-interaction parameters of $CsEuFe_4As_4$ in the context of density functional theory using the full-potential linearized augmented-plane-wave plus local orbitals (FP-LAPW + lo) method that is realized in the WIEN2k package [8]. This method is described thoroughly in Ref. [9]. Here, the valence wave functions in the interstitial

---

[*] Corresponding author.
E-mail address: stadnik@uottawa.ca (Z.M. Stadnik).

https://doi.org/10.1016/j.jpcs.2019.109137
Received 21 May 2019; Received in revised form 20 July 2019; Accepted 5 August 2019
Available online 07 August 2019
0022-3697/ © 2019 Elsevier Ltd. All rights reserved.

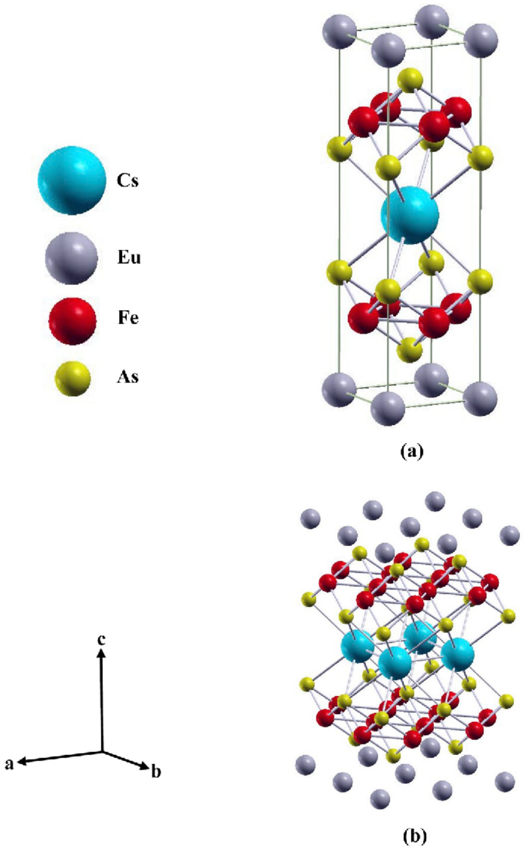

Fig. 1. (Color online) The unit cell (a) and the layered crystal structure (b) of $CsEuFe_4As_4$. (For interpretation of the references to colour in this figure legend, the reader is referred to the Web version of this article.)

region are expanded in spherical harmonics up to $l = 4$, while in the muffin-tin (MT) region they are expanded to a maximum of $l = 10$ harmonics. The values of 2.50, 2.50, 2.30, and 2.19 a.u. were used as the muffin-tin radii for Cs, Eu, Fe, and As, respectively. For the exchange-correlation potential, the generalized gradient approximation (GGA) scheme of Perdew, Burke, and Ernzerhof [10] was used. In addition, effective Hubbard-like interaction energies of 0.52 and 0.15 Ry were used for the Eu 4*f* and Fe 3*d* states, respectively [7,11]. The plane-wave cut-off parameter was set to $R_{MT} \times K_{MAX} = 7.0$, where R_{MT} is the smallest MT radius in the unit cell and K_{MAX} is the maximum K vector used in the plane-wave expansion in the interstitial region. A total number of 680 inequivalent *k*-points was used within a $32 \times 32 \times 9$ *k*-mesh in the irreducible wedge of the first Brillouin zone. The experimental lattice parameters (*a* and *c*) and the atomic position parameters from Ref. [6] were employed in the calculations.

3. Results and discussion

3.1. The crystal structure

Fig. 1 shows the unit cell and the layered crystal structure of $CsEuFe_4As_4$. Various connecting rods represent the interactions between the Cs, Fe, and As atoms. One can notice that the layers of Eu atoms are entirely isolated from the Fe_4As_4 blocks and that the sheets of Cs atoms along the *c*-direction separate the neighboring Fe_4As_4 blocks [6].

The layered structure and the network of the connecting rods [Fig. 1 (b)] point towards the existence of a combination of covalent and ionic bonds (*vide infra*) in the compound studied [6].

3.2. *Ab-initio* Calculations

3.2.1. Valence charge density distributions

The valence charge density distributions along various planes are shown in Fig. 2. The electronic charges of the atoms in $CsEuFe_4As_4$ were obtained through the Bader's analysis scheme [12]. The presence of a combination of ionic, covalent, and metallic bonds between various atoms in $CsEuFe_4As_4$ becomes evident by inspecting Fig. 2 in detail.

As one can notice from the charge density distribution in the (001) plane [Fig. 2(a)], there is the absence of valence charge in the regions between the Eu atoms (red regions). This indicates that the Eu atoms are chemically isolated from each other. Therefore, no chemical bonding is expected to exist between these atoms. This is depicted in Fig. 1 by the lack of connecting rods between the Eu atoms, which supports the argument given above. One also observes [Fig. 2(a)] that the valence electrons of Eu are strongly bound to the parent atom (the yellow, green, and blue rings surrounding each Eu atom). Furthermore, a fourth-fold shape of the half-filled 4*f* shell of Eu is evident [purple regions in Fig. 2(a)].

The valence charge density distribution in the (002) plane is shown in Fig. 2(b). This plane consists of sheets of Cs atoms which separate the neighboring Fe_4As_4 blocks in the *c*-direction. One can see that the charge density distribution around the Cs atoms is perfectly symmetric. In fact, what is shown in this figure is the closed shell structure of the Xe atom, with the *s* electrons of Cs completely transferred from their parent atom to the Fe_4As_4 blocks, in particular, to the As atoms. These electrons participate in the ionic bonding between the Cs sheets and the Fe_4As_4 blocks. The Cs atoms themselves are isolated from each other due to their relatively large separation. Consequently, no metallic interaction is likely to exist between them.

Fig. 2(c) shows the valence charge density distribution in the $z = 0.6726$ plane which consists of the As atoms located at the 2*g* sites. The presence of a very weak directional covalent bonding between the adjacent As atoms can be seen (faint yellow regions). These As atoms are isolated from each other by regions which have virtually no charge density. However, the As atoms located at the 2*h* sites [Fig. 2(d)] are involved in forming stronger covalent bonding with the neighboring Fe atoms [the $z = 0.6726$ plane in Fig. 2(d) passes through the Fe layers]. The valence charge density distribution in this plane indicates that the electronic charge is spread out between the Fe–Fe and Fe–As atoms. The Fe–Fe interactions are realized by forming metallic bonds as the Fe 4*s* electrons are widely spread throughout the Fe layers [green regions in Fig. 2(d)]. The electronic transport in the superconductor studied is expected to occur predominantly within these Fe layers and, to a smaller extent, within the metallic Fe_4As_4 blocks.

The valence charge density distribution in the (110) plane is shown in Fig. 2(e). This plane passes through the Eu and Cs atoms, and also through the As atoms located at the 2*h* sites. The presence of the As–As covalent bonds is clearly visible as the electrons are delocalized between these atoms (green regions). Furthermore, a complete charge transfer from the Cs and Eu atoms to the As layers is evident (red regions indicating the virtual absence of charge). This leads to the formation of two sets of ionic bonds: a strong ionic bond between the alkali Cs layers and the metalloid As layers, and a weaker ionic bond between the layers of the Eu and As atoms. One can interpret this result by considering the differences between the electronegativity of the Cs (0.79) and the Eu (1.2) atoms and that of the As (2.18) atoms. Based on these electronegativity values, the Cs–As bond is expected to be

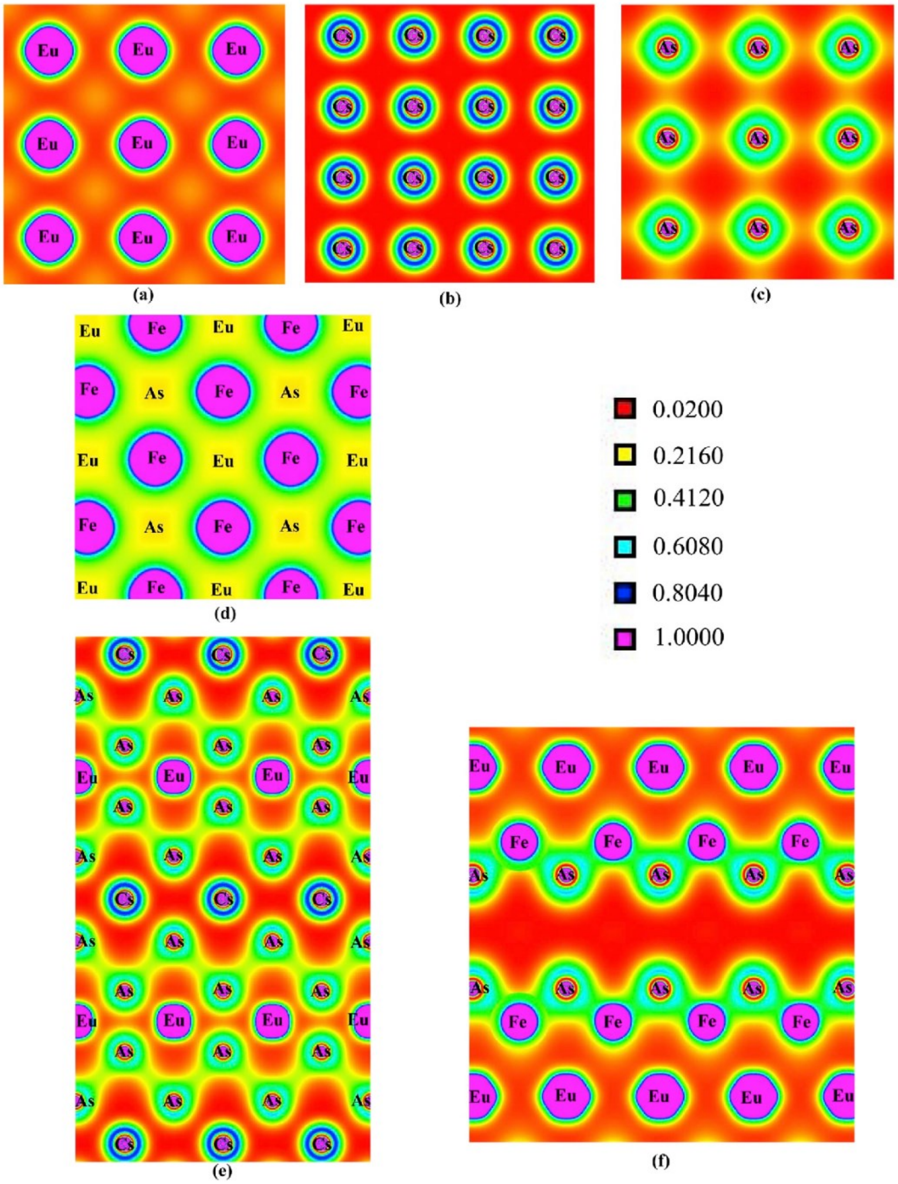

Fig. 2. (Color online) Electron charge density distribution (in units of e/Å^3) along the (001) (a), (002) (b), z = 0.6726 (c), z = 0.7738 (d), (110) (e), and (010) [(100)] (f) planes. (For interpretation of the references to colour in this figure legend, the reader is referred to the Web version of this article.)

stronger than the Eu–As bond. These two sets of ionic bonding are depicted in Fig. 2(e) by two red regions of different intensity. No electronic transport is expected to exist between the separate As layers due to the formation of these ionic bonds. As mentioned earlier, any transport (whether electrical or thermal) must be along the Fe_4As_4 blocks.

If one considers the symmetry of the space group *P4/nmm* and the crystal basis of $CsEuFe_4As_4$, then it becomes clear that the charge density distributions in the (010) and (100) planes are the same [Fig. 2(f)]. These planes pass through the Eu, As at the 2*g* sites, and Fe atoms. A careful inspection of this figure reveals the hexagonal shape of the cross-section of the Eu 4*f* orbitals with these planes. One also notices that the sheets of Eu atoms are separated from each other (the virtual absence of charge density indicated by red regions). The strong covalent As–Fe bonds are visible in the figure via delocalization of the valence states of the As and Fe atoms. This is indicated [Fig. 2(f)] by the

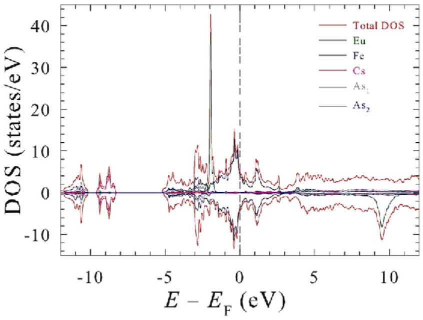

Fig. 3. (Color online) Spin-resolved, total and atom-resolved DOS in ferromagnetic $CsEuFe_4As_4$. (For interpretation of the references to colour in this figure legend, the reader is referred to the Web version of this article.)

presence of a comparatively high charge density (green regions which spread in between the As and Fe atoms).

3.2.2. *Density of states*

In this section, we bring the results of the DFT calculations for the total and partial density of states (DOS) in $CsEuFe_4As_4$. The integration in the *k*-space was done using the modified tetrahedron method [13].

The DOS below -8 eV (Fig. 3) is due to the atomic-like core electrons of Cs and As atoms. As these core states lie deep in energy, they practically do not contribute to any of the physical properties of the compound studied. In fact, the DOS of these states resembles that of isolated atomic states of the Cs and As atoms.

The DOS in the energy region between -5.0 and 2.8 eV, which includes the Fermi energy (E_F), determines most of the physical properties of $CsEuFe_4As_4$. Here the semi-core, valence, and conduction states form a continuum of DOS. A local minimum in the DOS at ~0.7 eV indicates the presence of a pseudogap that is due to a few Fe states. This pseudogap can be attributed to the Coulomb repulsion of the Fe electrons. The energy region between $-$ 1.5 eV and E_F is dominated by the delocalized Fe states. They form a valence band that is responsible for the formation of the metallic bonds between the Fe atoms within the Fe_4As_4 blocks. A sharp peak in the spin-up DOS in the energy region between $-$ 2.0 and $-$ 1.6 eV arises entirely from the localized Eu *f* electrons. The Eu *f* states have minimum overlap with the Fe *d* states. Below the energy region dominated by the Eu *f* states (between $-$ 3.1 and $-$ 2.1 eV), one observes contributions from the As and Fe atoms. The overlap between the As and Fe states in this region is indicative of covalent bonding between the As and Fe atoms. This covalent bonding is the result of the hybridization between the Fe *d* states with those of the As *p* states.

A characteristic feature of the DOS in Fig. 3 is that, in contrast to the energy separation and magnitude difference between the Eu spin-up and spin-down states, the spin-up and spin-down DOS contributions from the other atoms is symmetric. This results in almost negligible magnetic moments of the Cs, Fe, and As atoms (*vide infra*). As a consequence of the high asymmetry observed in the Eu DOS from its two spin components, a large magnetic moment of the Eu atoms is expected.

The near Fermi energy region is dominated by the Fe *d* states and, to a far less extent, by the As *p* states. These states are ultimately responsible for the conductive nature of $CsEuFe_4As_4$. There is almost zero DOS contribution from the Eu and Cs atoms in the Fermi energy region. This suggests that the conductivity in $CsEuFe_4As_4$ must be confined to the Fe–As layers, and thus is anisotropic.

Fig. 4(a) displays the spin-resolved DOS due to the Cs atoms. The symmetry of the spin-up and spin-down states is evident. Consequently, one expects no magnetic moment for the Cs atoms in $CsEuFe_4As_4$. One also observes that there is virtually no Cs contribution to DOS in the Fermi energy region. The core states of Cs are of the *p* character, and their DOS has three peaks at $-$ 9.4, $-$ 8.7, and $-$ 8.5 eV in the energy region between $-$ 9.8 and $-$ 8.3 eV. The much smaller DOS due to the core Cs *p* states is also in the other energy region between $-$ 11.5 and $-$ 8.5 eV.

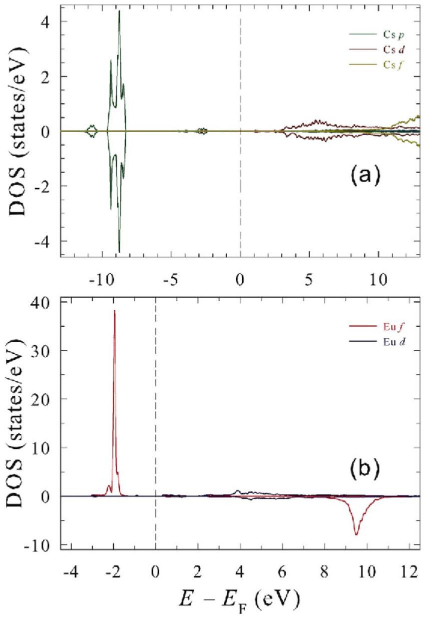

Fig. 4. (Color online) Spin-resolved DOS of the Cs (a) and Eu (b) atoms in ferromagnetic $CsEuFe_4As_4$. (For interpretation of the references to colour in this figure legend, the reader is referred to the Web version of this article.)

A highly localized DOS due to the Eu *f* states, as opposed to the extended one due to the Eu *d* states, can be seen in Fig. 4(b). The contribution to DOS from the Eu *d* states is minimal and symmetric for both spin orientations, whereas that from the Eu *f* is very large and asymmetric. The majority spin contribution is from the sharp *f* up states of Eu that are localized between $-$ 2.4 and $-$ 1.5 eV. On the other hand, the minority *f* down states of Eu lie in a relatively high-energy region (between 8.6 and 10.5 eV). Under normal conditions, these states are empty as no electron can have enough energy to occupy them. This significant difference in the population of the two spin configurations accounts for a large magnetic moment found experimentally in $CsEuFe_4As_4$ [4]. The majority of the Eu *d* states also lie above E_F. Though few, they are widely spread between 3.2 and 8.5 eV.

One observes an overlap between the Fe *s* and *p* states 3.2 eV [Fig. 5(a)]. Below E_F, these states are fairly separated with several peaks in the DOS. A small contribution of the Fe core states to the DOS is in the energy region between $-$ 12 and $-$ 10 eV. One notices that the Fermi energy region is almost empty of the Fe *s* and *p* states.

As mentioned earlier, the most significant contribution to the Fe DOS originates from the *d* orbitals. Fig. 5(b) displays the individual *d*-orbital-resolved contributions to the Fe *d* DOS. It is evident that the large peak in the Fe DOS originates mainly from the $d_{x^2-y^2}$ states located at about eV. These states are mainly localized and exist below E_F. The small peak in the DOS above E_F at about 1.0 eV originates from the d_{xy} and d_{z^2} orbitals. The d_{z^2} states also extend to the region below E_F and they peak at around $-$ 0.5 eV. The majority of the d_{xz} states are located in the vicinity of E_F and contribute to the peak at $-$ 0.15 eV. The conductive nature of $CsEuFe_4As_4$ can be related to these states. The

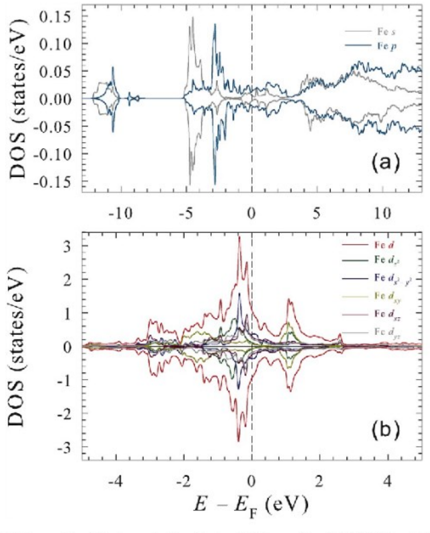

Fig. 5. (Color online) Spin-polarized, Fe orbital-resolved DOS (a) and Fe *d*-orbital-resolved DOS (b). (For interpretation of the references to colour in this figure legend, the reader is referred to the Web version of this article.)

smallest contribution to the Fe *d* DOS is from the d_{yz} states which are non-localized and predominantly spread below E_F into the valence region.

Fig. 6(a) displays the DOS due to the As_1 and As_2 atoms located at two different Wyckoff positions 2g and 2*f*, respectively [6]. One can notice that although the states due to the As_1 and As_2 atoms occupy the same energy region, they are slightly displaced from each other. The As

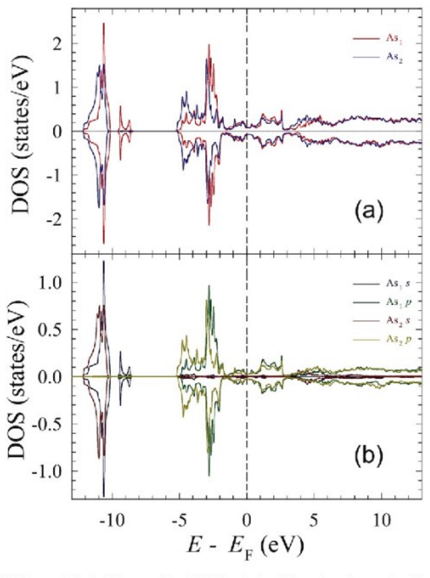

Fig. 6. (Color online) Spin-resolved DOS of As (a) and spin-resolved, orbital-resolved DOS of As. (For interpretation of the references to colour in this figure legend, the reader is referred to the Web version of this article.)

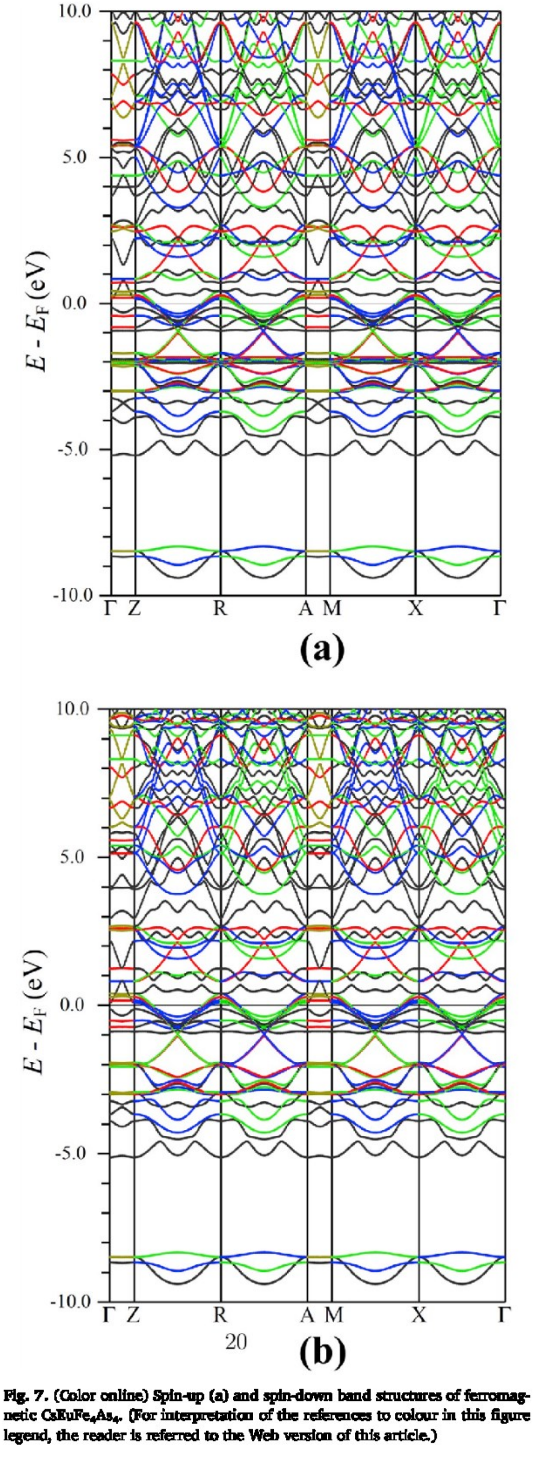

Fig. 7. (Color online) Spin-up (a) and spin-down band structures of ferromagnetic $CsEuFe_4As_4$. (For interpretation of the references to colour in this figure legend, the reader is referred to the Web version of this article.)

core states lying between -12 and -10 eV are localized and are of atomic-like character. The semi-core and valence states span an energy region between -5.0 and -1.6 eV and display sharp peaks in DOS between -3.0 and -2.7 eV. The conduction states extend from E_F to 2.8 eV. Above 2.8 eV, the mainly empty metallic, and perfectly overlapping As_1 and As_2 states are located. As a result of the presence of non-localized and overlapping states, the bonding between the As atoms in the compound studied is covalent.

As one can observe in Fig. 6(b), the core states lying deep in energy consist of *s*-type orbitals whereas the states close to E_F are dominated by the relatively extended *p* states (between -5.2 and -1.7 eV). The As_1 states are slightly more numerous than the As_2 states. The spin-up and spin-down contributions to the DOS from both atoms are almost identical, which yields nearly zero magnetic moments of the two As atoms.

3.2.3. *Energy band structure*

One can observe that for the spin-up configuration [Fig. 7(a)], the energy bands above E_F are greatly dispersive. In the vicinity of E_F, the bands are less dispersive. The bands at -2 eV are very dense and flattened. They originate from the Eu *f* states. The small dispersion of these bands indicates that they correspond to the extremely localized states. The small curvature of the bands points to a large corresponding effective mass m^* ($m^* \sim [\nabla^2_{\mathbf{k}} E(\mathbf{k})]^{-1}$), that is, the carriers occupying these bands are essentially immobile.

The characteristics of the bands for the spin-down configuration [Fig. 7(b)] are essentially the same as those for the spin-up configuration. The only difference is in the Eu *f* states that lie now high above E_F (at ~10 eV) and are numerous and flat. Similarly to the spin-up configuration, the E_F region is dominated by the Fe *d* states.

A common feature that can be observed for both spin-up and spin-down configurations (Fig. 7) is the merging of the energy bands along the high-symmetry points in the Brillouin zone, such as Γ, X, and R. As one moves away from these points, the symmetry on the *k*-space is broken and consequently the bands start to diverge from each other. The electronic states along these high-symmetry directions are localized and nested because any carrier in these regions will be subject to a null net electrostatic force, thus confining the carriers into regions in the vicinity of these special points.

3.2.4. *Atom-resolved energy band structure*

The spin-polarized, energy bands originating from the Fe, Eu, Cs, As_1, and As_2 atoms are presented in Fig. 8. In this figure, the thickness of the bands indicates their relative weight, that is, their relative contribution to the energy band structure of $CsEuFe_4As_4$. One can notice that the majority of the Fe energy bands [thick lines in Fig. 8(a) and (b)] lie in the vicinity and slightly below E_F. As mentioned earlier, they are mainly of the *d* character. The contributions from these states become smaller (represented by thinner lines), as one moves away from the E_F region in both directions.

There is a large difference between the spin-up and spin-down Eu energy bands [Fig. 8(c) and (d)], both in energy and in weight (thickness of the bands). This will lead eventually to a large magnetic moment carried by the Eu atoms. The energy bands for a spin-up configuration [Fig. 8(c)] are mainly confined to the energy region around -2 eV, whereas for a spin-down configuration [Fig. 8(d)] the numerous Eu *f* bands are located above 9 eV. This observation is consistent with an earlier discussion of the DOS originating from the Eu *f* states. In both figures in the energy region above 5 eV, a smaller but symmetric contribution from the Eu 3*d* states is observed.

As one can notice in Fig. 8(e) and (f), the largest contribution to the band structure due to the Cs states is in the atomic energy region as indicated by the thick bands between -9.5 and -8.5 eV. The contributions from both spin configurations are identical along all directions in the Brillouin zone, and consequently, the magnetic moment of the Cs atoms in $CsEuFe_4As_4$ is negligible. A careful examination of Fig. 8(e) and (f) shows that there is a small contribution from the Cs energy bands across E_F (as indicated by the thin energy bands).

At first glance at Fig. 8(g)−(j) one can notice that the As_1 and As_2 atoms do not contribute significantly to the energy band structure of the compound studied. There are, however, two energy regions in which the As contribution is not negligible. The first energy region is in the neighborhood of E_F. Here, although the bands are thin, they are thicker than the rest of the bands. The other energy region is around -2 eV.

3.2.5. *Orbital-resolved energy band structure of Fe*

Fig. 9 shows the spin-polarized band structure resulting from various Fe *d*-orbitals. One observes that the $d_{x^2-y^2}$ orbitals [Fig. 9(a) and (b)] dominate the E_F region. Multiple hole-like bands exist around the high symmetry points Γ, X, M, A, and R. Four regions of electron-like bands are observed midway between the connecting high symmetry directions Γ−X, M−X, A − R, and R − Z. One also observes a negligible dispersion along the A − M and Γ − Z directions.

The bands originating from the d_{z^2} orbitals [Fig. 9(c) and (d)] are similar to those due to the $d_{x^2-y^2}$ orbitals. However, they exhibit less dispersion across the Fermi level. Moreover, a fraction of these bands occupies another energy region below E_F (between -0.9 and -0.5 eV).

Most of the bands origination from the d_{xy}-orbitals are in the conduction region between 0.9 and 1.0 eV [Fig. 9(e) and (f)]. The contribution to the band structure of $CsEuFe_4As_4$ from the d_{xy} orbitals [Fig. 9(g) and (h)] and the d_{yz} orbitals [Fig. 9(i) and (j)] is minimal. One can conclude that the properties of the compound studied are determined mainly by the $d_{x^2-y^2}$ and d_{z^2} orbitals.

3.2.6. *Fermi surfaces*

The Fermi surfaces calculated in the first Brillouin zone are displayed in Fig. 10. The surfaces are plotted along the indicated high symmetry points. The hole-like Fermi surface sheets in the form of concentric cylinders are seen [Fig. 10(a)] in the central region of the Brillouin zone and along the Γ−Z direction. The hole pockets at the center of the Brillouin zone are not of the same size. Upon careful inspection of Fig. 10(a) one realizes that there is a small dispersion along k_z which increases at the outermost Fermi surface. The Fermi surface sheets are wider in diameter at Γ and become smaller towards Z in both directions. The four corners of the Brillouin zone consist of the Fermi surface sheets of the electron-like character, i.e., the electron pockets are aligned parallel to the A−M direction.

Similar features can be seen in the Fermi surfaces for the spin-down configuration [Fig. 10(b)]. The only difference is in the density of the Fermi surface sheets. This difference results from the fact that the bands for the spin-up configuration are more closely packed along the Fermi level than those for the spin-down configuration. The same Fermi surface topologies have been found in similar Fe-based superconductors [14–16].

3.2.7. *Magnetic moments and Mössbauer hyperfine parameters*

The calculated magnetic moment per formula unit of $CsEuFe_4As_4$ is 6.816 μ_B. This value consists of the contribution from the muffin-tin and the interstitial (0.2058 μ_B) regions. The calculated magnetic moments carried by the Cs, Eu, Fe, As_1, and As_2 atoms are 0.00, 6.91, -0.07, 0.00, and -0.01 μ_B, respectively. The calculated Eu magnetic moment is somewhat greater than the experimental moment of 5.9 $\mu_B$at 2 K [4] that was derived from the magnetization measurements. The nearly vanishing calculated magnetic moment of the Fe atoms is in excellent agreement with the experimental observation via ^{57}Fe Mössbauer spectroscopy [6] of a zero intrinsic magnetic moment of the Fe atoms down to 2.1 K. The values of the calculated magnetic moments indicate that ferromagnetism in $CsEuFe_4As_4$ is associated exclusively with the Eu atoms.

Three types of the hyperfine-interaction parameters can be derived from the fits of Mössbauer spectra [17]. These are: the isomer shift δ_0, the principal component of the electric field gradient tensor V_{zz} and the asymmetry parameter η, and the hyperfine magnetic field H_{hf}. They can

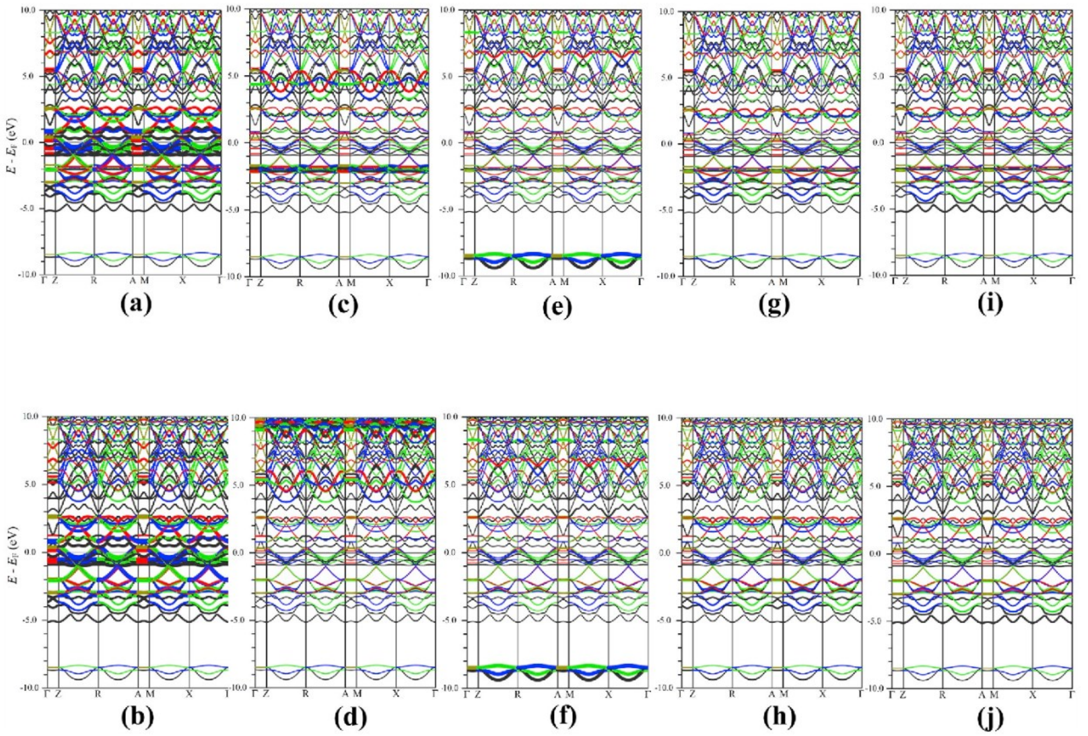

Fig. 8. (Color online) Spin-polarized and atom-resolved band structure of ferromagnetic $CsEuFe_4As_4$. The Fe spin-up (a) and spin-down (b) contributions. The Eu spin-up (c) and spin-down (d) contributions. The Cs spin-up (e) and spin-down (f) contributions. The As_1 spin-up (g) and spin-down (h) contributions. The As_2 spin-up (i) and spin-down (j) contributions. (For interpretation of the references to colour in this figure legend, the reader is referred to the Web version of this article.)

also be obtained from *ab initio* calculations carried out for any crystalline compound with known crystal structure [18].

The isomer shift can be calculated from the expression $\delta_0 = \alpha[\rho(0) - \rho_{ref}(0)]$, where $\rho(0)$ and $\rho_{ref}(0)$ are, respectively, the total electron densities at the Mössbauer nucleus in the compound studied and in the reference material, and α is a calibration constant. In calculating $\rho(0)$, relativistic spin-orbit effects were included to account for the possibility of the penetration of the $p_{1/2}$ electrons into the ^{57}Fe nuclei [19]. The reference material for ^{57}Fe Mössbauer spectroscopy is α-Fe metal (with the *bcc* structure and the lattice constant of 2.8665 Å). The calculated $\rho(0)$ and $\rho_{ref}(0)$ are 15308.539 and 15309.918 (a. u. $)^{-3}$, respectively. Using the calibration constant $\alpha = -0.291$(a. u. $)^3$(mm/s) [20], the calculated values of $\rho(0)$ and $\rho_{ref}(0)$ imply that $\delta_0 = 0.401$ mm/s (analogous calculations of δ_0 for ^{151}Eu Mössbauer spectra cannot be done as the corresponding α has not been established yet). The calculated δ_0 is close to the experimental value of 0.491 (1) mm/s [6].

The measured H_{hf} consists of three main contributions [21]: the Fermi contact term H_c, the magnetic dipolar term, H_{dip}, and the orbital moment term, H_{orb} [17]. The first term is generally much greater in magnitude than the other two terms. The Fermi contact term is calculated from the expression $H_c = \frac{8\pi}{3}\mu_B^2(\rho_\uparrow(0) - \rho_\downarrow(0))$, where $\rho_\uparrow(0)$ and $\rho_\downarrow(0)$ are the spin-up and spin-down densities at the Mössbauer nucleus, respectively. The calculated magnitudes of H_c at the ^{57}Fe and ^{151}Eu nuclei are 8.1 and 264.6 kOe, respectively. These should be compared with the corresponding experimental H_{hf} values (at 0 K) of 5.98 (13) and 272.9 (2.8) kOe [6].

The calculated V_{zz} and η are 7.142×10^{20} V/m^2 and 0.7795 for ^{57}Fe Mössbauer spectra [6]. The calculated V_{zz} and η imply that the value of the quadrupole splitting $\Delta = \frac{1}{2}eQ|V_{zz}|\sqrt{1 + \eta^2/3}$ ($Q = 0.15$ b is the electric quadrupole moment of the 14.4-keV excited state of ^{57}Fe [22]) should be 0.1222 mm/s. For ^{151}Eu Mössbauer spectra, the calculated V_{zz} and η are -0.580×10^{22} V/m^2 and 0.0 (the zero value is consistent with the point symmetry 4/*mmm* of the Eu site). The experimental Δ (at 0 K) of 0.1182 mm/s [6] is in excellent agreement with the predicted value of 0.1222 mm/s. Similarly, good agreement is found between the calculated values of V_{zz} and η and the corresponding experimental values (at 0 K) of $-0.516(5) \times 10^{22}$ V/m^2 and 0.0 derived from the ^{151}Eu Mössbauer spectra [6].

4. Summary

We present the results of *ab-initio* calculations of the electronic structure, magnetism, and hyperfine interaction parameters of the new 35 K superconductor $CsEuFe_4As_4$. The calculations suggest the presence of a mixture of ionic, covalent, and metallic bonding between the constituent atoms. We discuss in detail the electronic band structure and the density of states. We show that, in agreement with the experimental results, the magnetic moment is due to the strongly localized Eu *f* states. We demonstrate that an almost zero magnetic moment carried by the Fe atoms results from an apparent symmetry of the spin-up and spin-down states. We find that Fermi surfaces have the hole-like and electron-like pockets located at the center and corners of the Brillouin zone, respectively. We show that the calculated ^{57}Fe and ^{151}Eu Mössbauer hyperfine interaction parameters are in good agreement with the corresponding parameters derived from the Mössbauer spectra.

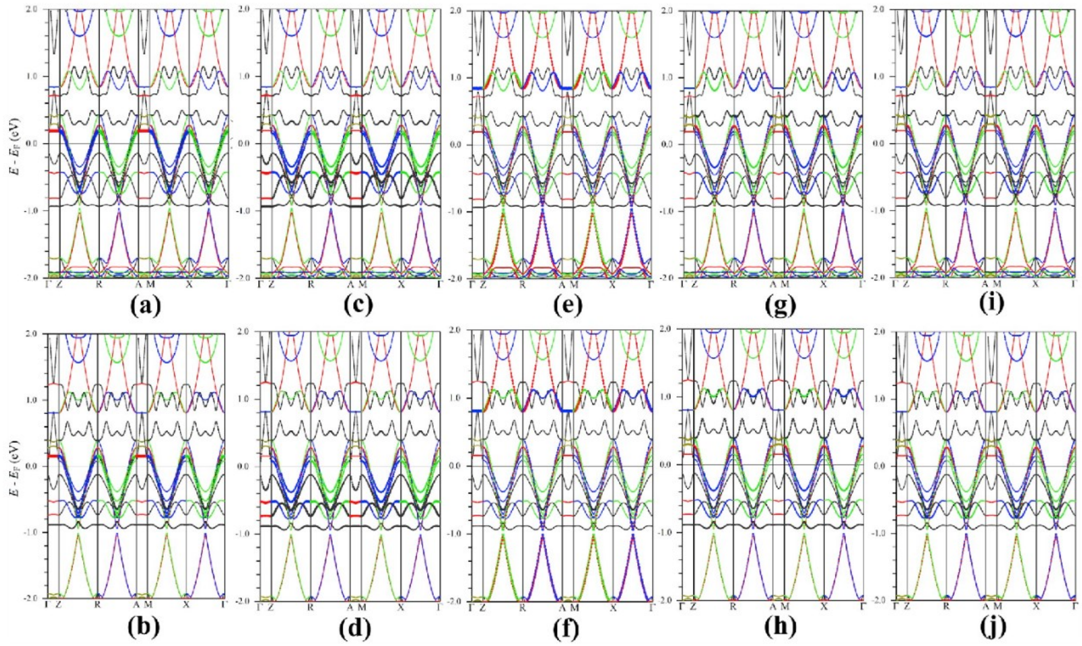

Fig. 9. (Color online) Spin-polarized band structure resulting from the Fe orbitals $d_{x^2-y^2}$ [(a), (b)], d_{z^2} [(c), (d)], d_{xy} [(e), (f)], d_{xz} [(g), (h)], and d_{yz} [(i), (j)]. (For interpretation of the references to colour in this figure legend, the reader is referred to the Web version of this article.)

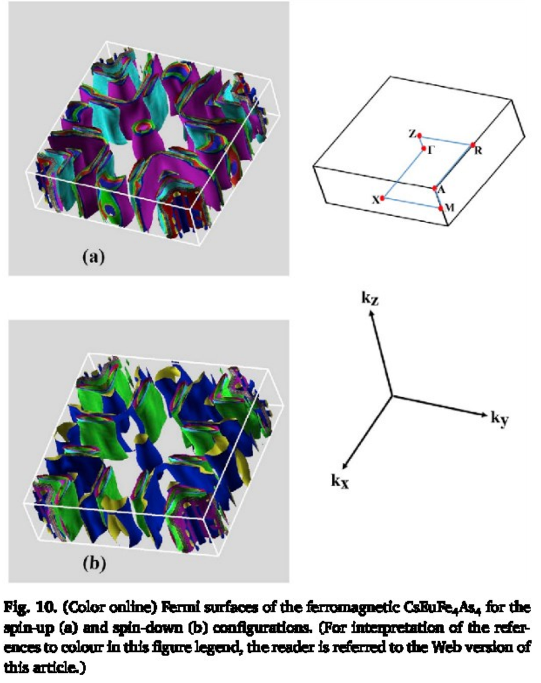

Fig. 10. (Color online) Fermi surfaces of the ferromagnetic CsEuFe$_4$As$_4$ for the spin-up (a) and spin-down (b) configurations. (For interpretation of the references to colour in this figure legend, the reader is referred to the Web version of this article.)

Acknowledgements

This work was supported by the Natural Sciences and Engineering Research Council of Canada (NSERC).

References

[1] A. Iyo, K. Kawashima, T. Kinjo, T. Nishio, S. Ishida, H. Fujihisa, Y. Gotoh, K. Kihou, H. Eisaki, Y. Yoshida, J. Am. Chem. Soc. 138 (2016) 3410.
[2] K. Kawashima, T. Kinjo, T. Nishio, S. Ishida, H. Fujihisa, Y. Gotoh, K. Kihou, H. Eisaki, Y. Yoshida, A. Iyo, J. Phys. Soc. Jpn. 85 (2016) 064710.
[3] Y. Liu, Y.-B. Liu, H. Jiang, Z.-C. Wang, A. Ablimit, W.-H. Jiao, Q. Tao, C.-M. Feng, Z.-A. Xu, G.-H. Cao, Phys. Rev. B 93 (2016) 214503.
[4] Y. Liu, Y.-B. Liu, Q. Chen, Z.-T. Tang, W.-H. Jiao, Q. Tao, Z.-A. Xu, G.-H. Cao, Sci. Bull. 61 (2016) 1213.
[5] L.N. Bulaevskii, A.I. Buzdin, M.L. Kulić, S.V. Panjukov, Adv. Phys. 34 (1985) 175 S. Zapf and M. Dressel, Rep. Prog. Phys. 80, 016501 (2017).
[6] M.A. Albedah, F. Nejadsattari, Z.M. Stadnik, Y. Liu, G.-H. Cao, J. Phys. Condens. Matter 30 (2018) 155803.
[7] C. Xu, Q. Chen, C. Cao, Commun. Phys. 2 (2019) 16.
[8] P. Blaha, K. Schwartz, G. Madsen, D. Kvasnicka, J. Luitz, WIEN2k, an Augmented Plane Wave Plus Local Orbitals Program For Calculating Crystal Properties, Technical Universität Wien, Austria, 1999 Karlheinz Schwarz.
[9] F. Nejadsattari, P. Wang, Z.M. Stadnik, Y. Nagata, T. Ohnishi, J. Alloy. Comp. 725 (2017) 1098.
[10] J.P. Perdew, S. Burke, M. Ernzerhof, Phys. Rev. Lett. 77 (1996) 3865.
[11] V.I. Anisimov, O. Gunnarsson, Phys. Rev. B 43 (1991) 7570 V. I. Anisimov, J. Zaanen, and O. K. Andersen, Phys. Rev. B 44, 943 (1991); V. N. Antonov, B. N. Harmon, and A. N. Yaresko, Phys. Rev. B 72, 085119 (2005).
[12] R.F.W. Bader, Atoms in Molecules: A Quantum Theory, Oxford University Press, Oxford, 1991.
[13] P.E. Blöchl, O. Jepsen, O.K. Andersen, Phys. Rev. B 49 (1994) 16223.
[14] X. Shi, G. Wang, J. Phys. Soc. Jpn. 85 (2016) 124714.
[15] F. Lochner, F. Ahn, T. Hickel, I. Eremin, Phys. Rev. B 96 (2017) 094521.
[16] D.V. Suetin, I.R. Shein, J. Supercond. Nov. Magnetism 31 (2018) 1683.
[17] N.N. Greenwood, T.C. Gibb, Mössbauer Spectroscopy, Chapman and Hall, London,

1971 P. Gütlich, E. Bill, and A. Trautwein, Mössbauer Spectroscopy and Transition Metal Chemistry (Springer, Berlin, 2011).
[18] P. Blaha, J. Phys. Conf. Ser. 217 (2010) 012009.
[19] F. Nejadsattari, Z.M. Stadnik, J. Żukrowski, J. Alloy. Comp. 639 (2015) 547.
[20] U.D. Wdowik, K. Reubenbauer, Phys. Rev. B 76 (2007) 155118.
[21] F. Nejadsattari, Z.M. Stadnik, J. Przewoźnik, K.H.J. Buschow, Physica B 477 (2015) 113.
[22] G. Martínez-Pinedo, P. Schwerdtfeger, E. Caurier, K. Langanke, W. Nazarewich, T. Söhnel, Phys. Rev. Lett. 87 (2001) 062701.

Chapter 9: Ab-initio study of $RbEuFe_4As_4$

PHILOSOPHICAL MAGAZINE
2020, VOL. 100, NO. 7, 894–916
https://doi.org/10.1080/14786435.2019.1704591

Taylor & Francis
Taylor & Francis Group

Ab-initio study of the $RbEuFe_4As_4$ superconductor

Farshad Nejadsattari[a], Mohammed A. Albedah[a,b] and Zbigniew M. Stadnik[a]

[a]Department of Physics, University of Ottawa, Ottawa, ON, Canada; [b]Department of Physics, Majmaah University, Zulfi, Saudi Arabia

ABSTRACT

The results of *ab-initio* calculations of the electronic structure and magnetism of the new superconductor $RbEuFe_4As_4$ are reported. The electronic band structure and the density of states are presented and discussed in detail. The electric charge density distributions along different crystallographic planes are presented, and the origin of the chemical bonding between the constituent atoms is discussed in detail. The evidence is provided for the existence of a mixture of ionic, covalent, and metallic bonding. It is demonstrated that the magnetic moment is mainly due to the strongly localised Eu 4*f* states. An almost negligible magnetic moment carried by the Fe atoms is shown to be due to the symmetry of the Fe spin-up and spin-down states. It is demonstrated that the electrical and chemical properties of $RbEuFe_4As_4$ are closely linked with the presence of the Fe 3*d* states in the Fermi energy region. The Fermi surfaces show the presence of hole-like and electron-like pockets, respectively, at the center and corners of the Brillouin zone. The results of the calculations of the elastic properties and the ^{57}Fe and ^{151}Eu hyperfine-interaction parameters are also presented.

ARTICLE HISTORY
Received 20 June 2019
Accepted 5 December 2019

KEYWORDS
Density of states; energy band structure; magnetic moment; hyperfine interactions

1. Introduction

The discovery of a new Fe-based class of superconductors $AeAFe_4As_4$ (Ae = Ca, Sr, Eu and A = K, Rb, Cs) with the critical temperature T_c in the range 31.6–36.8 K [1–5] is significant for two reasons. First, in contrast to the intensively studied solid solutions of $(Ba_{1-x}K_x)Fe_2As_2$ or $(Sr_{1-x}Na_x)Fe_2As_2$, the Ae and A atoms in $AeAFe_4As_4$ are located at the crystallographically inequivalent positions, which causes the change of the space group from $I4/mmm$ characteristic for solid-solution superconductors to $P4/mmm$. In these new superconductors, the Ae and A layers are alternately stacked along the crystallographic c-axis between the Fe_2As_2 slabs. Consequently, the absence of structural disorder in $AeAFe_4As_4$ allows for the investigations of their intrinsic physical properties

---

CONTACT Zbigniew M. Stadnik stadnik@uottawa.ca Department of Physics, University of Ottawa, Ottawa, ON, Canada K1N 6N5

This article has been republished with minor changes. These changes do not impact the academic content of the article.

© 2019 Informa UK Limited, trading as Taylor & Francis Group

that are not hindered by the structural disorder present in solid-solution superconductors. Second, the presence of the Eu and Fe atoms, which potentially can order magnetically, points toward the possibility of the coexistence of two, generally incompatible phenomena, magnetism and superconductivity [6,7].

The magnetic susceptibility measurements [2,3,8–10] indicate that the $RbEuFe_4As_4$ superconductor with $T_c = 35-36$ K has a magnetic transition at ~15.0 K. Such a magnetic transition has also been found in the heat capacity data at ~15 K [9,10] and at 16.54(8) K in the ^{151}Eu Mössbauer data [11]. The isothermal magnetisation data made it possible to identify this transition as being ferromagnetic [3,10]. Ferromagnetism in $RbEuFe_4As_4$ has been hypothesised [3,10] to be associated only with the Eu magnetic moments, that is, it has been assumed that the Fe atoms have no magnetic moment. These suggestions have been confirmed experimentally in the ^{151}Eu and ^{57}Fe Mössbauer study of $RbEuFe_4As_4$ [11].

The main goal of this work is to elucidate the origin of some of the physical properties of $RbEuFe_4As_4$ via detailed electronic structure calculations. In particular, the formation and type of chemical bonds in this compound and the charge transport properties are studied. The type of chemical interactions between different atoms in $RbEuFe_4As_4$ are similar to those observed in [12]. A thorough discussion of the Fermi surface topology allows for the understanding of the electronic characteristics of $RbEuFe_4As_4$. Furthermore, a framework to test and, to some extent, predict the properties of this compound is provided. A comparison is made between the calculated physical quantities and those obtained from the magnetic and Mössbauer spectroscopy measurements.

2. Theoretical method

We performed *ab initio* calculations of the electronic structure and Mössbauer hyperfine-interaction parameters of $RbEuFe_4As_4$ in the context of density functional theory using the full-potential linearised augmented-plane-wave plus local orbitals (FP-LAPW+lo) method that is realised in the WIEN2k package [13]. This method is described thoroughly in [14]. Here, the valence wave functions in the interstitial region are expanded in spherical harmonics up to $l = 4$, while in the muffin-tin region they are expanded to a maximum of $l = 10$ harmonics. The values of 2.50, 2.50, 2.30, and 2.19 a.u. were used as the muffin-tin radii for Rb, Eu, Fe, and As, respectively. For the exchange-correlation potential, the generalised gradient approximation (GGA) scheme of Perdew, Burke, and Ernzerhof [15] was used. In addition, effective Hubbard-like interaction energies of 0.52 and 0.15 Ry were used for the Eu 4*f* and Fe 3*d* states, respectively [12,16–18]. A total number of 680 inequivalent *k*-points was used within a $32 \times 32 \times 9$ *k*-mesh in the irreducible wedge of the first Brillouin zone. A separation energy of 6.0 Ry between the valence and core states of individual atoms in a unit cell was chosen. The plane-wave cut-off parameter was set to

$R_{MT} \times K_{MAX} = 7.0$, where R_{MT} is the smallest muffin-tin radius in the unit cell and K_{MAX} is the maximum K vector used in the plane-wave expansion in the interstitial region. A convergence criterion for self-consistent field calculations was chosen in such a way that the difference in energy between two successive iterations did not exceed 10^{-4} Ry. The experimental lattice parameters (a and c) and the atomic position parameters from [11] were employed in the calculations.

3. Results and discussion

3.1. The crystal structure

Figure 1 shows the layered crystal structure of $RbEuFe_4As_4$. Various connecting rods represent the interactions between the Rb, Fe, and As atoms. One can notice that the layers of Eu atoms are entirely isolated from the Fe_4As_4 blocks and that the sheets of Rb atoms along the c-direction separate the neighbouring Fe_4As_4 blocks [11].

The type of interactions between different atoms in the $RbEuFe_4As_4$ superconductor depend on their interatomic distances. In a solid, the prevalent physical interaction between the atoms is electromagnetic in origin. Thus, the strength of the Coulomb interaction between the atoms of the compound studied is expected to determine the kind of chemical bonding between them. It is evident (Figure 1) that the density of atoms within the Fe_4As_4 blocks is higher than that within the Rb and Eu sheets. Therefore, stronger electric interactions are expected within these blocks than within the sheets. These different interactions are depicted qualitatively in Figure 1 by a dense grid of connecting rods between the Fe and As atoms in the Fe_4As_4 blocks and the lack of such connecting rods between the Eu atoms in the Eu sheets [11].

One can notice (Figure 1) that the $RbFe_4As_4$ units are separated from each other by sheets of Eu atoms. Consequently, these units are not interacting chemically with each other, as indicated by the lack of connecting rods

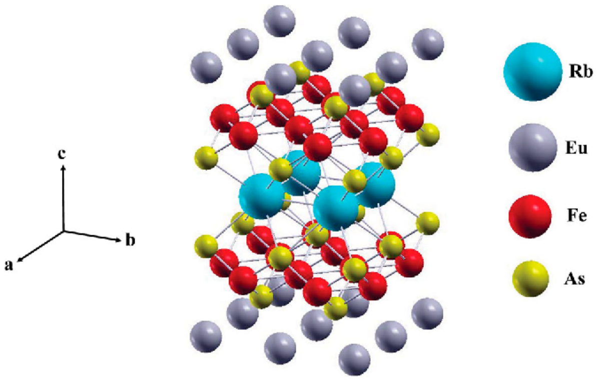

Figure 1. The layered crystal structure of $RbEuFe_4As_4$.

between the Eu atoms and the $RbFe_4As_4$ units. The Eu sheets constitute then the insulating layers along the *c*-axis. This may result from ionic interactions between the Eu sheets and the Fe_4As_4 blocks. Besides, as the tetragonal unit cell is elongated along the *c*-axis, there cannot be any significant interaction between the Eu layers. Consequently, no magnetic coupling should happen between the Eu atoms along the *c*-direction. One can thus expect that the interatomic interactions between the Eu atoms are in the *ab* plane, that is, there should exist a 2D magnetic interaction mechanism between neighbouring Eu atoms in each layer. One also notices that the Eu atoms in each layer do not interact with each other because they are isolated from one another. This is illustrated (Figure 1) by the lack of connecting rods between them [11].

The layered structure and the network of the connecting rods (Figure 1) point towards the existence of a combination of covalent and ionic bonds (*vide infra*) in the compound studied [11].

3.2. Valence charge density distributions

The valence charge density distributions along various planes are shown in Figure 2. The electronic charges of the atoms in $RbEuFe_4As_4$ were obtained through the Bader's analysis scheme [19]. The presence of a combination of ionic, covalent, and metallic bonds between different atoms in $RbEuFe_4As_4$ becomes evident by inspecting Figure 2 in detail.

As one can notice from the charge density distribution in the (001) plane [Figure 2(a)], valence charge is absent in the regions between the Eu atoms (red regions). This indicates that the Eu atoms are chemically isolated from each other. Therefore, no chemical bonding is expected to exist between these atoms. This is depicted in Figure 1 by the lack of connecting rods between the Eu atoms, which supports the argument given above. One also observes [Figure 2(a)] that the valence electrons of Eu are strongly bound to the parent atom (the yellow, green, and blue rings surrounding each Eu atom). Furthermore, a fourth-fold shape of the half-filled 4*f* shell of Eu is evident [purple regions in Figure 2(a)].

The valence charge density distribution in the (002) plane is shown in Figure 2(b). This plane consists of sheets of Rb atoms which separate the neighbouring Fe_4As_4 blocks in the *c*-direction. One can see that the charge density distribution around the Rb atoms is perfectly symmetric in the form of spheres. The electronic configuration of Rb is $[Kr]5s^1$. In fact, what is shown in this figure is the closed shell structure of the Kr atom, with the 5*s* electrons of Rb completely detached from their parent atoms and transferred to the Fe_4As_4 blocks, in particular, to the As atoms. These electrons participate in the ionic bonding between the Rb sheets and the Fe_4As_4 blocks. The Rb atoms themselves are isolated from each other due to their relatively large separation (7.34 a.u.). Consequently, no metallic interaction is likely to exist between them.

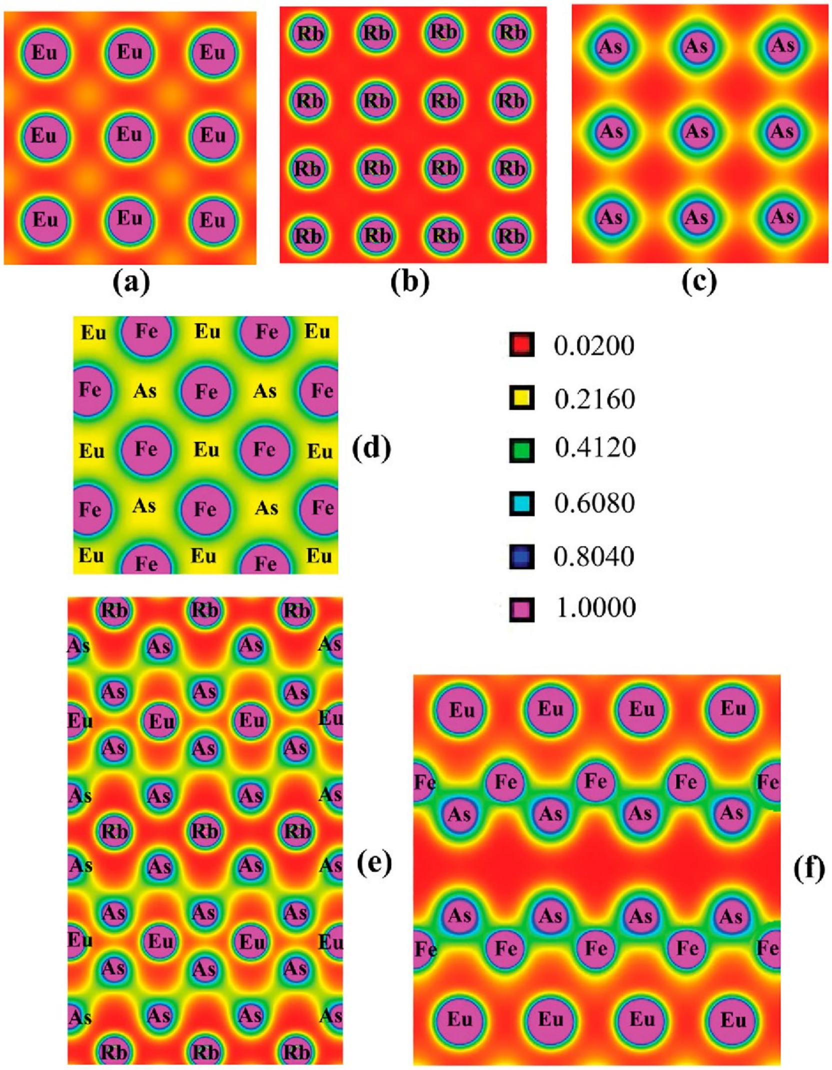

Figure 2. Electron charge density distribution (in units of e/Å^3) along the (001) (a), (002) (b), $z = 0.6638$ (c), $z = 0.7682$ (d), (110) (e), and (010) [(100)] (f) planes.

Figure 2(c) shows the valence charge density distribution in the $z = 0.6638$ plane which consists of the As atoms located at the 2*g* sites. The presence of a very weak directional covalent bonding between the adjacent As atoms can be seen (faint yellow bridges). These As atoms are isolated from each other by regions which have virtually no charge density. In contrast, the As atoms located at the 2*h* sites [Figure 2(d)] are involved in forming stronger covalent bonding with the neighbouring Fe atoms [the $z = 0.7782$ plane in Figure 2(d) passes through the Fe layers]. The valence charge density distribution in this plane indicates that the electronic charge is spread out between the Fe–Fe and Fe–As atoms. The green regions in Figure 2(d) correspond to the charge distribution of the Fe 4*s* electrons throughout the Fe layers, which leads to the formation of the metallic Fe-Fe bonds. The electronic transport in the superconductor studied is expected to occur predominantly within these Fe layers and, to a smaller extent, within the metallic Fe_4As_4 blocks.

The valence charge density distribution in the (110) plane is shown in Figure 2(e). This plane passes through the Eu and Rb atoms, and also through the As atoms located at the 2*h* sites. The presence of the As–As covalent bonds is visible as the electrons are delocalised between these atoms (green regions). Furthermore, a complete charge transfer from the Rb and Eu atoms to the As layers is evident (red regions indicating the virtual absence of charge). This leads to the formation of two sets of ionic bonds: a strong ionic bond between the alkali Rb layers and the metalloid As layers, and a weaker ionic bond between the layers of the Eu and As atoms. One can interpret this result by considering the differences between the electronegativity of the Rb (0.82) and the Eu (1.2) atoms and that of the As (2.18) atoms. Based on these electronegativity values, the Rb–As bond is expected to be stronger than the Eu–As bond. These two sets of ionic bonding are depicted in Figure 2(e) by two red regions of different intensity. No electronic transport is expected to exist between the separate As layers due to the formation of these ionic bonds. As mentioned earlier, any transport (whether electrical or thermal) must be along the Fe_4As_4 blocks.

When one considers the symmetry of the space group *P4*/*nmm* and the crystal basis of $RbEuFe_4As_4$, then it becomes clear that the charge density distributions in the (010) and (100) planes are the same [Figure 2(f)]. These planes pass through the Eu, As at the 2*g* sites, and Fe atoms. Because of the virtual absence of charge density [red regions in Figure 2(f)], it is clear that the sheets containing the Eu atoms are isolated from each other. The delocalisation of the valence charges of the As and Fe atoms leads to the formation of strong covalent As-Fe bonds. The green regions in between the As and Fe atoms indicate the presence of a relatively high charge density.

3.3. Density of states

In this section, we bring the results of the DFT calculations for the total and partial density of states (DOS) in $RbEuFe_4As_4$ using the modified tetrahedron method [20].

The spin-resolved, total, and atom-resolved DOS in the ferromagnetic $RbEuFe_4As_4$ is shown in Figure 3. The characteristic DOS features occur in four distinct energy regions. The DOS in the first energy region, which lies below ~ -10 eV, is due to the atomic-like core electrons of Rb and As atoms. More specifically, the Rb core electrons contribute to the DOS in the energy

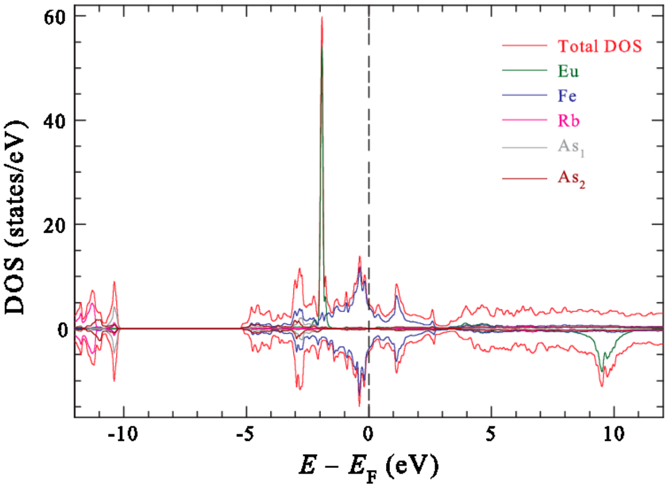

Figure 3. Spin-resolved, total and atom-resolved DOS in ferromagnetic $RbEuFe_4As_4$.

region below −11.1 eV whereas the contribution from the As core electrons is in the energy region between −11.6 and −10.1 eV. As these core states lie deep in energy, they practically do not contribute to any of the physical properties of the compound studied. The DOS of these states resembles that of isolated atomic states of the Rb and As atoms.

The second energy region between −10.1 and −5.2 eV contains a ~5 eV energy gap. This gap separates the core states from the semi-core and valence states. Its relatively large width ensures that the core states are isolated in energy. In addition, the electrons corresponding to these states are entirely bound to their host nuclei by strong electrostatic forces.

The DOS in the third energy region (between −5.0 and 3.0 eV), which includes the Fermi energy (E_F), determines most of the physical properties of $RbEuFe_4As_4$. Here the semi-core, valence, and conduction states form a continuum of DOS. A noticeable dip in the DOS at ~0.7 eV indicates the presence of a pseudogap that is due to a few Fe states. This pseudogap can be attributed to the Coulomb repulsion of the Fe electrons. The T_c values of the high-temperature superconductors are in the range 30–250 K [21]. For the $RbEuFe_4As_4$ superconductor, $T_c \approx 35.5$ K [2,3,8–10]. A relatively small energy gap is expected to exist in superconductors. It opens up above T_c and increases with increasing temperature. DFT calculations give the results for the ground state of a system. Therefore, one does not expect any energy gap across the E_F region in $RbEuFe_4As_4$ at temperatures below T_c. The predicted existence of a small pseudogap below T_c in the DOS of the Fe-3*d* contribution (Figure 3) constitutes a signature of the superconductivity in the compound studied. Such pseudogaps have also been observed experimentally for compounds of similar structure and containing the Fe-As blocks [22]. In addition, the Hubbard models for high-temperature superconductors predict the coexistence of magnetic ordering and superconductivity [23].

The delocalised Fe states dominate the energy region between −1.5 eV and E_F (Figure 3). They form the valence states that are responsible for the formation of the metallic bonds between the Fe atoms within the Fe_4As_4 blocks. A sharp peak in the spin-up DOS in the energy region between −2.0 and −1.6 eV arises entirely from the localised Eu 4*f* electrons. The Eu 4*f* states have minimum overlap with the Fe states, which can indicate the insulating characteristics of the compound studied. This agrees with the reasoning presented above (section B.). Below the energy region dominated by the Eu 4*f* states (between −3.6 and −2.1 eV), one observes contributions from the As and Fe atoms. The overlap between the As and Fe states in this region is indicative of covalent bonding between the As and Fe atoms. The valence and semi-core electrons form these chemical bonds. This covalent bonding can be considered to arise from the hybridisation between the Fe 3*d* states with those of the As 4*p* states.

The fourth energy region, which extends from 3.2 eV upwards, consists of empty states as no electrons are likely to be excited into these states. A relatively large peak in the spin-down DOS between 8.2 and 10.7 eV originates from the Eu 4*f* electrons. The origin of these localised Eu 4*f* states is discussed below in terms of Coulomb-interaction arguments.

A characteristic feature of the DOS in Figure 3 is that in contrast to the energy separation and magnitude difference between the Eu spin-up and spin-down states, the spin-up and spin-down DOS contributions from the other atoms are symmetric. This results in almost negligible magnetic moments of the Rb, Fe, and As atoms (*vide infra*). As a consequence of the high asymmetry observed in the Eu DOS from its two spin components, a large magnetic moment of the Eu atoms is expected. Thus, the magnetism of $RbEuFe_4As_4$ originates mainly from the Eu atoms.

The near Fermi energy region is dominated by the Fe 3*d* states and, to a far less extent, by the As 4*p* states. These states are ultimately responsible for the conductive nature of $RbEuFe_4As_4$. On the other hand, there is almost zero DOS contribution from the Eu and Rb atoms in the Fermi energy region. This suggests that the conductivity in $RbEuFe_4As_4$ must occur along specific directions. In other words, anisotropic conductivity along the Fe-As bonds is expected.

Figure 4(a) displays the spin-resolved DOS due to the Rb atoms for the 3*d* and 4*p* orbitals. The symmetry of the spin-up and spin-down states is evident. Consequently, one expects no magnetic moment for the Rb atoms in $RbEuFe_4As_4$. One also observes that there is virtually no Rb contribution to DOS in the Fermi energy region. The core states of Rb are of the 4*p* character, and their DOS shows three peaks at −11.7, −11.3, and −10.3 eV. The 4*p* core states occupy two energy regions: one between −12.0 and −10.8 eV and the other between −10.7 and −10.2 eV.

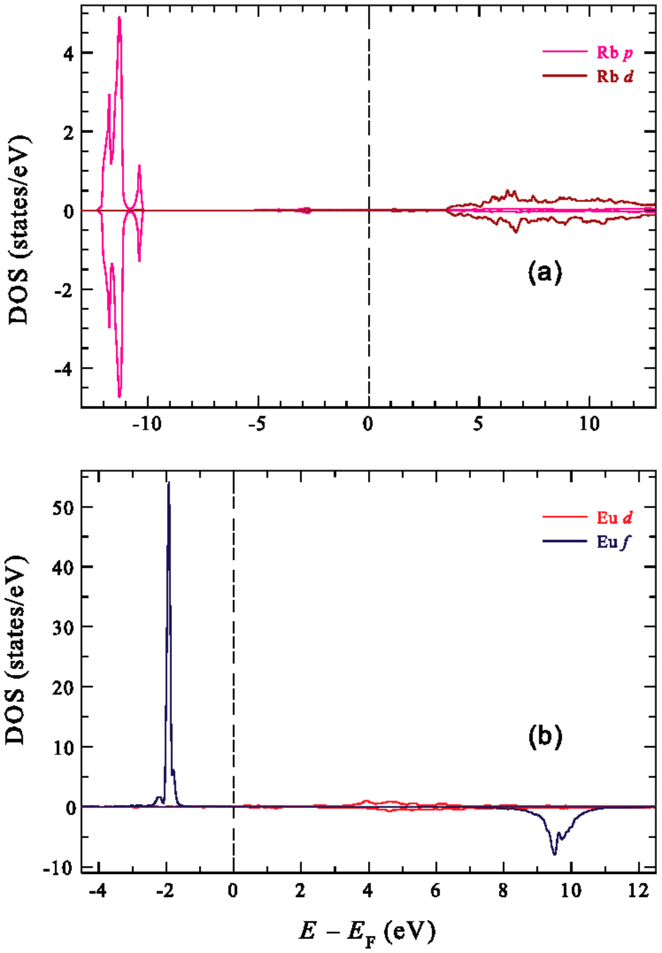

Figure 4. Spin-resolved DOS of the Rb (a) and Eu (b) atoms in ferromagnetic $RbEuFe_4As_4$.

The Rb 3*d* states are mainly distributed in the energy region above 3.5 eV [Figure 4(a)]. These conduction states are less numerous than those of the core 4*p* states and possess metallic-like characteristics. The 3*d* orbitals of Rb are essentially empty as they lie relatively high above E_F.

A highly localised DOS due to the Eu 4*f* states, as opposed to the extended and much less numerous DOS due to the Eu 3*d* states, can be seen in Figure 4(b). The contribution to DOS from the Eu 3*d* states is minimal and symmetric for both spin orientations, whereas that from the Eu 4*f* is very large and asymmetric. The majority spin contribution is from the sharp 4*f* up states of Eu that are localised between −2.4 and −1.5 eV. On the other hand, the minority 4*f* down states of Eu lie in a relatively high-energy region (between 8.4 and 10.5 eV). Under normal conditions, these states are empty as no electron can have enough energy to occupy them. This significant difference in the population of the two spin configurations accounts for a significant magnetic moment found experimentally in $RbEuFe_4As_4$ [3]. The majority of the Eu 3*d* states also lie above E_F. Though few, they are widely spread between 3.6 and 10.8 eV.

Figure 5(a) shows the spin-resolved DOS originating from the Fe 4*s*, 3*p*, and 3*d* orbitals. It is evident that the main contribution to the DOS is from the Fe 3*d* states and that the presence of such states across E_F accounts for the conductive

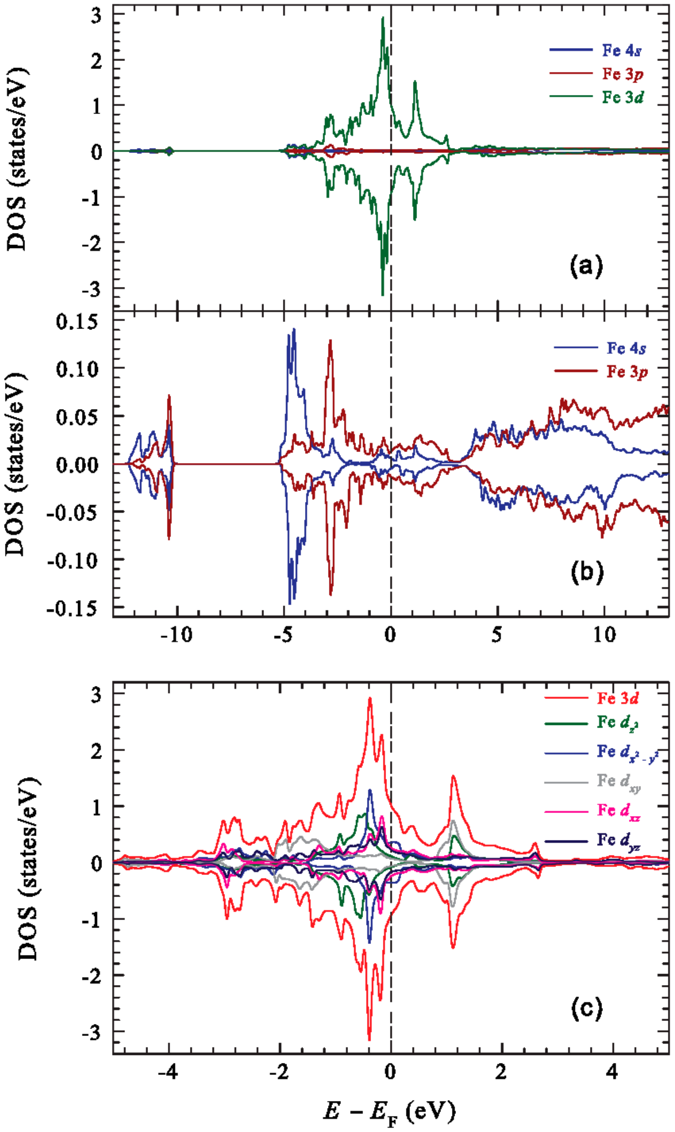

Figure 5. Spin-polarised, Fe orbital-resolved DOS [(a) and (b)] and Fe *d*-orbital-resolved DOS (c).

nature of the $RbEuFe_4As_4$ compound. The preponderance of the Fe states spans an energy region between −5.0 and 2.8 eV. The most intense peak in the Fe DOS occurs at ~ -0.4 eV, and then the Fe DOS decreases as one moves across E_F. A local minimum at 0.6 eV and a local maximum at ~1.0 K in the Fe DOS are observed. It is clear from Figure 5(a) that the spin-up and spin-down contributions to the Fe DOS are almost perfectly symmetric. This suggests a small magnetic moment carried by the Fe atoms in $RbEuFe_4As_4$. The contribution to the Fe DOS from the 4*s* and 3*p* states is almost negligible (the latter contributes slightly in the energy region between −3.0 and −1.8 eV).

The Fe 4*s* and 3*p* contributions to the Fe DOS are shown in more detail in Figure 5(b). One observes that in the energy region above 3.2 eV, the DOS is widely spread and there is an overlap between the 4*s* and 3*p* states. This broad DOS is indicative of the existence of metallic bonds. On the other hand, below E_F, the 4*s* and 3*p* states are fairly separated with several peaks in the DOS. These are localised valence and semi-core states. The strongest spin-up 3*p* and 4*s* DOS peaks are at −2.8 and −4.5 eV, respectively. A small contribution of the Fe core states to the DOS is in the energy region between −12.3 and −10.1 eV. One notices that the Fermi energy region is almost empty of the Fe 4*s* and 3*p* states.

As mentioned earlier, the most significant contribution to the Fe DOS originates from its 3*d* orbitals. Figure 5(c) displays the individual *d*-orbital-resolved contributions to the Fe *d* DOS. The large peak in the Fe DOS originates mainly from the $d_{x^2-y^2}$ states located at about −0.4 eV. These states are mainly localised and exist below E_F. The small peak in the DOS above E_F at about 1.0 eV originates from the d_{xy} and d_{z^2} orbitals. The d_{z^2} states also extend to the region below E_F and they peak at around −0.5 eV. The majority of the d_{xz} states are located in the vicinity of E_F and contribute to the peak at −0.15 eV. The conductive nature of $RbEuFe_4As_4$ can be related to these states. The smallest contribution to the Fe 3*d* DOS is from the d_{yz} states which are non-localised and predominantly spread below E_F into the valence region.

Figure 6(a) displays the DOS due to the As_1 and As_2 atoms located at two different Wyckoff positions 2*g* and 2*f*, respectively [11]. One can notice that although the states due to the As_1 and As_2 atoms occupy the same energy region, they are slightly displaced from each other. As core states lying between −12 and −10 eV are localised and are atomic-like. The semi-core and valence states span an energy region between −5.2 and −1.6 eV and display sharp peaks in DOS between −3.0 and −2.7 eV. The conduction states extend from E_F to 2.8 eV. Above 2.8 eV, the mainly empty metallic, and perfectly overlapping As_1 and As_2 states are located. As a result of the presence of non-localised and overlapping states, the bonding between the As atoms in the compound studied is covalent.

As one can observe in Figure 6(b), the core states lying deep in energy consist consist mainly of 4*s*-type orbitals of closed-shell structure, whereas the states

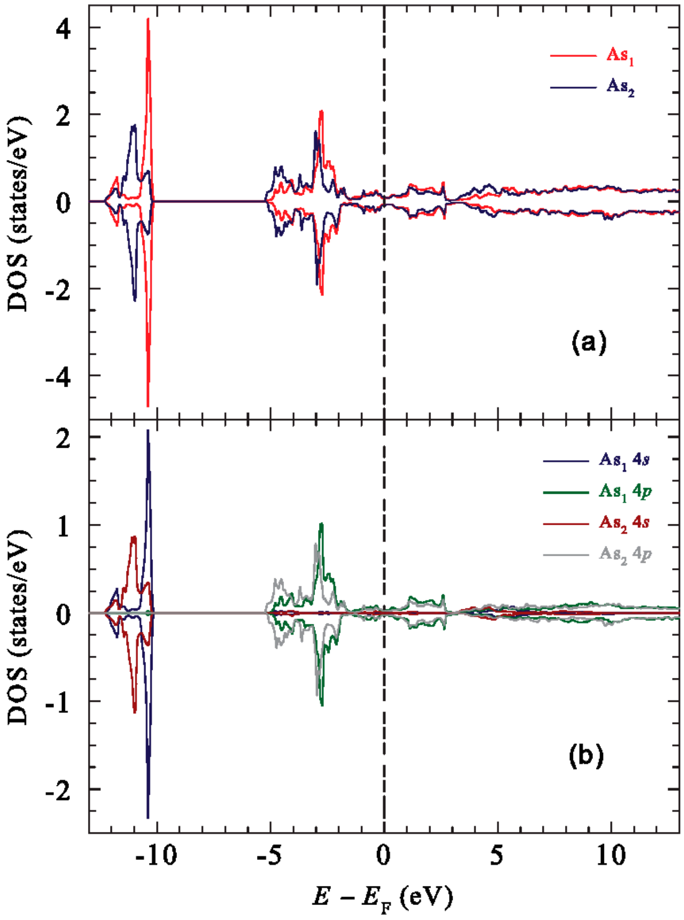

Figure 6. Spin-resolved DOS of As (a) and spin-resolved, orbital-resolved DOS of As.

closer to E_F are dominated by the relatively extended 4p states (between −5.2 and −1.7 eV). The As$_1$ 4p states are slightly more numerous than the As$_2$ 4p states. The spin-up and spin-down contributions to the DOS from both atoms are almost identical, which yields nearly zero magnetic moments of the two As atoms.

3.4. Energy band structure

The calculated band structure of the ferromagnetic $RbEuFe_4As_4$ (Figure 7) spans an energy region between −10 and 10 eV. It can be noted that for the spin-up configuration [Figure 7(a)], the energy bands above E_F are relatively dispersive, which indicates a conductive nature of the states residing along these bands. In the vicinity of E_F, the bands are less dispersive, and thus correspond to localised states originating from the Fe 3d orbitals. These states cross the Fermi level

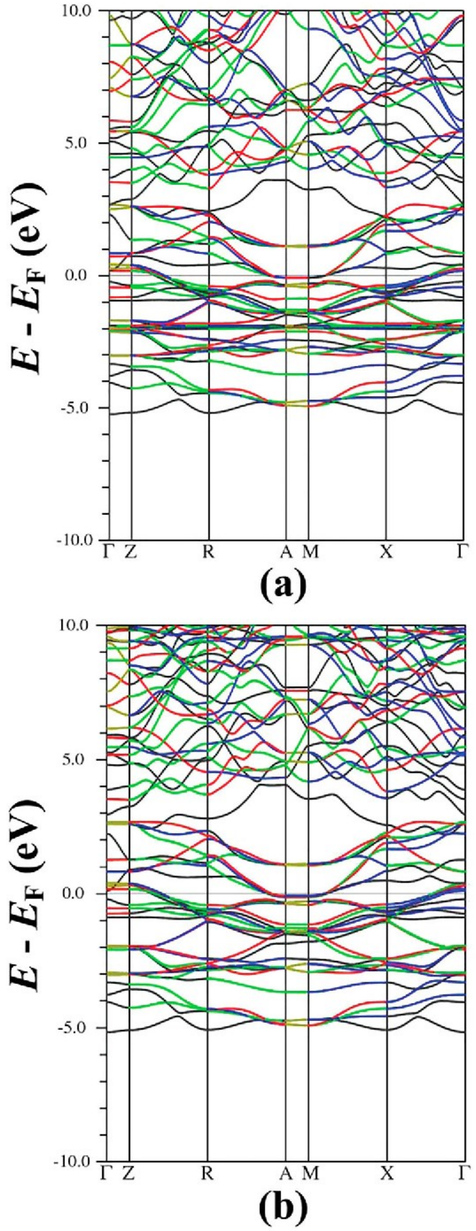

Figure 7. Spin-up (a) and spin-down band structures of ferromagnetic $RbEuFe_4As_4$.

mainly midway between the X and Γ-points, and also between the Z and R points. These Fermi energy crossing bands are responsible for the conductive nature of $RbEuFe_4As_4$. The bands at about −2 eV are very dense and flattened. They originate from the Eu 4*f* state contributions. The small dispersion of these bands indicates that they correspond to extremely localised states. The small curvature of the bands points to a large corresponding effective mass m^* ($m^* \sim [\nabla_{\mathbf{k}}^2 E(\mathbf{k})]^{-1}$), that is, the carriers occupying these bands are essentially immobile. The semi-core states of As and Rb lie further down, between −4 and −3 eV [Figure 7(a)]. They are relatively dispersive in energy, which reflects their *p* and *s* character. There are no energy bands below −5 eV [Figure 7(a) does not include energies below −10 eV where the atomic core states reside].

The characteristics of the bands for the spin-down configuration [Figure 7(b)] are mostly the same as those for the spin-up configuration. The only difference is in the Eu 4*f* states which lie high above E_F (at ~10 eV) and are numerous and less localised. Similarly to the spin-up configuration, the Fermi region is dominated by the Fe 3*d* states.

A common feature that can be observed for both spin-up and spin-down configurations (Figure 7) is the merging of the energy bands along the high-symmetry points in the Brillouin zone, such as Γ, X, and R. As one moves away from these points, the symmetry on the *k*-space is broken and consequently the bands start to diverge from each other. The electronic states along these high-symmetry directions are localised and nested. This indicates that any carrier in these regions will be subject to a null net electrostatic force, thus confining the carriers into regions in the vicinity of these particular points.

3.4.1. Atom-resolved energy band structure

The spin-polarised energy bands originating from the Fe, Eu, Rb, As_1, and As_2 atoms are presented in Figure 8. In this figure, the thickness of the bands indicates their relative weight, that is, their relative contribution to the energy band structure of $RbEuFe_4As_4$. One can notice that the Fe energy bands [Figure 8(a, b)] dominate the Fermi energy region and extend from −4.0 to 3.0 eV. These bands are mainly composed of the Fe 3*d* orbitals. The contributions from these states become smaller as one moves away from the Fermi region in both directions and thinner bands depict this in Figure 8(a,b). Moreover, no spin polarisation in the Fe bands is observed. This confirms the result of our earlier DOS calculations and agrees with the experimentally determined [11] zero intrinsic hyperfine magnetic field at ^{57}Fe nuclei, and thus zero Fe magnetic moment.

In contrast to the spin-resolved Fe energy bands, there is a large difference between the spin-up and spin-down Eu energy bands [Figure 8(c,d)], both in energy and in weight (thickness of the bands). This will lead eventually to a large magnetic moment carried by the Eu atoms. The energy bands for a spin-up configuration [Figure 8(c)] are mainly confined to the energy region around −2.0 eV, whereas for a spin-down configuration [Figure 8(d)] the numerous Eu 4*f* bands are located above 9.0 eV. This observation is consistent with an earlier discussion of the DOS originating from the Eu 4*f* states. In both

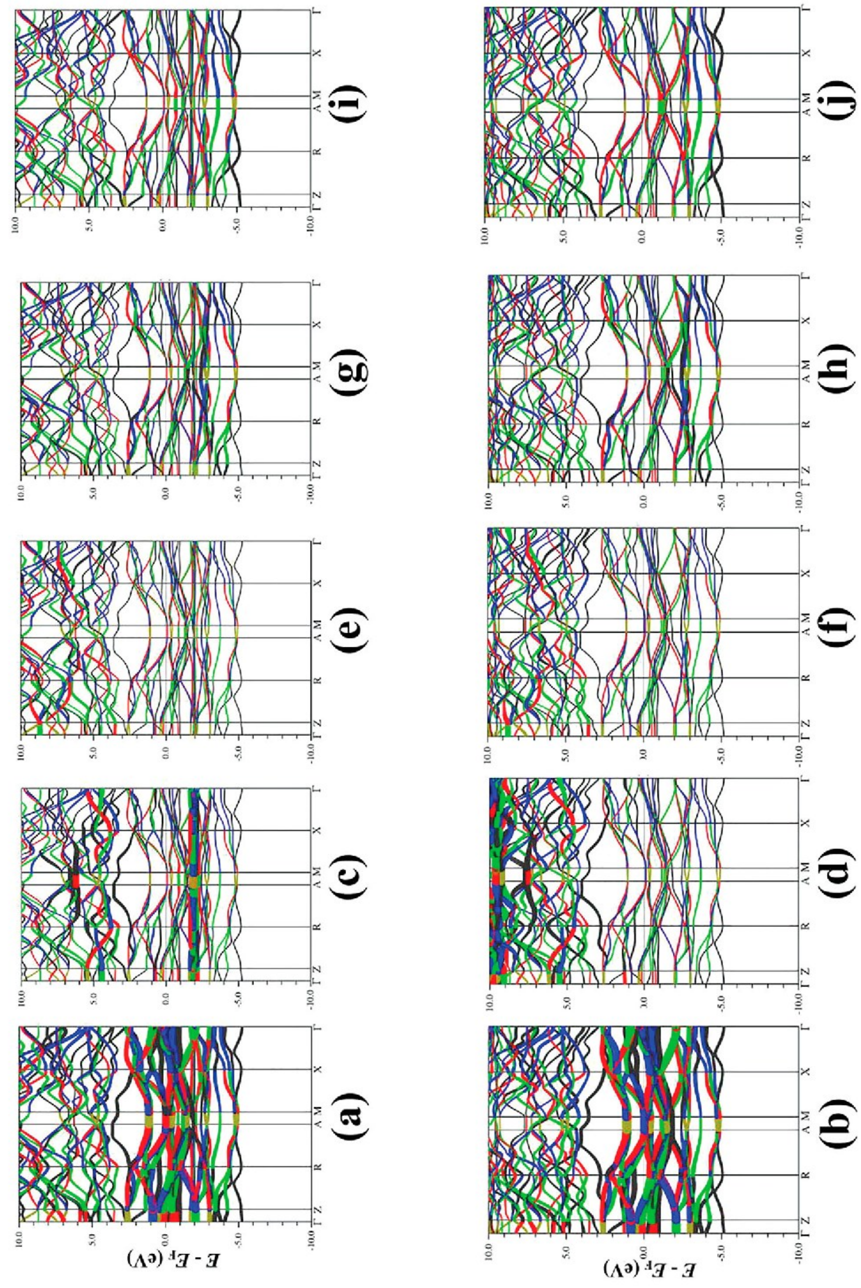

Figure 8. Spin-polarised and atom-resolved band structure of ferromagnetic $RbEuFe_4As_4$. The Fe spin-up (a) and spin-down (b) contributions. The Eu spin-up (c) and spin-down (d) contributions. The Rb spin-up (e) and spin-down (f) contributions. The As_1 spin-up (g) and spin-down (h) contributions. The As_2 spin-up (i) and spin-down (j) contributions.

figures in the energy region above 5 eV, a smaller but symmetric contribution from the Eu 3*d* states is observed.

As one can notice in Figure 8(e,f), the relatively thin bands indicate the small contribution of the Rb states to the total band structure of the superconductor. The contributions from both spin configurations are identical along all directions in the Brillouin zone, and consequently, the magnetic moment of the Rb atoms in $RbEuFe_4As_4$ is negligible. A careful examination of Figure 8(e,f) shows that there is a small contribution from the Rb energy bands across E_F (as indicated by the thinner bands).

At first glance at Figure 8(g–j) one can notice that the As_1 and As_2 atoms do not contribute significantly to the energy band structure of the compound studied. There are, however, two energy regions in which the As contribution is not negligible. The first energy region is in the neighbourhood of E_F. Here, although the bands are thin, they are depicted thicker than the rest of the bands. The other energy region is around −2.0 eV. Both energy regions contain a small number of bands originating from the As atoms.

3.4.2. Orbital-resolved energy band structure of Fe

Figure 9 shows the spin-polarised band structure resulting from various Fe 3*d*-orbitals. One observes that a few bands emerging from the Fe $d_{x^2-y^2}$ orbitals [Figure 9(a,b)] cross the E_F region. Multiple hole-like bands exist around the high symmetry points Γ, X, M, A, and R. Four regions of electron-like bands are observed midway between the connecting high symmetry directions of Γ–X, M–X, A–R, and R–Z. One also observes a negligible dispersion along the A–M and Γ–Z directions. This observation is based on the presence of a tiny slope of the bands in this energy region.

The bands originating from the d_{z^2} orbitals [Figure 9(c,d)] are similar to those due to the $d_{x^2-y^2}$ orbitals. However, they are heavier across E_F and lighter below E_F.

Most of the bands origination from the d_{xy}-orbitals are in the conduction region between 0.9 and 1.0 eV [Figure 9(e,f)]. The contribution to the band structure of $RbEuFe_4As_4$ from the d_{xy} orbitals [Figure 9(g,h)] and the d_{yz} orbitals [Figure 9(i,j)] is minimal. One can conclude that the properties of the compound studied are determined mainly by the $d_{x^2-y^2}$ and d_{z^2} orbitals.

3.4.3. Fermi surfaces

The Fermi surfaces calculated in the first Brillouin zone are displayed in Figure 10. The surfaces are plotted along the indicated high symmetry points. One observes in Figure 10(a) a four-fold hole-like Fermi surface sheet in the central region of the Brillouin zone and along the Γ–Z direction. The triplicate hole pockets at the center of the Brillouin zone are not of the same size. The four corners of the Brillouin zone consist of the Fermi surface sheets of electron-like character, i.e. the electron pockets are aligned parallel to the A–M direction.

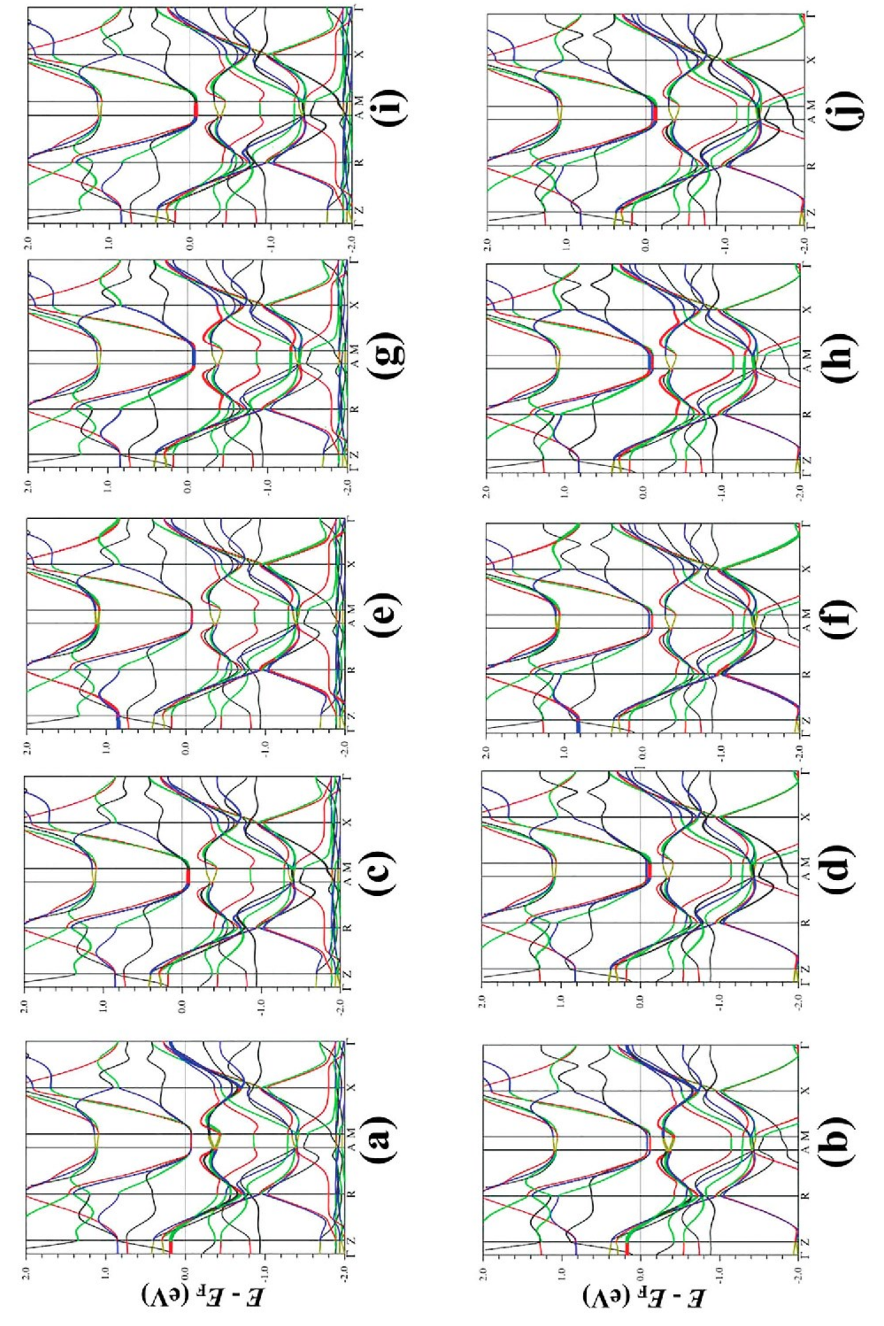

Figure 9. Spin-polarised band structure resulting from the Fe orbitals $d_{x^2-y^2}$ [(a), (b)], d_{z^2} [(c), (d)], d_{xy} [(e), (f)], d_{xz} [(g), (h)], and d_{yz} [(i), (j)].

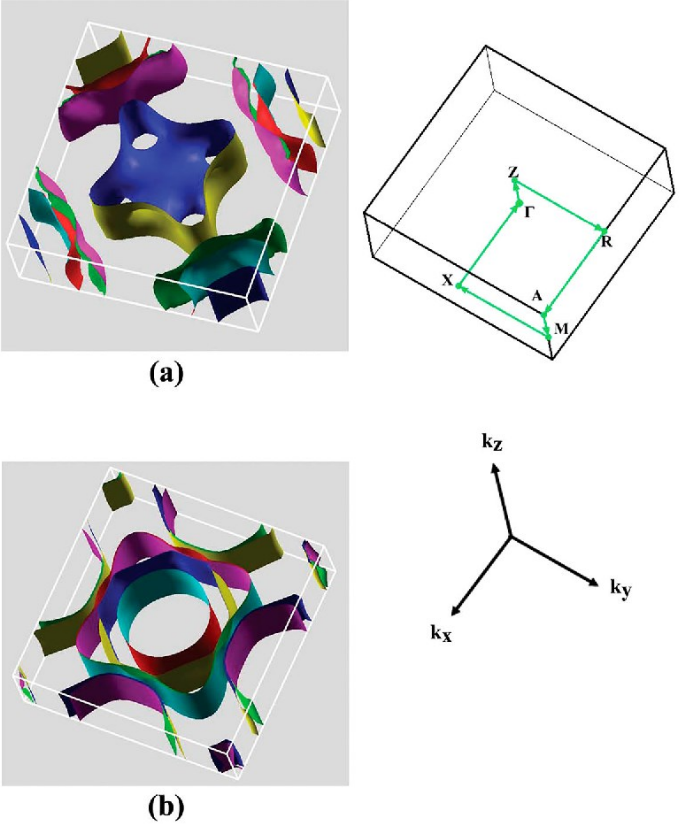

(a)

(b)

Figure 10. Fermi surfaces of the ferromagnetic $RbEuFe_4As_4$ for the spin-up (a) and spin-down (b) configurations.

For the spin-down configuration [Figure 10(b)], three hole-like Fermi sheets about the Γ point are observed. The central sheet is in the form of a uniform cylinder, and no dispersion along the k_z direction is observed. Two distorted cylindrical sheets surrounding the X point can be seen (they are not present for the spin-up configuration). The densities of the Fermi surface sheets in two spin configurations are different (Figure 10). This results from the fact that the bands in the spin-up configuration are closely packed along the Fermi level as compared to those for the spin-down configuration. For example, in Figure 10(a) one only observes a single Fermi surface at the center that is related to a hole pocket. The same Fermi surface topologies have been found in similar Fe-based superconductors [24–26].

The superconductivity of the compound studied has also a signature in the Fermi surface topology (Figure 10). The *d*-wave symmetry of the superconducting gap in high-temperature superconductors is an accepted fact that is used in the development of superconductivity theories and in the interpretation of the experimental results [27]. The largest gaps on the Fermi surfaces (Figure 10) are at the edges of the Brillouin zone and are located in the areas around the centre of the Brillouin zone boundary surfaces. The Fe 3*d* states near the E_F level play a similar role as those in other Fe-based superconductors [28].

3.5. Elastic properties

Some of the elastic parameters of $RbEuFe_4As_4$ were calculated for the optimised lattice parameters obtained from the minimisation of the total energy (Figure 11). The energy minimum of −55927.92 Ry occurs for the optimised volume of the primitive tetragonal unit cell of 1214.6259 a.u.^{3}, which is somewhat smaller than the value of 1358.3110 a.u.^{3} derived from the Rietveld refinement [11]. The calculated equilibrium bulk modulus, B_0 is 138.9 MPa, and its pressure derivative is 25.6. These parameters were obtained using the Birch-Murhanghan equation of state [29,30].

3.6. Magnetic moments and Mössbauer hyperfine parameters

The calculated magnetic moment per formula unit of $RbEuFe_4As_4$ is 6.913 μ_B. This value consists of the contribution (6.7301 μ_B) from the muffin-tin and 0.2099 μ_B) from the interstitial regions. The calculated magnetic moments carried by the Rb, Eu, Fe, As_1, and As_2 atoms are 0.0005, 6.9072, −0.0450, 0.0031, and −0.0152 μ_B, respectively. The calculated Eu magnetic moment is slightly larger than the experimental moment of 6.5 μ_B at 2 K [3] that was derived from the magnetisation measurements. The nearly vanishing calculated magnetic moment of the Fe atoms is in excellent agreement with the experimental observation via ^{57}Fe Mössbauer spectroscopy [11] of zero intrinsic magnetic moment of the Fe atoms down to 2.1 K. The values of the calculated magnetic moments indicate that ferromagnetism in $RbEuFe_4As_4$ is associated exclusively with the Eu atoms.

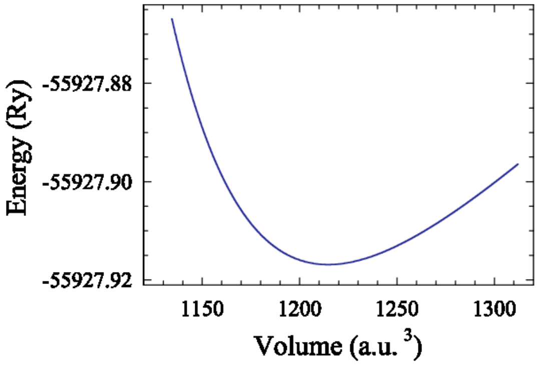

Figure 11. Total energy as a function of primitive cell volume of $RbEuFe_4As_4$.

Three types of hyperfine-interaction parameters can be derived from the fits of Mössbauer spectra [31,32]. These are: the isomer shift δ_0, the principal component of the electric field gradient tensor V_{zz} and the asymmetry parameter η, and the hyperfine magnetic field H_{hf}. They can also be obtained from *ab initio* calculations carried out for any crystalline compound with known crystal structure [33].

The isomer shift can be calculated from the expression $\delta_0 = \alpha[\rho(0) - \rho_{\mathrm{ref}}(0)]$, where $\rho(0)$ and $\rho_{\mathrm{ref}}(0)$ are, respectively, the total electron densities at the Mössbauer nucleus in the compound studied and in the reference material, and α is a calibration constant. In calculating $\rho(0)$, relativistic spin-orbit effects were included to account for the possibility of the penetration of the $p_{1/2}$ electrons into the ^{57}Fe nuclei [34]. The reference material for ^{57}Fe Mössbauer spectroscopy is α-Fe metal (with the *bcc* structure and the lattice constant of 2.8665 Å). The calculated $\rho(0)$ and $\rho_{\mathrm{ref}}(0)$ are 15308.530 and 15309.918 (a.u.)$^{-3}$, respectively. Using the calibration constant $\alpha = -0.291$ (a.u.)^3(mm/s) [35], the calculated values of $\rho(0)$ and $\rho_{\mathrm{ref}}(0)$ imply that $\delta_0 = 0.404$ mm/s (analogous calculations of δ_0 for ^{151}Eu Mössbauer spectra cannot be done as the corresponding α has not been established yet). The calculated δ_0 is close to the experimental value of 0.494(2) mm/s [11].

The measured H_{hf} consists of three main contributions [36]: the Fermi contact term H_c, the magnetic dipolar term, H_{dip}, and the orbital moment term, H_{orb} [31,32]. The first term is generally much greater in magnitude than the other two terms. The Fermi contact term is calculated from the expression $H_c = \frac{8\pi}{3}\mu_{\mathrm{B}}^2(\rho_{\uparrow}(0) - \rho_{\downarrow}(0))$, where $\rho_{\uparrow}(0)$ and $\rho_{\downarrow}(0)$ are the spin-up and spin-down densities at the Mössbauer nucleus, respectively. The calculated magnitudes of H_c at the ^{57}Fe and ^{151}Eu nuclei are 8.9 and 266.5 kOe, respectively. These should be compared with the corresponding experimental H_{hf} values (at 0 K) of 6.17(2) and 257.4(4.3) kOe [11].

The calculated V_{zz} and η are 5.270 × 10^{20} V/m^2 and 0.8734 for ^{57}Fe Mössbauer spectra [11]. The calculated V_{zz} and η imply that the value of the quadrupole splitting $\Delta = \frac{1}{2}\, eQ|V_{zz}|\sqrt{1+\eta^2/3}$ (Q = 0.15 b is the electric quadrupole moment of the 14.4-keV excited state of ^{57}Fe nucleus [37]) should be 0.0921 mm/s. For ^{151}Eu Mössbauer spectra, the calculated V_{zz} and η are -49.659×10^{20} V/m^2 and 0.0 (the zero value is consistent with the point symmetry $4/mmm$ of the Eu site). The experimental Δ (at 0 K) of 0.1182 mm/s [11] is in excellent agreement with the predicted value of 0.0921 mm/s. Similarly, good agreement is found between the calculated values of V_{zz} and η and the corresponding experimental values (at 0 K) of $-47.0(6) \times 10^{20}$ V/m^2 and 0.0 derived from the ^{151}Eu Mössbauer spectra [11].

4. Conclusions

We present the results of *ab-initio* calculations of the electronic structure, magnetism, and hyperfine interaction parameters of the new $RbEuFe_4As_4$

superconductor. The calculations suggest the presence of a mixture of ionic, covalent, and metallic bonding between the constituent atoms. We discuss in detail the electronic band structure and the density of states. We show that, in agreement with the experimental results, the magnetic moment is due to the strongly localised Eu 4*f* states. We demonstrate that an almost zero magnetic moment carried by the Fe atoms results from an apparent symmetry of the spin-up and spin-down states. The Fermi surfaces along various directions in the Brillouin zone are presented. We show that the calculated ^{57}Fe and ^{151}Eu Mössbauer hyperfine interaction parameters are in good agreement with the corresponding parameters derived from the Mössbauer spectra.

Disclosure statement

No potential conflict of interest was reported by the authors.

Funding

This work was supported by the Natural Sciences and Engineering Research Council of Canada (NSERC).

References

[1] A. Iyo, K. Kawashima, T. Kinjo, T. Nishio, S. Ishida, H. Fujihisa, Y. Gotoh, K. Kihou, H. Eisaki, and Y. Yoshida, *New-structure-type Fe-based superconductors: $CaAFe_4As_4$ (A = K, Rb, Cs) and $SrAFe_4As_4$ (A = Rb, Cs)*, J. Am. Chem. Soc. 138 (2016), pp. 3410–3415

[2] K. Kawashima, T. Kinjo, T. Nishio, S. Ishida, H. Fujihisa, Y. Gotoh, K. Kihou, H. Eisaki, Y. Yoshida, and A. Iyo, *Superconductivity in Fe-Based Compound $CaAFe_4As_4$ (A = Rb and Cs)*, J. Phys. Soc. Jpn. 85 (2016), p. 064710.

[3] Y. Liu, Y.-B. Liu, H. Jiang, Z.-C. Wang, A. Ablimit, W.-H. Jiao, Q. Tao, C.-M. Feng, Z.-A. Xu, and G.-H. Cao, *Superconductivity and ferromagnetism in hole-doped $RbEuFe_4As_4$*, Phys. Rev. B 93 (2016), p. 214503.

[4] Y. Liu, Y.-B. Liu, Q. Chen, Z.-T. Tang, W.-H. Jiao, Q. Tao, Z.-A. Xu, and G.-H. Cao, *A new ferromagnetic superconductor: $CsEuFe_4As_4$*, Sci. Bull. 61 (2016), pp. 1213–1220

[5] W.R. Meier, T. Kong, U.S. Kaluarachchi, V. Taufor, N.H. Jo, G. Drachuck, A.E. Böhmer, S.M. Saunders, A. Sapkota, A. Kreyssig, M.A. Tanatar, R. Prozorov, A.I. Goldman, F.F. Balakirev, A. Gurevich, S.L. Bud'ko, and P.C. Canfield, *Anisotropic thermodynamic and transport properties of single-crystalline $CaKFe_4As_4$*, Phys. Rev. B 94 (2016), p. 064501.

[6] L.N. Bulaevskii, A.I. Buzdin, M.L. Kulić, and S.V. Panjukov, *Coexistence of superconductivity and magnetism theoretical predictions and experimental results*, Adv. Phys. 34 (1985), pp. 175–261.

[7] S. Zapf and M. Dressel, *Europium-based iron pnictides: A unique laboratory for magnetism, superconductivity and structural effects*, Rep. Prog. Phys. 80 (2017), p. 016501.

[8] Y. Liu, Y.-B. Liu, Q. Tao, C.-M. Feng, and G.-H. Cao, *$RbEu(Fe_{1-x}Ni_x)_4As_4$: From a ferromagnetic superconductor to a superconducting ferromagnet*, Phys. Rev. B 96 (2017), p. 224510.

[9] J.-K. Bao, K. Willa, M.P. Smylie, H. Chen, U. Welp, D.Y. Chung, and M.G. Kanatzidis, *Single crystal growth and study of the ferromagnetic superconductor* $RbEuFe_4As_4$, Cryst. Growth Des. 18 (2018), pp. 3517–3523.

[10] M.P. Smylie, K. Willa, J.-K. Bao, K. Ryan, Z. Islam, H. Claus, Y. Simsek, Z. Diao, A. Rydh, A.E. Koshelev, W.-K. Kwok, D.Y. Chung, M.G. Kanatzidis, and U. Welp, *Anisotropic superconductivity and magnetism in single-crystal* $RbEuFe_4As_4$, Phys. Rev. B 98 (2018), p. 104503.

[11] M.A. Albedah, F. Nejadsattari, Z.M. Stadnik, Y. Liu, and G.-H. Cao, *Mössbauer spectroscopy measurements on the 35.5 K superconductor* $Rb_{1-\delta}EuFe_4As_4$, Phys. Rev. 97 (2018), p. 144426.

[12] C. Xu, Q. Chen, and C. Cao, *Unique crystal field splitting and multiband RKKY interactions in Ni-doped* $EuRbFe_4As_4$, Commun. Phys. 2 (2019), p. 16.

[13] P. Blaha, K. Schwartz, G. Madsen, D. Kvasnicka, and J. Luitz, *WIEN2k: An Augmented Plane Wave Plus Local Orbitals Program for Calculating Crystal Properties*, Karlheinz Schwarz, Technical Universität Wien, Austria, 1999.

[14] F. Nejadsattari, P. Wang, Z.M. Stadnik, Y. Nagata, and T. Ohnishi, *Ab-initio, magnetic, and* ^{155}Gd *Mössbauer spectroscopy study of* $GdRhO_3$, J. Alloys Compd. 725 (2017), pp. 1098–1105.

[15] J.P. Perdew, S. Burke, and M. Ernzerhof, *Generalized gradient approximation made simple*, Phys. Rev. Lett. 77 (1996), pp. 3865–3868.

[16] V.I. Anisimov and O. Gunnarsson, *Density-functional calculation of effective Coulomb interactions in metals*, Phys. Rev. B 43 (1991), p. 7570–7574.

[17] V.I. Anisimov, J. Zaanen, and O.K. Andersen, *Band theory and Mott insulators: Hubbard U instead of Stoner I*, Phys. Rev. B 44 (1991), p. 943–954.

[18] V.N. Antonov, B.N. Harmon, and A.N. Yaresko, *Electronic structure of mixed-valent and charge-ordered Sm and Eu pnictides and chalcogenides*, Phys. Rev. B 72 (2005), p. 085119.

[19] R.F.W. Bader, *Atoms in Molecules: A Quantum Theory*, Oxford University Press, Oxford, 1991.

[20] P.E. Blöchl, O. Jepsen, and O.K. Andersen, *Improved tetrahedron method for Brillouin-zone integrations*, Phys. Rev. B 49 (1994), pp. 16223–16233.

[21] A.P. Drozdov, P.P. Kong, V.S. Minkov, S.P. Besedin, M.A. Kuzovnikov, S. Mozaffari, J. Balicas, F.F. Balakirev, D.E. Graf, V.B. Prakapenka, E. Greenberg, D.A. Knyazev, M. Tkacz, and M.I. Eremets, *Superconductivity at 250 K in lanthanum hydride under high pressures*, Nature 569 (2019), pp. 528–531.

[22] Y.I. Seo, W.J. Choi, S. Kimura, and Y.S. Kwon, *Evidence for a preformed Cooper pair model in the pseudogap spectra of a* $Ca_{10}(Pt_4As_8)(Fe_2As_2)_5$ *single crystal with a nodal superconducting gap*, Sci. Rep. 9 (2019), p. 3987.

[23] A. Foley, S. Verret, A.-M.S. Tremblay, and D Sénéchal, *Coexistence of superconductivity and antiferromagnetism in the Hubbard model for cuprates*, Phys. Rev. B 99 (2019), p. 184510.

[24] X. Shi and G. Wang, *Electronic structure and magnetism of the multiband new superconductor* $CaRbFe_4As_4$, J. Phys. Soc. Jpn. 85 (2016), p. 124714.

[25] F. Lochner, F. Ahn, T. Hickel, and I. Eremin, *Electronic properties, low-energy Hamiltonian, and superconducting instabilities in* $CaKFe_4As_4$, Phys. Rev. B 96 (2017), p. 094521.

[26] D.V. Suetin and I.R. Shein, *Electronic properties and Fermi surface for new layered high-temperature superconductors* $CaAFe_4As_4$ *(A = K, Rb, and Cs): FLAPW-GGA calculations*, J. Supercond. Nov. Magn. 31 (2018), pp. 1683–1692.

[27] M. Hashimoto, I.M. Vishik, R.-H. He, and T.P. Devereaux, *Energy gaps in high-transition-temperature cuprate superconductors*, Nature Phys. 10 (2014), pp. 483–495.

[28] A. Chubukov, *Chubukov, Iron-based super conductivity*, in *Springer Series in Materials Science*, P. D. Johnson, G. Xu, W.-G. Yin, eds., Berlin: Springer, 2015. pp. 255–329.

[29] F. Birch, *Finite elastic strain of cubic crystals*, Phys. Rev. 71 (1947), pp. 809–824.

[30] F.D. Murhanghan, *The compressibility of media under extreme pressures*, Proc. Natl. Acad. Sci. 30 (1944), pp. 244–247.

[31] N.N. Greenwood and T.C. Gibb, *Mössbauer Spectroscopy*, Chapman and Hall, London, 1971.

[32] P. Gütlich, E. Bill, and A. Trautwein, *Mössbauer Spectroscopy and Transition Metal Chemistry*, Springer, Berlin, 2011.

[33] P. Blaha, *Calculations of Mössbauer parameters in solids by DFT bandstructure calculations*, J. Phys.: Conf. Series 217 (2010), p. 012009.

[34] F. Nejadsattari, Z.M. Stadnik, and J. Żukrowski, *Mössbauer spectroscopy study of a new layered iron oxyselenide* $Na_2Fe_2Se_2O$, J. Alloys Compd. 639 (2015), pp. 547–555.

[35] U.D. Wdowik and K. Reubenbauer, *Calibration of the isomer shift for the 14.4-keV transition in* ^{57}Fe *using the full-potential linearized augmented plane-wave method*, Phys. Rev. B 76 (2007), p. 155118.

[36] F. Nejadsattari, Z.M. Stadnik, J. Przewoźnik, and K.H.J. Buschow, *Mössbauer spectroscopy, magnetic, and ab-initio study of the Heusler compound* Fe_2NiGa, Physica B 477 (2015), pp. 113–122.

[37] G. Martínez-Pinedo, P. Schwerdtfeger, E. Caurier, K. Langanke, W. Nazarewich, and T. Söhnel, *Nuclear quadrupole moment of* ^{57}Fe *from microscopic nuclear and atomic calculations*, Phys. Rev. Lett. 87 (2001), p. 062701.